STUTTGARTER BEITRÄGE ZUR PRODUKTIONSFORSCHUNG

Philipp Reinhard Miermeister

»Model Selection and Parameter Optimization for Cable-Driven Parallel Robots«

Fraunhofer IPA

Universität Stuttgart

STUTTGARTER BEITRÄGE ZUR PRODUKTIONSFORSCHUNG BAND 128

Philipp Reinhard Miermeister

»Model Selection and Parameter Optimization for Cable-Driven Parallel Robots«

Herausgeber

Univ.-Prof. Dr.-Ing. Thomas Bauernhansl[1,2]
Univ.-Prof. Dr.-Ing. Dipl.-Kfm. Alexander Sauer[1,3]
Univ.-Prof. Dr.-Ing. Kai Peter Birke[4]
Univ.-Prof. Dr.-Ing. Marco Huber[1,2]

[1] Fraunhofer-Institut für Produktionstechnik und Automatisierung IPA, Stuttgart
[2] Institut für Industrielle Fertigung und Fabrikbetrieb (IFF) der Universität Stuttgart
[3] Institut für Energieeffizienz in der Produktion (EEP) der Universität Stuttgart
[4] Institut für Photovoltaik (*ipv*) der Universität Stuttgart

Kontaktadresse:
Fraunhofer-Institut für Produktionstechnik und Automatisierung IPA
Nobelstr. 12
70569 Stuttgart
Telefon 0711 970-1100
info@ipa.fraunhofer.de
www.ipa.fraunhofer.de

Bibliographische Information der Deutschen Nationalbibliothek

Die Deutsche Nationalbibliothek verzeichnet diese Publikation in der Deutschen Nationalbibliographie; detaillierte bibliografische Daten sind im Internet über http://dnb.de abrufbar.

Zugl.: Stuttgart, Univ., Diss., 2020

D 93

2021

Druck und Weiterverarbeitung:

Fraunhofer Verlag, Mediendienstleistungen, Stuttgart, 2021
Für den Druck des Buches wurde chlor- und säurefreies Papier verwendet.

Dieses Werk ist einschließlich aller seiner Teile urheberrechtlich geschützt. Alle Rechte, insbesondere die der Übersetzung, des Nachdrucks, der Wiedergabe, sind vorbehalten.

Model Selection and Parameter Optimization for Cable-Driven Parallel Robots

Von der Fakultät Konstruktions-, Produktions- und Fahrzeugtechnik
der Universität Stuttgart
zur Erlangung der Würde eines Doktor-Ingenieurs (Dr.-Ing.)
genehmigte Abhandlung

Vorgelegt von
Philipp Reinhard Miermeister
aus Aachen

Hauptberichter:	PD Dr.-Ing. Andreas Pott
1. Mitberichter:	Prof. Dr. rer. nat. Heinrich H. Bülthoff
2. Mitberichter:	Univ.-Prof. Dr.-Ing. Dr. h.c. mult. Alexander Verl
Tag der mündlichen Prüfung:	09. Oktober 2020

Institut für Steuerungstechnik der Werkzeugmaschinen und Fertigungseinrichtungen
(ISW)
der Universität Stuttgart

2021

Foreword of the Author

This thesis results from my work as a research fellow at the Fraunhofer Institute for Manufacturing Engineering and Automation IPA in Stuttgart and the Max Planck Institute for Biological Cybernetics in Tübingen, Germany.

I particularly want to thank Dr. Andreas Pott for the unique mentorship and outstanding engagement during all stages of my PhD thesis. His clear-minded critical thinking provided me with invaluable insights and was of great help to me while navigating the most complex topics. I am especially thankful to Prof. Heinrich H. Bülthoff for giving me the unique opportunity to be the central part of the CableRobot Simulator project and for his visionary thinking, which was always a great source of inspiration for me.

I want to thank my peers from the Fraunhofer Institute Dr. Valentin Schmidt, Dr. Werner Kraus, and Bernd Winkler for all their ideas, enthusiasm, and the great time we had together.

I wish to express my gratitude to my colleagues from the Max Planck Institute Rainer Boss, Maria Lächele, Joachim Tesch, Dr. Harald Teufel, and Michael Kerger for the good working atmosphere and all their efforts while bringing the CableRobot Simulator to life.

A special thanks goes to Dr. Fred Mäder from Waagner Biro Stage Systems for his exceptional commitment and belief in the project and to Prof. Alexander Verl for the review of my thesis and for being part of the committee.

I am most thankful to my parents, Anne-Marie und Reinhard for their kindness and unconditional support over the years and my brother Christian for the many welcome distractions from my desk work with our various exciting house restoration projects.

Finally, I want to express my deepest gratitude to my wonderful wife Ima for her love and uplifting spirit during the challenging moments and my little son Matthis who often amazes me with his insights on the nature of reality and adds so much joy to my life.

Zürich, December 2020 Philipp Miermeister

Zusammenfassung

Parallele Seilroboter sind vielseitige Robotersysteme, die skaliert und rekonfiguriert werden können, um den spezifischen Anforderungen verschiedenster Anwendungen gerecht zu werden. Während unterschiedliche Modelle, Berechnungsmethoden und Parameteridentifikationsschemata in der Seilroboterliteratur zu finden sind, fehlt bisher eine systematische Analyse des Modellauswahlprozesses für Seilroboter. Die Frage nach dem optimalen Modell für eine bestimmte Anwendung kann nur durch eine gleichzeitige Betrachtung der Modellstruktur zusammen mit seiner optimalen Parametrisierung gezeigt werden. Dies muss im Kontext eines eigenständigen physikalischen Robotermodells erfolgen, der auch diejenigen physikalischen Eigenschaften einbezieht, die im Kontrollmodell nicht vorhanden sind. In dieser Arbeit wird die Wirkung verschiedener Modellierungsannahmen für die Analyse der Genauigkeit der Positionsverfolgung und des Arbeitsbereichs mit Hilfe eines Meta-Modells untersucht. Mit Schwerpunkt auf den sicherheitskritischen Echtzeit-Anwendungen, stellt sich die eingeschränkte Modellkomplexität für einen zuverlässigen und sicheren Betrieb als unerlässlich dar. Am Anfang der hier gezeigten Arbeit stehen die Kinematikmodelle, die als Mindestanforderung für die Steuerung von Seilrobotern zu betrachten sind. Durch schrittweise Erhöhung der Modellkomplexität hin zu einem elastostatischen Modell, wird ermöglicht den inneren Spannungszustand abzubilden, der einem überbestimmten Seilroboter inhärent ist.

Die Kombination von Modellierung und Parameteroptimierung in der Analyse zusammen mit einem physikalischen Referenzmodell erlaubt es, die optimale Leistung abzuschätzen, die für eine bestimmte Modellklasse erreichbar ist. Dies ermöglicht fundierte Entscheidungen auf der Grundlage der geschätzten Leistung zu treffen. Die experimentelle Analyse und Validierung der Modelle erfolgt auf dem Cable-Robot-Simulator, der im Rahmen dieser Arbeit entwickelt wurde. Die Ergebnisse zeigen den Vorteil der gleichzeitigen Modellerstellung und Optimierung, welcher durch den Vergleich von optimierten Modellen und einem Nominalmodell erhalten wird. Mit diesem Ansatz kann die Genauigkeit eines nominalen Modells mit einem mittleren Positionsfehler von 39,8 mm und mittlereren Rotationsfehler von 1,19 Grad auf einen mittleren Positionsfehler von 2,73 mm und Rotationsfehler von 0,11 Grad für ein optimales elastostatisches Modell verbessert werden. Kraftvorhersagen für das elastostatische Modell wurden von 2426 N für das nominale Modell auf 582 N für das optimale Modell für einem Gesamtkraftbereich von 9000 N verbessert. Da der CableRobot-Simulator als höchst repräsentativ für Seilroboter bzgl. Architektur, Maßstab, Genauigkeit und Sicherheitsanforderungen anzusehen ist, sollten die Ergebnisse aus dieser Arbeit gut auf andere Systeme dieser Klasse übertragbar sein.

Short Summary

While various models, computation methods, and parameter identification schemes are proposed in the literature on CDPRs, a systematic analysis of the model selection process for CDPRs is missing. The answer to the question, which is the optimal model for a specific application, can only be provided by a concurrent consideration of the model structure together with its optimal parametrization. This must be done in the context of a distinct physical robot model which incorporates physical properties not present in the control model.

This thesis investigates the effect of different modeling assumptions using a meta-model for the analysis of the position tracking accuracy and workspace. Focusing on safety critical real-time applications such as motion simulation with human-in-the loop control, constrained model complexity is essential for reliable and safe operation. The investigation starts with kinematics models that can be considered as minimal requirement for the operation of CDPRs and gradually increases model complexity to an elastostatic model which allows to deal with the inner tension state inherent to overconstrained CDPRs.

Combining modeling and parameter optimization in the analysis together with a ground truth model allows to estimate the optimal performance which can be reached for a certain model class. This allows for an informed decision based on the estimated performance rating in context of the ground truth model. The experimental investigation and validation of the models is done on the Cable-Robot Simulator which was developed during this work. Results show the advantage of concurrent model building and optimization by comparing the prediction accuracy of optimized models of different complexity with the nominal model which is obtained by highly accurate laser-tracking measurements. With this approach the accuracy of a nominal model was improved from a mean position error of 39.8 mm and mean rotation error of 1.19 deg to a mean position error of 2.73 mm and rotation error of 0.11 deg for an optimal elastostatic model. Force predictions for the elastostatic model were improved from 2426 N for the nominal model to 582 N for the optimal model for a total force range of 9000 N. The main contribution to model accuracy is provided by an accurate estimate of the platform load and secondary by an accurate estimate of the system stiffness. Considering the CableRobot Simulator as highly representative for cable-driven parallel robots by means of architecture, scale, accuracy, and safety requirements, experimental results from this thesis should transfer well to other systems of this class.

Contents

Symbols

$\mathbf{A}^{\mathrm{T}}$	Structure matrix
$\mathbf{A}_{1}^{\mathrm{T}}$	Frist part of partitioned structure matrix
$\mathbf{A}_{2}^{\mathrm{T}}$	Second part of partitioned structure matrix
$\mathbf{A}_{[\mathrm{S_D}]}^{\mathrm{T}}$	Structure matrix for set of dependent cables
$\mathbf{A}_{[\mathrm{S_I}]}^{\mathrm{T}}$	Structure matrix for set of independent cables
$\mathbf{A}_{\mathrm{sf}}^{\mathrm{T}}$	Structure matrix for cabin truss
$\mathcal{K}_{\mathrm{M}}$	Cartesian reference frame of the control model
$\mathcal{K}_{\mathrm{PHYS}}$	Cartesian reference frame of the physical system
$\Delta\mathbf{a}$	Frame geometry adjustment matrix
$\Delta\mathbf{a}_{\mathrm{max}}$	Maximal frame adjustment value
$\Delta\mathbf{a}_{\mathrm{min}}$	Minimal frame adjustment value
$\Delta\mathbf{b}$	Cabin geometry adjustment matrix
$\Delta\epsilon_{\bar{\mathrm{f}}}$	Difference in mean force prediction error
$\Delta\epsilon_{\bar{\mathrm{x}}}$	Difference in mean pose error
$\Delta\mathbf{q}$	Cable elongation
$\Delta\bar{\mathbf{q}}$	Residual cable length for all poses
$\Delta\mathbf{w}_{\mathrm{xy}}$	Wrench projection on xy-plane
E	Wire rope elasticity module
$\mathbf{H}$	Matrix kernel
$\mathbf{I}$	Identity matrix
$\mathbf{I}_{\mathrm{d}}$	Inertia tensor of drum
$\mathbf{I}_{\mathrm{hc}}$	Inertia tensor of heli cabin
$\mathbf{I}_{\mathrm{hc,z}}$	Inertia tensor of heli cabin around yaw axis
$\mathbf{I}_{\mathrm{st}}$	Inertia tensor of stator
$\mathbf{J}_{\mathrm{qx}}$	Jacobian for mapping of platform and cable velocities
$\mathbf{J}_{\mathrm{xq}}$	Inverse mapping of platform and cable velocities
$\mathbf{K}$	Joint space stiffness
$\mathbf{K}_{[\mathrm{S_D}]}$	Joint space stiffness
$\mathbf{K}_{[\mathrm{S_I}]}$	Joint space stiffness
$\mathbf{K}_{\mathrm{sf}}$	Joint space stiffness for truss system
$\mathbf{K}_{\mathrm{C}}$	Joint space cable stiffness
$\mathbf{K}_{\mathrm{G}}$	Geometrical stiffness
$\mathbf{K}_{\mathrm{G}[\mathrm{S_D}]}$	Geometrical stiffness for dependent cables

$\mathbf{K}_{\mathrm{G[S_I]}}$	Geometrical stiffness for independent cables
$\mathbf{K}_{\mathrm{Ga}}$	Geometrical stiffness regarding changes in frame geometry parametrization a
$\mathbf{K}_{\mathrm{Gab}}$	Geometrical stiffness regarding changes in frame and platform geometry parametrization ab
$\mathbf{K}_{\mathrm{wx}}$	System stiffness
$\mathbf{M}$	Hessian
$\mathbf{0}$	Zero matrix
$\mathbf{J}_{\mathrm{P}}$	Geometric Jacobian
$\mathbf{R}_{0\mathrm{P}}$	Platform rotation matrix
$\mathbf{R}_{\mathrm{x}}(\phi_{\mathrm{x}})$	Elemental rotation around x-axis
$\mathbf{R}_{\mathrm{y}}(\phi_{\mathrm{y}})$	Elemental rotation around y-axis
$\mathbf{R}_{\mathrm{z}}(\phi_{\mathrm{z}})$	Elemental rotation around z-axis
$\mathrm{S_C}$	Paramter set
$\mathrm{S_D}$	Parameter set of dependent model structure
$\mathrm{S_I}$	Parameter set of independent model structure
S	Paramter set
$\mathbf{T}_{\mathrm{A}}$	Torque form heli platform
$\mathbf{T}_{\mathrm{M}}$	Heli motor torque
$\mathbf{a}_{\mathrm{N}}$	Nominal frame geometry
$\mathbf{a}_i$	Frame attachment point i
$\mathbf{a}_{\mathrm{ini}}$	Initial frame geometry
$\mathbf{a}_{\mathrm{opt}}$	Optimal frame geometry
$\mathbf{a}_{\mathrm{rand}}$	Random frame geometry matrix
$\mathbf{a}_{\mathrm{x_1}}$	Sub-vector element form frame geometry
α_{max}	Maximal angular acceleration for heli cabin
$\mathbf{b}_{\mathrm{N}}$	Nominal platform geometry
$\mathbf{b}_i$	Platform attachment point i
$\mathbf{b}_{\mathrm{opt}}$	Optimal platform geometry
β	Pulley angle around center axis
κ	Matrix condition number
$d_{\mathcal{W}}$	Max distance of a sample set
d_{a}	Max distance of cable attachment points
d_{r}	Drum radius
$\delta\mathbf{l}_i$	Differential cable vector
$\delta\boldsymbol{\phi}$	Infinitesimal euler rotations
$\delta\phi_{\mathrm{x}}$	Infinitesimal rotation around x-axis
$\delta\phi_{\mathrm{y}}$	Infinitesimal rotation around y-axis
$\delta\phi_{\mathrm{z}}$	Infinitesimal rotation around z-axis
$\delta\mathbf{u}_i$	Cable unit vector differential
$\mathbf{e}_{\mathrm{x}}$	Unit base vector x

$\mathbf{e}_{\mathrm{y}}$	Unit base vector y
$\mathbf{e}_{\mathrm{z}}$	Unit base vector z
$\boldsymbol{\kappa}_{\mathrm{lin}}$	Linear elastic model
$\epsilon_{\bar{\mathrm{f}}}$	Mean force tracking error
ϵ_{Φ}	Rotation error
$\epsilon_{\Phi_{\mathrm{x}}}$	Rotation error around x-axis
$\epsilon_{\Phi_{\mathrm{y}}}$	Rotation error around y-axis
$\epsilon_{\Phi_{\mathrm{z}}}$	Rotation error around z-axis
ϵ_{q}	Cable length error
$\epsilon_{\bar{\mathrm{q}}}$	Mean cable length error
$\epsilon_{\bar{\mathrm{q}}_{\mathrm{opt}}}$	Mean optimal cable length error
$\epsilon_{\bar{\mathrm{q}}_{\mathrm{V}}}$	Mean validation cable length error
ϵ_{r}	Position error
$\epsilon_{\mathrm{r}_{\mathrm{x}}}$	Position error x
$\epsilon_{\mathrm{r}_{\mathrm{y}}}$	Position error y
$\epsilon_{\mathrm{r}_{\mathrm{z}}}$	Position error z
ϵ_{x}	Pose error
$\epsilon_{\mathrm{x}_{\mathrm{N}}}$	Pose error for nominal model
ϵ_{x_j}	Pose error at pose j
$\epsilon_{\bar{\mathrm{x}}}$	Mean pose error
$\epsilon_{\bar{\mathrm{r}}}$	Mean position error
$\epsilon_{\bar{\mathrm{r}}_{\mathrm{opt}}}$	Mean optimal position error
$\epsilon_{\bar{\mathrm{r}}\mathrm{V}}$	Mean validation position error
$\epsilon_{\bar{\Phi}}$	Mean pose rotation error
$\epsilon_{\bar{\Phi}_{\mathrm{opt}}}$	Mean optimal rotation error
$\epsilon_{\bar{\Phi}_{\mathrm{V}}}$	Mean validation rotation error
$\epsilon_{\mathrm{x}_{\mathrm{opt}}}$	Pose error for optimal model
$\mathbf{f}$	Cable forces
$\mathbf{f}_{\mathrm{A}}$	Inner forces of heli platform
$\mathbf{f}_{[\mathrm{D}]}$	Forces of dependent cables
$\mathbf{f}_{[\mathrm{I}]}$	Forces of independent cables
$\mathbf{f}_{\mathrm{T}}$	Constant motor torque force
$\bar{\mathbf{f}}_{\mathrm{M}}$	Measured cable forces for sample set
$\hat{\mathbf{f}}$	Mixed force vector
$\mathbf{f}_{\mathrm{ref}}$	Reference cable forces
$f_{\mathrm{sf}i}$	Truss member force i
$\mathbf{f}_{\mathrm{M}}$	Measured cable forces
$\bar{\mathbf{f}}_{\mathrm{M}}$	Set of measured cable forces
$\mathbf{f}_{\mathrm{max}}$	Maximal allowed cable forces
$\mathbf{f}_{\mathrm{m}}$	Central cable forces
$\mathbf{f}_{\mathrm{min}}$	Minimal allowed cable forces

$\mathbf{f}_{\mathrm{P}}$	Predicted cable forces
$\mathbf{f}_{\mathrm{sf}}$	Internal forces of cabin space frame
$\boldsymbol{\upsilon}$	Forward kinematics
$\boldsymbol{\upsilon}_{\mathrm{el}}$	Elastostatic forward kinematics
$\boldsymbol{\upsilon}_{\mathrm{opt,c}}$	Optimal model from candidate set
$\hat{\boldsymbol{\upsilon}}$	Inverse kinematics of ground truth model
$\boldsymbol{\gamma}$	Statics for kinematics model
$\boldsymbol{\gamma}_{\mathrm{sk}}$	Statics for standard kinematics model
$\boldsymbol{\varphi}$	Inverse kinematics
$\boldsymbol{\varphi}_{\mathrm{N}}$	Nominal inverse kinematics
$\boldsymbol{\varphi}_{\mathrm{el}}$	Elastostatic model
$\boldsymbol{\varphi}_{\mathrm{ex}}$	Extended kinematics model
$\boldsymbol{\varphi}_{j}$	Evaluated model a j-th sampling point
$\boldsymbol{\varphi}_{\mathrm{opt}}$	Optimal model
$\boldsymbol{\varphi}_{\mathrm{opt,c}}$	Optimal model from candidate set
$\boldsymbol{\varphi}_{\mathrm{pl}}$	Pulley model
$\hat{\boldsymbol{\varphi}}$	Ground truth model
$\boldsymbol{\varphi}_{\mathrm{sg}}$	Surrogate model
$\boldsymbol{\varphi}_{\mathrm{sk}}$	Inverse kinematics standard model
$\mathbf{k}$	Cable stiffness
$\mathbf{k}_{\mathrm{F}}$	Cable unit stiffness
$\mathbf{k}_{\mathrm{F\,opt}}$	Optimal stiffness parameters
$\mathbf{k}_{\mathrm{sf}}$	Carbon fiber space frame stiffness
$\mathbf{l}_{i}$	Cable vector i
m	Number of cables
m_{I}	Number of independent cables
m_{c}	Cable mass
$\boldsymbol{\eta}$	Model composition
$\boldsymbol{\eta}_{\mathrm{el}}$	Standard model for elastostatics
n	Number of degrees of freedom (DOF)
n_{c}	Number of model candidates
n_{p}	Number of model parameters
n_{q}	Number of joint space sensor readings
n_{s}	Number of samples
$\mathbf{p}$	Parameter vector
$\mathbf{p}_{\mathrm{A},i}$	Pulley reference point
$\mathbf{p}_{\mathrm{B},i}$	Pulley cable contact point
$\mathbf{p}_{\mathrm{M},i}$	Pulley center point
$\mathbf{p}_{\mathrm{D}}$	Model design parametrization
$\hat{\mathbf{p}}$	Ground truth parametrization
$\mathbf{p}_{\mathrm{N}}$	Nominal model parametrization

$\mathbf{p}_{\mathrm{ab}}$	Geometric model parameters
$\mathbf{p}_{\eta}$	Parameterized model composition
$\mathbf{p}_{\eta_{\mathrm{opt}}}$	Optimal parametrization for model composition
$\mathbf{p}_{\kappa}$	Elastic model parametrization
$\mathbf{p}_{\mathrm{ex}}$	Parametrization for model extension
$\mathbf{p}_{\gamma}$	Statics model parametrization
$\mathbf{p}_{\mathrm{ini}}$	Initial model parametrization
p_j	Paramter j
$\mathbf{p}_k$	Parametrization k
$\mathbf{p}_{k+1}$	Parametrization $k+1$
$\mathbf{p}_{\varphi}$	Standard kinematics parameter vector
$\hat{\mathbf{p}}_{\varphi}$	Kinematics ground truth parametrization
$\mathbf{p}_{\mathrm{lin}}$	Linear elastic model parametrization
$\mathbf{p}_{\mathrm{opt}}$	Optimal model parametrization
$\mathbf{p}_{\mathrm{pl}}$	Pulley model parametrization
$\hat{\mathbf{p}}$	Physical or ground truth parameters
$\boldsymbol{\phi}$	Platform rotation vector
$\boldsymbol{\phi}_{\mathrm{m}}$	Measured platform rotation vector
$\mathbf{q}_{\mathrm{N}}$	Nominal cable length
$\mathbf{q}_0$	Initial cable length in workspace
$\mathbf{q}_{\mathrm{D}}$	Dependent cable length
$\mathbf{q}_{\mathrm{I}}$	Independent cable length
q_i	Free cable length in workspace
$\bar{\mathbf{q}}_{\theta_{\mathrm{M}}}$	Measured cable length
$\mathbf{q}_{\mathrm{off}}$	Cable offsets associated with the pretension state $\mathbf{f}_0$
$\mathbf{q}_{\mathrm{off,N}}$	Nominal cable offsets
$\mathbf{q}_{\mathrm{P}}$	Predicted cable length
$\mathbf{q}_{\mathrm{sf}}$	Length of truss members
$\mathbf{q}_{\theta}$	Controlled cable length
$\bar{\mathbf{q}}_{\theta}$	Controlled cable length for all samples
$\bar{\mathbf{q}}_{\theta\mathrm{V}}$	Input validation sample set
$\dot{\mathbf{q}}_{\theta}$	Controlled cable velocity
$q_{\theta i}$	Controlled cable length for individual cable
$\mathbf{q}_{\theta}^{*}$	Axio control cable length
$\mathbf{q}_{\theta_{\mathrm{tc}}}$	Twincat control cable length
$\mathbf{r}$	Platform position vector
$\mathbf{r}_{\mathrm{m}}$	Measured platform position vector
r_{p}	Pulley radius
r	System redundancy
r_{x}	x-position
r_{y}	y-position

r_z	z-position
$\boldsymbol{\rho}$	Residual function
$\boldsymbol{\rho}_\mathrm{q}$	Residual function for cable length
$\boldsymbol{\rho}_\mathrm{we}$	Residual function for wrench
τ	Motor torque
τ_ref	Motor torque reference
τ_x	Exerted torque by human subject around x-axis
τ_y	Exerted torque by human subject around y-axis
$\mathbf{u}_i$	Unit cable direction vector i
$\mathbf{u}_{\mathrm{sf}i}$	Unit vector of platform truss
$\mathbf{w}_\mathrm{A1}$	Internal wrench of heli axis for upper section
$\mathbf{w}_\mathrm{A2}$	Internal wrench of heli axis for lower section
$\mathbf{w}_\mathrm{T}$	Augmented wrench
w_{ρ_q}	Weighting factor for cable length residual
w_{ρ_we}	Weighting factor for wrench residual
$\mathbf{w}_\mathrm{sf}$	Joint loads of space frame
$\mathbf{w}_{\mathrm{sf}i}$	External wrench for truss node i
$\mathbf{w}_\mathrm{xy}$	Projected wrench on xy-plane
$\mathbf{w}_\mathrm{e}$	External wrench
$\mathbf{w}_{\mathrm{e}\mathrm{opt}}$	Optimal wrench from load identification
$\mathcal{W}_\mathrm{WF}$	Wrench feasible workspace
$\mathcal{W}_\mathrm{N}$	Nominal workspace
$\mathcal{W}_\mathrm{R}$	Reachable workspace
$\mathcal{W}_\mathrm{M}$	Control model workspace
$\mathcal{W}_\mathrm{GT}$	Ground truth workspace
$\mathcal{W}_\mathrm{OPT}$	Optimal workspace
$\mathcal{W}_\mathrm{PHYS}$	Physical workspace
$\mathbf{x}$	Platform pose, generalized coordinates
$\mathbf{x}_0$	Equilibrium state pose
$\hat{\mathbf{x}}$	Actual platform pose
$\bar{\mathbf{x}}$	Reference pose set
$\mathbf{x}_\theta$	Desired platform pose
$\dot{\mathbf{x}}$	Platform velocity
$\mathbf{x}_\mathrm{err}$	Pose error
$\mathbf{x}_\mathrm{ini}$	Initial platform pose
$\mathbf{x}_\mathrm{M}$	Measured pose
$\bar{\mathbf{x}}_\mathrm{M}$	Measured pose set
$\bar{\mathbf{x}}_\mathrm{MV}$	Validation pose set
$\mathbf{x}_\mathrm{max}$	Upper pose boundary
$\mathbf{x}_\mathrm{min}$	Lower pose boundary
$\mathbf{x}_\mathrm{P}$	Predicted pose

$\bar{\mathbf{x}}_{\mathrm{P}}$	Predicted pose set
$\mathbf{x}_{\mathrm{ref}}$	Reference pose
$\bar{\mathbf{x}}_{\mathrm{ref}}$	Reference pose set
$\mathbf{x}_{\mathrm{s}}$	Tracked position of human subject
$\mathbf{x}_{\mathrm{sf}}$	Truss node displacement

1 Introduction

The technology of cable-driven parallel robots (CDPRs) combines the concept of conventional parallel robots with the well established technology of cable-driven machines as used for stage systems, cranes, elevators, cable cars, and similar applications. Using cables for actuation has the goal of creating robots for large workspaces with minimized actuated mass and an increased dynamic range. While conventional parallel robots such as hexapod systems shown in Fig. 1.1a have a very limited workspace, the possibility of scaled up workspaces achievable with cable-driven parallel robots can immediately be seen by examples such as the cable cam or FAST telescope (Nan 2006; Tang et al. 2011) in Fig. 1.1b with a diameter of 500 m.

(a) Haxapod motion platform

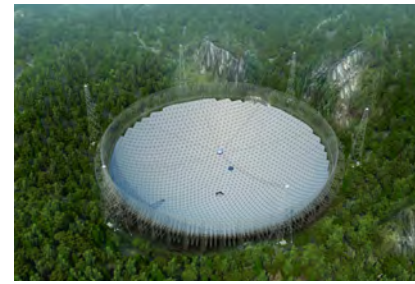

(b) FAST telescope

Figure 1.1: Examples for parallel kinematics with rigid and cable-driven links and different workspaces

There are many ways to design cable-driven parallel robots by varying the number of cables and geometric structure of the platform and frame. Fundamental research on cable-driven parallel robots regarding design (Gagliardini et al. 2014, 2018), control, kinematics, and system dynamics has been conducted by different research institutes around the world. Prototypes for industrial applications such as maintenance, 3D printing (Barnett and Gosselin 2015; Izard et al. 2017; Zhong and Qian 2018), storage and warehouse applications (Hassan and Khajepour 2009; Miermeister et al. 2014), and motion simulation (Miermeister et al. 2016) were developed. A comprehensive overview of the various designs and existing prototypes can be found in (Pott 2018a).

This thesis focuses on configurations with a redundantly constrained platform with $m = 8$ cables for robots with $n = 6$ degrees of freedom (DOF) which are widely used

in the research community such as the IPAnema family at Fraunhofer IPA (Pott 2013), CoGiRo at Lirmm (Lamaury and Gouttefarde 2013), MARIONET at Inria (Merlet 2010), Segesta at University of Duisburg-Essen (Hiller et al. 2005), and the CableRobot Simulator (Miermeister et al. 2016) at the Max Planck Institute for Biological Cybernetics. The CableRobot Simulator was developed during this thesis in an collaboration between the Max Planck Institute for Biological Cybernetics and the Fraunhofer IPA using the concept of CDPRs for the design of a new generation of motion simulators. Using cables to control the motion of the simulator cabin allowed to utilize the advantages of CDPRs to build a lightweight motion platform with high flexibility for the mounting of various cabins and an exceptional large workspace. An icosahedron cabin for general purpose scenarios and a helicopter cabin for flight simulation were integrated during this work and are shown in Fig. 1.2a, 1.2b.

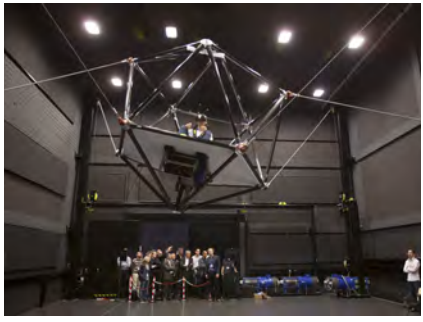

(a) The icosahedron shaped carbon fiber platform provides space for one or two seats while keeping the weight below 80 kg

(b) The helicopter simulator uses a chassis from a Cabri G2 helicopter which is mounted to an endless rotating yaw-axis

Figure 1.2: The CableRobot simulator in operation with two different cabins.

For any given application, the question of robot performance with regards to *position tracking accuracy*, the *reachable workspace*, and *safety and reliability* is essential. The key element influencing these three properties is the motion controller. As outlined in more detail in the next section, for any given CDPR setup, a motion control model has to be found which performs well regarding the stationary positioning accuracy and allows to reach the entire workspace. In general, the requirements for pose tracking accuracy may differ with the use case e.g. pick and place applications or 3D printers require a certain level in position accuracy. Motion simulators require accurate acceleration tracking which translates to a requirement on pose tracking accuracy for the low frequency components of vehicle motion. For high frequencies components of the motion signal such as engine vibrations, correct directional alignment is of less importance. A subject's perception of acceleration in a motion simulator is determined by the actual dynamic acceleration of the simulator cabin as well as the gravitational force. Motion cueing with tilt coordination

(Nesti et al. 2012) allows to use the gravitational force vector for the reproduction of sustained accelerations in the limited operational space of the simulator. Considering that the correct perception of the acceleration depends on the correct alignment of the gravitational force vector, platform orientation, and direction of motion, an accurate calibration of the system kinematics is essential.

Likewise to requirements for positioning accuracy, the requirement for the reachable workspace also varies with the application. To use the same example as above, a pick-and-place task with given target locations for example requires a very different workspace than a 3d printing process where the maximum reachable volume is of interest. While it is desirable to maximize the position accuracy and reachable workspace, this comes at the expense of increased model complexity, costly high accuracy sensors, and an increasing demand in computational power. For applications such as motion simulation it is important to limit model complexity for safety reasons. Models with an extensive number of parameters and system states are more difficult to check and maintain. The search for a simple yet accurate model relates directly to the question of parameter identification and sensitivity analysis in order to find the optimal model with regards to accuracy, reachable workspace, computational costs, and safety. In the following a detailed overview of these important aspects is given.

Position Tracking Accuracy is determined by the robot hardware and control model. An optimal hardware design tries to minimize the necessary model assumptions and puts less demands on the control model. For CDPR design this are point-like cable outlets, rigid lightweight cables, and simple powertrain mechanics. These design goals often cannot be met and point-like cable outlets have to be replaced by pulleys due to the minimal bending radii of the cables. Cables also have high elasticties compared to rigid links adding compliance to the system. The motion controller which drives the hardware influences the stationary as well as the dynamic position tracking accuracy. The stationary accuracy is determined by the kinematics, statics, and compliance of the CDPR which have to be accounted for by the control model. A model which considers all of these properties is called an elasto-geometric or elastostatic model. Having a properly designed elastostatic model is the foundation for accurate stationary and dynamic tracking accuracy. Models for dynamic tracking accuracy are usually used in a closed-loop configuration and rely on real-time sensor data to minimize the tracking error. This in general loosens the requirement for model position accuracy, but in case of CDPRs the platform position often is not measurable and has to be reconstructed from winch encoder values bringing back the requirement for an accurate model.

Workspace In contrast to serial and parallel kinematics with rigid links, the workspace of a CDPR is not geometrically defined by its joint limits and collision space but by the necessity to maintain a force and torque equilibrium at each pose using only positive cable forces resulting from the fact that cables can only exert pulling forces. The detailed

concept and definitions for the general workspace of CDPRs can be found in (Verhoeven et al. 1998a,b; Verhoeven 2004). Further types of workspaces where defined using different criteria to measure if poses belong to the workspace. The wrench-closure workspace or controllable workspace is defined by all poses which fulfill the static equilibrium condition with positive cable forces and also regarding the force transmission ratio of the individual cables to rate the quality of the pose (Gouttefarde and Gosselin 2004; Verhoeven and Hiller 2000). One of the most useful definitions for the workspace of CDPRs used in actual applications is the wrench-feasible workspace (Gouttefarde et al. 2007) which is defined by all poses that can be reached with positive cable forces in a predefined force range. This definition relates to the fact that cable forces have to obey to a lower limit to avoid slack cables and to an upper limit to avoid overload of the cables, drives, and guiding structures. Further definitions for CDPR workspaces consider cable collisions (Blanchet and Merlet 2014; Merlet 2004; Perreault et al. 2010) or system dynamics (Gosselin 2013) but are not further considered in this thesis.

Reliability and Safety Although essential for many CDPR applications not much work has been published with respect to the reliability and safety of motion controllers for CDPRs. This may be caused by the fact that most demonstrators are still operated at research facilities and not used in interaction with humans despite the fact that many application ideas target safety critical applications. Proposals for the use as a rescue system (Merlet and Daney 2010), as gait rehabilitation trainer (Lamine et al. 2017; Surdilovic and Bernhardt 2004; Wu et al. 2011), or motion simulation (Kljuno and Williams 2008; Schmidt 2013) are all safety critical and need careful consideration of the motion control architecture. Some aspects regarding the design of safe hardware for cable-driven thrill ride application is addressed in (Dietz et al. 2012). Safety applications in general demand a safe control architecture and safe control hardware and therefore limit the range of usable control architectures and computer hardware. While complex models may give better accuracy, implementation may not be feasible in safety critical applications.

Beside the CableRobot Simulator, only few other application exist where CDPRs are operated in close vicinity to humans. Mostly known is the Skycam (Cone 1985) which is a cable-driven suspended camera system that is operated above large crowds of people. Another application was implemented by the University of Stuttgart for the EXPO 2015 using a suspended CDPR design to move synchronized animation screens above a crowd of visitors (Tempel et al. 2015a) leading to SIL-3 safety requirements. The setup used certified stage equipment for the winches and space frame structures. Trajectories for the show were optimized with an offline path planning software considering workspace, force distributions, and collision space. The trajectories were tested, certified, and replayed during the show. The CableRobot Simulator (Miermeister et al. 2016) which was designed and used for the modelling in this thesis, also uses SIL-3 certified stage equipment in combination with an industrial rated control solution. This allows the use for realtime human-in-the loop physics simulations and with motion cueing algorithms which is shown

in more detail in Chap. 6.

1.1 Literature Review of Models for Position Control and Workspace Computation

The process of choosing a model structure is difficult to formalize and usually relies solely on the experience of the robot designer. With respect to the model structure, one can find many publications proposing models with various degree of complexity which can be chosen for the control of a CDPR but little work has been conducted on the systematic comparison of theses models with respect to pose accuracy and their impact on the workspace. This relates to the fact that most models are provided without a clear definition of their physical environmental context. A meaningful estimate of the model accuracy and the workspace can only be done for a defined physical context which allows to model deviations between model assumptions and environmental conditions. The standard model (Pott 2018a)is the most basic kinetostatic model for the control of CDPRs is extensively described in (Verhoeven 2004) including the analysis of force distributions. The model is used in most CDPR prototypes and methods for its parameter identification and measurements of the stationary control accuracy are reported in (Duan et al. 2014; Jin et al. 2018; Miermeister and Pott 2012; Miermeister et al. 2012; Sandretto et al. 2013).

Extensions of the standard model concerning the geometry of the redirection pulleys can be found in (Bruckmann et al. 2008; Miermeister and Pott 2010; Pott 2012; Schmidt and Pott 2013; Tempel et al. 2015b). A simulative analysis was conducted by (Pott 2012) comparing the pulley model to the standard kinematics model considering the outputs of the associated inverse kinematics, the outputs of the force distribution algorithm, and the impact on workspace computations. An experimental analysis was conducted by (Schmidt and Pott 2013) comparing the forward kinematics solution of the standard and pulley model to the respective laser tracker measurements on the IPAnema demonstrator.

An extension regarding the geometry and statics of sagging cables with mass is described in (Gouttefarde et al. 2012; Kozak et al. 2006; Nguyen et al. 2013; Riehl et al. 2009) and in combination with pulley kinematics in (Gouttefarde et al. 2014).

Models regarding the kinematics of the winch winding mechanism capture a variety of winch designs and are mostly specific to the respective CDPR assembly. Winch designs as used for the MARIONET CDPR (Merlet and Daney 2010) use a simplified winch assembly where the cable is wound up on the drum without guiding mechanism leading to overlapping of the cable on the winch and an unpredictable cable contact point and changing winding diameter. The deviations from predictions of the kinematics model caused by such assembly are difficult to model and sensor concepts for compensation are proposed using cameras for pose estimation (Miermeister et al. 2014)or color markers for accurate cable length measurements(Merlet 2019). Drums with helical grooves allow to capture the winding behavior with a geometric model considering the winding helix and the cable length between the drum contact point and the first redirection pulley. Such winch de-

signs are used in most stage system applications, as well as the CableRobot Simulator and CoGiRo demonstrator. More sophisticated designs use guiding mechanisms to synchronize the position of the first redirection pulley and the drum contact point. This mechanism is described in (Fang 2005) and is used in an industrial rated winch design developed at Fraunhofer IPA and also used for the IPAnema robots (Pott 2013). Even more detailed analysis of the winding process including cable ovalization was performed by (Schmidt and Pott 2016) measuring the effect of cable forces and cable speed on the winding behavior.

Beside geometry and statics, CDPRs are subject to compliance which are accounted for by elasticity models. The most simple approach approximates the elastic behavior of the cables by a linear spring and the associated well understood linear stiffness model as can be found in (Verhoeven 2004). While the linear model is a first approximation of the cable elasticity, measurement on different CDPRs showed nonlinear and hysteretic behavior (Kraus et al. 2013b; Miermeister et al. 2015, 2016). An extended stiffness model considering the effect of the cable catenary can be found in (Yuan 2015).

1.2 Model Classes and Complexity

All models of the previous section belong to the class of physical white-box models whose inner structure and parameters can be interpreted in a physical way. Black-box models in contrast use some abstract mathematical function which is parameterized in order to best fit a certain sample set recorded from the CDPR. This can be polynomial models, nonparametric models such as radial basis functions, or neural networks. Some authors used the black-box approach to predict cable forces or model the behavior of the powertrain (Piao et al. 2019).

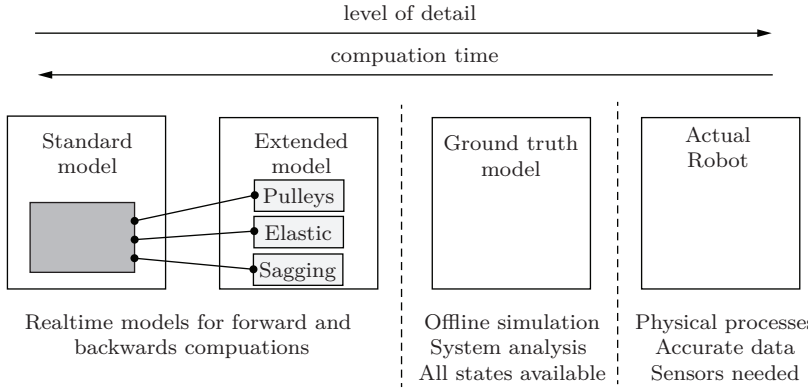

Figure 1.3: Incresing model complexity

Models are approximations of the physical reality underlying the actual CDPR assembly. The complexity of the model can vary as shown in Fig. 1.3 and the modeled effects mainly depend on the models intended use, ranging from models with low complexity for realtime control to ground truth models of high complexity which allow detailed simulative analysis at the cost of longer computation times. Since white-box modelling is mostly based on the intuition of a researcher, one must be very careful adding complexity to the models. Beginning with a simple physical white-box model which captures the most important features of the system behavior, such as the standard kinematics model for CDPRs, additional features can be added to the model. Extensions such as pulleys, sagging, friction etc. allow to achieve better model predictions but may lead to overfitting an divergence from physical reality. Proofing that the proposed model structure and parametrization actually aligns with some physical effect must be carefully done to make it distinct from a black-box model where similar results are achieved by physical unrelated abstract functions.

One should always keep in mind that a well parametrized simple model can perform better than a poorly parameterized complex model. Complex models with additional parameters are usually less general yielding higher variance and may tend to overfit, need more system resources for computation, are harder to maintain, and may show unpredictable behavior causing additional safety issues. Finding the optimal model with respect to prediction quality, one has to solve the bias-variance tradeoff problem as shown in Fig. 1.4 by the two black lines. The model prediction bias describes the error caused by model simplifications, while the variance relates to the error caused by errors in the sampling data which are used for parameter optimization. High variance models tend to cause large generalization and out-of sample errors. Considering only these two factors, the optimal model lies at the intersection of the bias and variance curve indicated by point A.

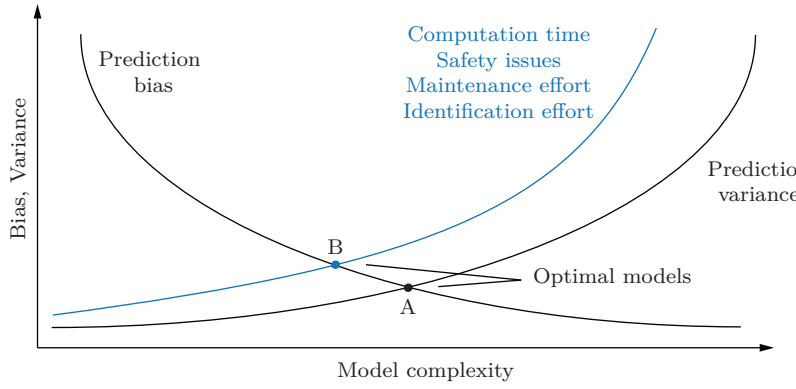

Figure 1.4: Optimal model complexity under the consideration of the bias-variance tradeoff and additional evaluation criteria

For actual applications additional criteria such as computational effort, reliability, or safety have to be considered for the control model. Adding these criteria to the overall cost function during the model selection process adds strong arguments for favoring simplicity over complexity and to use a pareto-optimal model that has a higher prediction bias as indicated by point B in Fig. 1.4.

1.3 Problem Definition

Starting with a specific CDPR configuration, the central problem is finding a motion control model which allows to achieve sufficient stationary positioning accuracy, controls the platform such that it reaches most of the workspace, while keeping the model complexity at a minimal level.

The requirements for positioning accuracy and workspace reachability can be associated with the CDPR setup leading to the question of the *maximal reachable workspace* and the related positioning accuracy or they can be associated with a specific task leading to the question if the model allows to reach the *task workspace* with sufficient accuracy.

The request for minimal model complexity usually comes from three directions. The model should be fast to compute and deterministic to run on a real-time system. It should be easy to test and understand the model to avoid unpredicted side effects which is especially important for safety critical applications. All parts of the model should contribute to the model prediction in a significant way. This relates to the fact that over-complex models with many parameters tend to overfit since different parts of the model provide similar contributions to the model output.

While the literature from the previous overview address different aspects of CDPRS which can be used in a model selection process, no systematic approach has been presented so far which allows to select, optimize, compare, and measure the impact of the models and their parameters with respect to the position accuracy, workspace, and model complexity.

1.4 Objective and Structure of this Thesis

The objective of this thesis is the systematic analysis of the model selection process and its application to the synthesis of an optimal kinetostatic control model for the CableRobot Simulator regarding its accuracy, workspace, and complexity. The CableRobot Simulator unites many of the features discussed in CDPR literature such as large pulley diameters, heavy steel cables which allow for significant sagging, and a large workspace. It also requires high performance yet safe control models which allow for human-in-the-loop motion simulation experiments. Results from model selection and analysis applied to the CableRobot Simulator should translate well to other CDPR systems.

The general structure of the selection process is shown in Fig. 1.5 and starts with the model design (1) where the model structure and parametrization is chosen, e.g. geometrical relations and parametrization of the platform, frame, and pulleys, or an elasticity model

with its stiffness parameters. Second, the optimization step (2) where the parametrization of the model is adjusted such that model predictions get optimally aligned with actual measurements, and finally the evaluation step (3) where the model is rated, analyzed, or compared to other models using specific performance criteria. In the following, the different parts of this process and the respective chapters in the thesis are outlined.

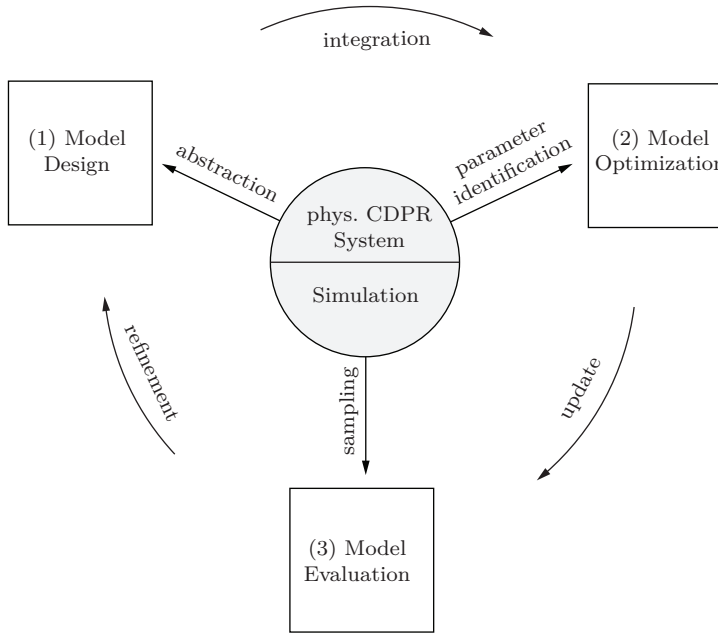

Figure 1.5: Meta model for control model generation

Starting with the model design (1), the models must be structured in perspective of the iterative refinement step (c) such that they allow for a incremental variation of the model complexity in terms of the structure and associated parametrization.

The second chapter derives the model structure and mathematical representations for the modelling of cable-driven parallel robots focusing on physical first principal models. The chosen physical representation is used to describe models of different complexity and provide the foundation to analyze the effect of structural variations on the model prediction accuracy and the workspace in chapter three. For each model, the forward and inverse description is provided which is required for combining control models and ground truth models in the proposed meta-modelling approach as well as the later parameter optimization. In perspective of optimization, parameter identification, and sensitivity analysis,

the associated gradient flow is derived analytically focusing on integrity with the modular approach and structural variations. This allows to create the model structure in an inheritive manner such that model extensions can be added or composed while keeping the meaning of its parametrization and the objective functions and Jacobians for optimization unchanged.

The third chapter derives a meta-modelling approach as foundation for a unified comparison of different models in the context of a ground-truth model which represents a system of higher complexity. The architecture of the meta-model involves the combination of different physicals models and allows to make the distinction between different types of model parametrizations, namely the nominal, physical, and optimal parametrization. This differentiation between types of parametrization is identified as essential to the goal of unified model comparison. In the following an analytic description of the pose accuracy in context of the meta-model is derived and the reachable workspace is defined. The reachable workspace extends the concepts of the wrench-feasible workspace allowing to regard the combination of different model assumptions for the control model and ground-truth model. The meta-model then is used to analyze control models of different structural complexity together with their parametrization to understand the possible impact on the previously defined pose tracking accuracy and reachable workspace based on the models from chapter two.

Chapter four deals with the model optimization and parameter identification complementing the structural analysis form chapter three. It shows the importance of a concurrent model building and optimization process for physical modelling to obtain optimal predictions and to avoid the problem of overfitting. The necessary objective function and the associated Jacobians as well as the sample selection and numeric conditioning of the optimization problem are derived based on the models and their differential counterparts form chapter one.

Chapter five provides a detailed description of the CableRobot Simulator providing the context for the following evaluation chapter. A detailed description of the control system architecture and cabin designs, as well as the use for safety critical applications is provided. System characteristics and results from the measurements of the different system components in individual test-bench experiments are given to complete the picture of the simulator.

The sixth chapter shows the model evaluation and the results for an optimal elastostatic control model for the CableRobot Simulator using the proposed meta-modelling and model selection process with the focus on minimal model complexity and comparing the different approaches on parameter identification. Using the standard kinematics model as starting point, its performance is analyzed comparing a model with a physical parametrization against its optimal parametrization variant.

In the following, model complexity is increased and the elastostatic model is used to compare a physical and optimal parametrization as well as the improvement with respect to the simpler kinematics model. The elastostatic model is also applied to show the im-

portance of model reduction taking the example of the constant orientation workspace which can be reached by a lower dimensional kinematic model neglecting the platform parameterization. In the final step, the elastostatic model allows to increase the reachable workspace by controlling the tension states of the CableRobot Simulator. Safety compliant integration of this more complex model into the real-time environment of the CableRobot Simulator is presented by means of a surrogate model which is operated in parallel to the kinematic model allowing deterministic real-time control of the tension state while staying in the safety margins of the control system. The increased reachable workspace is used as sampling volume to compute a final elastostatic control model which can be considered optimal for the given application and model structure showing significant accuracy improvements compared to the initially used models.

2 Cable-Driven Parallel Robot Models

Models are central to each phase of the life-cycle of a CDPR and needed for the design as well as the operational phase for the control of the CDPR. Each phase requires a model with a different level of accuracy and computational efficency as indicated in Fig. 2.1. In the design phase, models are used for the design of the robot assembly and componennts as well as the design of the robot controller. In the operational phase, they are used to generate motion signals for the winches. Models for system and component design are allowed to involve non-deterministic behavior and need to provide high efficiency to run design optimization iterations. Accuracy demands for the design phase are less critical as long as the general characteristics of the system is represented such that the required components can be derived.

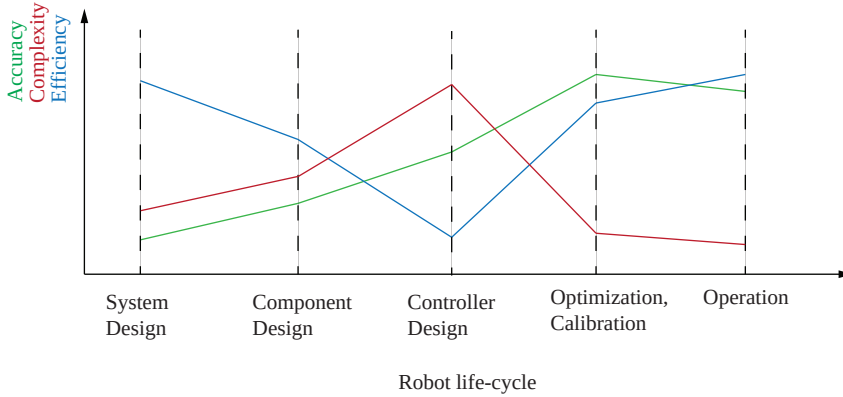

Figure 2.1: Model accuracy and efficiency for different phases of the robot life-cycle

For the controller design, a more complex and realistic model maybe required to analyze the effect of different operational conditions. Computational efficiency and real-time execution in this phase are secondary and different numerical methods such as variable step-width solvers can be used to optimize runtime behavior. For the operational phase, highly accurate and real-time capable models are essential. For applications such as the CableRobot Simulator, additional safety requirements have to be met. An optimization

and calibration step is required to reduce model complexity and runtime costs while increasing accuracy with parameter optimization. Understanding the impact of the control model on the pose accuracy and the workspace is crucial for the robot operation, but elaborate experimental investigation have to be performed to measure the effect. Models which are used for the design phase usually assume perfect alignment with physical reality. This chapter focuses on a set of models and their differential counterparts from the domain of physical first principal models as indicated in Fig. 2.2 which are shown to be most promising for the accurate modeling of the kinematics, statics, and cable elasticities of CDPRs. An overview of the various models with respect to their physical domain can be found in (Pott 2018a).

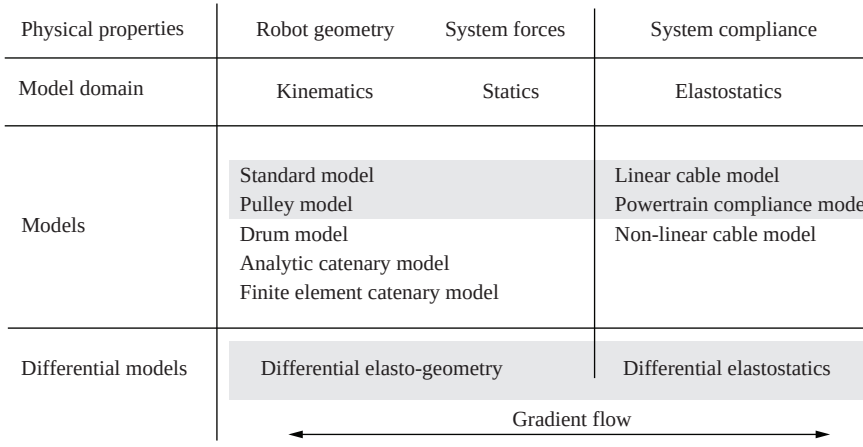

Figure 2.2: Model domains

Beside experimental investigation, the robot controller performance can be analyzed during controller synthesis applying a simulative approach. Using the CDPR models for control and simulation requires the computation of the inverse and forward solutions of the respective models. Reviewing the models and defining the model structure in perspective of the proposed control model selection and optimization process is part of this chapter. The definition of the structure is done such that combination of different sub-models and their differential counterparts can be used in a consistent way for model comparison, parameter optimization, and sensitivity analysis. Ideally, model extensions are parameterized such that a smooth transition between the base model and its extension can be performed. For example, the addition of a pulley model to the standard kinematics model structure can be performed using a pulley radius $r_\mathrm{p} = 0$ such that the behaviour of the base model and extended model are identical and all derivatives exist with respect to the parametrization.

In Sec. 2.1, the general model structure in perspective of a control model is outlined

addressing robot kinematics, statics, and elastostatics as general concepts. In the subsequent sections, the specific model definitions are and the their differential counterparts and gradient flows are derived. The structures of the inverse models are addressed when necessary.

2.1 Model Structure and Composition

The definition of the model structure in this section is the foundation for the definition of the meta-model in Chap. 3 and the systematic and unified comparison of control models and its parametrization in the later chapters. While this section provides the overview of the model architecture, the following sections provide the details of the specific model definitions.

Kinematics Models from the kinematic domain describe the geometric properties of the CDPR determining the relation between the platform pose $\mathbf{x}$ and the joint space variables $\mathbf{q}_\theta$ associated with the cable lengths and motor encoder values as shown in Fig. 2.3 where $\boldsymbol{\varphi}$ relates to standard inverse kinematics model with its paramterization $\mathbf{p}_\varphi = (\mathbf{a}, \mathbf{b})$ and $\mathbf{a}, \mathbf{b}$ refer to the frame and platform geometry respectively.

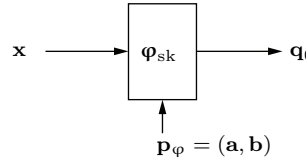

Figure 2.3: CDPR standard kinematics

The standard kinematic model can be replaced by models with increased complexity which allow to consider effects from the pulley geometry, drum winding mechanism, or the cable catenary for example. The detailed definitions for the standard kinematics and pulley model are given in Sec. 2.2, 2.3. The depicted model in Fig. 2.3 shows the inverse path for the standard kinematics which can be computed straight forward and in realtime. The respective forward kinematics problem, where the platform pose for a given controlled cable length has to be computed, is more difficult to solve and has to be computed in an iterative manner. An extensive analysis of all possible solutions of the forward kinematics problem can be found in (Husty 1996). Methods for finding a good initial guess and solving the forward kinematics problem in real-time can be found for example in (Pott 2010). Since the forward kinematics model can be considered as a special case of the elastostatic model as shown in Eq. (2.81), all related issues are addressed in the context of the elastostatic model.

Statics A static model $\boldsymbol{\gamma}_{\mathrm{sk}}$ as shown in Fig. 2.4 is based on the associated kinematic model and considers the stationary force distributions at the platform. The static model can be derived from the Jacobian $\frac{\partial \boldsymbol{\varphi}}{\partial \mathbf{x}}$ of the kinematics model described in Eq. (2.31) using the concept of the kinetostatic dualism which relates to the dual mapping of velocities and forces.

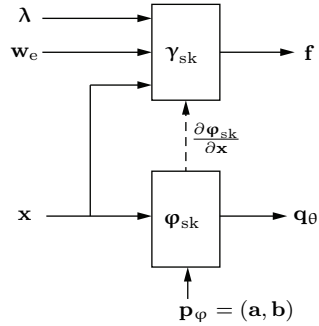

Figure 2.4: CDPR kinetostatics based on standard model

The static equilibrium for suspended or fully constrained CDPRs is uniquely determined by the external wrench $\mathbf{w}_{\mathrm{e}}$ and the cable forces $\mathbf{f}$. For overconstrained CDPRs with $m > n$, infinite number of solutions for the force distribution $\mathbf{f}$ exist, allowing a variation of the internal tension state using the scaling parameter $\boldsymbol{\lambda}$ for linear combinations of the nullspace vectors as shown in Eq. (2.40). This can be used to control the cable forces for a given pose and wrench combination or to identify valid pose states for the estimation of the robot workspace. For more complex models such as the catenary model, computation of the static force distribution gets more involved and the equilibrium state has to be found iteratively. While the static model can be used for system analysis such as workspace computations its use for the control of CDPRs takes additional effort which depends on the specific approach to force control. In the commonly used setup of CDPRs, cable forces are not directly controlled but the immediate consequence of cable length control. The associated elastostatic model is described in the next paragraph. Control of the cable forces can be done using an open-loop or closed-loop design. The development of a closed-loop force control is extensively discussed in (Kraus et al. 2015; Kraus 2016). This thesis focuses on the open-loop approach and model optimization to obtain accurate force tracking. Computation of the forward paths of the static model is done similarly to the forward kinematics and allows to find the stationary pose $\mathbf{x}$ and wrench $\mathbf{w}_{\mathrm{e}}$ for a given force distribution $\mathbf{f}$.

Elastostatics Elastostatics or elastostatic models as depicted in Fig. 2.5 regard the compliance of the system and connect cable forces $\mathbf{f}$ to geometric changes in the cable length

denoted by $\Delta\mathbf{q}$. A widespread model for cable elasticities uses a linear spring model which is parameterized by the stiffness constant $\mathbf{p}_\kappa = \mathbf{k}_\mathrm{F}$. The detailed description of the cable stiffness and its relation to the system stiffness is given in Eq. (2.33, 2.66), respectively. This concludes the structural overview of models for kinematics, statics, and elasticities which is the foundation for position and force control. Model extensions of the CDPR models are assigned as a modification to one of the subsystems $\boldsymbol{\varphi}, \boldsymbol{\gamma}_\mathrm{sk}, \boldsymbol{\kappa}_\mathrm{lin}$.

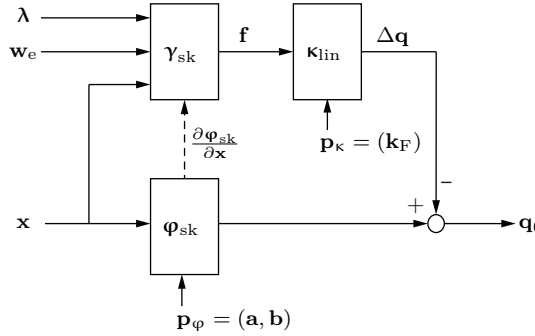

Figure 2.5: CDPR elastostatics based on standard model

Modifications to the subsystems must comply with the a priori definitions of the physical system and have to provide the respective interfaces between the submodules. For example the kinematics description of $\boldsymbol{\varphi}$ can be extended using additional geometric structures leading to $\boldsymbol{\varphi}_\mathrm{ex}$. To be compliant, the extended model at least has to provide the geometric parametrization $\boldsymbol{\varphi} = \mathbf{p}_\mathrm{ab}$ beside the parametrization for the extension $\mathbf{p}_\mathrm{ex}$. The model structure of the extension must be chosen such that there exists a $\mathbf{p}_\mathrm{ex}$ with

$$\boldsymbol{\varphi}_\mathrm{ex}(\mathbf{x}, \mathbf{p}_\mathrm{ex}) = \boldsymbol{\varphi}(\mathbf{x}, \mathbf{p}_\mathrm{ab}) \,\forall\, \mathbf{x} \tag{2.1}$$

considering the inverse computations of the model. This also must hold true for the forward computations $\mathbf{q} \rightarrow \mathbf{x}$. The formalism to solve the structure depends on the specific path and input-output configuration of the associated nonlinear equations. In some cases which are discussed in more detail in the next sections, an explicit solution cannot be computed and numerical methods such as Gauss-Newton or Levenberg-Marquardt (Marquardt 1963) have to applied to find the solution.

2.2 Cable Robot Kinematics Model

Based on the general model structure in Sec. 2.1, a detailed description of the different robot models is given in this and the following sections starting with the most fundamental concepts of the robot kinematics. Cable-driven parallel robots in a spatial three dimensional

configuration can be described by a mobile platform whose pose $\mathbf{x}$ is defined by the generalized coordinates $\mathbf{x}^{\mathrm{T}} = \begin{bmatrix} r_{\mathrm{x}} & r_{\mathrm{y}} & r_{\mathrm{z}} & \phi_{\mathrm{x}} & \phi_{\mathrm{y}} & \phi_{\mathrm{z}} \end{bmatrix}$ where $\mathbf{r}^{\mathrm{T}} = \begin{bmatrix} r_{\mathrm{x}} & r_{\mathrm{y}} & r_{\mathrm{z}} \end{bmatrix}$ refers to platform position and $\boldsymbol{\phi}^{\mathrm{T}} = \begin{bmatrix} \phi_{\mathrm{x}} & \phi_{\mathrm{y}} & \phi_{\mathrm{z}} \end{bmatrix}$ refers to the platform rotation defined by three elemental rotations

$$\mathbf{R}_{0\mathrm{P}} = \mathbf{R}_{\mathrm{x}}(\phi_{\mathrm{x}})\mathbf{R}_{\mathrm{y}}(\phi_{\mathrm{y}})\mathbf{R}_{\mathrm{z}}(\phi_{\mathrm{z}}) \ . \tag{2.2}$$

The platform's n degrees of freedom (DOF) are constrained by m cables which are connected to winches on a fixed machine frame. For $m \leq n+1$ the platform pose is fully controllable. The CableRobot Simulator which was used for modelling and experiments in this thesis uses $m = 8$ cables and a spatial configuration with $n = 6$ DOF. The actual platform pose $\hat{\mathbf{x}}$ is controlled by changing the cable length q_i with $i = 1 \ldots m$ using the inverse kinematics

$$\mathbf{q} = \boldsymbol{\varphi}(\mathbf{x}, \mathbf{p}_{\varphi}) \tag{2.3}$$

which is defined by the geometrical parameters

$$\mathbf{p}_{\varphi}^{\mathrm{T}} = \begin{bmatrix} \mathbf{a}_1^{\mathrm{T}} & \cdots & \mathbf{a}_m^{\mathrm{T}} & \mathbf{b}_1^{\mathrm{T}} & \cdots & \mathbf{b}_m^{\mathrm{T}} \end{bmatrix} \tag{2.4}$$

where $\mathbf{a}_i$ relates to the cables' outlet points at the proximal winch side and $\mathbf{b}_i$ relates to the distal anchor points on the mobile platform side as shown in Fig. 2.6. The inverse kinematics model allows to compute the cable vectors

$$\mathbf{l}_i = \mathbf{a}_i - \mathbf{r} - \mathbf{b}_i, \tag{2.5}$$

with

$$\mathbf{b}_i = \mathbf{R}_{0\mathrm{P}}\mathbf{b}_i^{(\mathrm{P})} \tag{2.6}$$

and their respective lengths

$$q_i = \|\mathbf{l}_i\|_2 \ , \ i = 1 \ldots m \ . \tag{2.7}$$

The unit vector in the direction of an individual cable is defined by

$$\mathbf{u}_i = \frac{\mathbf{l}_i}{q_i} \ . \tag{2.8}$$

These simplified model assumptions provide a first approximation to the actual robot configuration and have to be extended by more detailed models such as pulley and cable models to provide increased accuracy.

For the feed forward control of a CDPR, the desired platform pose $\mathbf{x}_{\theta}$ along a trajectory is provided as input to the controller which in turn computes the associated cable lengths in terms of the inverse kinematics from Eq. (2.5). For closed loop control and system identification it may also be necessary to solve the forward kinematics

$$\mathbf{x} = \boldsymbol{\upsilon} \tag{2.9}$$

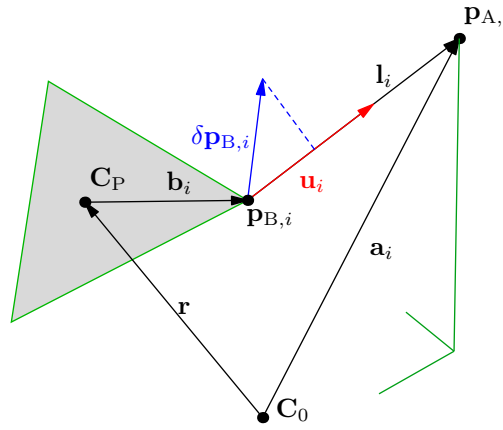

Figure 2.6: Cable robot kinematics

with the associated residual function

$$\boldsymbol{\rho}(\mathbf{x}, \mathbf{q}_\theta) = \mathbf{q}(\mathbf{x}) - \mathbf{q}_\theta \overset{!}{=} \mathbf{0} \tag{2.10}$$

in order to find a platform pose $\mathbf{x}$ for a given cable configuration $\mathbf{q}_\theta$. Solving the inverse kinematics problem is done straigth forward computing the vector loop. For the forward kinematics problem one has to solve the associated system of nonlinear equations defined by Eq. (2.10) which has mutliple solutions. The general appraoch to find all solutions of the forward kinematics of parallel robots is described in Husty 1996. For overconstrained CDPRs no solution exits for inconsistent cable length configurations. Assuming elasticity in the cables one may find the least squares solution by solving the associated optimization problem

$$\upsilon = \min_{\mathbf{x}} \left(\frac{1}{2} \boldsymbol{\rho}(\mathbf{x})^\mathrm{T} \boldsymbol{\rho}(\mathbf{x}) \right) = \min_{\mathbf{x}} \frac{1}{2} \left\| \mathbf{q}(\mathbf{x}) - \mathbf{q}_\theta \right\|_2^2 = \min_{\mathbf{x}} \frac{1}{2} \sum_{i=1}^{m} \left(q_i(\mathbf{x}) - q_{\theta,i} \right)^2. \tag{2.11}$$

Efficient numeric solvers such as the Gauss-Newton and Levenberg-Marquardt solver use the linear approximation $\frac{\partial \boldsymbol{\rho}}{\partial \mathbf{x}} = \frac{\partial \mathbf{q}}{\partial \mathbf{x}} = \mathbf{J}_{\mathrm{qx}}$ and the respective first order taylor expansion

$$\boldsymbol{\rho}(\mathbf{x}_0 + \Delta\mathbf{x}) = \boldsymbol{\rho}(\mathbf{x}_0) + \mathbf{J}_{\mathrm{qx}} \Delta\mathbf{x} \tag{2.12}$$

of the residual function to compute the optimum of the linearized residual function in each iteration step, i.e. find a $\Delta\mathbf{x}$ such that the residual gets minimal

$$\boldsymbol{\rho}(\mathbf{x}_0) + \mathbf{J}_{\mathrm{qx}} \Delta\mathbf{x} \overset{!}{=} \mathbf{0}. \tag{2.13}$$

Considering $\frac{\partial \mathbf{q}}{\partial \mathbf{x}} = -\mathbf{A}$ from Eq. (2.54) and $\boldsymbol{\rho}(\mathbf{x}_0) = \mathbf{q}(\mathbf{x}_0) - \mathbf{q}_\theta$ and $\mathbf{q}_\theta = \mathbf{q}_{\theta_0} + \Delta\mathbf{q}_\theta$, one obtains the overconstrained linear system

$$\underbrace{\mathbf{q}(\mathbf{x}_0) - \mathbf{q}_{\theta_0} - \Delta\mathbf{q}_\theta}_{\tilde{\mathbf{q}}} - \mathbf{A}\Delta\mathbf{x} = \mathbf{0} \tag{2.14}$$

whose solution is computed by the normal equation

$$\Delta\mathbf{x} = \left(\mathbf{A}^{\mathrm{T}}\mathbf{A}\right)^{-1}\mathbf{A}^{\mathrm{T}}\tilde{\mathbf{q}} \,. \tag{2.15}$$

For the special case where one starts from a geometrical consistent configuration on the constraint manifold $\mathbf{q}(\mathbf{x}_0) - \mathbf{q}_{\theta_0} = \mathbf{0}$ this simplifies to $\tilde{\mathbf{q}} = -\Delta\mathbf{q}_\theta$. Most solvers require a sufficient initial guess $\mathbf{x}_0$ to work efficiently. How to find a sufficient initial guess by interval analysis and solving the optimization problem with real-time constriants is shown in (Pott 2010; Schmidt et al. 2014). A summary of the standard kinematic model is shown in Fig. 2.7. The additional input $\mathbf{q}_{\mathrm{off}}$ deals with the initial force distribution which has to be chosen before operating the CDPR. This shows that a CDPR cannot be operated solely based on kinematic considerations but that cable forces are an essential part of the setup. Only combinations of $\mathbf{q}_{\mathrm{off}}$ which match with the wrench closure condition Eq. (2.31) lead to an accurate initial pose.

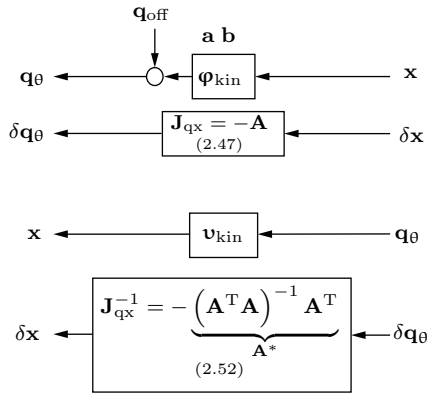

Figure 2.7: Standard kinematics model structure showing the input output relations for inverse and forward kinematics together with the respective sensitivities.

2.3 Pulley Kinematics

The cables of a CDPR are guided by redirection pulleys which are integrated in the drive train between the winch and actual robot workspace. To minimize the impact of the last pulley at the cable outlet point $\mathbf{a}_i$, ideally one would use pulleys with small radii to minimize the geometric influence of the pulleys but bounding conditions such as a minimal allowed bending radius for the cables and required meachnical durability put certain limits on the minimum pulley radius r_p. The formulation of the geometric relations associated with the pulley kinematics is based on (Pott 2012; Schmidt and Pott 2013) resulting in the inverse kinematics model

$$\mathbf{q}_\theta = \boldsymbol{\varphi}_\mathrm{pl}(\mathbf{x}, \mathbf{p}_\mathrm{pl}) \tag{2.16}$$

which considers the contact arc defined by angle β_i as shown in Fig. 2.8 so that the cable length computed by the inverse kinematics becomes

$$q_i = q_{\mathrm{f},i} + \beta_i r_\mathrm{p} \ . \tag{2.17}$$

The associated parameter set

$$\mathbf{p}_\mathrm{pl} = \begin{bmatrix} \mathbf{a} & \mathbf{b} & r_\mathrm{p} & \mathbf{u}_{\mathrm{A}z} \end{bmatrix} \tag{2.18}$$

consists of the base model paramterization $\mathbf{a}$, $\mathbf{b}$ and the additional paramters for the pulley radius $r_{\mathrm{p},i}$ and the pulley axis $\mathbf{u}_{\mathrm{A}z}$. The angle β_i is computed by

$$\beta_i = \arccos(\frac{q_{\mathrm{f},i}}{b_\mathrm{M}}) + \arccos(\frac{b_\mathrm{z}}{b_\mathrm{M}}) \tag{2.19}$$

using the relations of the rectangular triangles in the plane defined by $\mathbf{p}_{\mathrm{B},i}, \mathbf{p}_{\mathrm{M},i}, \mathbf{p}_{\mathrm{A},i}$ with

$$b_\mathrm{M} = \sqrt{(b_\mathrm{xy} - r_\mathrm{p})^2 + b_\mathrm{z}^2} \tag{2.20}$$

and

$$b_\mathrm{xy} = \sqrt{b_\mathrm{x}^2 + b_\mathrm{y}^2} \ . \tag{2.21}$$

The free cable length $q_{\mathrm{f},i}$ is computed according to

$$q_{\mathrm{f},i} = \|\mathbf{l}_i\|_2 = \sqrt{b_\mathrm{M}^2 - r_\mathrm{p}^2} \ . \tag{2.22}$$

The spatial position of contact point $\mathbf{p}_{\mathrm{A},i}$ is computed by rotating the radial vector

$$\mathbf{v}_\mathrm{r} = r_\mathrm{p}\mathbf{u}_{\mathrm{A}x} \tag{2.23}$$

about the pulley axis at point $\mathbf{p}_{\mathrm{M},i}$

$$\mathbf{n}_\mathrm{M} = \mathbf{u}_{\mathrm{A}x} \times \mathbf{u}_{\mathrm{A}z} \tag{2.24}$$

using the Rodrigues' rotation formula

$$\hat{\mathbf{v}}_\mathrm{r} = \mathbf{v}_\mathrm{r}\mathrm{cos}\beta + (\mathbf{n}_\mathrm{M} \times \mathbf{v}_\mathrm{r}) \ \mathrm{sin}\beta + \mathbf{n}_\mathrm{M}(\mathbf{n}_\mathrm{M} \cdot \mathbf{v}_\mathrm{r})(1 - \mathrm{cos}\beta) \tag{2.25}$$

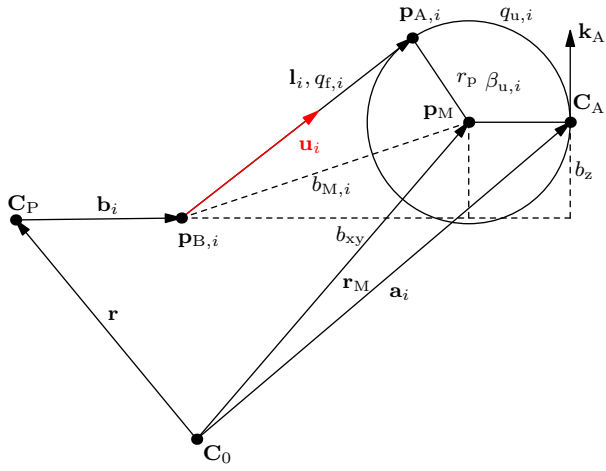

Figure 2.8: Pulley kinematics

so that the cable vector can be computed from

$$\mathbf{l}_i = \mathbf{p}_{\mathrm{A},i} - \mathbf{p}_{\mathrm{B},i} \tag{2.26}$$

using

$$\mathbf{p}_{\mathrm{A},i} = \mathbf{a}_i - \mathbf{v}_{\mathrm{r}} + \hat{\mathbf{v}}_{\mathrm{r}} \ . \tag{2.27}$$

The forward kinematics problem for the extended pulley kinematics can be solved in the same way as previously described in Eq. (2.10) using

$$q_i = q_{\mathrm{f},i} + q_{\mathrm{u},i} \tag{2.28}$$

with

$$q_{\mathrm{u},i} = \beta_i r_{\mathrm{p}} \tag{2.29}$$

for the residual function. The standard kinematics model and the pulley model allow a description of the robot geometry where the pulley model provides a consistent extension of the standard model keeping its paramterization and structure such that all differntial relations can be inherited as is shown in Sec. 2.7. While kinematic models provide a sufficient description for statically determined systems such as suspended cable robots, they are missing the description of the inner tension states inherent to overconstrained CDPRs. The problem of the geometric description arises for the forward kinematics solution where the platform pose $\mathbf{x}$ has to be computed as least squares approximation from a given set of cable lengths. In the next section, the elastostatics model is introduced which provides a more natural and accurate solution to the problem of the forwards kinematics leading to a weighted least squares problem Eq. (2.81) where the weighting matrix is defined by

the cable elasticities. The elastostatic model also allows to model the tension distribution propagation which describes the cable tension for all poses with respect to a given initial tension distribution as is described in Sec. 3.5.

2.4 Statics and Elastostatics Model

The statics of a CDPR is derived from the kinematic models of the previous sections by considering the platform as a free floating body whose position is solely determined by the force equilibrium of the cable forces $\mathbf{f}$ and the external wrench $\mathbf{w}_\mathrm{e}$. Using the cable unit vectors from the kinematic models as force direction vectors and merging it with the platform geometry one can establish the so-called structure equation

$$\underbrace{\begin{bmatrix} \mathbf{u}_1 & \cdots & \mathbf{u}_m \\ \mathbf{b}_1 \times \mathbf{u}_1 & \cdots & \mathbf{b}_m \times \mathbf{u}_m \end{bmatrix}}_{\mathbf{A}^\mathrm{T}} \underbrace{\begin{bmatrix} f_1 \\ \vdots \\ f_m \end{bmatrix}}_{\mathbf{f}} + \underbrace{\begin{bmatrix} \mathbf{f}_\mathrm{e} \\ \boldsymbol{\tau}_\mathrm{e} \end{bmatrix}}_{\mathbf{w}_\mathrm{e}} = \mathbf{0} \tag{2.30}$$

$$\boldsymbol{\gamma}_\mathrm{sk}(\mathbf{x}, \mathbf{f}, \mathbf{w}_\mathrm{e}) = \mathbf{A}^\mathrm{T}\mathbf{f} + \mathbf{w}_\mathrm{e} = \mathbf{0} \tag{2.31}$$

where the cable forces $\mathbf{f}$ are mapped onto the platform using the structure matrix $\mathbf{A}^\mathrm{T}$. The statics model can be used to compute valid pose states, estimate the workspace border, or to separate the internal and external cable forces. The connection between the cable forces $\mathbf{f}$ from the statics model in Eq. (2.31) and the computed cable lengths $\mathbf{q}_\theta$ of the kinematics model in Sec. 2.2 are established by the introduction of a cable elasticity model leading to the elastotstatic model of CDPRs.

The elastostatic model uses a linear elastic cable model which accounts for the mechanical compliance of the elastic cables and allows to establish a mapping between cable forces and the geometric joint space variables

$$\mathbf{f} \leftrightarrow \mathbf{q}_\theta \ . \tag{2.32}$$

The spring constant of the cable model is defined by

$$\mathbf{k} = \mathrm{diag}(\mathbf{q})^{-1}\mathbf{k}_\mathrm{F} \ . \tag{2.33}$$

where the specific stiffness $\mathbf{k}_\mathrm{F}$ is given by the cable cross section A and Young's modulus E with

$$k_{\mathrm{F}i} = EA_i \ . \tag{2.34}$$

The difference between the actual cable length $\mathbf{q}(\mathbf{x})$ and the controlled cable length $\mathbf{q}_\theta$ computed by the geometrical model is defined as

$$\Delta\mathbf{q} = \mathbf{q}(\mathbf{x}) - \mathbf{q}_\theta \tag{2.35}$$

and results in cable forces according to

$$\mathbf{f} = \mathrm{diag}(\mathbf{k})\Delta\mathbf{q} \ . \tag{2.36}$$

With Eq. (2.3, 2.35, 2.36) one obtains

$$\mathbf{q}_\theta = \boldsymbol{\varphi}_{\mathrm{el}}(\mathbf{x}, \mathbf{f}) = \boldsymbol{\varphi}(\mathbf{x}) - \Delta\mathbf{q}(\mathbf{f}) = \mathbf{q}(\mathbf{x}) - \mathrm{diag}(\mathbf{k})^{-1}\mathbf{f} \tag{2.37}$$

allowing to compute the cable length for a given platform pose $\mathbf{x}$ and desired cable force distribution $\mathbf{f}$. This formulation includes no assumptions about the external wrench and system statics and choosing sensible force input vectors $\mathbf{f}$ requires additional knowledge about the relation of the external wrench and cable forces as shown in Fig. 2.5 and described by the system statics Eq. (2.31) representing an underdetermined inhomogeneous system of equations with an infinite number of solutions $\mathbf{f}$ for a given wrench $\mathbf{w}_\mathrm{e}$. Force distributions which are not matched by the external wrench will lead to motion of the platform. The general solution to this problem is given by

$$\mathbf{f} = \underbrace{-\mathbf{A}^{+\mathrm{T}}\mathbf{w}_\mathrm{e}}_{\mathbf{f}_\mathrm{ext}} + \underbrace{\mathbf{H}\boldsymbol{\lambda}}_{\mathbf{f}_\mathrm{int}} \quad , \boldsymbol{\lambda} \in \mathbb{R}^{m-n} \tag{2.38}$$

where $\mathbf{f}_\mathrm{ext}$ are the external forces computed with the $m \times 6$ Moore-Penrose pseudo right inverse

$$\mathbf{A}^{+\mathrm{T}} = \mathbf{A}\left(\mathbf{A}^\mathrm{T}\mathbf{A}\right)^{-1} \ . \tag{2.39}$$

The expression $\mathbf{A}^\mathrm{T}\mathbf{A}^{+\mathrm{T}} = \mathbf{I}$ represents the part of the cable forces caused by the external wrench $\mathbf{w}_\mathrm{e}$ lying in the image or column space of the strucutre matrix $\mathbf{A}^\mathrm{T}$. The second part represents the internal forces $\mathbf{f}_\mathrm{int}$ lying in the nullspace or kernel of structure matrix $\mathbf{A}^\mathrm{T}$ where a basis is given by $\mathbf{H} = \begin{bmatrix} \mathbf{h}_1 & \cdots & \mathbf{h}_r \end{bmatrix}$ such that $\mathbf{A}^\mathrm{T}\mathbf{H}\boldsymbol{\lambda} = \mathbf{0}$ for any $\boldsymbol{\lambda} \in \mathbb{R}^{m-n}$. From Eq. (2.31, 2.38) it is possible to compute the internal part of a given force distribution $\mathbf{f}$ using

$$\mathbf{f}_\mathrm{int} = \mathbf{H}\boldsymbol{\lambda} = \left(\mathbf{I} - \mathbf{A}^{+\mathrm{T}}\mathbf{A}^\mathrm{T}\right)\mathbf{f} \tag{2.40}$$

where $\left(\mathbf{I} - \mathbf{A}^{+\mathrm{T}}\mathbf{A}^\mathrm{T}\right)$ is the projector onto the kernel of $\mathbf{A}^\mathrm{T}$. With Eq. (2.38) the elasto-geometrical model can be restated as

$$\mathbf{q}_\theta = \boldsymbol{\varphi}_{\mathrm{el}}(\mathbf{x}, \mathbf{w}_\mathrm{e}, \boldsymbol{\lambda}) = \mathbf{q}(\mathbf{x}) - \mathbf{K}^{-1}\mathbf{f}(\mathbf{x}, \mathbf{w}_\mathrm{e}, \boldsymbol{\lambda}) \tag{2.41}$$

now providing full control over the platform pose, extenal wrench, and internal tension state using the scaling parameter $\boldsymbol{\lambda}$. The associated forward kinematics model similar to Eq. (2.9) allows to compute the platform pose and cable forces for a given cable configuration and external platform wrench

$$(\mathbf{x}, \mathbf{f}) = \boldsymbol{\upsilon}_{\mathrm{el}}(\mathbf{q}_\theta, \mathbf{w}_\mathrm{e}) \tag{2.42}$$

minimizing the residual function

$$\boldsymbol{\rho}(\mathbf{x}) = \mathbf{A}^\mathrm{T}(\mathbf{x})\mathbf{f}(\mathbf{x}, \mathbf{q}_\theta) + \mathbf{w}_\mathrm{e} \ . \tag{2.43}$$

Minimization of a residual function requires an optimization algorithm which usually rely on the analytic Jacobians to improve runtime performance. The differential relations which allow to compute the associated Jacobian $\frac{\partial \mathbf{w}_\mathrm{e}}{\partial \mathbf{x}}$ can be found in the following differential kinematics section in Eq. (2.76). While differential relations are important for optimizer Jacobians, they are also essential to analyze the models from the last sections with respect to their parameter sensitivities and the impact on model compositions. The next sections provide the analytic differentials for the kinematics and elastostatics models and show the associated gradient flows which then are used for the model analysis in Chap. 3 and optimization in Chap. 4.

2.5 Differential Kinematics

Differential relations between parameters and state variables of the robot model are essential for system identification, sensitivity analysis, forward kinematics, and the computation of force distributions. For an arbitray system component $y = S(p)$, one can write the diffrential relation using the gradient of the system's output quantity y with respect to a parameter p yielding $\delta y = \frac{\partial S(p)}{\partial p}\delta p$. Beginning with the inverse kinematics model $\boldsymbol{\varphi}(\mathbf{x}, \mathbf{p}_\varphi)$ from Eq. (2.5, 2.7), infinitesimal changes in the platform pose are denoted by

$$\delta\mathbf{x} = \begin{bmatrix} \delta\mathbf{r}^\mathrm{T} & \boldsymbol{\omega}^\mathrm{T} \end{bmatrix}^\mathrm{T} \tag{2.44}$$

where $\boldsymbol{\omega}$ refers to the infinitesimal rotation vector similar to the angular velocity vector which is associated with time derivatives. The infinitesimal rotation vector is uniquely defined and more convenient to work with than the specific derivatives of the chosen rotation angle parametrization. For the angle parametrization from Eq. (2.2) the transformation from infinitesimal angles to the infinitesimal rotation vector is given by

$$\boldsymbol{\omega} = \mathbf{J}_\mathrm{P} \begin{bmatrix} \delta\phi_\mathrm{x} & \delta\phi_\mathrm{y} & \delta\phi_\mathrm{z} \end{bmatrix}^\mathrm{T} \tag{2.45}$$

with the 3×3 geometric Jacobian

$$\mathbf{J}_\mathrm{P} = \begin{bmatrix} \mathbf{e}_\mathrm{x} & \mathbf{R}_\mathrm{x}(\phi_\mathrm{x})\mathbf{e}_\mathrm{y} & \mathbf{R}_\mathrm{x}(\phi_\mathrm{x})\mathbf{R}_\mathrm{y}(\phi_\mathrm{y})\mathbf{e}_\mathrm{z} \end{bmatrix} . \tag{2.46}$$

The respective changes in the platform vectors $\mathbf{b}_i = \mathbf{R}_{0\mathrm{P}}\mathbf{b}_i^{(\mathrm{P})}$ and cable attachment points $\mathbf{p}_{\mathrm{B},i} = \mathbf{r} + \mathbf{b}_i$ are described by the 3×6 Jacobian

$$\frac{\partial \mathbf{b}_i}{\partial \mathbf{x}} = \begin{bmatrix} \mathbf{0} & -\tilde{\mathbf{b}}_i \end{bmatrix} \tag{2.47}$$

and

$$\frac{\partial \mathbf{p}_{\mathrm{B},i}}{\partial \mathbf{x}} = \begin{bmatrix} \mathbf{I} & -\tilde{\mathbf{b}}_i \end{bmatrix} \tag{2.48}$$

considering the relation between the cross product and the skew symmetric matrix expression

$$\delta\mathbf{b}_i = \boldsymbol{\omega} \times \mathbf{b}_i = -\tilde{\mathbf{b}}_i\boldsymbol{\omega} . \tag{2.49}$$

With $\mathbf{l}_i = \mathbf{a}_i - \mathbf{p}_{\mathrm{B},i}$ it follows

$$\frac{\partial \mathbf{l}_i}{\partial \mathbf{x}} = -\frac{\partial \mathbf{p}_{\mathrm{B},i}}{\partial \mathbf{x}} = [\ -\mathbf{I}\ \ \tilde{\mathbf{b}}_i\ ] \tag{2.50}$$

stating that the change in the cable vector $\mathbf{l}_i$ is inversely related to the change in the location of the associated platform attachment point $\mathbf{p}_{\mathrm{B},i}$. To obtain the derivative of the cable length q_i with respect to the platform pose $\mathbf{x}$, one can use the projection of $\delta\mathbf{p}_{\mathrm{B},i}$ onto the cable unit vector as shown in Fig. 2.8leading to

$$\delta q_i = -\mathbf{u}_i^{\mathrm{T}} \delta \mathbf{p}_{\mathrm{B},i} = \mathbf{u}_i^{\mathrm{T}} \delta \mathbf{l}_i\ . \tag{2.51}$$

Using Eq. (2.51, 2.48) leads to

$$\frac{\partial q_i}{\partial \mathbf{x}} = \left[\ -\mathbf{u}_i^{\mathrm{T}} \quad \mathbf{u}_i^{\mathrm{T}} \tilde{\mathbf{b}}_i\ \right]\ . \tag{2.52}$$

Restating Eq. (2.52) one obtains

$$\delta q_i = -\left[\ \mathbf{u}_i^{\mathrm{T}} \quad (\mathbf{b}_i \times \mathbf{u}_i)^{\mathrm{T}}\ \right] \delta \mathbf{x} \tag{2.53}$$

and

$$\delta \mathbf{q} = \frac{\partial \mathbf{q}}{\partial \mathbf{x}} \delta \mathbf{x} = -\mathbf{A} \delta \mathbf{x} \tag{2.54}$$

where the Jacobian $\mathbf{J}_{\mathrm{qx}} = \frac{\partial \mathbf{q}}{\partial \mathbf{x}}$ is expressed in terms of the transposed structure matrix $\mathbf{A}^{\mathrm{T}}$. The relation of $\delta\mathbf{q} = -\mathbf{A}\delta\mathbf{x}$ where the platform velocities are mapped to cable velocities and

$$\mathbf{w}_{\mathrm{e}} = -\mathbf{A}^{\mathrm{T}} \mathbf{f} \tag{2.55}$$

where the cable forces are mapped to the platform wrench is called kinetostatic dualism. Computing the derivative of the forward kinematics function $\boldsymbol{\upsilon}$ is done by implicit differentiation of the associated constraint manifold from Eq. (2.10)

$$\frac{\partial \mathbf{q}}{\partial \mathbf{x}} = \frac{\partial \mathbf{q}_\theta}{\partial \mathbf{x}} \tag{2.56}$$

so that

$$\delta \mathbf{x} = \frac{\partial \mathbf{x}}{\partial \mathbf{q}_\theta} \delta \mathbf{q}_\theta = -\mathbf{A}^{-1} \delta \mathbf{q}_\theta\ . \tag{2.57}$$

The inverse matrix of $\mathbf{A}^{(m \times n)}$ does not exist for overconstained CDPRs where $m > n$. Instead, one has to solve the minimization problem using $\bar{\mathbf{q}} = -\mathbf{q}_\theta$ which minimizes the residual

$$\min_{\delta \mathbf{x}} \|\mathbf{A}\delta\mathbf{x} - \delta\bar{\mathbf{q}}\| \tag{2.58}$$

to find the least square optimal solution leading to the normal equation already stated in Eq. (2.15)

$$\delta \mathbf{x} = -\underbrace{\left(\mathbf{A}^{\mathrm{T}}\mathbf{A}\right)^{-1} \mathbf{A}^{\mathrm{T}}}_{\mathbf{A}^*} \delta \mathbf{q}_\theta \tag{2.59}$$

where $\mathbf{A}^*$ is called the Moore-Penrose pseudo $6 \times m$ left inverse with $\mathbf{A}^*\mathbf{A} = \mathbf{I}$. This allows to compute the pose increment $\delta\mathbf{x}$ for an arbitrarily given cable length increment $\delta\mathbf{q}_\theta$. In case $\delta\mathbf{q}_\theta$ is consistent with Eq. (2.54) the unique solution and in case $\delta\mathbf{q}_\theta$ is inconsistent with Eq. (2.54) the least squares optimal solution is obtained. This result shows that a model solely based on geometrical relations is a simplification which misses some important properties of CDPRs since obviously one would have to explain the least squares solution for inconsistent cable lengths $\mathbf{x}$ in a physical way. In fact it is possible to derive the least squares solution of the forward kinematics as a special case of the elastostatic model as shown in Eq. (2.81) using a stiffness matrix $\mathbf{K} = \mathbf{I}$ and a zero wrench.

From Eq. (2.51)and

$$\mathbf{p}_{\mathrm{B},i} = \mathbf{a}_i - \mathbf{l}_i \tag{2.60}$$

one obtains the derivative

$$\frac{\partial q_i}{\partial \mathbf{l}_i} = \frac{\partial q_i}{\partial \mathbf{p}_{\mathrm{B},i}} \frac{\partial \mathbf{p}_{\mathrm{B},i}}{\partial \mathbf{l}_i} = -\frac{\partial q_i}{\partial \mathbf{p}_{\mathrm{B},i}} \mathbf{I} = \mathbf{u}_i^{\mathrm{T}} \ . \tag{2.61}$$

To complete the Jacobians of the kinematic standard model, the cable unit vector is derived with respect to the cable vector

$$\frac{\partial \mathbf{u}_i}{\partial \mathbf{l}_i} = \frac{\partial ({q_i}^{-1}\mathbf{l}_i)}{\partial \mathbf{l}_i} = {q_i}^{-2} \left(\frac{\partial \mathbf{l}_i}{\partial \mathbf{l}_i} q_i - \mathbf{l}_i \frac{\partial q_i}{\partial \mathbf{l}_i} \right) \tag{2.62}$$

leading to

$$\frac{\partial \mathbf{u}_i}{\partial \mathbf{l}_i} = \frac{1}{q_i} \left(\mathbf{I} - \mathbf{u}_i \mathbf{u}_i^{\mathrm{T}} \right) \ . \tag{2.63}$$

Finally the derivative of the cable unit vector with respect to the platform pose is obtained using the chain rule

$$\frac{\partial \mathbf{u}_i}{\partial \mathbf{x}} = \frac{\partial \mathbf{u}_i}{\partial \mathbf{l}_i} \frac{\partial \mathbf{l}_i}{\partial \mathbf{p}_{\mathrm{B},i}} \frac{\partial \mathbf{p}_{\mathrm{B},i}}{\partial \mathbf{x}} \ . \tag{2.64}$$

With Eq. (2.62, 2.60) and $\frac{\partial \mathbf{l}_i}{\partial \mathbf{p}_{\mathrm{B},i}} = -\mathbf{I}$ this leads to

$$\frac{\partial \mathbf{u}_i}{\partial \mathbf{x}} = \frac{1}{q_i} \left(\mathbf{u}_i \mathbf{u}_i^{\mathrm{T}} - \mathbf{I} \right) \begin{bmatrix} \mathbf{I} & -\tilde{\mathbf{b}}_i \end{bmatrix} \ . \tag{2.65}$$

The complete graph for the gradient flow for the pose related quantities of the standard kinematic model is shown in Fig. 2.9.

2.6 Differential Elastostatic Model

The differential relations of the elastostatic model are established using wrench closure condition Eq. (2.31). Considering that the structure matrix $\mathbf{A}^{\mathrm{T}}(\mathbf{x})$ depends on the generalized coordinates $\mathbf{x}$ and that cable forces are functions of the cable lengths which in turn are also expressed as functions of the generalized coordinates and the controlled cable

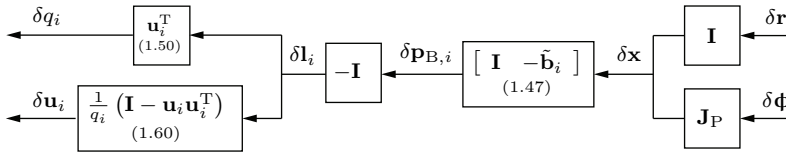

Figure 2.9: Standard kinematics model gradient flow

length i.e. $\mathbf{f}(\mathbf{q}(\mathbf{x}), \mathbf{q}_\theta)$ one obtains the implicit derivative with respect to $\mathbf{x}, \mathbf{q}_\theta$, and $\mathbf{w}_\mathrm{e}$ using sum notation

$$\left(\frac{\partial \mathbf{A}^{\mathrm{T}}}{\partial \mathbf{x}}\mathbf{f} + \mathbf{A}^{\mathrm{T}}\frac{\partial \mathbf{f}}{\partial \mathbf{q}}\frac{\partial \mathbf{q}}{\partial \mathbf{x}}\right)\delta\mathbf{x} + \mathbf{A}^{\mathrm{T}}\frac{\partial \mathbf{f}}{\partial \mathbf{q}_\theta}\delta\mathbf{q}_\theta + \delta\mathbf{w}_\mathrm{e} = \mathbf{0}. \tag{2.66}$$

Here the derivative

$$\mathbf{K}_{\mathrm{gsk}} = \frac{\partial \mathbf{A}^{\mathrm{T}}}{\partial \mathbf{x}}\mathbf{f} = \sum_{i=1}^{m}\frac{\partial \mathbf{v}_{\mathrm{A},i}}{\partial \mathbf{x}}f_i \tag{2.67}$$

with

$$\mathbf{v}_{\mathrm{A},i} = \begin{bmatrix} \mathbf{u}_i \\ \mathbf{b}_i \times \mathbf{u}_i \end{bmatrix}. \tag{2.68}$$

is called the geometrical stiffness. The partial derivatives $\frac{\partial \mathbf{v}_{\mathrm{A},i}}{\partial \mathbf{x}}$ follow using $\frac{\partial \mathbf{u}_i}{\partial \mathbf{x}}$ from Eq. (2.65) and

$$\frac{\partial \mathbf{b}_i}{\partial \mathbf{x}} = \frac{\partial \mathbf{p}_{\mathrm{B},i}}{\partial \mathbf{x}} - \frac{\partial \mathbf{r}}{\partial \mathbf{x}} = [\ \mathbf{0}\ \ \tilde{\mathbf{b}}_i\ ] \tag{2.69}$$

from Eq. (2.48) and relation

$$\frac{\partial\left(\mathbf{b}_i \times \mathbf{u}_i\right)}{\partial \mathbf{x}} = \tilde{\mathbf{b}}_i\frac{\partial \mathbf{u}_i}{\partial \mathbf{x}} - \tilde{\mathbf{u}}_i\frac{\partial \mathbf{b}_i}{\partial \mathbf{x}}\ . \tag{2.70}$$

The effect of the geometrical stiffness $\mathbf{K}_\mathrm{G}$ relates to the change of the wrench caused by the changing cable force directions when the platform is moved.

The second and third term in Eq. (2.66) describe the relation of the cable forces with respect to change in the cable lengths with

$$\frac{\partial f_i}{\partial q_i} = -\frac{\partial\left(k_{\mathrm{F}i}(1 - q_{\theta i}{q_i}^{-1})\right)}{\partial q_i} = \frac{k_{\mathrm{F}i}q_{\theta i}}{{q_i}^2} = k_i\frac{q_{\theta i}}{q_i} \tag{2.71}$$

and

$$\frac{\partial f_i}{\partial q_{\theta i}} = -\frac{k_{\mathrm{F}i}}{q_i} = -k_i \tag{2.72}$$

which can be simplified to

$$\frac{\partial \mathbf{f}}{\partial \mathbf{q}} = -\frac{\partial \mathbf{f}}{\partial \mathbf{q}_\theta} = \mathbf{K} = \mathrm{diag}(\mathbf{k}) \tag{2.73}$$

for $\mathbf{q} \approx \mathbf{q}_\theta$. Considering Eq. (2.54, 2.67, 2.73) one can rewrite Eq. (2.66) so that

$$\left(\mathbf{K}_\mathrm{G} - \mathbf{A}^\mathrm{T}\mathbf{K}\mathbf{A}\right)\delta\mathbf{x} - \mathbf{A}^\mathrm{T}\mathbf{K}\delta\mathbf{q}_\theta + \delta\mathbf{w}_\mathrm{e} = \mathbf{0} \tag{2.74}$$

A complete picture of the elastostatic gradient flow is given in Fig. 2.10.

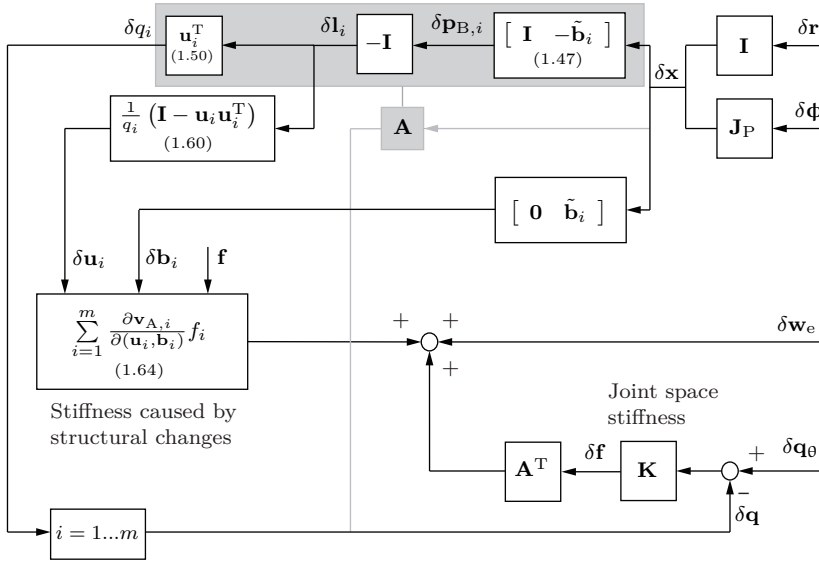

Figure 2.10: Elastostatic gradient flow

The differential relation between the external wrench $\mathbf{w}_\mathrm{e}$ and the platform pose $\mathbf{x}$ is established under the assumption of a fixed controlled cable length $\delta\mathbf{q}_\theta = \mathbf{0}$ using Eq. (2.74) and considering

$$\mathbf{K}_\mathrm{C} = \mathbf{A}^\mathrm{T}\mathbf{K}\mathbf{A} \tag{2.75}$$

yielding

$$\frac{\partial \mathbf{w}_\mathrm{e}}{\partial \mathbf{x}} = -\mathbf{K}_\mathrm{wx} = -\mathbf{K}_\mathrm{G} + \mathbf{K}_\mathrm{C} \tag{2.76}$$

where the system stiffness $\mathbf{K}_\mathrm{wx}$ is composed of the cable stiffness matrix $\mathbf{K}_\mathrm{C}$ and the geometrical stiffness matrix $\mathbf{K}_\mathrm{G}$ from Eq. (2.67). The stiffness matrix $\mathbf{K}_\mathrm{C}$ maps the incremental change of the platform pose to the joint space and the resulting cable forces back to the cartesian space. The magnitude of the geometrical stiffness is low compared to

the stiffness resulting from the cables and depends on the magnitude of the cable forces, i.e. higher tension states result in higher geometrical stiffness. The low contribution of the geometrical stiffness to the overall stiffness can be seen by comparing the change of the magnitude of the cable forces caused by a directional change compared with the force caused by a change in the cable length. The directional change of the cable force is described by Eq. (2.65) showing that the impact for the geometric stiffness is inversely related to the cable length. For typical setups where $b < q$ and the tension states between 10 N $<$ f $<$ 10000 N the expected stiffness is $<$ 10 kN/m. As comparison, the typical stiffness for the cables of a CDPR lies between $500 - 3000$ kN/m.

The associated compliance matrix as inverse of the stiffness matrix is denoted as

$$\mathbf{C}_{\mathrm{xw}} = {\mathbf{K}_{\mathrm{wx}}}^{-1}. \tag{2.77}$$

and exists for the square $n \times n$ stiffness matrix if $\det(\mathbf{K}_{\mathrm{wx}}) \neq 0$ so that

$$\delta\mathbf{x} = -\mathbf{C}_{\mathrm{xw}}\delta\mathbf{w}_{\mathrm{e}} \ . \tag{2.78}$$

The differential relation between platform pose $\mathbf{x}$ and the controlled cable length $\mathbf{q}_\theta$ is derived from Eq. (2.74) assuming a constant external wrench i.e. $\delta\mathbf{w}_{\mathrm{e}} = \mathbf{0}$ and using

$$\mathbf{K}_{\mathrm{wq}} = \mathbf{A}^{\mathrm{T}}\mathbf{K} \tag{2.79}$$

leading to

$$\delta\mathbf{x} = \underbrace{\left(\mathbf{K}_{\mathrm{G}} - \mathbf{K}_{\mathrm{C}}\right)^{-1}\mathbf{K}_{\mathrm{wq}}}_{\mathbf{J}_{\mathrm{x}\theta}}\delta\mathbf{q}_\theta \ . \tag{2.80}$$

The extension from a solely geometrical model to an elastostatic model allows to describe the mapping of velocities from joint space to Cartesian space for redundant CDPRs in a physically consistent way. The connection to the forward kinematics can be shown with Eq. (2.66, 2.74) for the special case of $\mathbf{f} = \mathbf{0}, \mathbf{w}_{\mathrm{e}} = \mathbf{0}, \delta\mathbf{w}_{\mathrm{e}} = \mathbf{0}$, where the obtained solution corresponds to the modified normal equation with the weight matrix $\mathbf{W} = \mathbf{K}$,

$$\delta\mathbf{x} = -\left(\mathbf{A}^{\mathrm{T}}\mathbf{W}\mathbf{A}\right)^{-1}\mathbf{A}^{\mathrm{T}}\mathbf{W}\delta\mathbf{q}_\theta \ . \tag{2.81}$$

Choosing $\mathbf{W} = c\mathbf{I}, c > 0$ with the identity matrix $\mathbf{I}$, one obtains Eq. (2.59), the solution of the foward kinematics where all residuals of the cable lengths are treated with the same weight. In this sense, the forward kinematics provides a good approximation for robot states with low cable forces and equal spring constants for all cables. It also should be noted that the result is independent of the scaling factor c and that the result relies only on the ratio between the individual spring constants.

Finally, the relation between incremental changes in the actual cable lengths $\mathbf{q}$ and the controlled cable lengths $\mathbf{q}_\theta$ can be computed using Eq. (2.54, 2.80) yielding

$$\delta\mathbf{q} = -\mathbf{J}_{\mathrm{qx}}\left(\mathbf{K}_{\mathrm{G}} + \mathbf{K}_{\mathrm{C}}\right)^{-1}\mathbf{K}_{\mathrm{wq}}\delta\mathbf{q}_\theta \ . \tag{2.82}$$

2.7 Differential Pulley Model

The differentials of the pulley model are closely related to the standard geometric model and can be derived without consideration of the trigonometric functions which are used to describe the pulley orientations.

The Jacobian $\mathbf{J}_{\mathrm{qx}} = -\mathbf{A}$ is computed identical to the standard kinematic model considering the pulley contact point $\mathbf{p}_{\mathrm{A},i}$ instead of the attachment point $\mathbf{a}_i$ for the computation of the structure matrix. This is due to the fact that the involute of the pulley as indicated in Fig. 2.11 has the same tangent vector as a circle around $\mathbf{p}_{\mathrm{A},i}$ and that the differential arc length $\delta q_{\mathrm{u},i}$ and differential free cable length $\delta q_{\mathrm{f},i}$ cancel out each other.

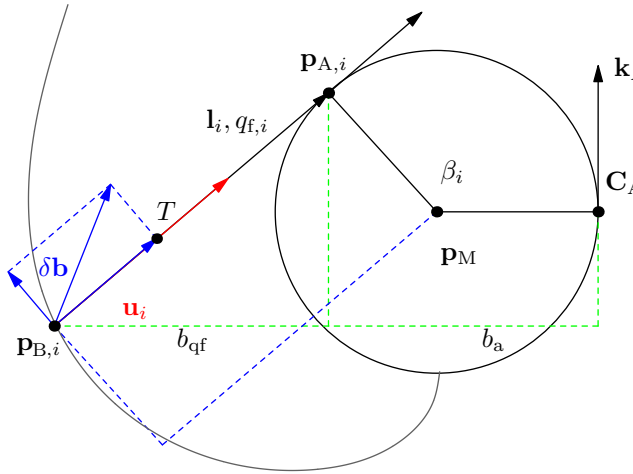

Figure 2.11: Pulley involute an differentials

For computations of the system stiffness and sensitivity analysis it is also important to know the differentials of the free cable length and pulley arc length which can be computed using the angular speed of the pulley about its center axis at $\mathbf{p}_{\mathrm{M},i}$ with

$$\boldsymbol{\omega} = \frac{\|\delta\mathbf{b}_{\perp}\|_2}{q_{\mathrm{f}}} \tag{2.83}$$

and $\delta\mathbf{b}_{\perp}$ being the projection onto the involute tangent vector $\delta\mathbf{b}_{\perp} = \delta\mathbf{b}\hat{\mathbf{u}}_{\mathrm{r}}$ so that

$$\delta q_{\mathrm{u}} = \|\delta\mathbf{b}_{\perp}\|_2 \frac{r_{\mathrm{p}}}{q_{\mathrm{f}}} \ . \tag{2.84}$$

Using Eq. (2.48) one obtains the Jacobian formulation for cable arc lenght

$$\mathbf{J}_{\mathrm{qux},i} = \hat{\mathbf{u}}_{\mathrm{r},i} \frac{r_{\mathrm{p},i}}{q_{\mathrm{f},i}} \mathbf{J}_{\mathrm{pBx},i} \ . \tag{2.85}$$

The differential relation of the free cable length is derived in accordance with Eq. (2.50) considering the pose dependent contact point in $\mathbf{l}_i = \mathbf{p}_{\mathrm{A},i}(\mathbf{x}) - \mathbf{p}_{\mathrm{B},i}(\mathbf{x})$. The associated Jacobian $\mathbf{J}_{\mathrm{pAx}_i}$ is computed by

$$\mathbf{J}_{\mathrm{pAx}_i} = \mathbf{n}_{\mathrm{M}} \frac{b_{\mathrm{a}}}{b_{\mathrm{xy}}} \mathbf{J}_{\mathrm{pBx},i} + \mathbf{u}_i \mathbf{J}_{\mathrm{qux},i} \tag{2.86}$$

where the first part relates to the component perpendicular to the pulley plane and the second part relates to the component on the pulley plane. Relation Eq. (2.50) now can be restated as

$$\mathbf{J}_{\mathrm{l}x,i} = \frac{\partial \mathbf{l}_i}{\partial \mathbf{x}} = \mathbf{J}_{\mathrm{pAx}_i} - \mathbf{J}_{\mathrm{pBx},i} \ . \tag{2.87}$$

The elasto-geometrical relations for the pulley kinematics model can be adopted from Sec. 2.6 without changes.

3 Control Model Analysis

Analyzing and comparing the performance of different models is an essential task for the optimal configuration of a CDPR system. The answer to the question, which is the optimal model for a specific application, can only be provided by a concurrent consideration of the model structure together with its optimal parametrization. This must be done in the context of a distinct physical robot model which incorporates physical properties not present in the control model. The comparison must be done with respect to a distinct set of evaluation criteria where the pose tracking accuracy and the workspace are the most important beside others as outlined in the next Sec. 3.1. This chapter derives a meta-model as foundation for a unified comparison of different models in the context of a ground-truth model which represents a system of higher complexity. The architecture of the meta-model involves the combination of different physicals models and allows to make the distinction between different types of model parametrizations, namely the nominal, physical, and optimal parametrization as described in Sec. 3.2. The differentiation between types of parametrization is identified as essential to the goal of unified model comparison. The meta-model allows the analytic description of the pose accuracy in context of the ground-truth model and is derived in Sec. 3.4 together with the definition of the reachable workspace in Sec. 3.5. The reachable workspace extends the concept of the wrench-feasible workspace allowing to regard the combination of different model assumptions for the control model and ground-truth model. The meta-model then is used to analyze control models of different structural complexity together with their parametrization to understand the possible impact on the previously defined pose tracking accuracy and reachable workspace based on the models from the last chapter.

3.1 Evaluation Criteria

Selecting the best model from the candidate set can only be done in perspective of a requirement definition with respect to a specific application from which a set of evaluation criteria is derived. The evaluation criteria then can be used in the sense of a knock-out criteria defining a threshold which must be fulfilled by the model to get validated or in the sense of a performance rating to compare the models of the canidated set against each other. A list of evaluation criteria relevant for control models of CDPRs is stated below.

- **Position accuracy** is the main criterion focused on in this thesis and describe more precisely in the next sections.

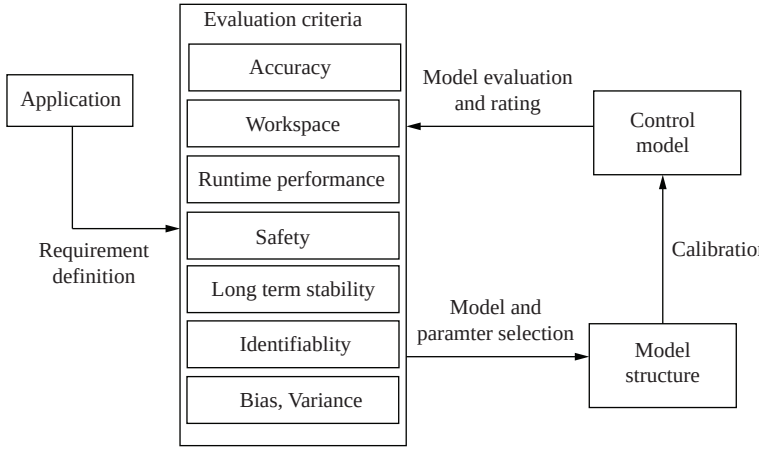

Figure 3.1: Model selection based on the application requirement definition and associated evaluation criteria.

- **Workspace** defines the volume which can be reached by CDPR using a specific the control model.

- **Identifiability** considers the chosen model parametrization with respect to possible measurements. The model must be chosen such that structural identifiability (Khalil and Dombre 2004) is guaranteed and that it is possible to reach the necessary sample space that leads to a well conditioned observation matrix as shown in Sec. 4.3. The question of structural identifiability is closely coupled to the available sensors which determine the observability of system states. Problems arise when the model is structural unidentifiable i.e. the observation matrix is rank deficient no matter how many different samples are taken from the possible sample space.

- **Runtime performance** is related to the complexity of the model in so far as each additional submodel increases computational complexity and gets especially critical for models whose solution has to be computed in an iterative manner using optimization algorithms.

- **Safety** can be understood in the sense of simplicity. Complex models are more difficult to understand and to test with respect to unintentional input-ouput behavior.

- **Long term stability** refers to the sensitivity of the model prediction with respect to drifting model parameters and the possibility of parameter updates based on in-process sensor data.

- **Bias, Variance** refers to the prediction accuracy with respect to changes in measurements or sample set.

While all these criteria are relevant for model evaluation, this thesis focuses mainly on stationary pose prediction accuracy and the reachable workspace volume achievable with the respective models. The influence of the other criteria are mentioned when necessary in case they impact the goal of maximizing pose prediction accuracy and workspace volume. In the next sections, the meta-model is derived and methods for the analysis and the estimation of the evaluation of the pose prediction accuracy and workspace volume for different models are derived.

3.2 Meta Model for Control Model Analysis

Comparing models with respect to the aforementioned evaluation criteria in a systematic way requires a standardized context which allows to model the impact of variations in the model structure and parametrization. This section introduces the meta model for the simulative optimization and analysis of stationary accurate control models based on model compositions from Chap. 2 and a ground truth model $\hat{\boldsymbol{\upsilon}}$ which relates to a model of higher complexity regarding the number of represented physical effects. The meta model is used to analyze the influence of the model structure and its parametrization with regards to different parts of the model selection process such as model optimization, measurements, model prediction accuracy, and the reachable workspace. While the ground truth model in principal does not need to be real-time capable and can be used to simulate computational expensive effects, it makes sense to chose the same model structure as for the final control model. This allows a more meaningful analysis as shown in Sec. 3.4 for position error analysis and in Sec. 3.5 for the workspace analysis. That relates to the fact that deviations between the control model and the ground truth model usually are small and a linear analysis can be performed.

The basic structure of the meta-model is given in Fig. 3.2 showing the model composition $\boldsymbol{\eta}_{\mathrm{el}}$ for the standard elastostatic model and the ground truth model $\hat{\boldsymbol{\upsilon}}$.

Changing the model structure in terms of the model composition $\boldsymbol{\eta}$ relates to the model design step (1) in the model selection process from Fig. 1.5. The impact of these structural changes on the model evaluation (3) with respect to pose accuracy and workspace is part of this chapter. Changing the model parametrization of $\boldsymbol{\eta}$ is mainly of interest for the model optimization step (2) and is discussed in the respective chapter. For the structural analysis in this chapter, the control model parametrization $\mathbf{p}_{\eta}$ is directly derived from so called physical parametrization $\hat{\mathbf{p}}$ providing the best value obtainable by direct measurement of $\hat{\boldsymbol{\upsilon}}$. A more detailed distinction of the different model parametrization is given later in this section.

Publications which propose new models or do experimental evaluations of these models often make different assumptions about the context in which they are analyzed. This makes

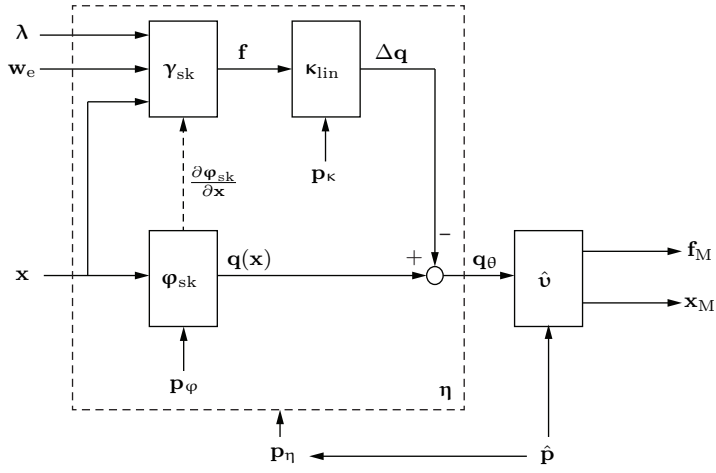

Figure 3.2: Meta model for the numerical analysis of model compositions $\boldsymbol{\eta}$ in the context of a ground truth model $\hat{\boldsymbol{\upsilon}}$

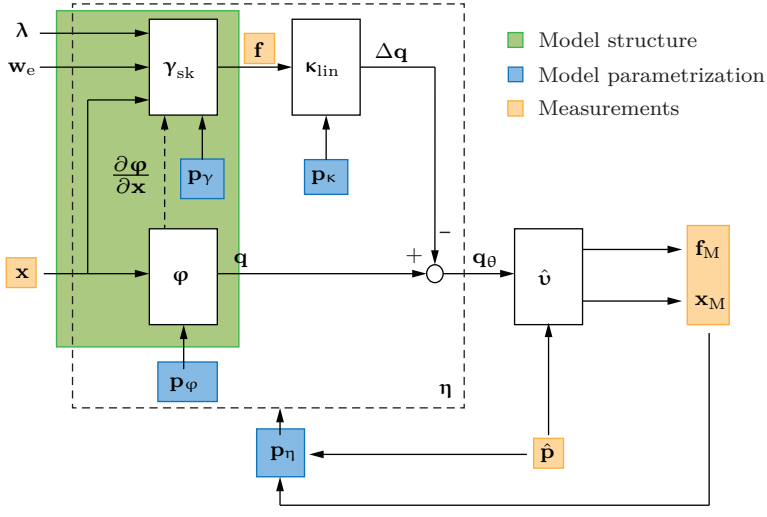

Figure 3.3: Model analysis $\boldsymbol{\eta}$ in the context of a ground truth model $\hat{\boldsymbol{\upsilon}}$

it difficult to compare the models and to make an informed choice on model selection for a given application.

Using model compositions $\boldsymbol{\eta}$ in the context of a ground truth model allows to address different issues arising for the selection of the optimal model structure, the optimal model parametrization, and the measured system quantities as shown in Fig. 3.3 and discussed in the following.

1) Model structure Extensions to the model structure indicated by the green area in Fig. 3.3, implicitly are analyzed under the assumption of idealized conditions i.e. the model perfectly matches with reality. For example the workspace and stiffness properties of the elastostatic standard model are computed without consideration of a possible misalignment between the model geometry and the model stiffness parameters compared to the physical system parameters. In the meta-model, this would coincide with a model structure $\boldsymbol{\eta} = \hat{\upsilon}$ and a parametrization of $\mathbf{p}_{\eta} = \hat{\mathbf{p}}$ such that $\mathbf{x}_{\mathrm{M}} = \mathbf{x}$ and $\mathbf{f}_{\mathrm{M}} = \mathbf{f}$. The proposed structure allows to analyze the presumed impact of the surrounding system under predefined conditions.

2) Model parametrization In the case of two models $\boldsymbol{\eta}_{\mathrm{A}}, \boldsymbol{\eta}_{\mathrm{B}}$ with different underlying structures, i.e. modifications to $\boldsymbol{\varphi}, \boldsymbol{\gamma}, \boldsymbol{\kappa}_{\mathrm{lin}}$ which are evaluated using measurements $(\mathbf{x}, \mathbf{f})$, the problem of comparability is induced mostly by the associated model parametrization. In perspective of model selection and evaluation, it is therefore important to distinguish different sets of parameters which in the context of this thesis will be called *nominal parameters*, *physical parameters*, and *optimal parameters*: The difference between nominal and physical parameters results form e.g. manufacturing and assembly errors.

- **Nominal parameters $\mathbf{p}_{\mathrm{N}}$** are defined during the design phase and resemble the parameter set which should be realized on the CRPR system under idealized conditions. These parameters are used before the implementation stage to investigate different system properties and run analysis such as system stiffness, workspace, or collision spaces analysis. They are also used as first best guess on the robot controller before more exact measurements are available.

- **Physical parameters $\hat{\mathbf{p}}$** denote the best estimate of the real physical properties which are represented by the model. This would be the accurate locations of the redirection pulleys as measured after assembly, or the cable stiffness coefficients measured during a cable elongation test performed on a test bench, or the platform mass determined by a scale.

- **Optimal parameters $\mathbf{p}_{\mathrm{opt}}$** denote the parametrization which is found by an optimization procedure with respect to some input-output quantities, e.g. joint space encoder values and platform pose measurements. They represent the best choice for a given model to mimic the behavior which is determined by the taken measurements. The optimal parameters depend on the number and distribution of measurements. Comparing optimal parameters one-by-one with physical parameters can show significant differences although the parameter set in its entity provides good predictions.

Model parametrizations can be obtained in two different ways, that is with direct measurement or indirectly via parameter identification. In case of parameter identification, the distinction between a partial or full parameter identification has to be made. Sometimes a combination of the methods is used.

In the case of direct measurements, a specialized measurement device is used to determine a physical property of the system. This can be a laser-tracking system to measure the geometric properties of a CDPR, or a scale or inertial measurement unit to measure the mass properties of the platform, or a force sensor on a test bench to measure the elasticity of a cable segment. In the meta-model from Fig. 3.3, this distinct parametrizations $\mathbf{p}_{\eta_A}, \mathbf{p}_{\eta_B}$ for the two different models in case of error-free measurements is represented by

$$\mathbf{p}_{\eta_A}, \mathbf{p}_{\eta_B} \subset \hat{\mathbf{p}} \wedge \mathbf{p}_{\eta_A} \neq \mathbf{p}_{\eta_B} \tag{3.1}$$

where each model represents a different subset $\mathbf{p}_{\eta_A}, \mathbf{p}_{\eta_B}$ of the physical reality $\hat{\mathbf{p}}$. In practice, this approach has the drawback that CDPR assemblies are prone to systematic measurement errors which can accumulate, be amplified, and influence the output behavior in unpredictable ways. Direct measurement of a parameter value is defined by the measurement precision and accuracy (Walther and Moore 2005) as shown in Fig. 3.4 where accuracy relates to the closeness of the measurement $\mathbf{p}_\varphi$ and the true value $\hat{\mathbf{p}}$, and precision relates to the reproducibility of the measurements. Based on this definition and referring to the direct measurements of the geometric parameters with a laser-tracker, the laser-tracker provides high precision measurements but cannot guarantee high accuracy. The accuracy of the measurement is not as much a property of the measurement device as of the measurement process.

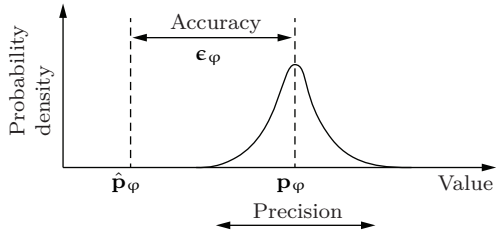

Figure 3.4: Precision and accuracy of parameter measurements

For the geometry model, the measurement process defines the actual location $\mathbf{p}_\varphi$ of the laser-tracker measurements and while this defined location $\mathbf{p}_\varphi$ can be measured with high precision, it may not represent the accurate location assumed by the model. These systematic errors are caused by model simplifications leading to a difference of the physical and modelled entity as is best seen in Fig. 3.5 where a platform anchor point and a redirection pulley are shown which both are essential for the kinematics model of a CDPR. A direct measurement of the kinematic parameters relates to a measurement of the cable contact

points at the platform and frame. A measurement device such as a laser-tracker provides position data with a precision of some 0.01 mm, but from the components in the photos it can be seen that systematic measurement errors are likely to be introduced since the point-shaped end-point of the cable model cannot be physically determined. The measurement accuracy largely depends on the specific hardware design and the way the measurement is performed. One has to reconstruct the actual contact point from a geometry in the close vicinity as seen in Fig. 3.5b for the redirection pulley where the laser target is placed on top of the pulley mechanism.

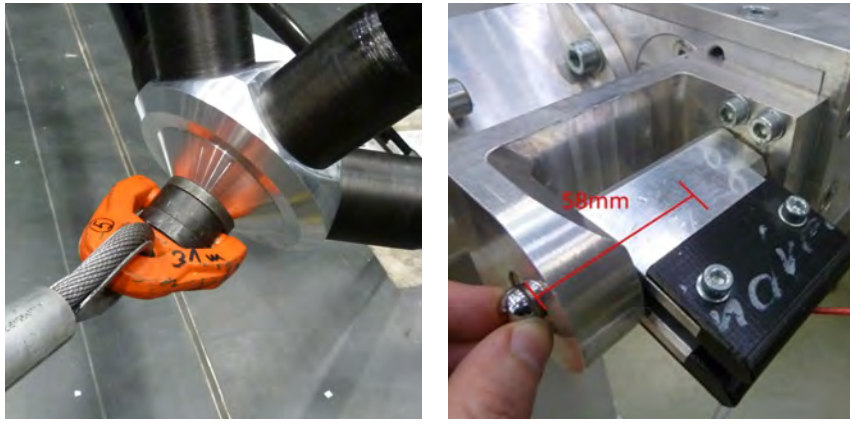

(a) Platform anchor point at the CRS carbon fiber cabin

(b) Cable outlet with tilt pulley from the high accuracy winch system from Fraunhofer IPA

Figure 3.5: CDPR components essential to the kinematics model

While the precision of the measurement device is known and can be compensated for or be reported together with the evaluation results, this is not possible for the unknown systematic errors of the measurement of the component. For the analysis in the meta-model, the influence of measurement precision is neglected and only measurement accuracy is considered which is expressed as

$$\mathbf{p}_\varphi = \hat{\mathbf{p}}_\varphi + \boldsymbol{\epsilon}_\varphi \ . \tag{3.2}$$

Together with Eq. (3.1), the final position accuracy and workspace of the CDPR is now influenced by the unknown systematic parameter errors and their interaction with unmodeled parts of the CDPR. This makes analyzing the contribution of the model structure difficult with regards to model performance.

The effects of direct measurement may also lead to over-complex models, that do not show increases in the performance level compared to simpler models. Due to its cumulative nature, each additional model adds new parameters with a systematic error and while

the contribution of each additional model to the final model prediction gets smaller, the systematic error increases until it exceeds the benefits. This is closely related to the bias variance trade-off problem from Fig. 1.4.

Using the meta model from Fig. 3.2 allows to address the issues stated in Par. 1 above by allowing the interaction of models with different structures and parametrizations and the issues stated in Par. 2 by analyzing the impact of complete parameter set with respect to the output behavior. In the following sections, the meta-model is used to analyze the pose accuracy and to define the reachable workspace of a given control model. The control model $\boldsymbol{\varphi}$ and its parametrization is chosen from a model candidate set together with a ground truth model $\hat{\boldsymbol{\upsilon}}$ which incorporates some properties which the control model $\boldsymbol{\varphi}$ should be tested against. The control model in general expects a desired pose and/or force signal as input and returns the associated geometric joint space values which in turn are processed by the ground truth model to determine the actual platform pose and force distribution. The resulting actual pose and cable length values than can be compared to the desired values computing the performance of the different models using a common predefined error metric as shown in the following section.

3.3 Error Metrics

The definition of an error metric is essential for the comparison of model candidates. While the specific metric may vary depending on the intended use it is important to keep the defined metric fixed for the entire model selection and optimization process. Not providing the specific error metrics and sample space is a common problem when the results from different source models in literature are compared against each other. Starting with the most common error metric, the accuracy for a pose set $\mathcal{W}_\mathrm{X}$ with $n_\mathrm{s} = |\mathcal{W}_\mathrm{X}|$ samples, is computed in the sense of the absolute mean pose prediction error by

$$\epsilon_{\mathrm{x}_j} = \left\| \mathbf{x}_{\mathrm{P}_j} - \mathbf{x}_{\mathrm{M}_j} \right\|_2 \tag{3.3}$$

$$\epsilon_{\bar{\mathrm{x}}}(\bar{\mathbf{x}}_\mathrm{P}, \bar{\mathbf{x}}_\mathrm{M}) = \sum_{j=1}^{n_\mathrm{s}} \epsilon_{\mathrm{x}_j} n_\mathrm{s}^{-1} \tag{3.4}$$

where n_s is the number of samples in the input-output sample space $\mathcal{W}_\mathrm{Q} \rightarrow \mathcal{W}_\mathrm{X}$ defined by the joint space input sample vector $\bar{\mathbf{q}}_\theta = \begin{bmatrix} \mathbf{q}_{\theta 1} & \cdots & \mathbf{q}_{\theta n_s} \end{bmatrix}, \mathbf{q}_{\theta j} \in \mathcal{W}_\mathrm{Q}$ which is used to compute model predictions $\mathbf{x}_{\mathrm{P}_j} = \boldsymbol{\varphi}(\mathbf{p}, \mathbf{q}_{\theta j})$ for a given parametrization $\mathbf{p}$ and to generate the associated pose measurements $\bar{\mathbf{x}}_\mathrm{M} = \begin{bmatrix} \mathbf{x}_{\mathrm{M}_1} & \cdots & \mathbf{x}_{\mathrm{M}_{n_s}} \end{bmatrix}, \mathbf{x}_{\mathrm{M}_j} \in \mathcal{W}_\mathrm{X}$. From that, the relative mean pose prediction error is given by

$$\hat{\epsilon}_\mathrm{x} = \frac{\epsilon_{\bar{\mathrm{x}}}}{d_\mathcal{W}} \tag{3.5}$$

where

$$d_\mathcal{W} = \max(\mathrm{dist}(\mathcal{W}_\mathrm{S})) \tag{3.6}$$

is the distance between the most distant sample elements. For sampling patterns with a simple bounding box spanned by the diagonal vector $\mathbf{v}_{\mathrm{bb}}$ this leads to

$$d_{\mathcal{W}} = \|\mathbf{v}_{\mathrm{bb}}\|_2 \ . \tag{3.7}$$

The relative error can be used as scale independent performance parameter. The absolute and relative mean pose error are metrics which allows to evaluate the general usability of a controller and are well suited for processes where no rigid limits for position accuracy are required such as motion simulation or camera inspection tasks. For more demanding process with strict limits on the maximum positioning error, it is necessary to use the respective error metric for maximum loss (Shalev-Shwartz and Wexler 2016)

$$\epsilon_{\mathrm{x_{max}}} = \max_{j\in\{1\dots n_{\mathrm{s}}\}} \left\| \mathbf{x}_{\mathrm{P}_j} - \mathbf{x}_{\mathrm{M}_j} \right\|_2 \ . \tag{3.8}$$

Evaluating and comparing model candidates with respect to pose prediction accuracy can be done in perspective of a specific application or in context of other model candidates as shown in Fig. 3.6 under predefined environmental conditions with the goal of finding the optimal feed forward control model. An optimal model $\boldsymbol{\varphi}_{\mathrm{opt}} = \boldsymbol{\varphi}(\mathbf{p}_{\mathrm{opt}})$ is defined by its optimal parametrization $\mathbf{p}_{\mathrm{opt}}$ which minimizes the error metric from Eq. (3.3) with

$$\min_{\mathbf{p}} \sum_{j=1}^{n_{\mathrm{s}}} \left\| \boldsymbol{\varphi}(\mathbf{p}, \mathbf{q}_{\theta j}) - \mathbf{x}_{\mathrm{M}_j}(\mathbf{q}_{\theta j}) \right\|_2 \tag{3.9}$$

or the error metric from Eq. (3.8) minimizing the maxium loss

$$\min_{\mathbf{p}} \max_{j\in\{1\dots n_{\mathrm{s}}\}} \left\| \boldsymbol{\varphi}(\mathbf{p}, \mathbf{q}_{\theta j}) - \mathbf{x}_{\mathrm{M}_j}(\mathbf{q}_{\theta j}) \right\|_2 \ . \tag{3.10}$$

for a validation sample set $(\bar{\mathbf{q}}_{\theta \mathrm{V}}, \bar{\mathbf{x}}_{\mathrm{MV}})$ under predefined environmental conditions. Both optimality criteria lead to the same minimizer if $\epsilon_{\bar{\mathrm{x}}}(\mathbf{p}_{\mathrm{opt}}) = 0$. For the more usual case of $\epsilon_{\bar{\mathrm{x}}}(\mathbf{p}_{\mathrm{opt}}) > 0$ the minmax criterion is the stronger error bound since $\epsilon_{\mathrm{x_{max}}}(\mathbf{p}) \geq \epsilon_{\bar{\mathrm{x}}}(\mathbf{p})$ and therefore is the preferred criterion when strict limits on the pose error are demanded by the application. On the downside finding the minmax minimizer is more difficult than finding the mean average minimizer and it is not robust with respect to outliers in the sample data as the objective function is not always continuous differentiable.

The optimal model from a model candidate set with n_{c} candidates is defined by

$$\boldsymbol{\varphi}_{\mathrm{opt,c}} = \min \left(\epsilon_{\bar{\mathrm{x}}}(\bar{\mathbf{x}}_{\mathrm{Popt},1}, \bar{\mathbf{x}}_{\mathrm{M}}), \cdots \epsilon_{\bar{\mathrm{x}}}(\bar{\mathbf{x}}_{\mathrm{Popt},n_s}, \bar{\mathbf{x}}_{\mathrm{M}}) \right) \tag{3.11}$$

where the pose prediction sample vectors $\bar{\mathbf{x}}_{\mathrm{Popt},j}$ are computed by the respective optimal configuration of each individual model with

$$\mathbf{x}_{\mathrm{Popt}_j} = \upsilon_{\mathrm{kin},j}(\mathbf{p}_{\mathrm{opt}}) \ . \tag{3.12}$$

From this, it gets clear that it is not possible to rate a specific model structure without finding its optimal parametrization e.g. it is not possible to compare an elastostatic model

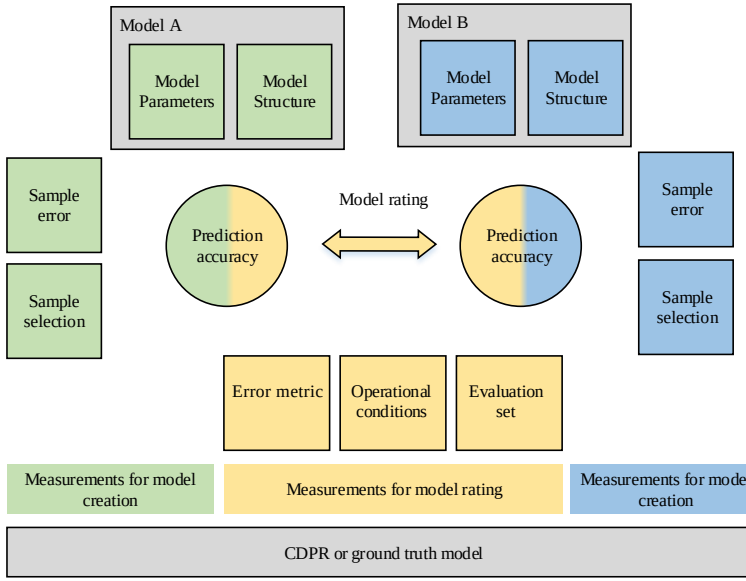

Figure 3.6: Model rating of two exemplary models A, B, based on a common error metric, operational conditions, and evaluation set. Keeping the conditions fixed for the entire optimization and evaluation process is essential for the validity of the results.

with a pulley model without finding the optimal parametrization of each model beforehand. Therefore, the model rating process is closely tied to the optimization and calibration process and may suffer from the same problems such as local minima.

Evaluation and optimization of the models with the predescribed error metrics is usually done with a sample set $\bar{\mathbf{x}}_{\mathrm{M}}$ recorded on the CDPR. Modelling this process of error evaluation and parameter optimization using the meta-model described in Sec. 3.2, allows to derive an analytic description of the effects that can be expected for different model assumptions. In the following section, the meta-model is used to simulate the process of measurement and predict the pose error with respect to model structure and parameter variations.

3.4 Pose Accuracy

In order to compare different models with respect to their maximal reachable pose accuracy for a given application, one has to do an actual implementation of a control model, acquire a sample set, run a parameter optimization, and use the optimized model to create a second sample set for the final model evaluation. The same has to be done for the other model candidates subject to the comparison. Finally, one can use an error metric from Sec. 3.3 to rate and select the model with the best pose prediction accuracy.

For the theoretical analysis of the stationary pose tracking accuracy of the control model and the associated optimization methods, the meta model from Fig. 3.2 is used to compute pose deviations $\Delta\mathbf{x}$ for CDPR model compositions $\boldsymbol{\eta}$ according to Chap. 2 in the context of a ground truth model $\hat{\boldsymbol{\upsilon}}$ as depicted in Fig. 3.7.

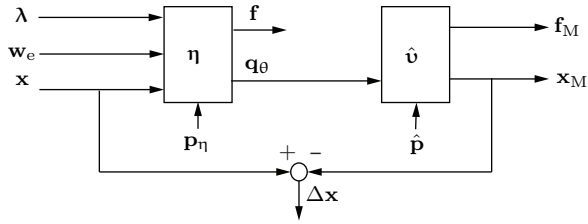

Figure 3.7: Pose error estimation

For the following analysis of the pose accuracy, certain conditions have to be fulfilled by the ground truth model $\hat{\boldsymbol{\upsilon}}$:

1) The ground truth model must be of equal or higher complexity as the control model and the parametrization of the control model must be different or a subset of the ground truth model parametrization.

2) The ground truth model must be at least an elastostatic model to provide a meaningful interpretation of the pose accuracy.

3) The initial conditions and parametrization of the control model must be closely aligned in order to perform linear analysis.

The following analysis is performed with the standard elastostatic model for the ground truth model. The control model is to be assumed closely aligned with the ground truth model using a subset of the ground-truth parametrization

$$\mathbf{p}_\eta \subset \hat{\mathbf{p}} \tag{3.13}$$

and identical initial conditions. The remaining parameters of $\hat{\mathbf{p}}$ are assumed to have small impact on the results, e.g. the pulley radius parameter for a pulley model would be small compared to the workspace size such that the impact becomes neglectable.

The operational conditions are defined by the initial configuration $\mathbf{x}_{\text{ini}}$ with the associated initial geometrical cable lengths $\mathbf{q}_{\theta_{\text{ini}}} = \boldsymbol{\varphi}(\mathbf{x}_{\text{ini}})$ and the initial cable offset defined by

$$\mathbf{q}_{\text{off}} = \hat{\boldsymbol{\varphi}}(\mathbf{x}_{\text{ini}}) - \mathbf{q}_{\theta_{\text{ini}}} \tag{3.14}$$

resulting in the initial cable force distribution $\mathbf{f}_{\text{ini}}$ subject to wrench closure condition Eq. (2.31) and the external wrench $\mathbf{w}_{\text{e}}$ which for simplicity is assumed to be constant during operation. The initial cable offset $\mathbf{q}_{\text{off}}$ does not change during robot operation so that the actual platform pose becomes

$$\hat{\mathbf{x}} = \hat{\boldsymbol{\upsilon}}(\boldsymbol{\varphi}(\mathbf{x}) + \mathbf{q}_{\text{off}}). \tag{3.15}$$

The pose error $\mathbf{x}_{\text{err}} = \hat{\mathbf{x}} - \mathbf{x}$ for the nominal configuration $\mathbf{p}_{\text{N}}$ can now be computed using the full elasto-geometric forward kinematics $\hat{\boldsymbol{\upsilon}}$ or using the linearized version which provides accurate results in most cases as shown in the following.

Let $\mathbf{x}_0, \mathbf{q}_{\theta_0}$ be a pose and consistent controlled cable length, respectively, such that the wrench-closure condition $\boldsymbol{\gamma}_{\text{sk}}(\mathbf{x}_0, \mathbf{q}_{\theta_0}) = \mathbf{0}$ holds true and let

$$\Delta\mathbf{w} = \mathbf{A}^{\text{T}}\mathbf{f}(\mathbf{q}_\theta) + \mathbf{w}_{\text{e}} \tag{3.16}$$

be the residual wrench for an arbitrary controlled cable length $\mathbf{q}_\theta$ and cable force $\mathbf{f} = \mathbf{K}\left(\mathbf{q}(\mathbf{x}) - \mathbf{q}_\theta\right)$ then the associated residual cable force follows using Eq. (2.38) with

$$\Delta\mathbf{f} = -\mathbf{A}^{+\text{T}}\Delta\mathbf{w} \ . \tag{3.17}$$

The residual wrench and residual forces $\Delta\mathbf{w}, \Delta\mathbf{f}$ show the deviation from the equilibrium point and cause undesired motion of the platform. Considering decomposition of an arbitrary force vector into its internal, external, and residual forces

$$\mathbf{f} = \underbrace{\mathbf{f}_{\text{ext}} + \mathbf{f}_{\text{int}}}_{\mathbf{f}_0} + \Delta\mathbf{f}, \tag{3.18}$$

then the force equilibrium point $\mathbf{f}_0$ which fulfills the wrench closure condition is obtained using Eq. (2.38, 2.40) yielding

$$\mathbf{f}_0 = -\mathbf{A}^{+\text{T}}\mathbf{w}_{\text{e}} + \left(\mathbf{I} - \mathbf{A}^{+\text{T}}\mathbf{A}^{\text{T}}\right)\mathbf{f}(\mathbf{q}_\theta) \ . \tag{3.19}$$

The associated cable lengths are given by

$$\mathbf{q}_{\theta_0} = \mathbf{q}(\mathbf{x}_0) - \mathbf{K}^{-1}\mathbf{f}_0 \ . \tag{3.20}$$

Using the linearized elasto-geometric model around the equilibrium point $\mathbf{x}_0, \mathbf{q}_{\theta_0}$ one obtains the tangential plane

$$\boldsymbol{\gamma}_{\text{sk}}\left(\mathbf{x}_0 + \Delta\mathbf{x}, \mathbf{f}_0 + \Delta\mathbf{f}\right) = \boldsymbol{\gamma}_{\text{sk}}(\mathbf{x}_0, \mathbf{q}_{\theta_0}) + \left(\mathbf{K}_{\text{G}} - \mathbf{K}_{\text{C}}\right)\Delta\mathbf{x} + \underbrace{\mathbf{A}^{\text{T}}\Delta\mathbf{f}}_{\Delta\mathbf{w}} \ . \tag{3.21}$$

or alternatively using the residual cable length $\Delta\mathbf{q}_\theta$ associated with the residual cable forces $\Delta\mathbf{f}$ reads

$$\boldsymbol{\gamma}_{\mathrm{sk}}\left(\mathbf{x}_0+\Delta\mathbf{x},\mathbf{q}_{\theta_0}+\Delta\mathbf{q}_\theta\right)=\boldsymbol{\gamma}_{\mathrm{sk}}(\mathbf{x}_0,\mathbf{q}_{\theta_0})+(\mathbf{K}_{\mathrm{G}}-\mathbf{K}_{\mathrm{C}})\,\Delta\mathbf{x}+\mathbf{A}^{\mathrm{T}}\mathbf{K}\Delta\mathbf{q}_\theta\ . \tag{3.22}$$

With $\boldsymbol{\gamma}_{\mathrm{sk}}(\mathbf{x}_0,\mathbf{q}_{\theta_0})=\mathbf{0}$ one obtains the pose error with respect to the residual wrench or cable length

$$\Delta\mathbf{x}=(\mathbf{K}_{\mathrm{G}}-\mathbf{K}_{\mathrm{C}})^{-1}\left(\mathbf{A}^{\mathrm{T}}\mathbf{K}\Delta\mathbf{q}_\theta\right)=\mathbf{C}_{\mathrm{xw}}\Delta\mathbf{w}\ . \tag{3.23}$$

It is important to notice that the geometrical stiffness matrix $\mathbf{K}_{\mathrm{G}}(\mathbf{x}_0,\mathbf{q}_{\theta_0})$ must be computed at the correct linearization point $\mathbf{f}_0=\mathbf{f}(\mathbf{q}_{\theta_0})$.

For a kinematics control model $\boldsymbol{\varphi}$, the residual wrench is a function of the initial cable force distribution whose magnitude stays constant but whose directional changes are determined by the structure matrix causing the pose deviation

$$\Delta\mathbf{x}(\mathbf{f}_{\mathrm{ini}})=\mathbf{C}_{\mathrm{xw}}\left(\mathbf{A}^{\mathrm{T}}(\mathbf{x},\mathbf{p})\mathbf{f}_{\mathrm{ini}}+\mathbf{w}_{\mathrm{e}}\right)\ . \tag{3.24}$$

An example is shown in Fig. 3.8 where the error contour and vector field of the pose deviations is depicted.

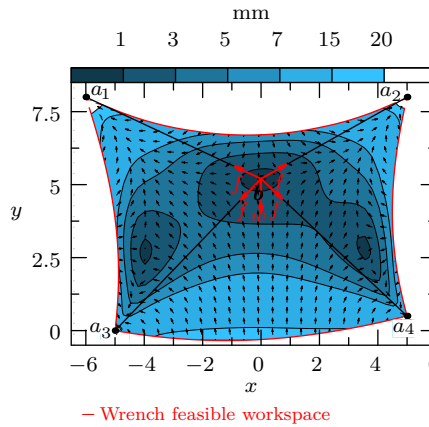

Figure 3.8: Linearized workspace analysis showing error contour plots and the associated vector field for the pose deviations $\Delta\mathbf{x}$.

Depending on the redundancy of the CDPR, the initial force distribution can be optimized for multiple locations simultaneously.

For force control, the pose deviation only depends on the misalignment between the control model and the physical system. Starting from the ideal elastostatic control model where

$$\mathbf{p}_\eta=\hat{\mathbf{p}} \tag{3.25}$$

the residual wrench cancels for the entire workspace

$$\Delta\mathbf{w} = \mathbf{0} \ . \tag{3.26}$$

Linearizing the structure equation around the equilibrium state with respect to the elastostatic model parameters $\mathbf{p}_\eta = (\mathbf{a}, \mathbf{b}, \mathbf{k}_\mathrm{F}, \mathbf{w}_\mathrm{e})$ and the platform pose leads to

$$\underbrace{\left(\frac{\partial \mathbf{A}^\mathrm{T}}{\partial(\mathbf{p}_\mathrm{ab})}\mathbf{f} + \mathbf{A}^\mathrm{T}\frac{\partial \mathbf{f}}{\partial \mathbf{p}_\mathrm{ab}}\right)}_{\mathbf{J}_\mathrm{wab}} \Delta\mathbf{p}_\mathrm{ab} + \underbrace{\mathbf{A}^\mathrm{T}\frac{\partial \mathbf{f}}{\partial \mathbf{k}_\mathrm{F}}}_{\mathbf{J}_\mathrm{wkF}} \Delta\mathbf{k}_\mathrm{F} + \mathbf{I}\Delta\mathbf{w}_\mathrm{e} + \underbrace{\frac{\partial \mathbf{A}^\mathrm{T}\mathbf{f}}{\partial \mathbf{x}}}_{-\mathbf{K}_\mathrm{wx}} \Delta\mathbf{x} = \mathbf{0} \tag{3.27}$$

so that the pose deviation with respect to model errors can be stated as

$$\Delta\mathbf{x}(\Delta\mathbf{p}_\mathrm{ab}, \Delta\mathbf{k}_\mathrm{F}, \Delta\mathbf{w}_\mathrm{e}) = \mathbf{C}_\mathrm{xw}\left(\mathbf{J}_\mathrm{wab}\Delta\mathbf{p}_\mathrm{ab} + \mathbf{J}_\mathrm{wkF}\Delta\mathbf{k}_\mathrm{F} + \Delta\mathbf{w}_\mathrm{e}\right) \ . \tag{3.28}$$

A detailed description of the respective Jacobians is given in the model optimization chapter Sec. 6.4. An example for the parameter sensitivity is shown in Fig. 3.9 where the sensitivity $\frac{\Delta\mathbf{x}}{\Delta a_{\mathrm{x}_1}}$ is depicted by the iso-contours and vector field.

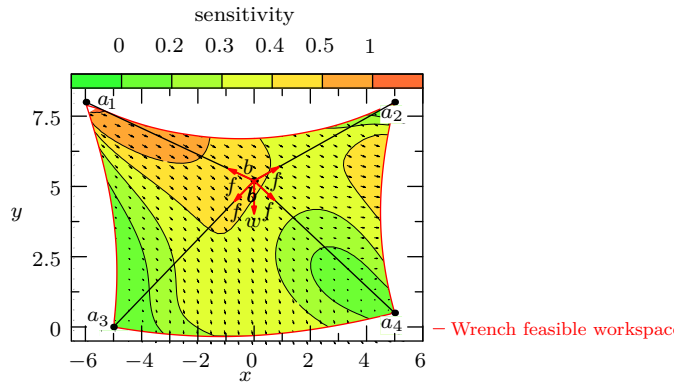

Figure 3.9: Sensitivity of the pose error $\Delta\mathbf{x}$ for changes in the robot frame parameterization, examplary shown for $\mathbf{a}_{\mathrm{x}_1}$ where green indicates areas with low sensitivity and red indicates areas with a sensitivity close to one. The vector field shows the associated gradients.

The green areas indicate low sensitivity or high robustness with respect to model parameter variations, the red areas indicate a sensitivity close to one. The sensitivity for CDPRs always stays below one due to the nature of its geometry. This and the fact that parts of the parameter variation vector $\Delta\mathbf{p}_\mathrm{ab}$ lie in the nullspace of $\mathbf{J}_\mathrm{wab}$ explain the robustness of CDPRs with respect to errors in the geometry model. For system identification, the sensitivity of the system can be increased by increasing the geometric stiffness in $\mathbf{J}_\mathrm{wab}$

applying higher cable forces. The analytic description of the pose error and the sensitivity are used in the following to compare model variations and optimize the model geometry in Chap. 4. The pose deviation analysis for the example above shows that the initial cable force distribution significantly impacts the pose accuracy when a kinematics control model is used although the geometry of the control model and physical ground truth model are identical. This is caused by the force propagation from one pose to another when the cable forces are not actively controlled. The force propagation effect also impacts the workspace of a CDPR as is shown in the next section.

3.5 Model Workspaces

Beside position accuracy, the workspace is one of the most important characteristics of a CDPR and a lot of research has been performed on this topic mainly regarding methods for analysis and the impact of different models on the workspace as well as structural optimization of CDPRs to maximize the workspace.

The workspace of a CDPR can be defined considering different aspects such as wrench feasibility, cable collision, and the system dynamics. Focusing on the system statics, the so-called wrench-closure workspace (Gouttefarde et al. 2007) $\mathcal{W}_{\mathrm{WF}}$ is define by the set of all poses where the wrench-closure condition Eq. (2.31) is fulfilled while the cable tensions stay positive $\mathbf{f} > 0$. For practical applications, cable forces have to be limited to a predefined range such that cable sagging and overload are avoided

$$\mathcal{W}_{\mathrm{WF}} = \{\mathbf{x} : \mathbf{A}^{\mathrm{T}}(\mathbf{x})\mathbf{f}(\mathbf{x}) + \mathbf{w}_{\mathrm{e}} = \mathbf{0} \wedge \mathbf{f}_{\min} \leq \mathbf{f}(\mathbf{x}) \leq \mathbf{f}_{\max}\} \ . \tag{3.29}$$

The definition from Eq. (3.29) commonly implies perfect alignment between the model and physical reality as well as the availability of force control. Rewriting definition Eq. (3.29) in terms of a general statics model $\boldsymbol{\gamma}$ with a parametrization $\mathbf{p}$ leads to

$$\mathcal{W}_{\mathrm{WF}} = \{\mathbf{x} : \boldsymbol{\gamma}(\mathbf{x}, \mathbf{p}) = \mathbf{0} \wedge \mathbf{f}_{\min} \leq \mathbf{f}(\mathbf{x}, \mathbf{p}) \leq \mathbf{f}_{\max}\} \ . \tag{3.30}$$

Considering Eq. (3.29) and the meta-model as shown in Fig. 3.10, different workspaces with respect to model structure and parametrization can be defined which in the following are called the model workspace

$$\mathcal{W}_{\mathrm{M}} = \mathcal{W}_{\mathrm{WF}}(\boldsymbol{\gamma}, \mathbf{p}), \tag{3.31}$$

the physical workspace

$$\mathcal{W}_{\mathrm{PHYS}} = \mathcal{W}_{\mathrm{WF}}(\hat{\boldsymbol{\gamma}}, \hat{\mathbf{p}}), \tag{3.32}$$

and the reachable workspace

$$\mathcal{W}_{\mathrm{R}} = \{\mathbf{x} : \hat{\boldsymbol{\gamma}} \circ \boldsymbol{\eta}(\mathbf{x}, \hat{\mathbf{p}}) = \mathbf{0} \wedge \mathbf{f}_{\min} \leq \mathbf{f}_{\mathrm{M}} \leq \mathbf{f}_{\max} \wedge \|\mathbf{x} - \mathbf{x}_{\mathrm{M}}\|_2 < \Delta\mathbf{x}_{\max}\} \tag{3.33}$$

where $\mathbf{f}_{\mathrm{M}}, \mathbf{x}_{\mathrm{M}}$ are the measured cable forces and poses, respectively.

The model workspace and physical workspace are assumed to be identical by most publications on workspace analysis. Differentiating between both workspaces allows to

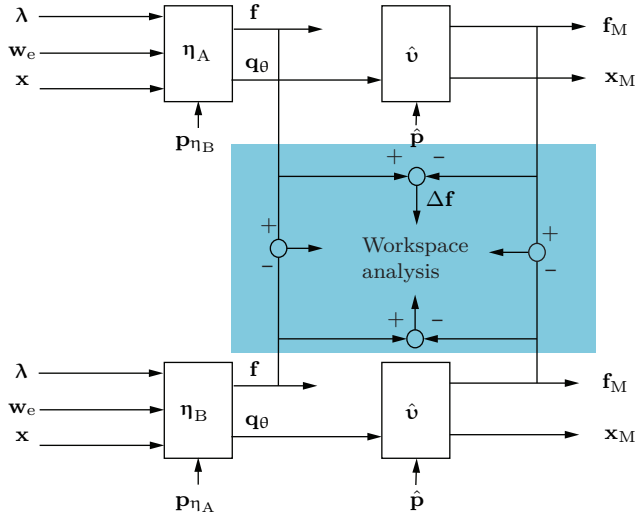

Figure 3.10: Workspace estimation

study the effect of incomplete control models. This is addressed by introducing the so-called *reachable workspace* from Eq. (3.33) as the workspace of the control model $\boldsymbol{\eta}$ in context of the ground truth model $\hat{\boldsymbol{\upsilon}}$ regarding the emerging force distribution and pose deviation $\boldsymbol{\Delta x}$ which is of special interest for overconstrained CDPRs with kinematic control models. For fully determined robotic systems with $m = n$ such as serial kinematic robots, a control model $\boldsymbol{\eta}$ which is solely based on kinematic considerations provides a good approximation of the system behaviour $\hat{\boldsymbol{\upsilon}}$ and therefore one obtains accurate results using $\boldsymbol{\eta}$ for a geometric workspace analysis. For CDPRs with $m \leq n$ cables, a static analysis is sufficient to determine valid poses in the workspace fulfilling Eq. (3.29). Small geometric deviations of the kinematics and statics model do not have much impact on the workspace geometry. Overconstrained CDPRs in contrast have to be modeled as an elastostatic system whose properties are not reflected in a solely kinematic or statics model. Deviations from the physical model lead to the emergence of cable force distribution which impact the reachable workspace and cannot be influenced actively by the kinematics controller. The reachable workspace $\mathcal{W}_{\mathrm{R}}$ of such setup is always smaller than the physical workspace $\mathcal{W}_{\mathrm{PHYS}}$. Active cable force control models allow to influence the cable forces during operation such that most of the physical workspace $\mathcal{W}_{\mathrm{PHYS}}$ can be reached assuming a close alignment between control model parametrization $\mathbf{p}_{\eta}$ and physical parametrization $\hat{\mathbf{p}}$.

The analysis of the reachable workspace requires a method which allows to find the valid force distribution for each pose. The analysis in practice therefore depends in the same

way on the force distriubution algorithm as the wrench feasible workspace Eq. (3.33)

To compute the geometry of the reachable workspace, a visual representation of the set defined by Eq. (3.33) has to be found. Two useful methods for this are the grid sampling method and the workspace hull method proposed by (Pott 2008). These requires checking the existence of a valid force distribution $\mathbf{f}_{\mathrm{M}}$ and the pose displacement $\Delta\mathbf{x}$ which is done according to Eq. (3.23). For the computation of the force distribution two cases are differentiated, that is the reachable workspace of kinematics control models and the reachable workspace of open loop force control models. In the first case, the validity of the cable forces must be checked for

$$\mathbf{f}_{\min} \leq \mathbf{f}_0 + \Delta\mathbf{f} \leq \mathbf{f}_{\max} \tag{3.34}$$

with

$$\mathbf{f}_0 + \Delta\mathbf{f} = \mathbf{f}_0 + \mathbf{K}\Delta\mathbf{q} = \mathbf{f}_0 + \mathbf{K}\mathbf{J}_{\mathrm{qx}}\Delta\mathbf{x} \; . \tag{3.35}$$

where $\Delta\mathbf{x}$ is computed according to Eq. (3.24). In the second case, the reachable workspace is identical with the wrench-feasible workspace for $\mathbf{p}_\eta = \hat{\mathbf{p}}$ and deviates according to Eq. (3.28) for $\mathbf{p}_\eta \neq \hat{\mathbf{p}}$.

In the context of model selection and system identification, the *reachable workspace* $\mathcal{W}_{\mathrm{R}}$ is a key element required for the planning of the sampling space and the model evaluation itself. For system identification, the questions is answered how the workspace is influenced by the model parameters, how it evolves during optimization, and how it can be used as primary objective for optimization itself. The workspace description in terms of the model parametrization and model structure can be used to compute workspace differences between two models in context of the meta-model for different cases as shown in Fig. 3.10. Two control models $\boldsymbol{\eta}_{\mathrm{A}}, \boldsymbol{\eta}_{\mathrm{B}}$ can be compared with respect to their different outputs in the cable force distributions linked to the workspace hull. The comparison of two models with small parametric deviations leads to the concept of the differential hull which was introduced by (Pott 2018b) and can be used for the analysis and optimization of control models. Computing the deviation between the predicted cable forces $\mathbf{f}$ and the emerging cable forces $\mathbf{f}_{\mathrm{M}}$ allows to predict the deviation of the reachable workspace with respect to the model workspace. Comparing the emerging cable forces of two different control models leads to the concept of the differential hull of the reachable workspace $\mathcal{W}_{\mathrm{R}}$ which is depicted in Fig. 3.9 showing the nominal reachable workspace indicated by the blue line and the workspace differential indicated by the blue vector set and magenta outline caused by the parameter variation Δa_{x_1}. The theories form this and the previous sections are investigated in a detailed simulative analysis in the following sections.

3.6 Simulative Analysis

The following simualative analysis has the purpose to show the importance of the proposed methodology to create a more realistic picture of the positioning behavior and workspace of

CDPRs under the usual condition of incomplete control models. Especially the phenomena of force propagation impacts the position accuracy and the reachable workspace depending on the intial force conditions and paramter misalignment. The results from simulation with a nominal parametrization also show the problem of using direct measurements of the CDPR geometry for kinematic model parametrization. The results form the nominal model are used as reference for the later model optimization in the next chapter.

The section starts with a comparison of the linear approximation and the full elastotstatic forward kinematics for the estimation of the pose error and reachable workspace. For the purpose of clarity, the examples are shown for a two-dimensional CDPR allowing better visualization.

The pose tracking error of a motion controller using the standard kinematics model $\boldsymbol{\varphi}$ which is operated on a physical system represented by an elastostatic ground truth model $\hat{\boldsymbol{\upsilon}} = \boldsymbol{\upsilon}_{\mathrm{el}}$ is computed from the system compliance given in Eq. (3.23) and the initial conditions from Eq. (3.14).

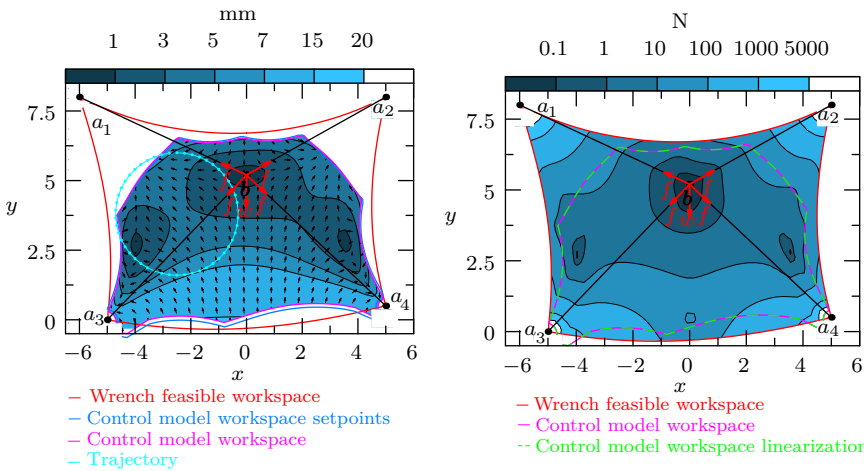

(a) Pose prediction accuracy using a linearized kinematics model $\boldsymbol{\varphi}$ with an elastic CDPR. The vector field and contours show the pose deviation $\Delta\mathbf{x}$, $\|\Delta\mathbf{x}\|_2$, respectively.

(b) Linearization error using stiffness matrices for pose displacement computations and showing the wrench residual for the first step of the elastostatic forward kinematics.

Figure 3.11: Pose prediction accuracy and linearization error for a kinematics control model apllied to an elastostatic ground truth model.

A visualization of this setup is shown in Fig. 3.11awhere the cable stiffness of the physical system is to be assumed

$$k_{\mathrm{F}i} = 2000 \ \frac{\mathrm{kN}}{\mathrm{m}} \tag{3.36}$$

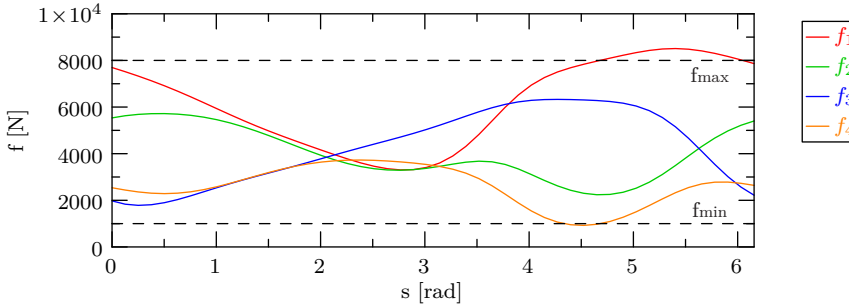

Figure 3.12: Cable forces caused by the force propagation form the initial tension state and kinematics model paramterization causing force limit vialations before $\mathcal{W}_{\mathrm{WF}}$ is reached.

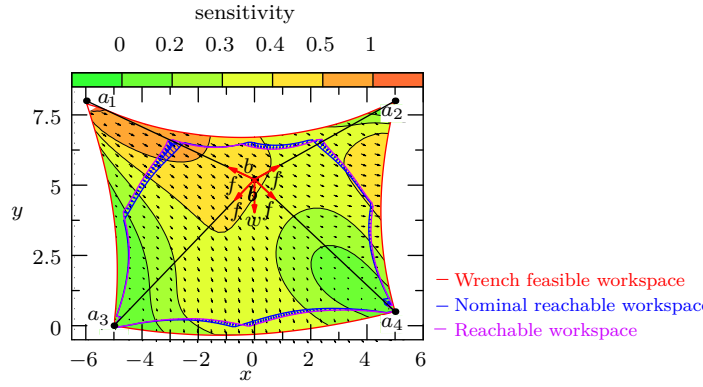

Figure 3.13: Parameter sensitivity

and the wrench and initial force distribution at the initial pose

$$\mathbf{x}_{\mathrm{ini}} = \begin{bmatrix} 0 & 5.2 \end{bmatrix} \tag{3.37}$$

are chosen as

$$\mathbf{w}_{\mathrm{e}} = \begin{bmatrix} -1962.0 & 0 \end{bmatrix} \ \mathrm{N} \tag{3.38}$$

and

$$\mathbf{f}_{\mathrm{ini}} = \mathbf{f} \tag{3.39}$$

respectively. The geometric parameters of the frame are given by

$$\mathbf{a} = \begin{bmatrix} -6.000 & 8.000 \\ 5.000 & 8.000 \\ -5.000 & 0.000 \\ 5.000 & 0.500 \end{bmatrix} . \tag{3.40}$$

In Fig. 3.11a, the positioning error $\Delta\mathbf{x}$ is represented by the arrows of the vector field and the associated magnitude of the error by a contour plot providing information about the direction and magnitude of the expected pose error. The pose tracking error zeros at three locations inside the workspace including the initial position where the force distribution was chosen such that the physical system is in a force equilibrium state. The two other locations result from the initial force distribution which is propagated through the system such that the wrench-closure condition is fulfilled at these locations. The maximum pose errors occur close to the physical workspace border with a maximal error of 20 mm for the depicted configuration.

The boundary of the wrench feasible workspace of the ground truth model (physical workspace $\mathcal{W}_{\mathrm{PHYS}}$) is indicated by the red line describing all poses which can be reached without violating the force conditions of the physical CDPR assembly. The workspace contour of $\mathcal{W}_{\mathrm{PHYS}}$ is computed using a line search algorithm which is applied to the wrench-feasible condition Eq. (3.29) to map a polyhedron onto the workspace boundary as described in (Pott 2008). The boundary of the reachable workspace $\mathcal{W}_{\mathrm{R}}$ is shown by the magenta line including all poses which can be reached by the standard kinematics model for a given initial tension state $\mathbf{f}_0$ without violating the physical force limits. The cable force predictions for an exemplary circular trajectory outlined in Fig. 3.11a are shown in Fig. 3.12 together with the physical force limits and the constraint violation of $\mathbf{f}_1, \mathbf{f}_2$ at the reachable workspace border. The poses of the workspace boundary relate to $\mathbf{x}_{\mathrm{M}}$ and therefore represent the actual poses reached when operating the CDPR at the workspace border. The blue boundary line indicates the reachable workspace border with respect to control model reference poses $\mathbf{x}$ and therefore relate to all poses which can be provided as reference pose to the controller without causing force violations in the system. The difference in both representations is equal to the pose tracking error at the workspace border as can be seen in the lower region of the workspace where the pose tracking error is largest. Computing the areas of the reachable and physical workspace according to (Pott 2018a), it can be seen that the reachable workspace of the kinematic controller with a reachable area of 51 m^2 covers only 73 percent of the physical workspace with an reachable area of 70 m^2. The definition of the reachable workspace in Eq. (3.33) allows to apply a combined criterion of force limits and pose deviation limits. Using the combined criterion leads to workspace boundaries indicated by the iso-lines from the pose deviation plot. Narrowing the constraints on the pose tracking accuracy, the reachable workspace becomes disconnected leading to separate regions where the CDPR can be operated with sufficient accuracy.

While the analysis of the reachable workspace $\mathcal{W}_\mathrm{R}$ in Fig. 3.11a is done computing the full elastostatic forward kinematics, one can obtain accurate results using the linear model according to Eq. (3.23) when the control model and ground truth model are similar enough with respect to the structure and parametrization. This is shown in Fig. 3.11b where computations of the pose deviations and reachable workspace for the linear model are shown together with the linearization error indicated by the magnitude of residual platform force depicted with the iso-lines. The impact of the linearization error in general is small as can be seen by the green line compared to the magenta line which is associated with the full elastogeometric forward kinematics. In the lower left and right region, it can be seen that the linear approximation deviates significantly from the nonlinear analysis, although a large part of this region already lies outside the wrench-feasible workspace.

The model also allows to optimize the initial tension state such that the tension for a given region or trajectory becomes optimal with respect to some predefined criterion. A criterion which regards the lower and upper force limits is defined by (Pott et al. 2009) where the desired cable force is defined with a maximum distance from the force limits that is $\mathbf{f}_\mathrm{m} = 0.5\,(\mathbf{f}_\mathrm{min} + \mathbf{f}_\mathrm{max})$. The least squares optimal force distribution with respect to $\mathbf{f}_\mathrm{m}$ along the trajectory is defined by

$$\mathbf{f}_\mathrm{ref} = \mathbf{f}_\mathrm{m} - \mathbf{A}^{+\mathrm{T}} \left(\mathbf{w}_\mathrm{e} + \mathbf{A}^\mathrm{T} \mathbf{f}_\mathrm{m} \right) \ . \tag{3.41}$$

Another criterion proposed by (Kraus et al. 2013a) finds the minimal force distribution to increase energy efficiency of the CDPR. The optimal initial tension distribution with respect to $\mathbf{f}_\mathrm{ref}$ along a given trajectory is computed by minimizing the path integral

$$\min_{\mathbf{f}_\mathrm{ini}} \int_s \left(\mathbf{f}_\mathrm{ref}(s) - \mathbf{f}(s, \mathbf{f}_\mathrm{ini}) \right)^2 \mathrm{d}s \tag{3.42}$$

or surface integral for areas and triple integral for volumes, respectively. Using Eq. (3.41) as criterion and the trajectory from Fig. 3.11a as path for the path integral, the minimization leads to a force distribution for the trajectory as shown in Fig. 3.14 where the dotted lines show the reference force distribution according to Eq. (3.41) and the solid lines show the least squares optimal approximation which is realized by choosing $\mathbf{f}_\mathrm{ini}$. The associated modified reachable workspace is shown in Fig. 3.15. The trajectory now complies to the force limits and optimally tracks the reference force $\mathbf{f}_\mathrm{ref}$.

3.7 System Parameter Analysis

While the meta-model allows to analyze the performance of a control model for a given robot setup, it also allows to study the impact of certain system parameters in context of the robot life cycle as depicted in Fig. 3.16. Row (D) shows the different phases of the life-cycle. Row (A) and (B) depict the main parameters of two different physical implementations of a CDPR system. Row (C) relates to the parametrization of the robot control model. Usually the parameters of a CDPR are just stated as a fixed configuration

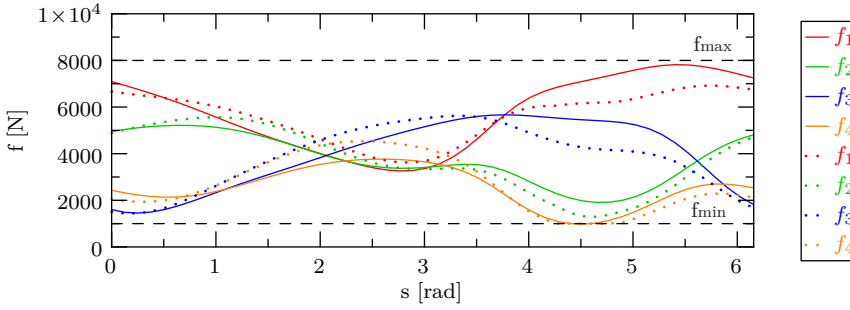

Figure 3.14: Optimized cable forces

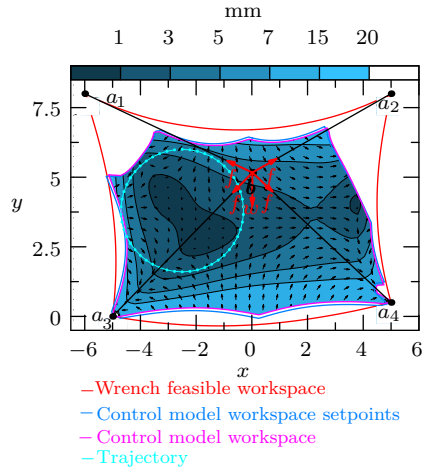

Figure 3.15: Reachable workspace for optimized tension state for the kinematics control model $\boldsymbol{\varphi}$ with an elastic CDPR.

for a specific model neglecting the overall context of the robot life-cycle with respect to final aim of application performance.

The final robot performance can be analyzed with respect to three factors which are the robot design (A,B), the robot model (C), and the impact of each phase of the life-cycle. The robot design phase defines the final achievable performance by setting the physical limits and defining the complexity of the system which has to be matched by the controller. For example, setting the geometry parameters defines the physical limits of the wrench feasible workspace. The robot performance is impacted by the hardware design parameters (A,B) and the model parameters (C) as was derived for the positioning accuracy and reachable workspace in the last sections. Optimal performance can be achieved by optimization of the

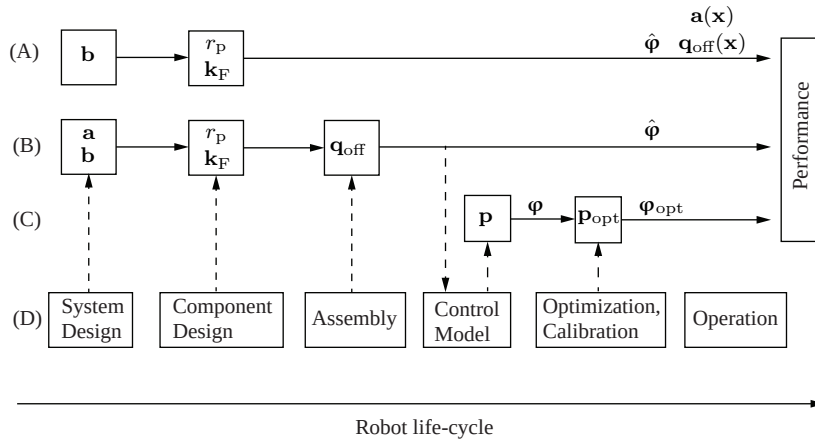

Figure 3.16: System and model parameters during the different phases of the system life-cycle.

model parameters minimizing the prediction error of (C) and measurements from (A,B). A good alignment of the model (C) and physical reality (A,B) can be achieved by either reducing complexity of the physical system in the design phase or by an increased model complexity for the control model. Depending on the design of a CDPR, various parameters may be considered for the selection of the optimal configuration such as the frame and platform geometry, cable stiffness, cable offsets, pulley diameter, pulley orientation, power train transfer behavior etc. .

A good design tries to minimize usage of components which have high sensitivity and may impact the system performance when they are not correctly represented in the model. For example, a design of a CDPR with point-like cable outlets is preferable to designs with significant pulley diameters, when other requirements such as the minimal bending radius of the cables can be avoided. While the final parameter space of the physical system may vary largely with the final hardware components, some properties are common to all CDPRs which are the spatial geometry of the platform and frame defined by $\mathbf{b}, \mathbf{a}$, the tilt pulley radius r_p , the cable stiffness defined by $\mathbf{k}_\mathrm{F}$, and the cable offsets $\mathbf{q}_\mathrm{off}$ which are used to create a valid tension state $\mathbf{f}_\mathrm{ini}$.

Considering the aim of optimal robot operation with respect to pose accuracy and workspace reachability, these parameters have different meaning in context of the different parts of the robot life cycle depicted in Fig. 3.16. The robot design phase and optimization process usually relates to geometry defintion and its optimization (B): $\mathbf{a}, \mathbf{b}$. Component design then defines properties of individual parts such as the cable or pulleys which are necessary for the implementation (B): $r_\mathrm{p}, \mathbf{k}_\mathrm{F}$. The assembly and setup process

may requires to set parameters such as the cable offset (B): $\mathbf{q}_{\text{off}}$ to generate the initial cable tension. While a standard CDPR with a kinematics model operates with a fixed set of these parameters, more sophisticated robot designs allow to change the robot geometry during operation by additional actuators depicted as (A): $\mathbf{a}(\mathbf{x})$ or the cable offsets using force control (A): $\mathbf{q}_{\text{off}}(\mathbf{x})$. An example for a CDPR which allows for real-time modification of the frame geometry is Segesta prototype from University Duisburg-Essen using linear rails for the redirection pulleys (Reichert et al. 2015). In the following the effect of the parameters $r_{\text{p}}, \mathbf{k}_{\text{F}}, \mathbf{q}_{\text{off}}$ on the expected performance of the robot system $\hat{\boldsymbol{\varphi}}$ is investigated using the meta-model and a fixed geometry configuration $\mathbf{a}, \mathbf{b}$. The next chapter then deals with the optimization of the control model $\boldsymbol{\varphi}$ covering the second part of the robot life-cycle depicted in Fig. 3.16.

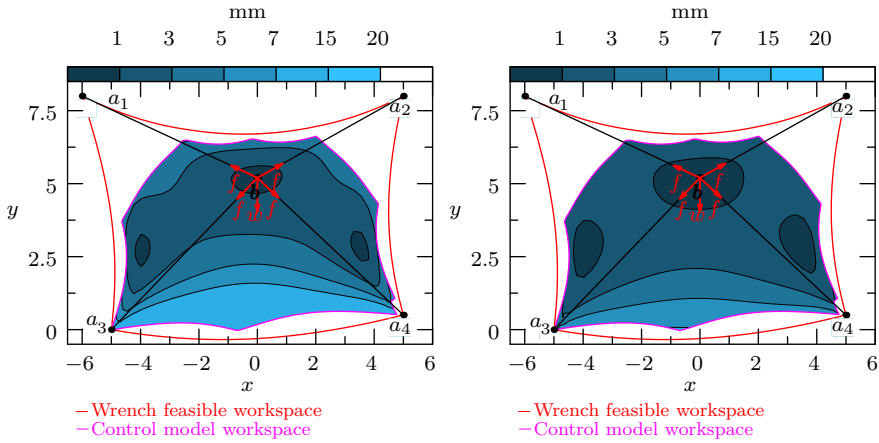

(a) Pose prediction accuracy and reachable workspace border for $\mathbf{f}_{\text{ini}} = \begin{bmatrix}5808 & 5909 & 2390 & 2421\end{bmatrix}$ N, cable stiffness $\mathbf{k}_{\text{F}} = 1000\ \frac{\text{kN}}{\text{m}}$, and $\mathbf{w}_{\text{e}} = \begin{bmatrix}0 & -1962\end{bmatrix}$ N .

(b) Pose prediction accuracy and reachable workspace border for $\mathbf{f}_{\text{ini}} = \begin{bmatrix}5808 & 5909 & 2390 & 2421\end{bmatrix}$ N, cable stiffness $\mathbf{k}_{\text{F}} = 3500\ \frac{\text{kN}}{\text{m}}$, and $\mathbf{w}_{\text{e}} = \begin{bmatrix}0 & -1962\end{bmatrix}$ N .

Figure 3.17: Stiffness variation

In Fig. 3.18 the impact of different design parameters with respect to the physical wrench feasible workspace $\mathcal{W}_{\text{PHYS}}$, the reachable workspace $\mathcal{W}_{\text{R}}$, and pose tracking accuracy is shown. The physical wrench feasible workspace is only impacted by the chosen model geometry and external wrench. Fig. 3.17a, 3.17b show the same geometry and wrench with the same wrench feasible workspace. Fig. 3.18a, 3.18b show the same setup with a zero wrench and the associated wrench feasible workspace. Choosing cables with higher stiffness allows to increase positioning accuracy but does not allow to increase the reachable

workspace as shown in Fig. 3.17a for $\mathbf{k}_\mathrm{F} = 1000\ \frac{\mathrm{kN}}{\mathrm{m}}$ and Fig. 3.17b for $\mathbf{k}_\mathrm{F} = 3500\ \frac{\mathrm{kN}}{\mathrm{m}}$.

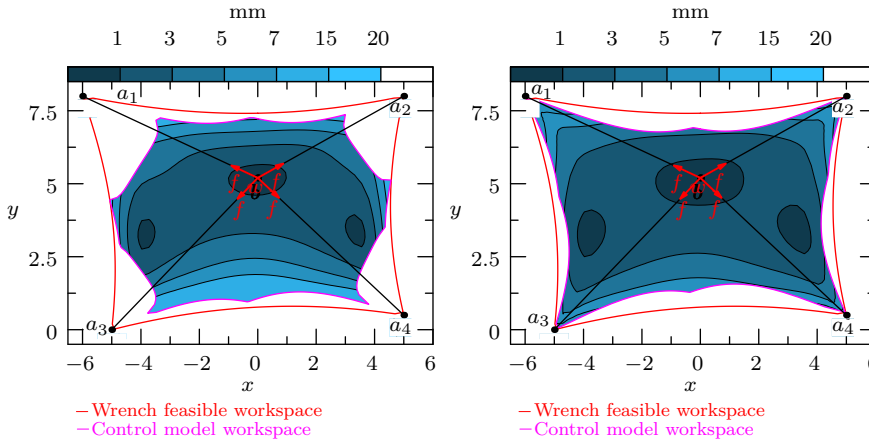

(a) Pose prediction accuracy and reachable workspace border for $\mathbf{f}_\mathrm{ini} = \begin{bmatrix}5196 & 5247 & 3380 & 3394\end{bmatrix}$ N, cable stiffness $\mathbf{k}_\mathrm{F} = 1000\ \frac{\mathrm{kN}}{\mathrm{m}}$, and $\mathbf{w}_\mathrm{e} = \begin{bmatrix}0 & 0\end{bmatrix}$ N .

(b) Pose prediction accuracy and reachable workspace border for $\mathbf{f}_\mathrm{ini} = \begin{bmatrix}3464 & 3498 & 2253 & 2263\end{bmatrix}$ N ,cable stiffness $\mathbf{k}_\mathrm{F} = 1000\ \frac{\mathrm{kN}}{\mathrm{m}}$, and $\mathbf{w}_\mathrm{e} = \begin{bmatrix}0 & 0\end{bmatrix}$ N .

Figure 3.18: Cable tension variation

A complete exemplary analysis of the positioning accuracy which can be expected for a kinematics control model with respect to a given cable stiffness is shown in Fig. 3.19. The graph shows the proportion of the physical workspace which can be reached for a predefined required accuracy using cables with a specified stiffness $\mathbf{k}_\mathrm{F}$. The blue line for example indicates the size of the reachable workspace for a required accuracy of $\Delta\mathbf{x}_\mathrm{max} = 5$ mm . The limit of the reachable workspace for the given setup and any possible stiffness $\mathbf{k}_\mathrm{F}$ or required accuracy $\Delta\mathbf{x}_\mathrm{max}$ is indicated by the horizontal dashed line.

Changing the internal tension state impacts the positioning accuracy as well as the reachable workspace as shown in Fig. 3.18a for $\mathbf{f}_\mathrm{max} = 8000$ N and Fig. 3.18b for $\mathbf{f}_\mathrm{max} = 3000$ N . Although higher tension in the cables may lead to better positioning accuracy of the platform in case of wrench disturbances due to the increased geometrical stiffness, these results show that tension state propagation significantly impacts the positioning accuracy and that higher tension states lead to larger residual wrenches. Secondary the reachable workspace is impacted significantly by the initial tension state and the optimal tension level depends on the physical force limits $\mathbf{f}_\mathrm{min}, \mathbf{f}_\mathrm{max}$ as shown in Fig. 3.20. The graph shows the proportion of the physical workspace which can be reached for a given required accuracy $\Delta\mathbf{x}_\mathrm{max}$ and initial force distribution computed by Eq. (3.41) with $\mathbf{f}_\mathrm{min} = 1000$ N

and $\mathbf{f}_{\max}$ as given on the x-axis.

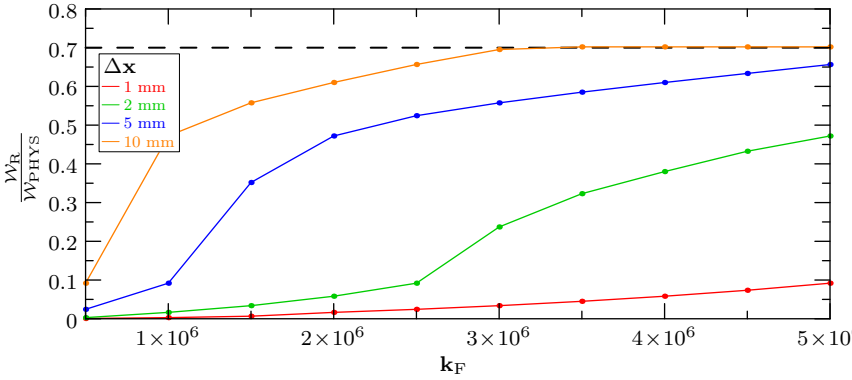

Figure 3.19: Relative workspace size for stiffness variation and error thresholds $\Delta\mathbf{x} = \{1, 2, 5, 10\}$ mm

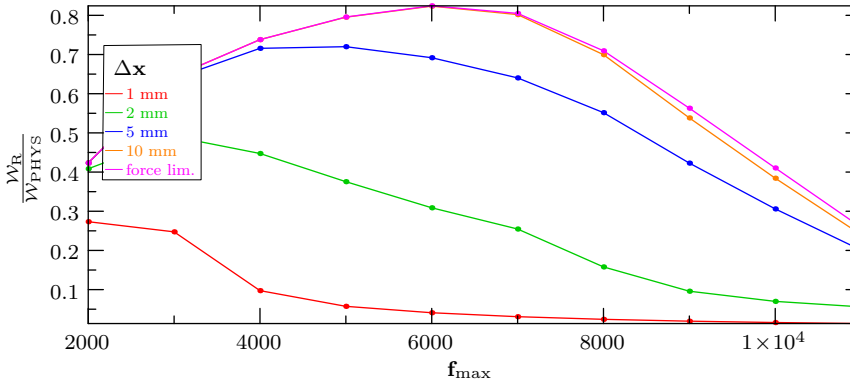

Figure 3.20: Relative workspace size for cable tension variation and error thresholds $\Delta\mathbf{x} = \{1, 2, 5, 10\}$ mm

The impact of the tension state in neglect of unknown disturbances varies depending on the chosen required accuracy and depends on two factors. The first factor is the residual wrench and as mentioned before, lower tension leads to higher accuracy which can be seen for $\Delta\mathbf{x}_{\max} = 1$ mm indicated by the red line. The second factor is the relation of the initial force distribution with respect to the given physical force limits of the system. In case the initial force distribution gets close to the lower or upper limits, a drop in the reachable workspace can be expected as shown by the magenta line. This effect is the

more important the more the accuracy requirement in Eq. (3.33) is relaxed and the force distribution criterion takes over. Combining the results from Fig. 3.19, 3.20 the initial force distribution defines the reachable workspace for which the positioning accuracy can be adjusted by changing the system stiffness or decreasing the tension at the cost of the reachable workspace. For system identification, the stiffness of the robot maybe unknown at the beginning but based on this results it is possible to find the optimal initial force distribution to maximize the initial sampling space for the measurement process. For the example configuration, the optimal tension state for the maximal sampling range is given by $\mathbf{f}_{\max} \approx 6000$ N or the respective reference value $\mathbf{f}_{\mathrm{M}} \approx 2500$ N .

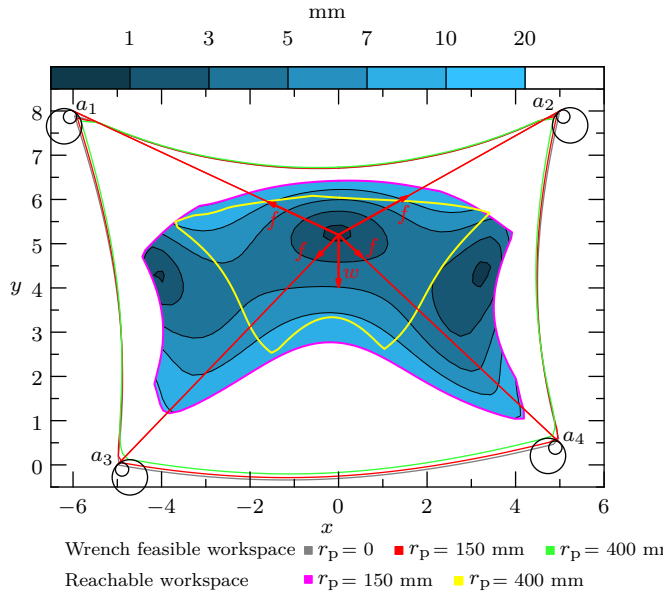

Figure 3.21: Pose prediction accuracy using a kinematics model $\boldsymbol{\varphi}$ with an elastic CDPR with pulleys.

3.8 Influence of Pulley Kinematics

Redirection pulleys are an essential component of most CDPRs and are used for the powertrain to guide the cables to the outlet points. From a control perspective, it would be useful to avoid pulleys entirely and design the cable outlet such that it has point-like properties and does not change during operation. Practical design requirements such as minimal bending radii for cables and the use of cost efficient components usually lead to the

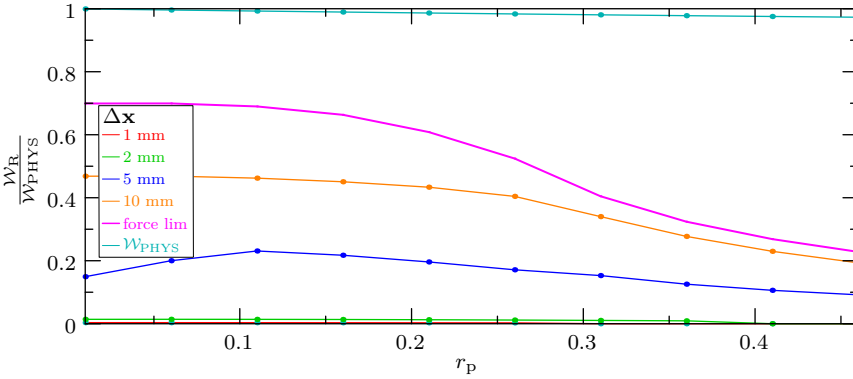

Figure 3.22: Relative workspace size for pulley variation

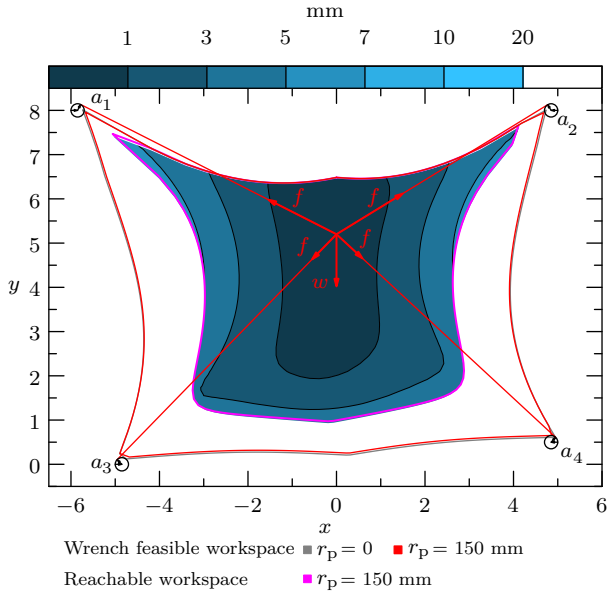

Figure 3.23: Pose prediction accuracy using force control$\boldsymbol{\varphi}$ with an elastic CDPR with pulleys.

use of standard tilt pulley mechanisms for the cable redirection. The pulley model as an extension of the standard kinematics model was first proposed by (Bruckmann et al. 2008).

An real-time capable approach for solving the forward kinematics of the pulley model was proposed by (Schmidt and Pott 2013) A real-time capable dynamics model including the pulley model was introduced in (Miermeister and Pott 2010) and used for hardware-in-the loop dynamics simulations of CDPRs. A similar approach was used for the dynamic analysis of CDPRs in (Tempel et al. 2015b). While the modelling of pulleys intuitively makes sense to improve the geometry model not much work has been conducted on analyzing the impact of the model on the positioning accuracy and the robot workspace beside (Pott 2012) where the effect of the pulley kinematics with respect to the cable length deviation and wrench feasible workspace was performed and (Schmidt and Pott 2013) where an experimental evaluation was conducted. Here a similar approach is used in combination with the meta-model to complete the picture of the pulley model with respect to the expected positioning error and expected impact on the reachable workspace.

The ground truth model $\hat{\boldsymbol{\upsilon}}$ is extended by the pulley model from Sec. 2.3 where the Jacobians for the forward kinematics are augmented by the respective differential relations given in Sec. 2.7. The pulley radii are chosen as $r_\mathrm{p} = 150$ mm which is close to the radius of the CableRobot Simulator with a rope diamater of 14 mm and a typical value considering that the bending radius for steel ropes should be as high as possible but at least ten times the rope diameter $r_\mathrm{p} = 10 d_\mathrm{r}$ to increase durability of the cables. The difference of the control model with and without the pulley kinematics is shown for the pyhsical wrench feasible and reachable workspace in Fig. 3.21. The pulley reference points are aligned such that the tangential outlet point for all pulley radii is identical for the initial configuration. The effect on the physical wrench feasible workspace is quite limited as was also reported in (Pott 2012) and can be seen only for large variations in the pulley radii. The workspaces $\mathcal{W}_\mathrm{PHYS}$ for $r_\mathrm{p} = \{0, 150, 400\}$ mm are shown by the gray, red and green outline respectively. The relative sizes of the workspaces for $r_\mathrm{p} = \{150, 400\}$ mm in relation to $r_\mathrm{p} = 0$ mm are 98.95, 97.54 percent, respectively. The small impact on the physical wrench feasible workspace is due to the fact that the pulleys are relatively small in comparison to the workspace and that the geometry of the static system is not much changed by the pulleys. The size of the associated reachable workspaces for $r_\mathrm{p} = \{150, 400\}$ mm is shown by the magenta and green line. A more complete picture of the relative size and positioning accuracy for $\mathcal{W}_\mathrm{PHYS}$ and $\mathcal{W}_\mathrm{R}$ is shown in Fig. 3.22. The limit of the reachable workspace with respect to pulley size is indicated by the magenta line. The stronger dependency on the pulley radius is caused by the distortion of the cable forces which add to the residual wrench causing an increase in the position error and a decrease in the reachable workspace. The associated regions which can be reached with a predefined accuracy $\Delta\mathbf{x}_\mathrm{max} = \{1, 2, 5, 10\}$ mm are given by the red, green, blue, and yellow line.

For a control model with force control the position accuracy and reachable workspace are significantly increased as shown in Fig. 3.23. In contrast to the analysis of the wrench feasible physical workspace, the misalignment of the geometry is included in the analysis and therefore provides a more accurate picture of the impact which is to be expected for the unmodeled pulley geometry.

This concludes the analysis of the physical system by means of the meta-model and pose accuracy and reachable workspace as performance criteria. While this analysis provides insights in the different factors which have to be considered for the initial setup of the CDPR to maximize workspace and positioning accuracy using a nominal kinematics control model, optimization and force control are further measures which allow to increase the system performance and are discussed in the next chapter.

4 Model Optimization

The previous chapter introduced the meta-model which is used to compare the impact of different model structures and parametrizations with respect to selected evaluation criteria from Sec. 3.4, 3.5 and error metrics from Sec. 3.3. Using the meta-modelling approach, the kinematic and elastostatic control models were analyzed using the pose prediction accuracy and the reachable workspace as evaluation criteria. While the analysis allows to estimate and compare the expected performance of a model for a predefined parametrization, the question of an optimal parametrization for a given model structure remains. Parameter optimality is essential for the model selection process and is needed for the rating of two model candidates $\boldsymbol{\eta}_\mathrm{A},\ \boldsymbol{\eta}_\mathrm{B}$ according to Eq. (3.11). In Fig. 4.1, two model candidates are shown with the model structure $\boldsymbol{\eta}_\mathrm{A},\ \boldsymbol{\eta}_\mathrm{B}$ and their respective nominal and optimal parametrization $\mathbf{p}_\eta,\ \mathbf{p}_{\eta_\mathrm{opt}}$. Using the methodology from the previous chapter it is possible to compare the model candidates with respect to their pose prediction accuracy indicated by $\Delta\epsilon_{\bar{\mathrm{x}}}$ as well as the workspace and force predictions (not shown here). Considering the four system configurations of the meta-model S1, S2, S3, S4, most publications on the modelling of CDPRs report results with respect to experimental or stimulative data from a single model candidate $\mathbf{p}_{\eta_\mathrm{A}}$ which corresponds to the system configuration S1 where the nominal parametrization is used to operate the CDPR and estimate $\epsilon_{\bar{\mathrm{x}}}$. Some publications use the nominal parametrization to compare different models $\mathbf{p}_{\eta_\mathrm{A}},\ \mathbf{p}_{\eta_\mathrm{B}}$ which corresponds to an estimate of $\Delta\epsilon_{\bar{\mathrm{x}}}$ for system configuration S1, S3. For a meaningful comparison and computation of $\Delta\epsilon_{\bar{\mathrm{x}}}$ careful reporting of the associated model parametrization $\mathbf{p}_{\eta_\mathrm{A}}, \mathbf{p}_{\eta_\mathrm{B}}$ is essential. Unknown parametrizations and experimental conditions make it difficult to compare results from different publications.

Some publications report on the performance of optimal parameterized models $\boldsymbol{\eta}_\mathrm{A}(\mathbf{p}_{\eta_{\mathrm{A\,opt}}})$ which correlates with the system configuration S2 and the estimation of $\epsilon_{\bar{\mathrm{x}}}(\mathbf{p}_{\eta_{\mathrm{A\,opt}}})$. To the best of the authors knowledge, no publications exist where the model performance of models for CDPRs with different structures and optimal parametrization are compared to each other. This equates to the computation of $\Delta\epsilon_{\bar{\mathrm{x}}}, \Delta\epsilon_{\bar{\mathrm{f}}}$ for $\boldsymbol{\eta}_\mathrm{A}(\mathbf{p}_{\eta_{\mathrm{A\,opt}}}), \boldsymbol{\eta}_\mathrm{B}(\mathbf{p}_{\eta_{\mathrm{B\,opt}}})$ in system configuration S2, S4. One of the key issues often observed for the proposal of new physical first principal models, is the change of the model structure without a thorough system identification and parameter optimization step. Therefore obtaining the optimal parametrization for proper model comparison is part of this chapter. The following evaluation chapter provides an experimental evaluation for models of different complexity reporting the respective $\Delta\epsilon_{\bar{\mathrm{x}}}, \Delta\epsilon_{\bar{\mathrm{f}}}$ which allow to assess the usability of the model for the specified application. The integration of the optimization process into the overall model

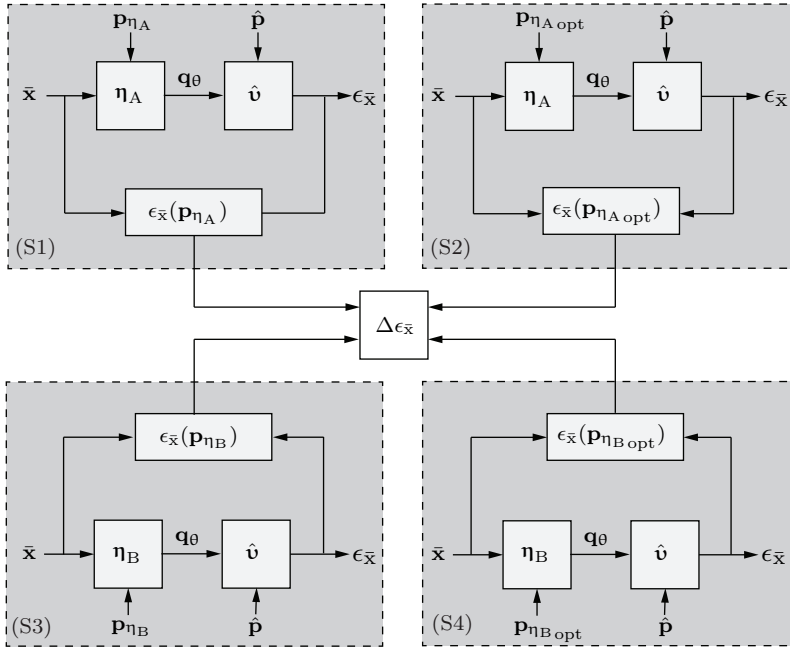

Figure 4.1: Structure and parameter comparison

selection and evaluation process is shown in Fig. 4.2. The meta-model from the previous chapter is used to describe the final evaluation of the optimal model as well as the data acquisition and sampling process which itself depends on the initial control model.

4.1 Kinematics Model Optimization

Depending on the available measurements and models, different approaches can be used for parameter identification. The parameter identification for the kinematics model in Eq. (2.5, 2.7) can be achieved by direct measurement of the geometric parameters, direct measurements of the platform pose also called open loop calibration (Hollerbach and Wampler 1996; Mooring et al. 1993), or by measuring the encoder values leading to a closed loop or auto-calibration scheme (Hanqi Zhuang and Lixin Liu 1996; Khalil and Besnard 1999). Using direct measurement for calibration allows to determine errors in the geometry parameters with respect to the nominal robot design. The resulting model is accurate in the sense that the geometric relations of the control model and the actual robot assembly match, but nonetheless does not provide the best positioning accuracy as mentioned in the previous chapter. A numeric example is shown later in Fig. 4.6. In the

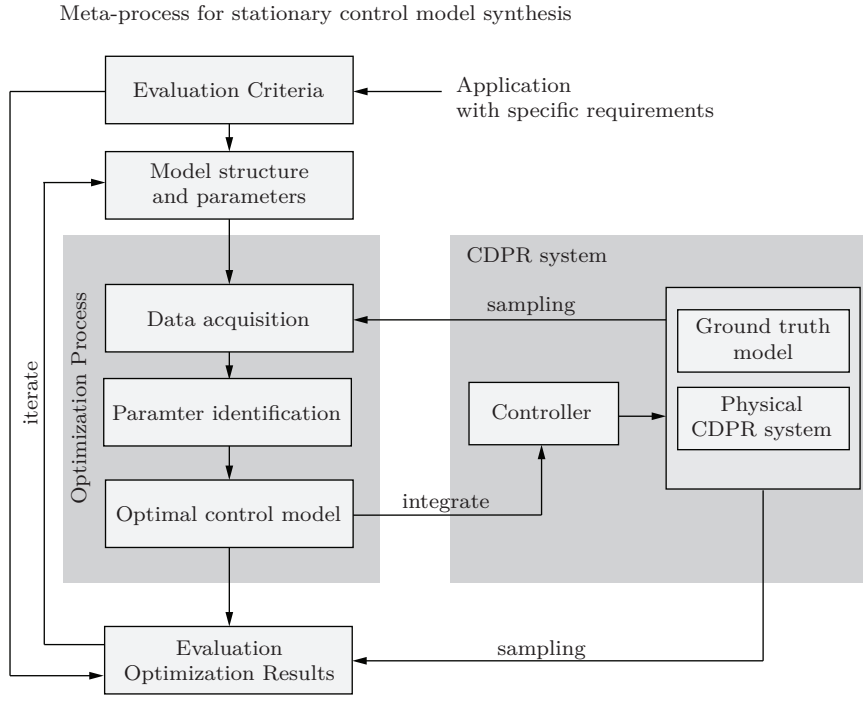

Figure 4.2: Model optimization process

second case where the method of open loop calibration is used, direct pose measurements are recorded to generate a sample set which allows calibration for CDPRs with arbitrary number of cables including suspended cable-mechanisms. The third case, internal encoder signals are used to record the sample set which is used for the auto-calibration procedure. The application of an auto-calibration scheme using winch encoder signals is only possible for overconstrained CDPRs with $m > n$. Using additional information from cable force sensors also allows the identification for CDPRs in suspended configuration and with less cables than degrees of freedom.

Considering the calibration method using direct pose measurements, in general one can find a parameter set which minimizes the sum of errors between the model predictions

$$\bar{\mathbf{x}}_{\mathrm{P}} = \boldsymbol{\upsilon}_{\mathrm{kin}}(\bar{\mathbf{q}}_{\boldsymbol{\theta}}, \mathbf{p}) \tag{4.1}$$

in operational space and the pose measurements

$$\bar{\mathbf{x}}_{\mathrm{M}} = \boldsymbol{\upsilon}_{\mathrm{el}}(\bar{\mathbf{q}}_{\theta}, \mathbf{p}_{\mathrm{N}}) \tag{4.2}$$

as shown in Fig. 4.3 using the information of n_{s} samples $\mathbf{q}_{\theta j}$, $j = 1 \dots n_{\mathrm{s}}$ and the loss function from Eq. (4.3).

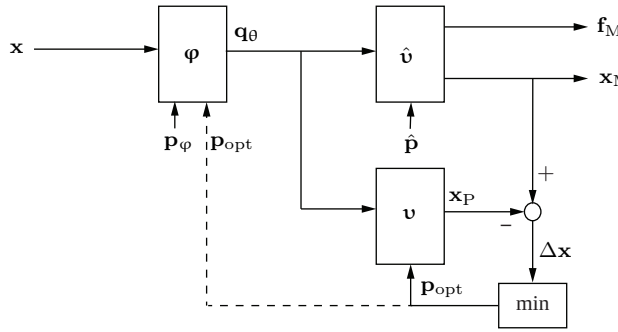

Figure 4.3: Kinematics model optimization in cartesian space

An initial control model is needed in order to acquire the sample set. The allowed error of the initial model is limited by the requirement of cable tension boundaries on all cables. Poses which cannot be reached within the force constraints i.e. poses with loose or overtensioned cables leading to the definition of the reachable workspace $\mathcal{W}_{\mathrm{R}}$ from Eq. (3.33). Usually an iterative scheme has to be applied where a small sample set is captured to improve the initial model and to allow sample capturing in a larger workspace volume. This approach allows to identify models for underconstrained and overconstrained CDPRs with arbitrary numbers of cables but requires additional measurement equipment such as laser or camera based pose trackers. Deriving the associated objective function

$$\boldsymbol{\rho}(\mathbf{p}) = \bar{\mathbf{x}}_{\mathrm{P}}(\mathbf{p}) - \bar{\mathbf{x}}_{\mathrm{M}} \tag{4.3}$$

with respect to the geometrical parameters $\mathbf{p} = (\mathbf{a}, \mathbf{b})$ in terms of the forward kinematics $\boldsymbol{\upsilon} = \mathbf{x}(\mathbf{q})$ one obtains the Jacobian according to

$$\frac{\partial \mathbf{g_s k}(\mathbf{p})}{\partial \mathbf{p}} = \frac{\partial \mathbf{x}(\mathbf{q}(\mathbf{p}))}{\partial \mathbf{p}} = \frac{\partial \mathbf{x}}{\partial \mathbf{q}} \frac{\partial \mathbf{q}}{\partial \mathbf{p}}. \tag{4.4}$$

For $\frac{\partial \mathbf{x}}{\partial \mathbf{q}}$ the inverse or pseudo-inverse $\frac{\partial \mathbf{q}}{\partial \mathbf{x}}^{-1} = -\mathbf{A}^{*}$ in accordance with Eq. (2.59) has to be computed. The Jacobian $\frac{d\mathbf{q}}{d\mathbf{p}}$ is obtained considering $\mathbf{l}_i = \mathbf{a}_i - \mathbf{p}_{\mathrm{B},i}$ and the associated derivative

$$\mathbf{J}_{\mathrm{lab},i} = \frac{\partial \mathbf{l}_i}{\partial (\mathbf{a}_i, \mathbf{b}_i^{(\mathrm{P})})} = \begin{bmatrix} \mathbf{I} & -\mathbf{R}_{0\mathrm{P}} \end{bmatrix} \tag{4.5}$$

and Eq. (2.61) so that

$$\mathbf{J}_{\mathrm{qab},i} = \frac{\partial q_i}{\partial(\mathbf{a}_i, \mathbf{b}_i)} = \mathbf{u}_i^{\mathrm{T}} \mathbf{J}_{\mathrm{lab},i}. \tag{4.6}$$

After optimization one obtains the calibrated model

$$\bar{\mathbf{x}}_{\mathrm{M}} \approx \bar{\mathbf{x}}_{\mathrm{P}} = \boldsymbol{\upsilon}_{\mathrm{el}}(\bar{\mathbf{q}}_{\theta}, \mathbf{p}_{\mathrm{opt}}) \tag{4.7}$$

whose inverse $\boldsymbol{\varphi}(\mathbf{q}_{\theta}, \mathbf{p}_{\mathrm{opt}})$ is used to control the robot. Transforming the optimization problem into the joint space leads to a structure as shown in Fig. 4.4 and with the transformation of the pose error from Eq. (4.3) into the model joint space one gets the vector of residuals

$$\boldsymbol{\rho} = \boldsymbol{\varphi}(\bar{\mathbf{x}}_{\mathrm{M}}, \mathbf{p}) - \bar{\mathbf{q}}_{\theta} \tag{4.8}$$

$$\min_{\mathbf{p}} \sum_{j=1}^{n_{\mathrm{s}}} \left\| \boldsymbol{\varphi}(\mathbf{x}_{\mathrm{M}j}, \mathbf{p}) - \mathbf{q}_{\theta j} \right\|_2. \tag{4.9}$$

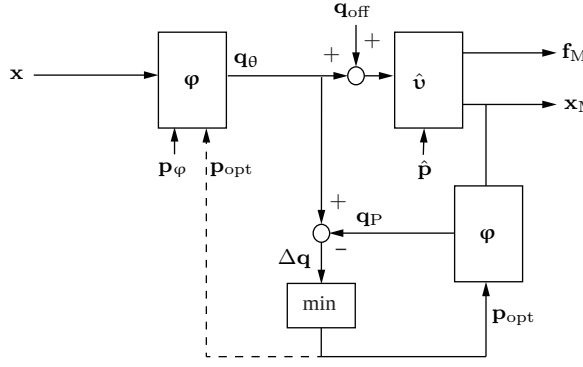

Figure 4.4: Kinematics model optimization in joint space

Restating the residuals in terms of the inverse kinematics avoids the computation of the inverse matrix associated with the forward kinematics. The results for a calibration of the geometric control model are later shown exemplary for two sampling sets covering a large and small area inside the workspace as shown in Fig. 4.6a, 4.6b. Minimizing the residual function from Eq. (4.8) is a central aspect of the optimization problem. Efficient numerical methods which allow to find local minimizer are part of the next section.

4.2 Residual Function Minimization

Considering the scalar multi-variable objective function $\epsilon_{\mathrm{q}}(\mathbf{p}) = \frac{1}{2}\boldsymbol{\rho}(\mathbf{p})^{\mathrm{T}}\boldsymbol{\rho}(\mathbf{p})$ based on the vector residual from Eq. (4.8) and let $\bar{\mathbf{q}}_{\theta_{\mathrm{M}}} = \boldsymbol{\varphi}(\bar{\mathbf{x}}_{\mathrm{M}}, \mathbf{p}, ,)$ one has to find the optimal

parameter set $\mathbf{p}_{\text{opt}}$ with

$$\min_{\mathbf{p}} \left(\frac{1}{2} \boldsymbol{\rho}(\mathbf{p})^{\mathrm{T}} \boldsymbol{\rho}(\mathbf{p}) \right) = \min_{\mathbf{p}} \frac{1}{2} \left\| \bar{\mathbf{q}}_{\theta_{\mathrm{M}}}(\mathbf{p}) - \bar{\mathbf{q}}_{\theta} \right\|_2^2 = \min_{\mathbf{p}} \frac{1}{2} \sum_{i=1}^{n_{\mathrm{s}} m} (q_{\mathrm{M}i}(\mathbf{p}) - q_{\theta i})^2. \tag{4.10}$$

Finding the optimal parametrization $\mathbf{p}_{\text{opt}}$ for Eq. (4.10) is a nonlinear least squares optimization problem whose solution can be found using a gradient descent solvers (Ruder 2016) or more advanced schemes such as the Gauss-Newton (Nocedal and Wright 2006) or Levenberg Marquardt solver (Moré 1978) which allow faster convergence. Starting from a sufficient initial guess $\mathbf{p}_{\text{ini}}$ for the model parameters, the basic step in each iteration of the Gauss-Newton method is to find the least squares solution for the linearized system

$$\mathbf{p}_{k+1} = \min_{\mathbf{p}} \left\| \epsilon_{\mathrm{q}}(\mathbf{p}_k) + \mathbf{J}_{\mathrm{q}p}(\mathbf{p}_k) \left(\mathbf{p} - \mathbf{p}_k \right) \right\|_2 \tag{4.11}$$

and use the solution as best guess for the next iteration. The gradient of the objective function $\epsilon_{\mathrm{q}}(\mathbf{p})$ follows from the chain rule with

$$\nabla \epsilon_{\mathrm{q}}(\mathbf{p}) = \mathbf{J}_{\mathrm{q}p}^{\mathrm{T}} \boldsymbol{\rho}(\mathbf{p}) \tag{4.12}$$

where the Jacobian is computed from the vector residual

$$\mathbf{J}_{\mathrm{q}p} = \frac{\partial \boldsymbol{\rho}(\mathbf{p})}{\partial \mathbf{p}}. \tag{4.13}$$

The first-order necessary condition for an optimal parametrization is defined by

$$\nabla \epsilon_{\mathrm{q}}(\mathbf{p}) = \mathbf{J}_{\mathrm{q}p}^{\mathrm{T}} \boldsymbol{\rho}(\mathbf{p}) = 0. \tag{4.14}$$

The second order sufficient condition is given by the positive definite Hessian

$$\mathbf{M} = \nabla^2 \epsilon_{\mathrm{q}} = \mathbf{J}_{\mathrm{q}p}^{\mathrm{T}} \mathbf{J}_{\mathrm{q}p} + \sum_{i=1}^{m} \rho_i \nabla^2 \rho_i \text{ is pos. definite.} \tag{4.15}$$

For small residual vectors $\boldsymbol{\rho}$, one obtains a good approximation of the Hessian just using the Jacobian expression

$$\mathbf{M} \approx \mathbf{J}_{\mathrm{q}p}^{\mathrm{T}} \mathbf{J}_{\mathrm{q}p}. \tag{4.16}$$

For the parameter optimization to work, it is necessary to have a well conditioned Jacobian which is mainly influenced by the selected sample set and the weighting of the residuals as shown in the next sections.

4.3 Sample Selection and Matrix Condition

Sample selection aims at maximizing the information which is obtained form the system during measurement. Methods for pose sample selection for parallel robots are described extensively in (Hollerbach and Wampler 1996; Wampler et al. 1995) and regarding the optimal number of poses in (Verl et al. 2008). All methods use the singular values of the Jacobian to determine the quality of the selected sample set. Using the first order Taylor expansion of the residual function from Eq. (4.8) leads to the normal equation comparable to Eq. (4.10, 2.15) with

$$\Delta \mathbf{p}_{\mathrm{ab}} = \underbrace{\left(\mathbf{J}_{\mathrm{qab}}^{\mathrm{T}} \mathbf{J}_{\mathrm{qab}}\right)^{-1} \mathbf{J}_{\mathrm{qab}}^{\mathrm{T}}}_{\mathbf{J}_{\mathrm{qab}}^{*}} \Delta \bar{\mathbf{q}} \tag{4.17}$$

where $\Delta\bar{\mathbf{q}}$ contains the joint space errors between pose predictions and measurements for all m cables and n_{s} sample poses resulting in a linear system of $n_{\mathrm{q}} = n_{\mathrm{s}} m$ equations. Solving the linear least squares normal equation allows to determine the parameter correction vector $\Delta\mathbf{p}_{\mathrm{ab}}$. The $n_{\mathrm{q}} \times n_{\mathrm{p}}$ Jacobian $\mathbf{J}_{\mathrm{qab}}$ represents the sensitivity for the parameter vector with respect to the measurements and can be used to rate the quality of the underlying model and the selected sample set computing the condition number with respect to the inverse of a full rank $n \times n$ square matrix

$$\kappa(\mathbf{A}) = \|\mathbf{A}\|_2 \left\|\mathbf{A}^{-1}\right\|_2 = \frac{\sigma_1}{\sigma_n} \tag{4.18}$$

where σ_1, σ_n are the largest and smallest singular value of $\mathbf{A}$, respectively. The condition κ is a measure for the relative sensitivity of the different parameter dimensions. A well-conditioned matrix should have a condition number close to one such that a change in each individual parameter has nearly the same effect on the output. This is the case when all sample configurations are linear independent and the Jacobian becomes orthogonal with $\kappa(\mathbf{A}) = 1$. Larger condition numbers indicate that some degree of multicolinearity between the sample configurations exists (Montgomery et al. 2012). For a sample set with more samples than number of model parameters i.e. $n_{\mathrm{q}} > n_{\mathrm{p}}$ the condition of the Jacobian matrix $\mathbf{J}_{\mathrm{qab}}$ is defined in a similar way with repsect to the Moore-Penrose pseudo left inverse by considering the singular value decomposition (SVD) for

$$\mathbf{J}_{\mathrm{qab}} = \mathbf{U}\boldsymbol{\Sigma}\mathbf{V}^{\mathrm{T}} \tag{4.19}$$

and

$$\mathbf{J}_{\mathrm{qab}}^{*} = \mathbf{U}\boldsymbol{\Sigma}^{*}\mathbf{V}^{\mathrm{T}} \tag{4.20}$$

where $\boldsymbol{\Sigma}$ is the diagonal matrix with the singular values of $\mathbf{J}_{\mathrm{qab}}$ with

$$\boldsymbol{\Sigma} = \begin{bmatrix} \boldsymbol{\Sigma}_{\mathrm{r}} \\ \mathbf{0} \end{bmatrix} \in \mathbb{R}^{n_{\mathrm{q}} \times n_{\mathrm{p}}}, \qquad \boldsymbol{\Sigma}_{\mathrm{r}} = \mathrm{diag}(\sigma_1, \ldots, \sigma_r, 0, \ldots, 0) \in \mathbb{R}^{n_{\mathrm{p}} \times n_{\mathrm{p}}} \tag{4.21}$$

$$\boldsymbol{\Sigma}^{*} = \begin{bmatrix} \boldsymbol{\Sigma}_{\mathrm{r}}^{*} & \mathbf{0} \end{bmatrix} \in \mathbb{R}^{n_{\mathrm{p}} \times n_{\mathrm{q}}}, \qquad \boldsymbol{\Sigma}_{\mathrm{r}}^{*} = \mathrm{diag}\left(\frac{1}{\sigma_1}, \ldots, \frac{1}{\sigma_r}, 0, \ldots, 0\right) \in \mathbb{R}^{n_{\mathrm{p}} \times n_{\mathrm{p}}} \tag{4.22}$$

leading to

$$\kappa(\mathbf{J}_{\mathrm{qab}}) = \left\|\mathbf{J}_{\mathrm{qab}}\right\|_2 \left\|\mathbf{J}^*_{\mathrm{qab}}\right\|_2 = \frac{\sigma_1}{\sigma_r}. \tag{4.23}$$

While the selected sample set has significant impact on the condition number it is only one of four influencing factors associated with the condition number for a specific calibration problem which are the model structure, the model parameters, the parameter scaling, and the sample set as shown in Fig. 4.5. The sample selection aims at minimizing the number of samples while maximizing the obtained information. This may be achieved by distributing the samples within the workspace

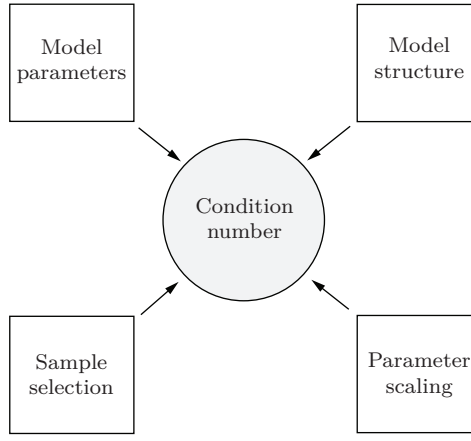

Figure 4.5: Influences on matrix condition number.

While a low condition number indicates a well-posed calibration problem, the cause for a high condition number may be difficult to identify due to the influences of the different aspects of the calibration process. Sec. 6.4 shows these influencing factors in the context of the elastostatics model where different issues with respect to sample selection and parameter scaling arise.

4.4 Model Rating

For the use of the a model it is important to rate the prediction accuracy of a model in respect of the specific application requirements. As mentioned in Sec. 3.2 the prediction accuracy depends on the model structure and its parametrization. In the following, an error metric based on the mean average pose error from Eq. (3.3) is used to rate the

model with respect to a given design parameter set

$$\mathbf{a}_{\mathrm{D}} = \begin{bmatrix} -6.0 & 8.0 \\ 5.0 & 8.0 \\ -5.0 & 0.0 \\ 5.0 & 0.5 \end{bmatrix} \text{ m} \tag{4.24}$$

assuming an error free assembly process, that is $\mathbf{a}_{\mathrm{N}} = \mathbf{a}_{\mathrm{D}}$. Using the nominal parametrization for comparison shows the possible increase in performance for a given model class without increasing model complexity. Choosing a sufficient sample set is essential for the comparison and a standardized method must be used to obtain comparable results. In case of a specific given application, the sample set can be defined by the respective requirements, for example measuring and optimizing the accuracy of the system for certain operation points. Obviously, the increase in accuracy depends on the size and location of the areas and in general increase the closer and smaller such areas become. To make a more general comparison of different models it makes sense to compare the mean prediction error for an evenly sampled reachable or wrench feasible workspace $\mathcal{W}_{\mathrm{R}}$. As an example a first sample set with 25 samples is taken from an equidistant grid with $n_{\mathrm{x,y}} = [5, 5]$ steps in each direction of a bounding box with range ((-4, 0.5), (4, 6)) leading to the sample set as depicted in Fig. 4.6a and defined by

$$\mathcal{W}_{\mathrm{T}1} = \{-4, -2.4, \cdots, 4\} \times \{0.5, 1.6, \cdots, 6\} \tag{4.25}$$

with the condition number from Eq. (4.23) being

$$\mathrm{cond}(\mathbf{J}_{\mathrm{qab}}) = 3.2. \tag{4.26}$$

The second sample set with 16 samples is taken from an equidistant grid with $n_{\mathrm{x,y}} = [4, 4]$ steps in each direction of a bounding box with range ((-3, 0.4), (2, 1)) in the lower workspace leading to the sample set

$$\mathcal{W}_{\mathrm{T}2} = \{-3, -1.75, \cdots, 2\} \times \{0.4, 0.55, \cdots, 1\} \tag{4.27}$$

with the condition number

$$\mathrm{cond}(\mathbf{J}_{\mathrm{qab}}) = 19.3. \tag{4.28}$$

So both sample sets provide sufficient information to identify the geometric cable outlet points. An additional sample set with 2500 samples is used to cross validate the model outside the task sample space with an equidistant grid with $n_{\mathrm{x,y}} = [50, 50]$ steps in each direction of a bounding box with range ((-6.4, -0.5), (5.5, 8.5)) regarding the wrench fesible workspace leading to

$$\mathcal{W}_{\mathrm{V}} = \{-6.40, -6.16, \cdots, 5.50\} \times \{-0.50, -0.32, \cdots, 8.50\} \cap \mathcal{W}_{\mathrm{WF}} \tag{4.29}$$

where $\mathcal{W}_{\mathrm{WF}}$ is the workspace definition from Eq. (3.29). The operational conditions are defined by a constant external wrench of $\mathbf{w}_{\mathrm{e}} = \begin{bmatrix} 0.00 & -1962.00 \end{bmatrix}$ N and a specific cable stiffness of $\mathbf{k}_{\mathrm{F}} = \begin{bmatrix} 200000.00 & 200000.00 & 200000.00 & 200000.00 \end{bmatrix} \frac{\mathrm{N}}{\mathrm{m}}$. Running the

parameter optimization of the geometric control model as described in Sec. 6.1 for both scenarios one obtains the optimal parameter set $\mathbf{a}_{\text{opt}} = \mathbf{a}_{\text{D}} + \Delta\mathbf{a}$ with

$$\Delta\mathbf{a}_1 = \begin{bmatrix} 15.077 & 69.386 \\ -40.895 & 74.302 \\ 10.081 & 1.128 \\ -12.443 & 15.892 \end{bmatrix} \text{ mm}, \Delta\mathbf{a}_2 = \begin{bmatrix} 18.400 & 131.750 \\ -145.129 & 197.131 \\ 34.803 & -135.463 \\ -42.338 & -203.331 \end{bmatrix} \text{ mm} . \tag{4.30}$$

Using the nominal paramterization $\mathbf{a}_{\text{N}}$ and optimal parametrization $\mathbf{a}_{\text{opt}}$, the absolute and relative mean error as well as the absolute and relative improvement are measured. The optimal parametrization $\mathbf{a}_{\text{opt}}$ leads to an increase in accuracy by 29.00 % reducing the mean absolute pose error defined in Eq. (3.3) from $\epsilon_{\text{x}_\text{N}} = 5.71$ mm to $\epsilon_{\text{x}_\text{opt}} = 4.06$ mm for the nominal configuration $\mathbf{a}_{\text{N}}$ and sample set $\mathcal{W}_{\text{T}1}$. The relative error is computed as defined in Eq. (3.5) with $d_{\mathcal{W}} = 9.71$ m leading to $\hat{\epsilon}_{\text{x}_\text{N}} = 0.589\,\%$ and $\hat{\epsilon}_{\text{x}_\text{opt}} = 0.418\,\%$.

For the associated workspace cross validation set $\mathcal{W}_{\text{V}}$ one obtains an increase in accuracy by 9.52 % reducing the mean pose error from $\epsilon_{\text{x}_\text{N}} = 9.61$ mm to $\epsilon_{\text{x}_\text{opt}} = 8.69$ mm .

In the second case, the optimal paramterization leads to an increase in accuracy by 80.64 % reducing the mean absolute pose error from $\epsilon_{\text{x}_\text{N}} = 11.78$ mm to $\epsilon_{\text{x}_\text{opt}} = 2.28$ mm for the sample set $\mathcal{W}_{\text{T}2}$. For the associated workspace cross validation set $\mathcal{W}_{\text{V}}$ the accuracy level changes by -33.57 % changing the mean pose error from $\epsilon_{\text{x}_\text{N}} = 9.61$ mm to $\epsilon_{\text{x}_\text{opt}} = 12.84.$ mm

Obviously the improvement is best for the sampled area for the first and second case. For very specific task spaces as in the second example the increase may be even more significant but coming with the cost of less out-of-sample performance.

The example shows that the accuracy of the kinematic standard model is quite limited when applied to an elastic CDPR. Since one cannot reach a better performance than $\epsilon_{\text{x}_\text{opt}}$, the only way for reaching better performance without changing the model class is to reduce the task workspace as shown in the example with $\mathcal{W}_{\text{T}1}, \mathcal{W}_{\text{T}2}$. The mean adjustment vector norms are $\Delta\mathbf{a}_1, \text{mean} = 46.537$ mm and $\Delta\mathbf{a}_2, \text{mean} = 181.344$ mm. These deviations from the nominal model are quite significant considering the accuracy with which the nominal parameters can be measured using laser tackers and inversely it raises the question how much effort should be put in direct measurement of the nominal parameters using high precision devices.

4.5 Identification of the Elastostatic Model

The elastostatic model is founded on the structure equation Eq. (2.31) which describes the static condition for all poses in the equlibrium state and the underlying structure from the geometrical standard model described in Eq. (2.3) or the extended pulley kinematics model from Eq. (2.16). Identification of the elastostatic model is more involved than the

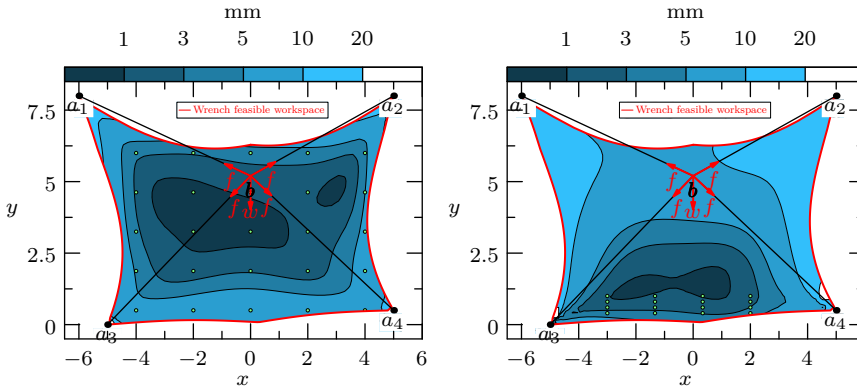

(a) Pose prediction accuracy for the optimized kinematics model $\boldsymbol{\varphi}$ with an elastic CDPR yields a mean error of 4.06 mm compared to the nominal model with a mean error of 5.71 mm over the sample set. The mean pose error for the wrench feasible workspace for the opmtized model is 8.69 mm in comprison to the nominal model with 9.61 mm.

(b) Pose prediction accuracy for the optimized kinematics model $\boldsymbol{\varphi}$ with an elastic CDPR yields a mean error of 2.28 mm compared to the nominal model with a mean error of 11.78 mm over the sample set. The mean pose error for the wrench feasible workspace for the opmtized model is 12.84 mm in comprison to the nominal model with 9.61 mm.

Figure 4.6: Pose prediction accuracy for two different sample sets.

identification of the standard kinematics model due to the different scales of the parameters, different scales and reliability of the sensor inputs, and the possibility to optimize the model with respect to different objective functions. Parameters for the geometry model and parameters for the stiffness model for example have vastly different impact on the combined error function. The same is true for the heterogeneous sensor data when position measurements from a coordinate measurement system are combined with measurements from the force sensors. These aspects are analyzed in more detail in the following sections. Using a sample set with single samples defined by the given controlled cable lengths $\mathbf{q}_{\theta j}$, the measured pose $\mathbf{x}_{\mathrm{M}_j}$ in equilibrium state, and the measured cable forces $\mathbf{f}_{\mathrm{M}}$ one has to find the optimal parametrization for $\mathbf{p}_\kappa = (\mathbf{a}, \mathbf{b}, \mathbf{k}_{\mathrm{F}}, \mathbf{w}_{\mathrm{e}})$ which minimizes the residual wrench of the elastic model from Eq. (2.31) to guarantee a stable stationary state with a valid force distribution and which minimizes the elastostatic inverse model according to Eq. (2.37) to guarantee consistency of the geometric relations and stiffness properties. The residual function according to Fig. 4.8 is stated as

$$\boldsymbol{\rho} = \begin{bmatrix} \bar{\mathbf{x}}_{\mathrm{P}} \\ \bar{\mathbf{f}}_{\mathrm{P}} \end{bmatrix} - \begin{bmatrix} \bar{\mathbf{x}}_{\mathrm{M}} \\ \bar{\mathbf{f}}_{\mathrm{M}} \end{bmatrix}. \tag{4.31}$$

In this case the states of the elastostatic model are treated as outputs which are computed

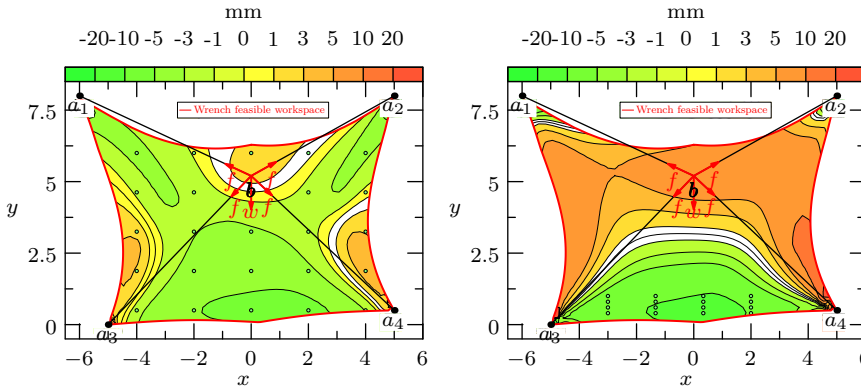

(a) Pose prediction accuracy for the optimized kinematics model $\boldsymbol{\varphi}$ for an elastic CDPR in comparison to the nominal parametrization. Green values show regions with improved accuracy, red valuesshow regions with decreased accuracy.

(b) Pose prediction accuracy for the optimized kinematics model $\boldsymbol{\varphi}$ for an elastic CDPR in comparison to the nominal parametrization. Green values show regions with improved accuracy, red valuesshow regions with decreased accuracy.

Figure 4.7: Pose prediction accuracy for two different sample sets.

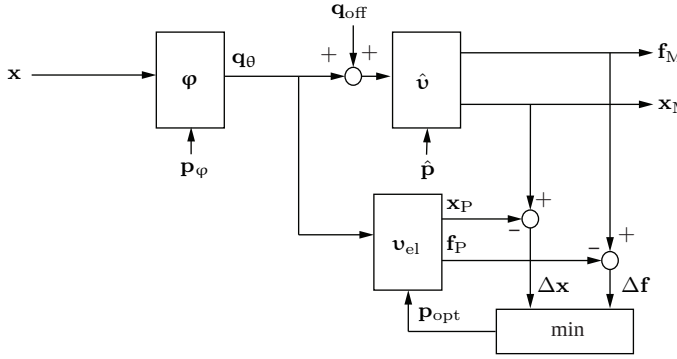

Figure 4.8: Elastostatic model optimization in cartesian space

by the elastostatic forward kinematics minimizing

$$\min_{\mathbf{p}} \begin{cases} \sum_{j=1}^{n_{\text{s}}} \left\| \mathbf{x}_j - \mathbf{x}_{\text{M}_j} \right\|_2 \\ \sum_{j=1}^{n_{\text{s}}} \left\| \mathbf{A}^{\text{T}}(\mathbf{x}_j, \mathbf{p}) \mathbf{K} \left(\mathbf{q}(\mathbf{x}_j, \mathbf{p}) - \mathbf{q}_{\theta j} \right) + \mathbf{w}_{\text{e}} \right\|_2 \\ \sum_{j=1}^{n_{\text{s}}} \left\| \mathbf{K} \left(\mathbf{q}(\mathbf{x}_j, \mathbf{p}) - \mathbf{q}_{\theta j} \right) - \mathbf{f}_{\text{M}} \right\|_2 \\ \sum_{j=1}^{7m+n} \lambda |p_j| \end{cases} \tag{4.32}$$

where the minimizer $\mathbf{p}$ minimizes the four stated error functions. This is a complete description of the objective functions for the optimization of elastostatic CDPR control models which allow for optimal position and force control. While the general structure of these residuals does not change for more complex models such as the pulley kinematics, the parameter space and associated Jacobians do. The first and second part of Eq. (4.32) describe the pose error under the boundary constraint of the force equilibrium. The platform load $\mathbf{w}_\mathrm{e}$ and system stiffness are linear dependent with respect to the pose measurements and therefore the third residual has to be included using the measured cable forces for load and stiffness identification. The last equation is used to penalize the magnitude of the parameters and to avoid overfitting for overcomplex models. In the specific case above, the penalty term represents the lasso regularization. Using a quadratic penalty term leads to the ridge regularization (**Hastie2013**; Hastie et al. 2009). The general concept for the ridge and lasso regularization is indicated in Fig. 4.9. Using the p_1-norm of the lasso regularization allows to zero certain model parameters and therfore reduces the parameter space and model complexity.

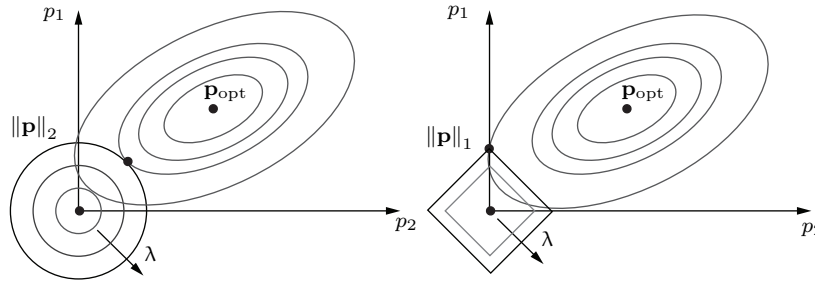

Figure 4.9: Ridge and lassor regularization

With that, the system consists of $(2n+m)\,n_\mathrm{s}+1$ nonlinear equations and $7m+n$ parameters. The Jacobian for the j-th platform pose follow from Eq. (3.27, 3.28) with

$$\delta\mathbf{x}_j = \mathbf{C}_{\mathrm{xw}_j}\left(\mathbf{J}_{\mathrm{wab}_j}\delta\mathbf{p}_\mathrm{ab} + \mathbf{J}_{\mathrm{wkF}_j}\delta\mathbf{k}_\mathrm{F} + \delta\mathbf{w}_\mathrm{e}\right). \tag{4.33}$$

Neglecting the pose index j, the Jacobian for the geometric parameters reads

$$\mathbf{J}_\mathrm{wab} = \frac{\partial\boldsymbol{\gamma}_\mathrm{sk}}{\partial(\mathbf{a},\mathbf{b})} = \mathbf{K}_\mathrm{Gab} + \mathbf{A}^\mathrm{T}\mathbf{K}\mathbf{J}_\mathrm{qab}. \tag{4.34}$$

The partial derivatives for the cable stiffness coefficients follow from $\mathbf{f}(\mathbf{k}_\mathrm{F}) = \frac{\mathbf{k}_\mathrm{F}}{\mathbf{q}}\left(\mathbf{q}-\mathbf{q}_\theta\right)$ with

$$\mathbf{J}_\mathrm{wkF} = \frac{\partial\boldsymbol{\gamma}_\mathrm{sk}}{\partial\mathbf{k}_\mathrm{F}} = \mathbf{A}^\mathrm{T}\mathrm{diag}\left(\mathbf{e}-\frac{\mathbf{q}_\theta}{\mathbf{q}}\right). \tag{4.35}$$

The 6×38 Jacobian for the elastostatic model with respect to the j-th sample then reads

$$\mathbf{J}_{\mathrm{wp}_j} = \begin{bmatrix} \mathbf{J}_{\mathrm{wab}_j} & \mathbf{J}_{\mathrm{wkF}_j} & \mathbf{I} \end{bmatrix} \tag{4.36}$$

and the full $6n_\mathrm{s} \times 38$ Jacobian for all n_s samples is composed by

$$\mathbf{J}_{\mathrm{xp}} = \begin{bmatrix} \mathbf{C}_{\mathrm{xw}_1}\mathbf{J}_{\mathrm{wp}_1} & \mathbf{0} & \mathbf{0} \\ \mathbf{0} & \ddots & \mathbf{0} \\ \mathbf{0} & \mathbf{0} & \mathbf{C}_{\mathrm{xw}_{ns}}\mathbf{J}_{\mathrm{wp}_{ns}} \end{bmatrix} . \tag{4.37}$$

The objective function from Eq. (4.32) requires to solve the forward kinematics for all sample poses. Stating the residual in terms of the inverse elastostatic model reads

$$\min_{\mathbf{p}} \begin{cases} \sum_{j=1}^{n_\mathrm{s}} \left\| \mathbf{A}^\mathrm{T}(\mathbf{x}_{\mathrm{M}_j}, \mathbf{p})\mathbf{f}_j + \mathbf{w}_\mathrm{e} \right\|_2 \\ \sum_{j=1}^{n_\mathrm{s}} \left\| \boldsymbol{\varphi}(\mathbf{x}_{\mathrm{M}_j}, \mathbf{p}) - \Delta\mathbf{q}(\mathbf{f}_j, \mathbf{p}) - \mathbf{q}_{\theta j} \right\|_2 \\ \sum_{j=1}^{7m+n} \lambda |p_j| \end{cases} \tag{4.38}$$

with $(n+m)\,n_\mathrm{s}+1$ nonlinear equations and $7m+n$ parameters. The associated structure is shown in Fig. 4.10. One should recall that the wrench closure condition in the first part of Eq. (4.38) does not incorporate any assumptions about system stiffness and is a solely geometrical property regarding the force distribution. Together with inverse kinematics from the second part of Eq. (4.38), one merges the position sampling data and the force sampling data to establish the correct robot geometry. The additional part $\Delta\mathbf{q}(\mathbf{f})$ regards the elastic properties of the CDPR providing the information on how to translate actuator values into cable forces.

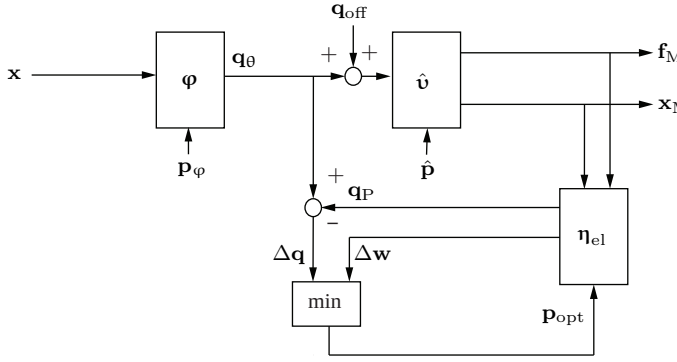

Figure 4.10: Identification of the inverse elastostatic ground-truth model

The residual for the elastostatic inverse kinematics can be rewritten as

$$\boldsymbol{\gamma}_\mathrm{el} = \mathbf{q}(\mathbf{x}, \mathbf{a}, \mathbf{b}) \left(1 - \mathrm{diag}(\mathbf{k}_\mathrm{F})^{-1}\mathbf{ef}\right) - \mathbf{q}_\theta = 0. \tag{4.39}$$

The partial derivative with respect to the geometric parameters yields

$$\mathbf{J}_{\mathrm{qab}_{el}} = \frac{\partial \boldsymbol{\gamma}_{\mathrm{el}}}{\partial(\mathbf{a},\mathbf{b})} = \mathbf{J}_{\mathrm{qab}} \left(1 - \left(\mathrm{diag}(\mathbf{k}_{\mathrm{F}})^{-1}\mathbf{ef}\right)\right). \tag{4.40}$$

The partial derivative with respect to the stiffness parameters yields

$$\mathbf{J}_{\mathrm{q}kF} = \frac{\partial \boldsymbol{\gamma}_{\mathrm{el}}}{\partial \mathbf{k}_{\mathrm{F}}} = \mathbf{q}(\mathbf{x})\mathrm{diag}(\mathbf{k}_{\mathrm{F}})^{-2}\mathbf{ef}. \tag{4.41}$$

The elastostatic model can be optimized with regards to the kinematics constraints or with respect to the wrench closure condition making it possible to weigh the criteria with respect to the application. Optimizing the geometric parameters such that $\boldsymbol{\varphi}(\mathbf{x}_{\mathrm{M}}) \rightarrow \mathbf{q}_{\theta}$ implies a reproduction of the measured system behavior with $\hat{\boldsymbol{\upsilon}}\left(\boldsymbol{\varphi}(\mathbf{x}_{\mathrm{M}}), \mathbf{q}_{\mathrm{off}}\right) \rightarrow \mathbf{f}_{\mathrm{M}}$. The so found model replicates the measured system behavior in an optimal way but may not perform optimal for out of sample predictions, especially extrapolation. Using an kinematics model for the initial sampling leads to a sample coverage as shown in Fig. 4.11 and additional samples from the force space may have to be recorded separately to obtain accurate results. The sampling the workspace volume with the kinematics model allows to cover around 74 % of the wrench feasible workspace regarding the pose data, but the force space is only sampled at one location for each individual pose sample as is shown in Fig. 4.11. Experiments showed that the stiffness parameter may not be estimated correctly when the CDPR is operated at only one tension level as is shown in the evaluation chapter in Fig. 5.7 since the stiffness itself changes with the tension level. An extensive sampling of the 15 dimensional pose and force space in general is expensive but due to the coupling of the cable forces, one only has to define the samples in the nullspace of the force space reducing the overall sample space to 8 dimensions for a CDPR with $m - n = 2$.

The initial sample set is obtained with a standard kinematics model with which the control set points $\mathbf{q}_{\theta j}$ are computed as indicated in Fig. 4.8. The initial tension state of the robot configuration is defined by $\mathbf{q}_{\mathrm{off}}$ leading to sample set defined by the reachable workspace $\mathcal{W}_{\mathrm{R}}$ from Eq. (3.33).

Running parameter identification for the elastostatic model requires a well conditioned Jacobian $\mathbf{J}_{\mathrm{wp}}$. As shown in Sec. 4.3, Fig. 4.5the condition of the Jacobian is influenced by the sample set, the parameter scales, and the parameter selection itself. Choosing an optimal sample set corresponds to finding a set of linear independent vectors. The magnitude of all paramters should be in the same range to obtain a suffiecient optimization landscape. The choice of parameters also influences the condition matrix and the sample selection in so far as they have to be observable and linear independent from each other.

In contrast to the geometric standard model from Sec. 6.1 the elasto geometric model includes parameters of vastly different manitudes as for example the geometry parameters $\mathbf{a}$ within a typical range of ± 10 m and the cable spring constants $\mathbf{k}_{\mathrm{F}}$ with typical values around $1000\,\frac{\mathrm{kN}}{\mathrm{m}}$.

This difference may lead to a ill conditioned Jacobian $\mathbf{J}_{\mathrm{wp}}$ and to slow convergence of the optimization algorithm as well as larger errors in the final optimization result. Stopping

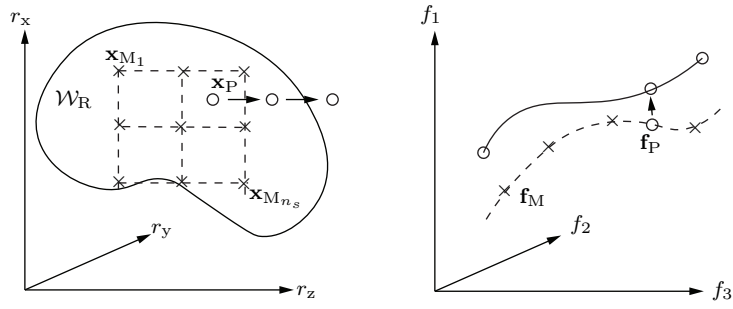

Figure 4.11: Sampling spaces and model predictions for elastostatic identification with a kinematics control model

criteria are more difficult to formulate in a consistent way for the different dimensions. To avoid these problem, a preconditioning matrix can be used which allows to reduce the conditioning number of the augmented linear system. The simplest preconditioning matrix is the identity matrix while the optimal preconditioning matrix would be the inverse so one would obtain the identity matrix with $\kappa(\mathbf{J}_\mathrm{wp}) = 1$ as a result. One common approach to improve the condition is to use a scale-based condition matrix.

In the following the parameter identification and evaluation process for an elastostatic control model from Sec. 4.4 with respect to an elastostatic ground truth model with pulley kinematics and a parametrization as given in Tab. (4.1) is presented. The two most important steps are the determination of the sampling space, and the determination of the parameter preconditioning matrix. The optimal sampling space is determined by maximizing the information criterion as well as by the reachable workspace. For accurate initial control models the reachable sampling space is sufficiently large to obtain enough information for parameter optimization. For largely unknown model parameters it maybe necessary to use a force based identification scheme which does not rely on the the robot geometry. Different algorithms and design of experiments methodologies (DOE) can be used to select the optimal sample set based on the underlying model such as full-factorial design, D-optimal, or I-optimal design (Antony 2014; Atkinson 2015). For the following example, a full-factorial experiment is conducted and the workspace is uniformly sampled with a grid of 5x5 points providing sufficient information for parameter identification. Starting with the geometric parameters of the elasto-geometric model, the influence of the different model parameters with respect to the condition of the Jacobian matrix is shown in the following using an initial configuration as shown in Tab. (4.2) and Fig. 4.16a. Fig. 4.16a also shows the sampling set inside the predicted workspace.

$\mathbf{a}$	[[-6. 8.] [5. 8.] [-5. 0.] [5. 0.5]]	m
r_p	0.15	m
$\mathbf{k}_\mathrm{F}$	[200000. 200000. 200000. 200000.]	$\frac{\mathrm{N}}{\mathrm{m}}$
$\mathbf{q}_\mathrm{off}$	[0. 0. 0. 0.]	m
$\mathbf{w}_\mathrm{e}$	[0. -1962.]	N

Table 4.1: Ground truth parametrization

$\mathbf{a}$	[[-6. 8.] [5. 8.] [-5. 0.] [5. 0.5]]	m
$\mathbf{k}_\mathrm{F}$	[200000. 200000. 200000. 200000.]	$\frac{\mathrm{N}}{\mathrm{m}}$
$\mathbf{q}_\mathrm{off}$	[0. 0. 0. 0. 0. 0. 0. 0.]	m
$\mathbf{w}_\mathrm{e}$	[0. -1962.]	N

Table 4.2: Initial parametrization

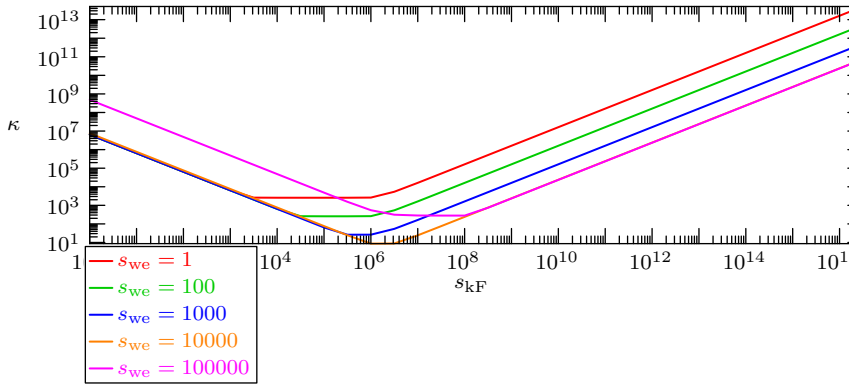

Figure 4.12: Condition of $\mathbf{J}_{wp}$ with respect to parameter scaling weights $s_\mathrm{kF}, s_\mathrm{we}$

The condition numbers for the individual parameter sets $\mathbf{a}, \mathbf{k}_\mathrm{F}, \mathbf{w}_\mathrm{e}$ in Tab. (4.3) case a), b), c) show that the individual residuals are sensitive to changes in the model parametrization and that the optimization problem is well conditioned when a geometry optimization, a stiffness estimation, or load identification should be performed. While this works well for partially unknown model parametrizations, usually all parameters are unknown for the control model synthesis and should be calibrated simultaneously. Just using initial conditions from Tab. (4.2) and the Jacobian from Eq. (2.66) leads to an ill posed prob-

Case	Parameters	Condition number	Jacobian size
a)	$\mathbf{p} = \mathbf{a}$	$\kappa(\mathbf{J}_{\mathrm{wa}}) = 1.9$	152×8
b)	$\mathbf{p} = \mathbf{k}_{\mathrm{F}}$	$\kappa(\mathbf{J}_{\mathrm{wkF}}) = 1.7$	148×4
c)	$\mathbf{p} = \mathbf{w}_{\mathrm{e}}$	$\kappa(\mathbf{J}_{\mathrm{we}}) = 1.0$	146×2
d)	$\mathbf{p} = (\mathbf{a}, \mathbf{k}_{\mathrm{F}}, \mathbf{w}_{\mathrm{e}})$	$\kappa(\mathbf{J}_{\mathrm{we}}) = 6416799.6$	158×14
e)	$\mathbf{p} = (\mathbf{a}, \mathbf{k}_{\mathrm{F}}, \mathbf{w}_{\mathrm{e}}), s_{\mathrm{kF}} = 10^6, s_{\mathrm{we}} = 10^3$	$\kappa(\mathbf{J}_{\mathrm{we}}) = 55.0$	158×14

Table 4.3: Condition of the jacobian matrices $\mathbf{J}_{wp}$ for different parameter sets and preconditioning factors.

lem. For the example configuration and the parameter vector $\mathbf{p} = (\mathbf{a}, \mathbf{k}_{\mathrm{F}}, \mathbf{w}_{\mathrm{e}})$ one would obtain a 158×14 jacobian matrix $\mathbf{J}_{wp}$ with a condition number of 6.42e+06 indicated in Tab. (4.3) by case d) which is caused by the difference in parameter magnitudes of $\mathbf{k}_{\mathrm{F}}$ and $\mathbf{a}$. Introducing the preconditioning matrix

$$\mathbf{W}_{\mathrm{pc}} = \mathrm{diag}\,(s_{\mathrm{kF}}, s_{\mathrm{we}})) \tag{4.42}$$

allows to change the relative scaling of the parameters. The impact of the weighting parameters on the matrix condition is shown in Fig. 4.12. Optimization of both meta-parameters leads to $s_{\mathrm{kF}} = 10^6, s_{\mathrm{we}} = 10^3$ and a condition of 55.02 as shown in Tab. (4.3) case e).

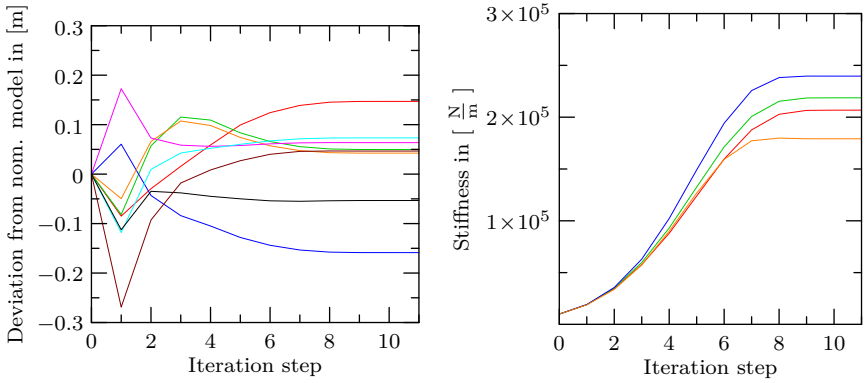

(a) Robot frame geometry $\Delta\mathbf{a}$

(b) Cable stiffness $\mathbf{k}_{\mathrm{F}}$

Figure 4.13: Optimization progress

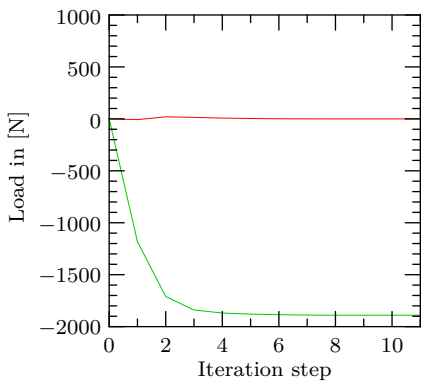

(a) Load indentification $\mathbf{w}_e$

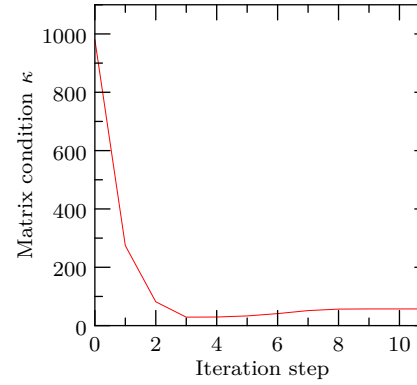

(b) Progression of condition number κ

Figure 4.14: Optimization progress

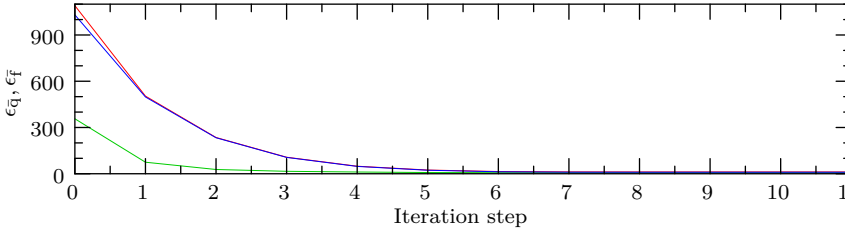

Figure 4.15: Residual progression κ

$$\mathbf{a}_{\text{opt}} = \begin{bmatrix} -5.853 & 8.050 \\ 4.841 & 8.042 \\ -4.936 & 0.073 \\ 4.947 & 0.547 \end{bmatrix}, \qquad \Delta\mathbf{a} = \mathbf{a}_{\text{opt}} - \mathbf{a} \begin{bmatrix} 0.147 & 0.050 \\ -0.159 & 0.042 \\ 0.064 & 0.073 \\ -0.053 & 0.047 \end{bmatrix} \tag{4.43}$$

$\mathbf{a}$	[[-5.853 8.05][4.841 8.042][-4.936 0.073][4.947 0.547]]	m
$\mathbf{k}_F$	[206771.909 218680.096 239626.621 179146.542]	$\frac{N}{m}$
$\mathbf{w}_e$	[-0.526 -1889.905]	N

Table 4.4: Optimal parametrization

Running the nominal elastostatics control model with the paramterization from Tab. (4.2) and active force control using the compuation scheme form Eq. (3.41) leads to a pose error

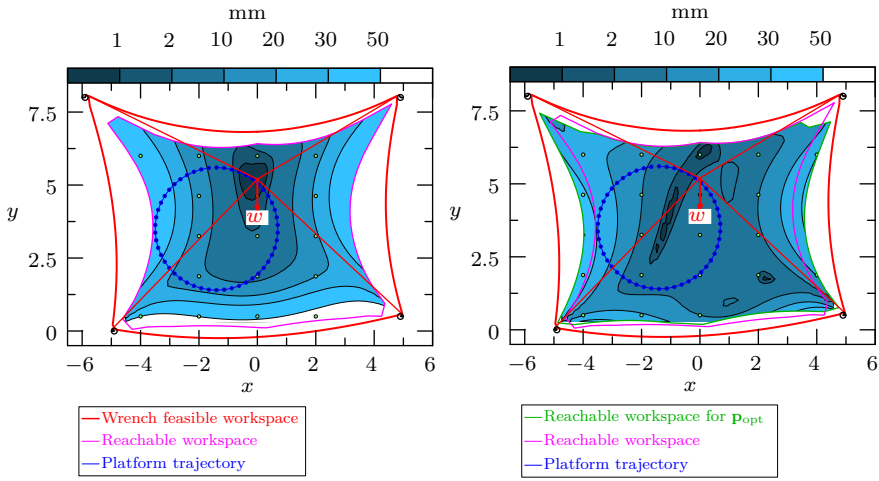

(a) Nominal elastostatics control model on elastostatics ground-truth model with pulley kinematics.

(b) Optimal elastostatic control model with optimized geometry parameters $\mathbf{a}_{\text{opt}}$, system stiffness $\mathbf{k}_{\text{F opt}}$, and wrench $\mathbf{w}_{\text{e opt}}$

Figure 4.16: Elastostatic control model optimization

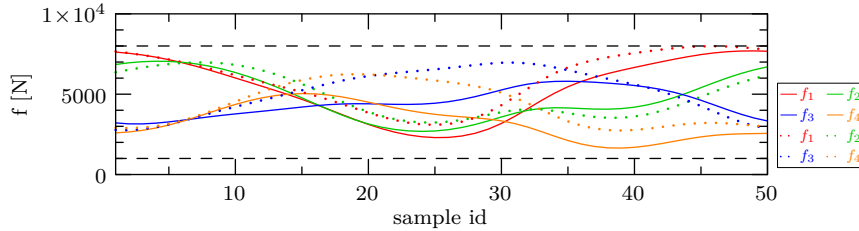

Figure 4.17: Force tracking accuracy example for circular trajectory

distribution as shown in Fig. 4.16a with a mean of

$$\epsilon_{\bar{\mathrm{x}}} = 43.33 \text{ mm} \tag{4.44}$$

inside the reachable workspace $\mathcal{W}_{\mathrm{R}}(\mathbf{p})$. The force tracking error for the nominal model is shown for an exemplary circular trajectory from Fig. 4.16a in Fig. 4.17. The deviation from the reference force is significant but does not constitute the main optimization criterion for applications where mainly positioning accuracy is required. Optimization of the elastostatic model is done with the respective pose and force measurements $\bar{\mathbf{x}}_{\mathrm{M}}, \bar{\mathbf{f}}_{\mathrm{M}}$ and a weighting factor $w_{\rho_{\mathrm{we}}} = 1$ and $w_{\rho_{\mathrm{q}}} = 10000$ for the residuals from Eq. (4.38) and the preconditioning matrix $\mathbf{W}_{\mathrm{pc}}$ with scaling factors as indicated in Tab. (4.3) e). The states

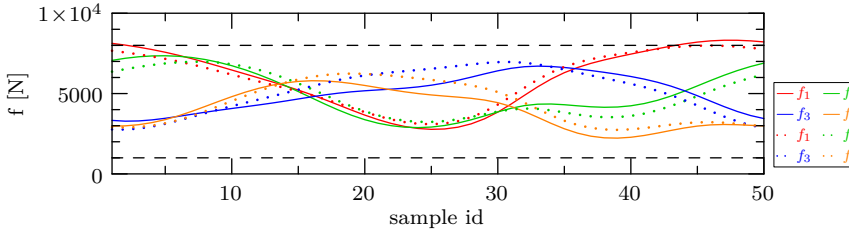

Figure 4.18: Force tracking accuracy for optimal control model on circular trajectory

for each iteration step of the optimization are shown for the robot geometry, system stiffness and load identification in Fig. 4.13a, 4.13b, 4.14a respectively. The progression of the Jacobian and residuals are shown in Fig. 4.14b, 4.15 leading to the optimal control model with $\mathbf{p}_{\text{opt}}$ as shown in Tab. (4.4) . The regularization parameter could be set to $\boldsymbol{\lambda} = 0$ since all parameters of the model show linear independency with respect to measurements. An example, where model reduction is necessary, is shown in the evaluation chapter with a model optimization for the translational workspace. Running the optimal elastostatic control model allows to obtain a mean positioning error of

$$\epsilon_{\bar{\mathrm{x}}} = 30.05 \text{ mm} \tag{4.45}$$

inside the reachable workspace. The force tracking accuracy for the trajectory increases as shown in Fig. 4.18. Although the results indicate that pulleys may have large impact on the accuracy and the reachable workspace, it should also be noted that an optimal parametrization of a standard kinematics model already reduces the error in large areas of the workspace $\epsilon_{\mathrm{x}} < 10$ mm and larger observed errors in the position accuracy should first be reduced by parameter optimization and subsequently by model extension. The possible performance increase through parameter optimization is shown in more detail in the evaluation chapter.

5 The CableRobot Simulator

The CableRobot Simulator (CRS) is a novel motion simulation device which was developed during this thesis and its data are used as basis for the following evaluation chapter. The overall system development included the design of the mechanic frame structure, the control architecture, and the design of two different simulator platforms, one icosahedron shaped platform for general purpose experiments and a specialized helicopter training platform incorporating an actual helicopter cabin. The system represents a completely new kind of motion simulator and builds on the extensive research on cable-driven parallel robots performed in the recent years at Fraunhofer IPA (Pott 2013, 2018a). Motion simulators usually are based on parallel kinematic machines such as hexapod systems (Freeman et al. 1995; Salcudean et al. 1994) or more recently, on serial kinematic robots as was demonstrated by (Bellmann et al. 2011; Nieuwenhuizen and Bülthoff 2013; Teufel et al. 2007) which provide larger workspaces. Using the concept of CDPRs for the implementation of the CableRobot Simulator allowed the design of a versatile motion simulator with high payload capacity and unique motion capabilities. The following sections provide an overview of the most relevant parts of the system architecture and design parameters.This system is the main experimental testbed for the results presented in this thesis. Therefore, the system setup is described in detail in the next sections. Actual measurements and results from system identification for the relevant components are shown to provide a reference setting for the parameter optimization in the following evaluation chapter.

5.1 Structural Design and System Properties

The initial structural design of the CRS was chosen to provide a large simulation space for a large variety of motion perception studies ranging form basic research of the vestibulary system to transport system comfort studies. The simulator cabin design is optimized with regards to stability, cabin volume, and weight. Using an icosahedron truss structure allows to minimize the weight while maximizing the cabin volume, since it provides the optimal use of components regarding the tension flow through the structure. On the other side it provides an optimal relation of nodes and edges with regards to a sphere enclosure. Using carbon fiber rods for the edges and aerospace alloy for the nodes keeps the weight below 80 kg for the whole cabin without instrumentation. For the cable topology a cross over configuration as shown in the figures was chosen to maximize the pitch and roll capability of the cabin.

The CableRobot Simulator uses a set of eight winches mounted on the floor at two

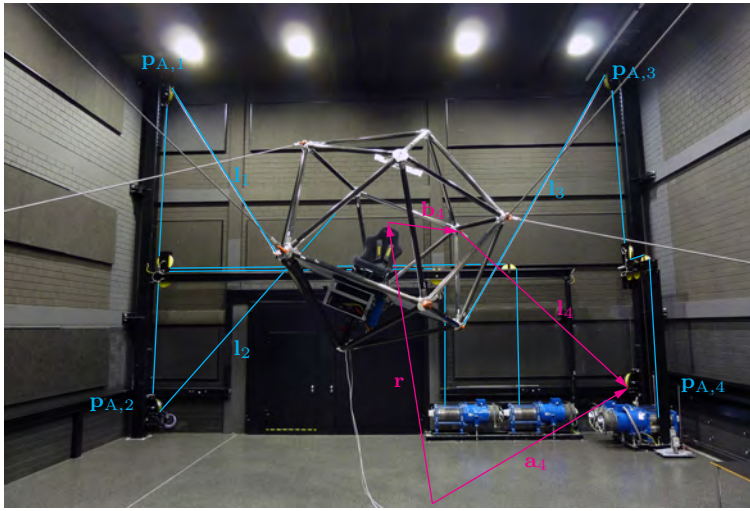

Figure 5.1: Kinematics structure of the CableRobot Simulator and the cable routing from the winches over the proximal anchor points $\mathbf{p}_{\mathrm{A},i}$ to the distal platform points $\mathbf{p}_{\mathrm{B},i}$.

locations to actuate eight 14 mm steel cables which are guided by a pulley system and connected to the simulator platform. The arrangement of the winches and powertrains is mainly determined by the boundary constraints of the floor layout and the maximum distance between the winches to the control cabinet which needs to be minimized to reduce power losses and signal disturbances. Using two locations with respectively four winches as shown in the floor plan Fig. 5.2 leads to cable length variations between 12 and 25 m depending on the specific drive train path and the length inside the simulator workspace as shown in Fig. 5.1 for $\mathbf{l}_1$ to $\mathbf{l}_4$. The length in the workspace is associated with the inverse kinematics of the CRS. The additional cable length inside the drive train is not considered for the kinematics but adds compliance to the system and is therefore relevant for the elastostatic modelling (see Sec. 6.4).

Each winch is driven by a 48 kW synchronous motor with a standstill torque of 3230 Nm allowing for a maximum static cable force of 21180 N. Dimensioning of the system allows a maximum cable force of 14000 N for each cable. Overload in the cables is prevented by load monitoring using force sensors in the pulley axes. The acceleration capability depends on the internal force states and the current system load. The system is designed such that it is possible to reach platform accelerations of $a = 14\mathrm{ms}^{-2}$. A summary of the technical specification is given in Tab. (5.1)

A more detailed analysis of the simulators system dynamics and transfer characteristics is shown in the bode plot from Fig. 5.3 where the amplitude and phase response for an

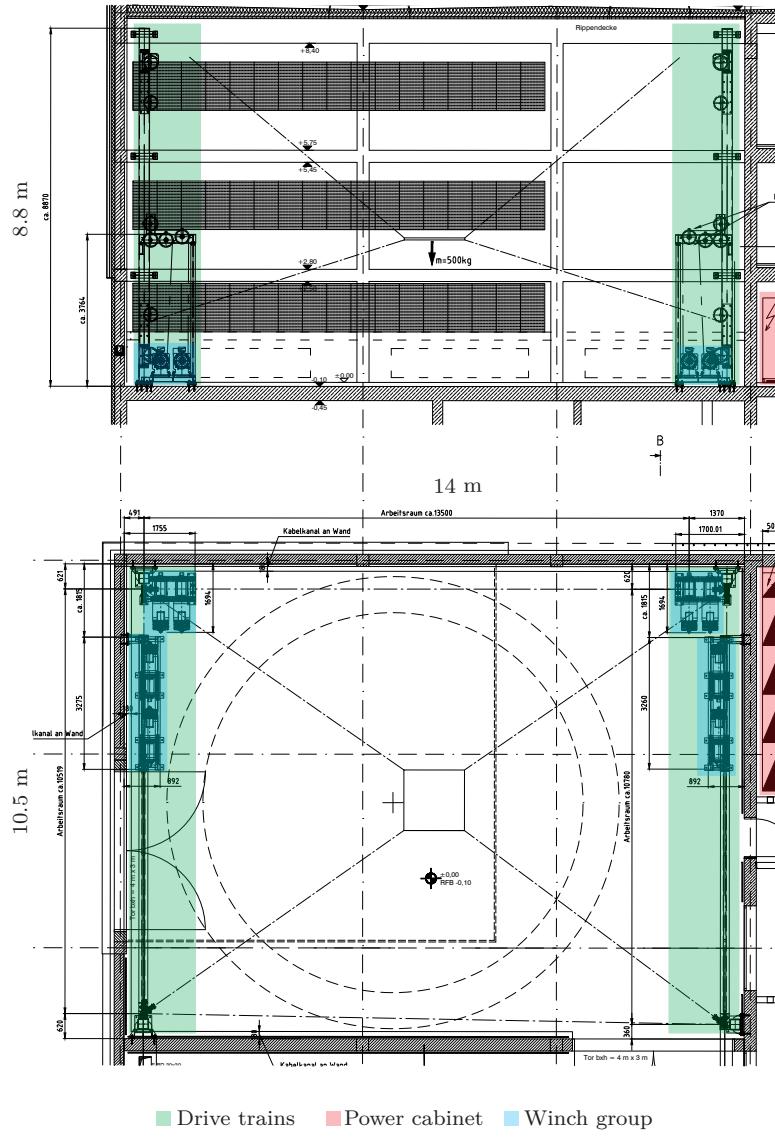

Figure 5.2: Simulator floor plan.

Max. linear and rotary acceleration	$\left[\begin{array}{cc} 14\ \frac{\mathrm{m}}{\mathrm{s}^2} & 100^\circ\ \frac{1}{\mathrm{s}^2} \end{array}\right]$
Max. linear and rotary velocity	$\left[\begin{array}{cc} 5\ \frac{\mathrm{m}}{\mathrm{s}} & 100^\circ\ \frac{1}{\mathrm{s}} \end{array}\right]$
Approximate translational workspace	$\left[\begin{array}{ccc} 4\ \mathrm{m} & 5\ \mathrm{m} & 5\ \mathrm{m} \end{array}\right]$
Approximate rotational workspace	$\left[\begin{array}{ccc} 4^\circ & 5^\circ & 5^\circ \end{array}\right]$
Feasible cable tension range	$\left[\begin{array}{cc} 1000\ \mathrm{N} & 14000\ \mathrm{N} \end{array}\right]$
Max. payload including platform and passengers	1000 kg
Cut-off frequency dep. on weight and cable tension	$5 - 14\ \frac{1}{\mathrm{s}}$
Safety level of controller	SIL 3
Drive power	8×48 kW
Pulley radius	161 mm
Winding diameter of winches	305 mm
Rope diameter	14 mm

Table 5.1: Technical specification of the CableRobot simulator

array of varying cable forces is depicted. Beside the cable tension state f, the overall cable length l_0, and the direction of motion $s_\mathrm{m} = \mathrm{sign}(\frac{\mathrm{d}l}{\mathrm{d}t})$ also impact the transfer behavior but are not further considered here. The measurement of the transfer behavior in Fig. 5.3 is stated with respect to a powertrain model using the motor torque τ_ref as reference input and the measured cable force $f_\mathrm{M} = g(\tau_\mathrm{ref})$ determined at the pulley axis as indicated in Fig. 5.4.

The identification is done by fixing the cables to the ground and applying a chirp signal $T(s)$ to the powertrain system from Fig. 5.4 to obtain the frequence response

$$F(s) = G(s)T(s) \tag{5.1}$$

where the powertrain system $G(s)$ includes the dynamics of the motor current and vector control, the drum and rotor inertia $\mathbf{I}_\mathrm{d}$, the cable mass m_c, and cable elasticities $\mathbf{k}$, as well as pulley inertia $\mathbf{I}_\mathrm{p}$. The trace of the shift in the cutoff frequencies and peak gains for the varying tension states which lead to the curve array from Fig. 5.3 are depecited in Fig. 5.5 showing the dependence of the transfer behavior with respect to the tension state. Varying the cable tension between 1000 N and 10000 N leads to bandwidth variation from 12 to 19 Hz for control of the cable forces.

While the analysis of the input output behavior provides an accurate description of the powertrain system dynamics, it does not provide detailed information about the different

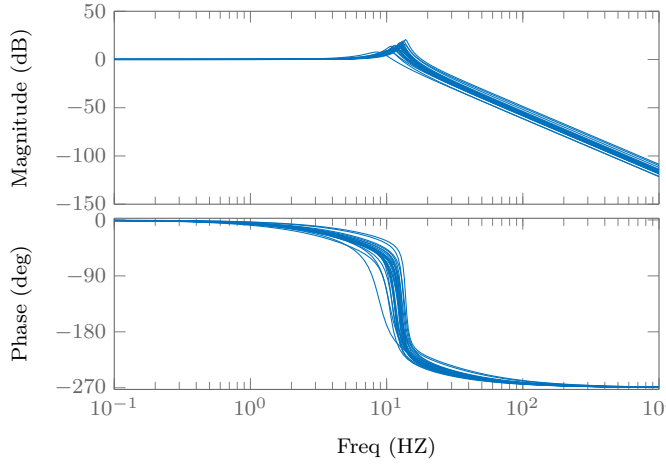

Figure 5.3: Power train transfer function

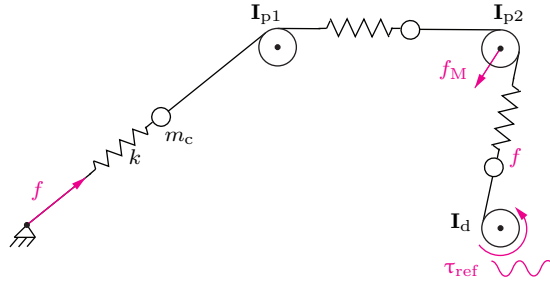

Figure 5.4: Powertrain model

physical effects which lead to the observed behavior. A detailed analysis of the cable dynamics of the CableRobot simulator with respect to the unsupported cable segments in the workspace are performed in (Schenk et al. 2017) using a VICON tracking system as external measurement device. With this camera based approach it is possible to measure individual elastic coordinates of the cables with a sampling rate of 250 Hz. Using the spatial data as shown in Fig. 5.6 provides the possibility to run a parameter identification on finite element models as proposed by (Andersen et al. 2014).

The static behavior of the powertrain is measured with the same setup as indicated in Fig. 5.4 showing a hysteretic behavior as depicted in Fig. 5.7 (A) which is an effect that can be observed for most CDPRs, compare (Miermeister et al. 2015; Miyasaka et al.

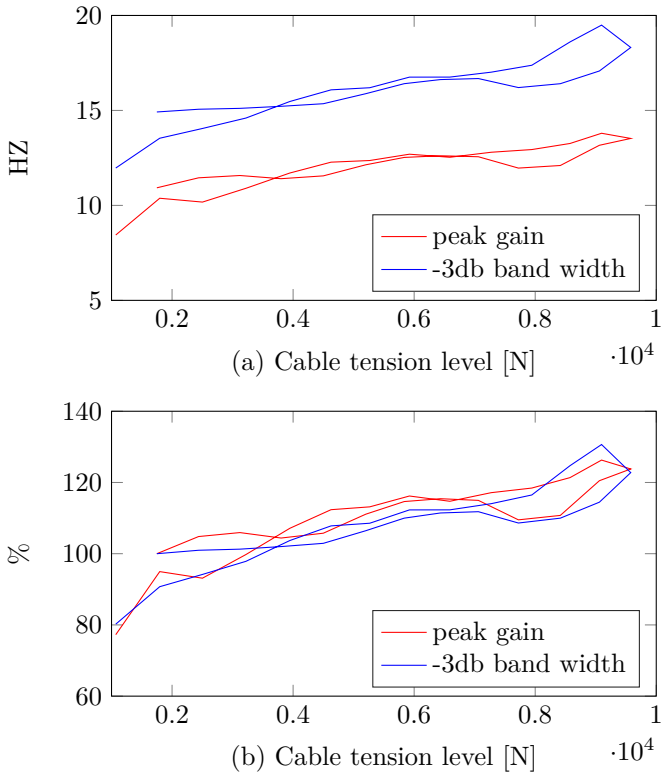

Figure 5.5: Shift in cutoff frequency and peak gain due to tension state

2016). Using simplified linear spring models in an elastostatic control model as described in Sec. 2.4 whose parameters are determined by a least square linear fit to the measured data of a single powertrain lead to errors up to 600 N. The magnitude of the error determined by direct measurement of a single powertrain correlates closely with the mean error which is obtained for a full elastostatic model optimization as is performed in Sec. 6.4 with an error of $\epsilon_{\bar{f}} = 582$ N.

Using a piecewise polynomial model for the loading and unloading path allows to reduce the prediction error significantly. In Fig. 5.7 (A) the overlay of the measured data and model predictions is indistinguishable and the error is reduced to around 0.5 % as shown in Fig. 5.7 (B) for the loading and unloading polynomial. The associated change in the cable stiffness is depicted in Fig. 5.7 (C) showing that the cable stiffness varies between 38 $\frac{\text{kN}}{\text{m}}$ and 580 $\frac{\text{kN}}{\text{m}}$ for cable elongations of 0 to 4.5 mm and the associated tensions states between 500 N and 12000 N. While the polynomial hysteresis model provides an accurate

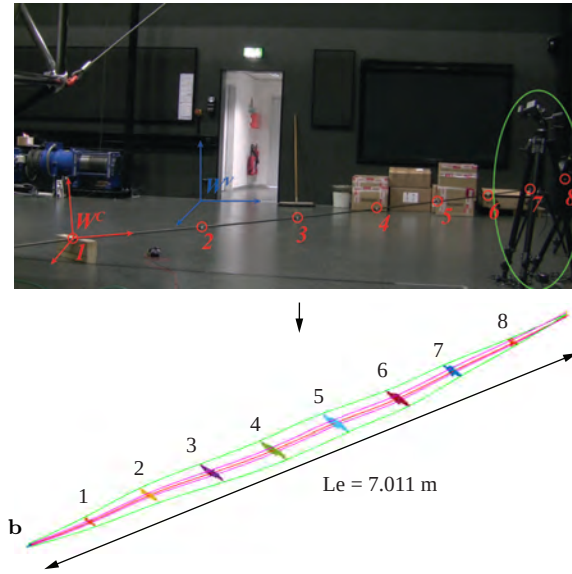

Figure 5.6: VICON camera cable tracking. Longitudinal and lateral motion of eight markers are shown in the cross sections. A detailed analysis can be found in (Schenk et al. 2017)

model for a single powertrain and fixed cable length, it introduces more complexity by the additional parameters of the polynomials and the need for additional information such as the direction of motion to accurately compute the model predictions. The increased effort for modelling the hysteresis effect may be taken into account for applications where the CDPR is operated with focus on the process wrench such as impedance control. For the motion simulator, cable forces are only of concern as a criterion for minimal and maximal cable forces and the reachable workspace. Using a linear elastic cable model allows robust identification of the associated stiffness parameters and provides sufficient prediction accuracy as shown in Sec. 6.4.

5.2 Icosahedron Platform

The platforms for the CRS are a central part of the system and described in the following to complete the description of the experimental testbed of this thesis. The icosahedron platform is designed to provide a lightweight versatile cabin which can be used for various motion experiments such as vehicle simulation, perception threshold studies, motion sickness experiments, and passenger comfort studies. The scope of experiments requires the platform to be usable for motion experiments with passengers in sitting and upright

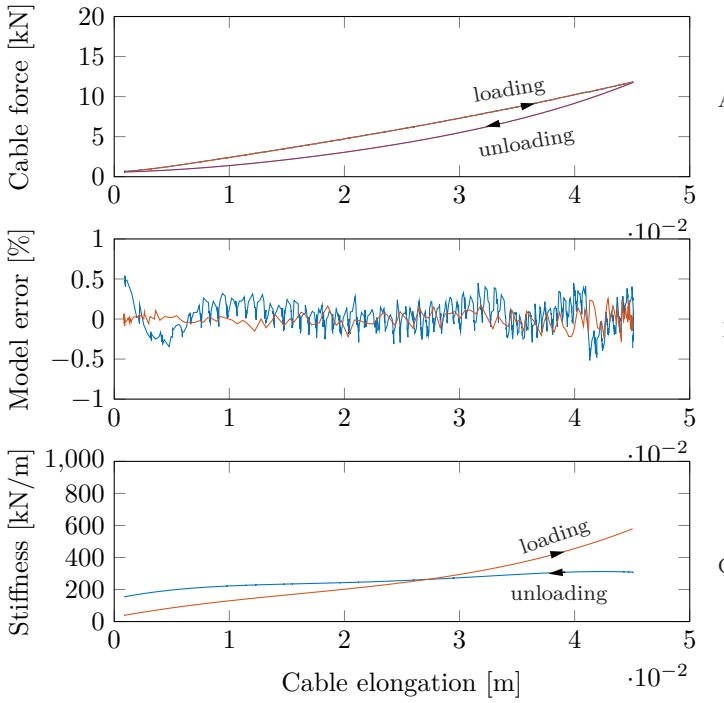

Figure 5.7: Cable hysteresis behavior

standing position leading to a space frame design. It allows mounting a seat with body tracking equipment shown in Fig. 5.8a and provides a spherical enclosure allowing to secure probands also in standing position as shown in Fig. 5.8b.

To provide optimal structural force transfer between the cables around the spherical enclosure with a diameter of 2.8 m, an icosahedron structure is chosen which provides the best approximation to the sphere while keeping the number of force transmission elements minimal. Using carbon fiber rods as connection elements provides high stiffness and breaking loads while keeping the mass of the space frame at 80 kg. The use of carbon fiber in general allows to minimize the cabin weight but adds to the complexity of the design and manufacturing process since it is difficult to predict the load capacity and failure behaviour due to the anisotropic behavior of the carbon fabrics (Knops 2008). Manufacturing the parts and creating reliable connectors also involves complex processes and test procedures to obtain certified structural components which can be used in safety critical applications such as the CRS. Using an icosahedron shaped space frame reduces complexity compared to monocoque or unibody designs. Only one-dimensional load cases have to be considered

(a) Configuration 1: Icosahedron cabin with seat mounting and optical tracking for vestibulary system studies.

(b) Configuration 2: Icosahedron cabin with upright standing passenger for transport system comfort study.

Figure 5.8: Icosahedron cabin configurations for different simulation use cases.

for the force transmission elements which allows to use certified processes for carbon fiber tube manufacturing and to define the respective interactions between adjacent elements. Also, only one type of structural component has to be manufactured reducing manufacturing cost for the most expensive carbon fiber parts. The rods are designed for a maximal compression and expansion force of 151 kN where the critical load is defined for compression using the Euler case 2 buckling criterion (Gross et al. 2014). Connecting carbon fiber materials and metal components to transfer large dynamic forces requires fatigue resistant connectors which need specialized design to cope with the inherent anisotropic nature of composite materials and the complex fracture behavior as well as the wide variety of failure modes. All failure modes have to be accounted for to create the optimal joint design (Camanho and Hallett 2011). Here, the connection between the aluminum nodes and carbon fiber rods is established using a clamp connector with a radial wound roving which is used to take up the expansion forces of the inner conus element to provide the frictional forces for the axial load transfer as shown in Fig. 5.9b. All connection points have a self-centering conic shape and can be used as cable attachment points allowing fast reconfiguration of the cabin. A detailed methodology for cable robot reconfiguration can be found in (Trautwein et al. 2018) and is not further considered in this thesis. The cables are connected to the cones using universal joints where the rotational center $\mathbf{p}_{\mathrm{B},i}$ as depicted in Fig. 5.9a is used for the nominal geometry of the control model.

To check the stability of the cabin hull, the load distribution in the icosahedron space frame is computed using a linear elastic model for the carbon fiber rods with a stiffness of $\mathbf{k}_{\mathrm{sf}}$. Analyzing the internal forces of the icosahedron cabin is done with the matrix stiffness

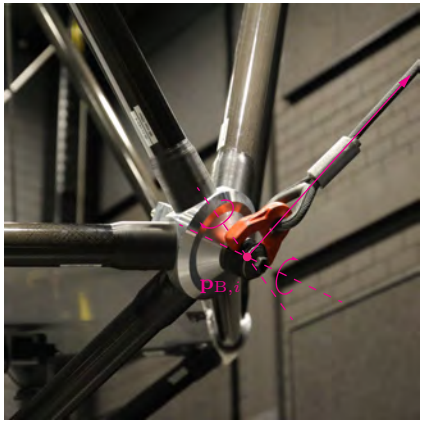

(a) Icosahedron cabin cable connectors

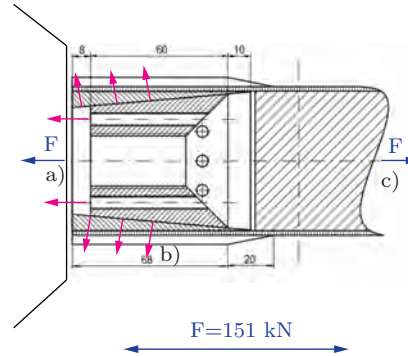

(b) Carbon fiber clamp connector load transfer

Figure 5.9: Icosaheron cabin structural components

method (Karnovsky and Lebed 2010) which provides a general formalism to analyze the statics of truss structures. The formalism can be well integrated with the elastotstatic model of cable-driven parallel robots from Sec. 2.6 since it resembles the same structure and one can see the elastic model of a CDPR as a special case of a more general elastic truss structure where the cables represent truss members or used as external load for the platform truss. Using the same naming convention as used in the cable robot literature, the positions and loads of the joints of the space frame (sf) are denoted by $\mathbf{x}_{\mathrm{sf}}, \mathbf{w}_{\mathrm{sf}}$ and the length and inner forces of the truss members are denoted by $\mathbf{q}_{\mathrm{sf}}, \mathbf{f}_{\mathrm{sf}}$ respectively. Writing the structure equation for the truss system one obtains

$$\mathbf{A}_{\mathrm{sf}}^{\mathrm{T}}\mathbf{f}_{\mathrm{sf}} + \mathbf{w}_{\mathrm{sf}} = \mathbf{0} \tag{5.2}$$

where the structure for an exemplary configuration for a two-dimensional truss as depicted in Fig. 5.10a yields

$$\mathbf{A}_{\mathrm{sf}}^{\mathrm{T}} = \begin{bmatrix} \mathbf{u}_{\mathrm{sf}1} & -\mathbf{u}_{\mathrm{sf}2} & \mathbf{0} \\ \mathbf{0} & \mathbf{u}_{\mathrm{sf}2} & \mathbf{u}_{\mathrm{sf}3} \\ -\mathbf{u}_{\mathrm{sf}1} & \mathbf{0} & -\mathbf{u}_{\mathrm{sf}3} \end{bmatrix}_{(6\times 3)} \tag{5.3}$$

using the truss unit vectors $\mathbf{u}_{\mathrm{sf}i}$,

$$\mathbf{f}_{\mathrm{sf}} = \begin{bmatrix} f_{\mathrm{sf}1} \\ f_{\mathrm{sf}2} \\ f_{\mathrm{sf}3} \end{bmatrix}_{(3\times 1)} \tag{5.4}$$

for the truss member forces $f_{\mathrm{sf}i}$, and

$$\mathbf{w}_{\mathrm{sf}} = \begin{bmatrix} \mathbf{u}_1 & \mathbf{0} & \mathbf{0} & \mathbf{0} \\ \mathbf{0} & \mathbf{u}_2 & \mathbf{0} & \mathbf{u}_4 \\ \mathbf{0} & \mathbf{0} & \mathbf{u}_3 & \mathbf{0} \end{bmatrix}_{(6\times 4)} \begin{bmatrix} f_1 \\ f_2 \\ f_3 \\ f_4 \end{bmatrix}_{(4\times 1)} \tag{5.5}$$

using the cable unit vectors $\mathbf{u}_i$ and the cable forces f_i . For a given load set $\mathbf{w}_{\mathrm{sf}}$, the joint displacements are computed from the stiffness matrix $\mathbf{K}_{\mathrm{Csf}} = \mathbf{A}_{\mathrm{sf}}^{\mathrm{T}}\mathbf{K}_{\mathrm{sf}}\mathbf{A}_{\mathrm{sf}}$ under the assumption that no initial load is present such that the impact of the geometrical stiffness can be neglected (compare Sec. 2.6) with

$$\delta\mathbf{x}_{\mathrm{sf}} = \mathbf{K}_{\mathrm{C}_{\mathrm{sf}}}^{-1}\mathbf{w}_{\mathrm{sf}}. \tag{5.6}$$

For a system with n degrees of freedom, it is necessary to fix some joints to make the system solvable by removing the ambiguities which would arise through the possible rigid body transformations. Reversely, the member forces $\mathbf{f}_{\mathrm{sf}}$ follow from the node displacements $\delta\mathbf{x}$ by

$$\mathbf{f}_{\mathrm{sf}} = \mathbf{K}_{\mathrm{sf}}\mathbf{A}_{\mathrm{sf}}\delta\mathbf{x}. \tag{5.7}$$

In Fig. 5.10b an example for a worst case load analysis of the icosahedron cabin is shown, where loads of 10 kN are applied to all joints beside the cable forces in order to simulate equipment which is attached to the respective joints during motion simulation. Joints indicated by the blue dots have fixed coordinates to remove rigid body motion for the analysis.

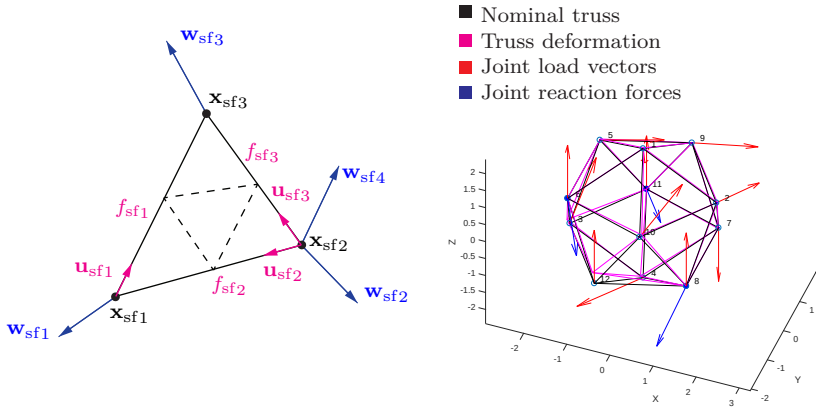

(a) FEM space frame statics (b) Icoshaderon space frame analysis

Figure 5.10: Icosahedron stability analysis

An overview of the entire icosahedron platform setup and the basic configuration is shown in Fig. 5.11 where the parametrization $\mathbf{a}_i, \mathbf{b}_i$ of the nominal model is given by the rows of the parameter matrices

$$\mathbf{a} = \begin{bmatrix} -5.380 & 7.677 & 6.524 \\ -5.421 & 7.668 & -1.242 \\ 5.016 & 7.555 & 6.503 \\ 5.117 & 7.638 & -0.754 \\ 5.152 & -6.182 & 6.642 \\ 5.218 & -6.304 & -0.615 \\ -5.451 & -6.492 & 6.630 \\ -5.461 & -6.509 & -1.067 \end{bmatrix}, \quad \mathbf{b} = \begin{bmatrix} -1.383 & 0.528 & -0.747 \\ -0.799 & 1.245 & 0.746 \\ 1.454 & 0.370 & -0.748 \\ 0.954 & 1.147 & 0.745 \\ 0.819 & -1.268 & -0.746 \\ 1.403 & -0.551 & 0.746 \\ -0.935 & -1.170 & -0.746 \\ -1.434 & -0.393 & 0.748 \end{bmatrix}. \tag{5.8}$$

The depicted workspace hull in Fig. 5.11 shows the wrench feasible constant orientation workspace for the nominal configuration and a rotation with $\boldsymbol{\phi} = \mathbf{0}$. The cabin can be operated inside the workspace in an open-loop control mode for trajectory replay, or in a human-in-the-loop mode using standard controllers. Operating the cabin in the close-loop mode while providing a safe control strategy for the complex workspace boundary is still subject to research. While most closed-loop experiments can be conducted using standard input devices such as control sticks and pedals the design of the CRS also allows the implementation force sensing schemes for the control of the icosahedron cabin. Due to the size of the icosahedron cabin and the force sensors in the tilt pulleys, it is possible to track the forces of passengers in standing and sitting position with high accuracy if an accurate model is provided as is shown in the next section.

5.3 Icosahedron Cabin Force Sensing

The seat configuration mainly is used with a virtual reality head mounted displays together with an optical head tracking system which is robust against cabin acceleration in comparison to the integrated IMU based trackers. Using the cabin in standing configuration allows to implement balancing experiments and transportation comfort studies. This configuration also allows the use of novel control schemes where the motion simulator interactively reacts to weight rebalancing using the internal forces sensors of the redirection pulleys. Although the system forces and loads are high with up to 10000 N per cable compared to the differential weight changes caused by a subject with a weight of around 80 kg, is possible to track the motion of the subject estimating the center of gravity using the structure equation from Eq. (2.31) and the projection onto the xy-plane

$$\mathbf{w}_{\mathrm{xy}}(\mathbf{x}_{\mathrm{s}}) = \begin{bmatrix} 0 & 0 & 0 & 1 & 0 & 0 \\ 0 & 0 & 0 & 0 & 1 & 0 \end{bmatrix} \mathbf{A}^{\mathrm{T}}(\mathbf{x})\mathbf{f}(\mathbf{x}, \mathbf{x}_{\mathrm{s}}) - \mathbf{w}_{\mathrm{e}} \tag{5.9}$$

where

$$\mathbf{w}_{\mathrm{xy}} = \mathbf{0} \tag{5.10}$$

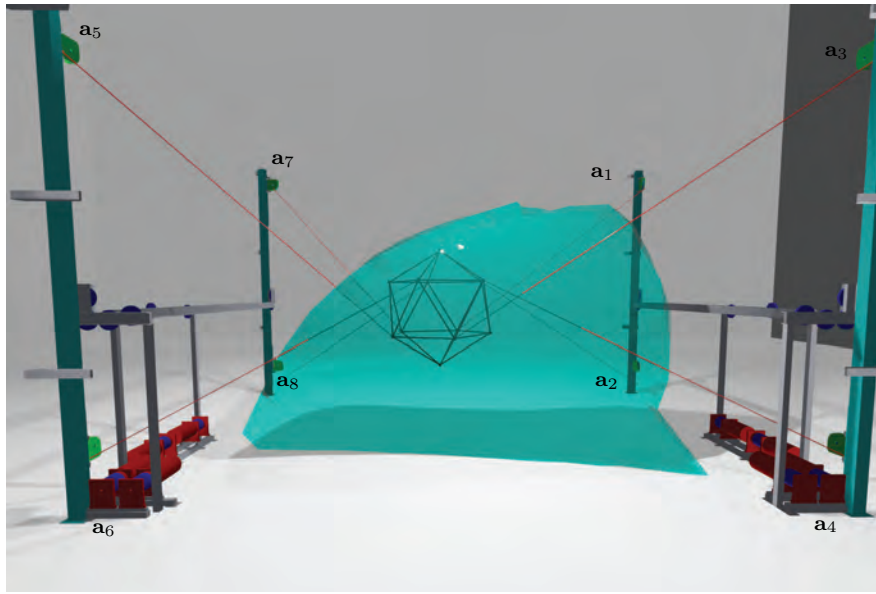

Figure 5.11: CableRobot Simulator with icosahedron cabin and wrench feasible constant orientation workspace

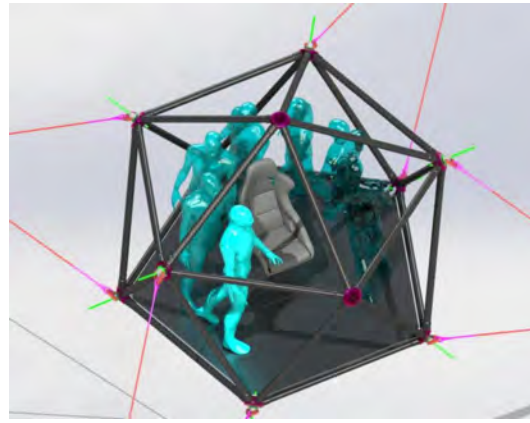

Figure 5.12: Test walking trajectory for dynamic load tracing

for the unloaded state. In Fig. 5.12 the experimental setup for load tracing on the icosahedron platform is outlined. The wrench data for $\mathbf{w}_{\mathrm{xy}}$ from the recorded experiment is

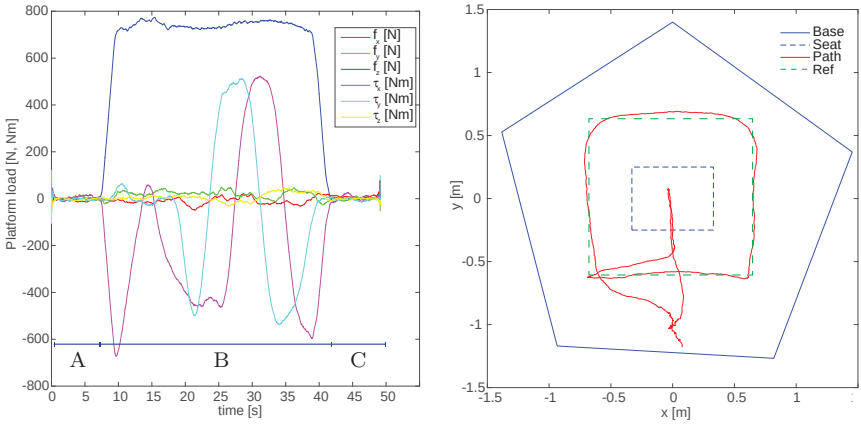

(a) Wrench tracing signal showing current platform torque and cartesian forces

(b) Load position tracking using cable force sensors in the redirection pulleys on the frame

Figure 5.13: Interactive load tracking using platform wrench estimation

shown in Fig. 5.13a. Phase A and C show the initial and final state $\mathbf{w}_{xy} = \mathbf{0}$ before the platform is accessed and after it is exited by the subject. Phase B shows the weight f_z of the subject and the exerted torque during the walk which is used to compute the subjects relative positions $\mathbf{x}_s$ as depicted in Fig. 5.13b. The values are recorded for a fixed zero pitch and roll angle which allows a tracking accuracy of ± 9.7 cm comparing the estimated pose (red line) with the reference (green line). Increasing the roll and pitch angles leads to a decrease in sensitivity since position changes in z-direction do not change the exerted torque and cannot be detected. Beside the angle of the platform, the accuracy mainly is influenced by the accuracy of geometry model which is used to compute the structure matrix $\mathbf{A}^T$, Eq. (5.9). Obtaining the accurate kinematics model and load estimator for the CRS is part of the evaluation chapter. While the icosahedron platform is designed as a versatile general purpose platform, it lacks some features such as large rotation angles and realistic interior design required for helicopter simulation. For this scenario, an additional simulator platform based on an actual helicopter cabin was designed which is described in the next section.

5.4 Helicopter Platform

For the simulation of hover flight scenarios a Cabri G2 helicopter cabin from Guimbal depicted in Fig. 5.14a is integrated into the CableRobot Simulator as shown in Fig. 5.14b. Adding the helicopter cabin provides additional realism for the simulation of flight experiments, especially hover maneuvers which can be replicated without additional motion

cueing filters. The platform configuration diverges significantly from the Icosahedron cabin in so far as the cables are attached to the lower and upper part of the platform without any over-crossing of the cables in vertical direction as can be seen in Fig. 5.16, 5.18. This design decision had to be made in order to integrate the additional endless rotation yaw axis shown in Fig. 5.16, 5.17a which allows free rotation of the helicopter cabin. Since this measure reduces the angle of the four upper cables, the workspace in z-direction is much more limited than for the icosahedron cabin as can be seen by comparing the wrench feasible constant orientation workspace of the helicopter cabin to the icosahedron cabin as depicted in Fig. 5.15.

(a) Guimbal Cabri G2 Helicopter (A. Tarditi - Hélicoptères Guimbal)

(b) Guimbal Cabri G2 helicopter cabin mounted to the CRS.

Figure 5.14: Helicopter simulator

Driving the endless yaw axis can be done with an onboard motor unit or more advanced concepts with additional cables and an external motor unit as proposed in (Miermeister and Pott 2015; Pott 2012; Reichenbach et al. 2019). The use of a cable-actuated yaw-axis allows to reduce the cabin weight and may remove the necessity of power and signal supply for some CDPR designs. Using an onboard motor solution on the other side provides more accurate and easier control of the yaw axis and allows to use standard solutions for the certified and safe operation of the yaw axis.

Additional requirements for the platform attachment points regard the minimization of the exerted torque on the actuated yaw axis while still allowing to counteract torque from the accelerated helicopter cabin. Furthermore, the height of the yaw axis has to be minimal to minimize the negative impact on the workspace. Considering the torque and forces which have to be transferred by the yaw axis, a mechanical model as shown in Fig. 5.17b is applied. Compared to the design of other platforms for CDPRs where no

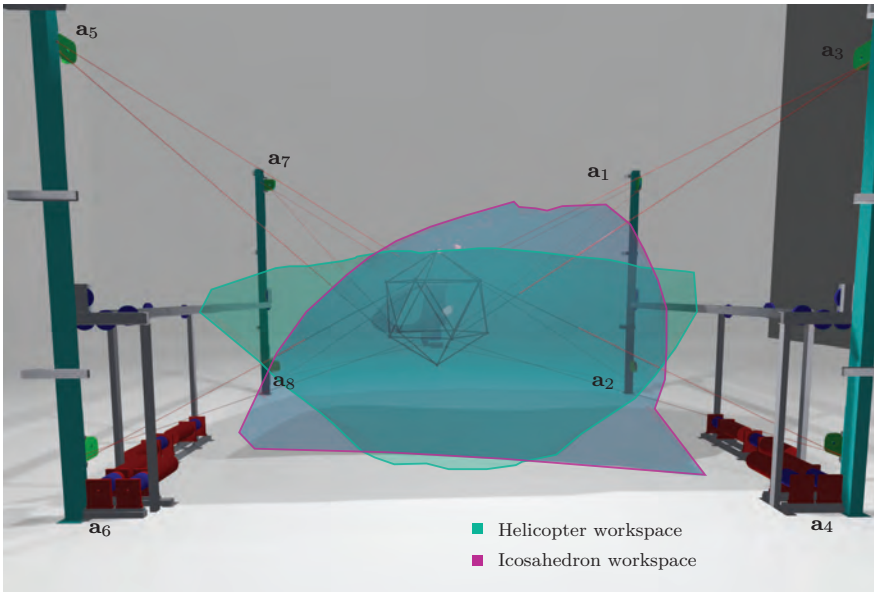

Figure 5.15: Workspace comparison for the two different platform configurations using the icosahedron and the helicopter cabin.

tight spatial restrictions for the general design of the space frame apply, the design of a stator and rotor system which can be placed inside the helicopter hull is more challenging. For stability, the stator must provide a large diameter to resists torque and bending forces from the upper and lower cables. This can best be achieved by a hollow shaft design which provides optimal torque transmission while keeping the weight at a minimum as shown in Fig. 5.16.

The complementary rotor is driven by a belt and planetary gear unit as is indicated in Fig. 5.16 (Drive unit). The upper part of the rotor shaft integrates a slip ring which allows the transmission of signals and power for the helicopter controls. While the rotor and stator unit are at a very similar position as the rotor shaft in the actual helicopter setup, the load cases for operation in the simulator are not. This prohibits the reuse of existing rotor shaft mounting points inside the helicopter cabin. Instead, the passenger seats are decoupled from the carbon fiber structure of the cabin and are directly mounted to the rotor frame as depcited in Fig. 5.16 to avoid any load transfer to the helicopter cabin.

Simulation of the stator and rotor forces is done using the free body model indicated in Fig. 5.17b and partitioning of the structure matrix. Using a reference force distribution computed according to Eq. (3.41), the wrenches $\mathbf{w}_{A1}, \mathbf{w}_{A2}$ depicted in Fig. 5.17b for the

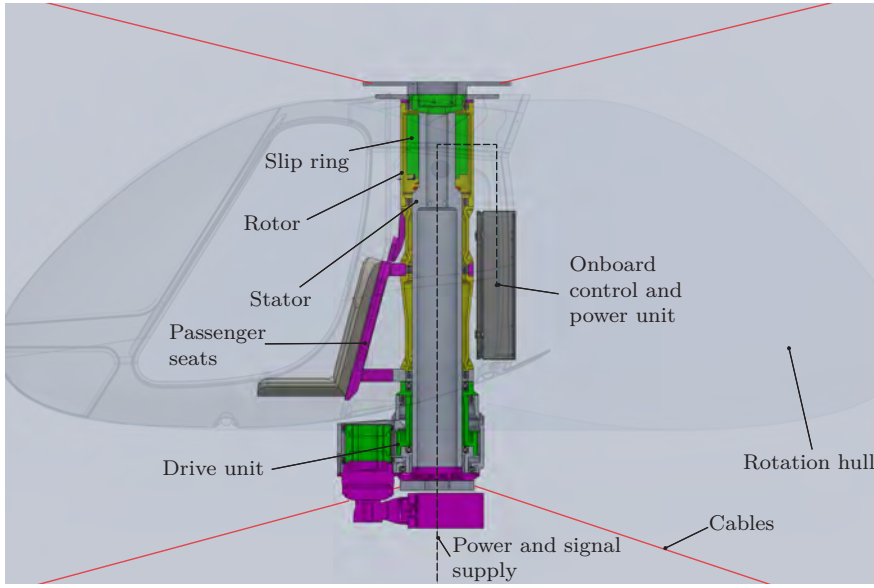

Figure 5.16: Endless rotating yaw-axis for helicopter cabin

upper and lower mouting unit are computed by

$$\begin{bmatrix} \mathbf{w}_{A1} \\ \mathbf{w}_{A2} \end{bmatrix} = \begin{bmatrix} \mathbf{A}_1^{\mathrm{T}} & \mathbf{0} \\ \mathbf{0} & \mathbf{A}_2^{\mathrm{T}} \end{bmatrix} \left(\mathbf{f}_{\mathrm{m}} - \mathbf{A}^{+\mathrm{T}} \left(\mathbf{w}_{\mathrm{e}} + \mathbf{A}^{\mathrm{T}} \mathbf{f}_{\mathrm{m}} \right) \right) \tag{5.11}$$

where the matrix partitions $\mathbf{A}_1^{\mathrm{T}}, \mathbf{A}_2^{\mathrm{T}}$ relate to the respective cable forces. The external wrench $\mathbf{w}_{\mathrm{e}}$ for the static case is computed by total load of the rotor and stator system including the helicopter cabin and two passengers as

$$\mathbf{w}_{\mathrm{e}} = \begin{bmatrix} 0 & 0 & -7500\ \mathrm{N} & 0 & -600\ \mathrm{Nm} & 0 \end{bmatrix}^{\mathrm{T}} \tag{5.12}$$

for the initial orientation of the cabin. For dynamic motion and rotation of the helicopter cabin, the inertia tensors of the stator is estimated from CAD data with

$$\mathbf{I}_{\mathrm{st}} = \begin{bmatrix} 90.8 & 0 & 0 \\ 0 & 87 & 0 \\ 0 & 0 & 4.7 \end{bmatrix} \ \mathrm{kg\ m^2} \tag{5.13}$$

and

$$\mathbf{I}_{\mathrm{hc}} = \begin{bmatrix} 117 & 0 & 0 \\ 0 & 121 & 0 \\ 0 & 0 & 62.5 \end{bmatrix} \ \mathrm{kg\ m^2} \tag{5.14}$$

for the cabin with two passengers. The rated maximum angular acceleration of the helicopter cabin is specified with

$$\alpha_{\max} = 300 \ \frac{\text{deg}}{\text{s}} \tag{5.15}$$

leading to a required maximum torque of

$$\mathbf{T}_{\text{M}} = \mathbf{I}_{\text{hc,z}} \alpha_{\max} = 327 \text{ Nm}. \tag{5.16}$$

Using the platform configuration for the helicopter cabin given by

$$\mathbf{b} = \begin{bmatrix} 0.233 & 0.404 & 0.753 \\ 0.327 & 0.120 & -1.054 \\ -0.327 & 0.050 & 0.865 \\ -0.233 & 0.453 & -0.940 \\ -0.327 & -0.050 & 0.865 \\ -0.233 & -0.453 & -0.940 \\ 0.233 & -0.404 & 0.753 \\ 0.327 & -0.120 & -1.054 \end{bmatrix} \tag{5.17}$$

and the frame parametrization $\mathbf{a}$ from Eq. (5.8) and using the examplary configuartion $\mathbf{x} = \begin{bmatrix} 0 & 0 & 2.5 & 0 & 0 & 0 \end{bmatrix}$ and the external wrench for maximum rotary cabin acceleration $\mathbf{w}_{\text{e}} = \begin{bmatrix} 0 & 0 & -7500 \text{ N} & 0 & -600 \text{ Nm} & 327 \text{ Nm} \end{bmatrix}^{\text{T}}$ with Eq. (5.11) and $\mathbf{f}_{\min} = 1000$ N, $\mathbf{f}_{\max} = 9000$ N leads to the cable forces

$$\mathbf{f} = \begin{bmatrix} 7491 & 2431 & 7146 & 3049 & 7929 & 3156 & 8360 & 2679 \end{bmatrix} \text{ N}. \tag{5.18}$$

The associated section wrenches $\mathbf{w}_{\text{A1}}$ define by the upper cable set 1,3,5,7 and $\mathbf{w}_{\text{A2}}$ defined by the lower cable set 2,4,6,8 yield

$$\mathbf{w}_{\text{A1}} = \begin{bmatrix} -728 & -100 & 10472 & -156 & 829 & -372 \end{bmatrix} \text{ N, Nm} \tag{5.19}$$

$$\mathbf{w}_{\text{A2}} = \begin{bmatrix} 728 & 100 & -2972 & 156 & -229 & 45 \end{bmatrix} \text{ N, Nm}. \tag{5.20}$$

Using the wrench set to estimate the load transfer between the lower and upper part of the cabin allows for realtime processing and monitoring of the internal cabin forces.

5.5 Helicopter Simulation

Using a helicopter cabin together with a cable actuation system as depicted in Fig. 5.18 provides a similar visual user experience as an actual helicopter hover flight since the cables to do not obfuscate the field of view. Since the helicopter is operated without visual cues, the application of motion cueing techniques such as tilt coordination (Berger et al. 2010) is also limited and and motion perception relies on an accurate physics model which replicates the helicopter behavior. While the implementation of realistic helicopter models has its own field of research and the implementation of various helicopter models on the

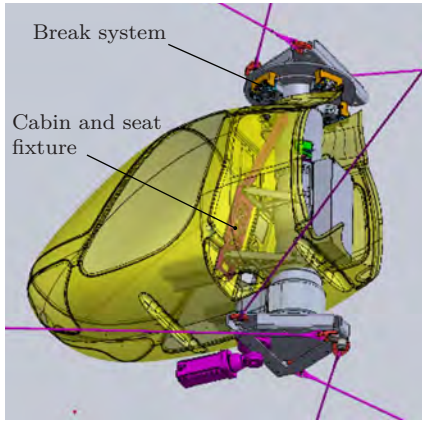

(a) Helicopter cabin structure

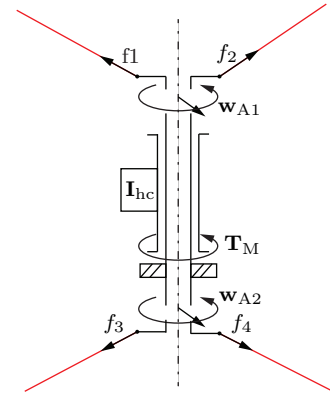

(b) Free body model of helicopter yaw axis

Figure 5.17: Load transmission for helicopter yaw axis

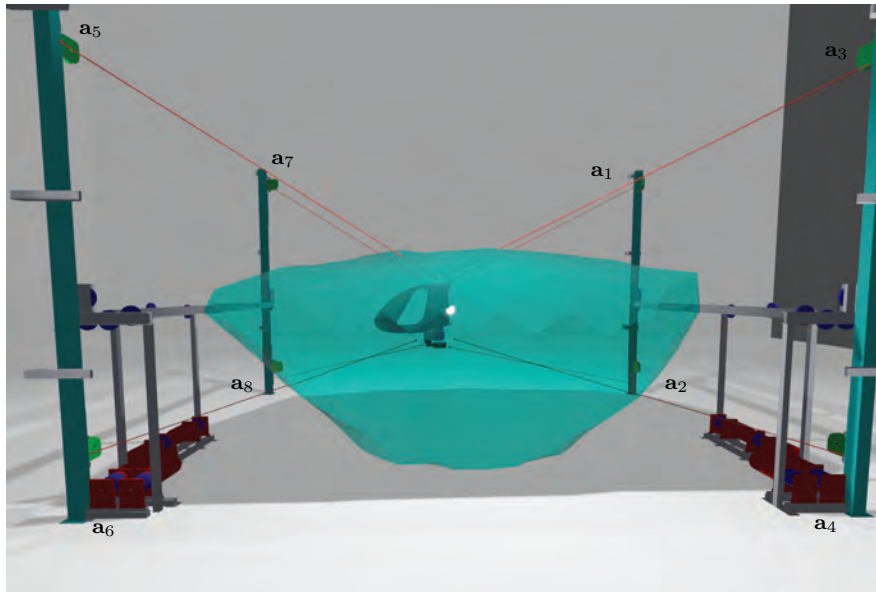

Figure 5.18: CableRobot Simulator with helicopter cabin and wrench feasible constant orientation workspace

CableRobot Simulator is still in development, here a simplified physical first principal helicopter model is implemented which provides the general template for more complex models and allows human-in-the-loop control. Using physics based models in contrast to linearized helicopter state space models also requires a physical representation of the workspace border to keep the simulation states consistent with the actual cabin behavior. Using a Newton-Euler rigid body model as shown in Eq. (5.21) which can be controlled externally by manipulating thrust, pitch, roll, and yaw using the control inputs $\mathbf{f}_{\mathrm{th}}, \boldsymbol{\tau}_{\mathrm{th}}$

$$\begin{bmatrix} m_{\mathrm{P}}\mathbf{E} & \mathbf{0} \\ \mathbf{0} & \mathbf{I}_{\mathrm{P}} \end{bmatrix} \begin{bmatrix} \ddot{\mathbf{x}} \\ \boldsymbol{\alpha} \end{bmatrix} + \begin{bmatrix} \mathbf{0} \\ \boldsymbol{\omega} \times (\mathbf{I}_{\mathrm{P}}\boldsymbol{\omega}) \end{bmatrix} = \begin{bmatrix} \mathbf{D}_{\mathrm{lin}} & \mathbf{0} \\ \mathbf{0} & \mathbf{D}_{\mathrm{rot}}\mathbf{Q} \end{bmatrix} \begin{bmatrix} \dot{\mathbf{x}} \\ \dot{\mathbf{q}} \end{bmatrix} + \begin{bmatrix} \mathbf{f}_{\mathrm{th}} + \mathbf{f}_{\mathrm{e}} + \mathbf{g} \\ \boldsymbol{\tau}_{\mathrm{th}} + \boldsymbol{\tau}_{\mathrm{e}} \end{bmatrix} \tag{5.21}$$

The environmental model provides aerial damping $\mathbf{D}_{\mathrm{lin}}, \mathbf{D}_{\mathrm{rot}}$, and elastic safety walls whose stiffness k_{w} and damping coefficient d_{w} can be chosen according to the test scenario

$$\mathbf{f}_{\mathrm{e}} = (\Delta\mathbf{x} \cdot \mathbf{n})\, k_{\mathrm{w}}\mathbf{e} + (\dot{\mathbf{x}} \cdot \mathbf{n})\, d_{\mathrm{w}}\mathbf{e}. \tag{5.22}$$

All six axes can be automatic controlled by PID-controllers operating in the helicopter fixed frame to assist the passenger during flight. The motion data is mapped directly to the motion controller of the cabin and therefore resembles a 1:1 mapping of simulated and real motion without motion cueing and filtering. The reproducibility of physical simulations on the cable robot is validated by an inertia measurement system on the platform which allows to measure the linear and angular acceleration.

The simulation scenario can be parametrized to fit different applications such as helicopter hover training, disturbance control, and coupled mass experiments which allow to simulate object handling during flight. Although this artificial simulation scenario is solely ment for test purposes and has no claims on realistic flight simulation it contains all necessary elements for various test cases with human-in-the-loop control allowing to change flight dynamics, environmental properties, and safety borders. The difficulty level of the application can be controlled by changing the support of the pitch, yaw, and roll controller during flight. For the evaluation experiment as shown in Figure 5.19a, a bounding box for collision detection with a size of $3 \times 4 \times 2$ m^3 with regards to the local reference frame of the helicopter model was chosen. All axes can be controlled by a human operator using the original helicopter controls. The acceleration tracking results of the test flight are shown in Figure 5.19b. The data show that maximum accelerations during flight simulation where around ± 10 m/s^2. The steep spikes indicate bounce backs from the safety zone around the training area. The flight simulation modules are out of scope of this work, however the capabilities determined with this simplified models allow for a large variety of simulations. More sophisticated models which allow for load balancing and ground effect training are in development. From the applications described in the previous sections, it becomes obvious that the motion control system of the CRS must be SIL-3 certified and provide signal round-trip times of around 1 ms to match the the requirements for human-in-the-loop simulations. The next section provides a detailed description of the control architecture.

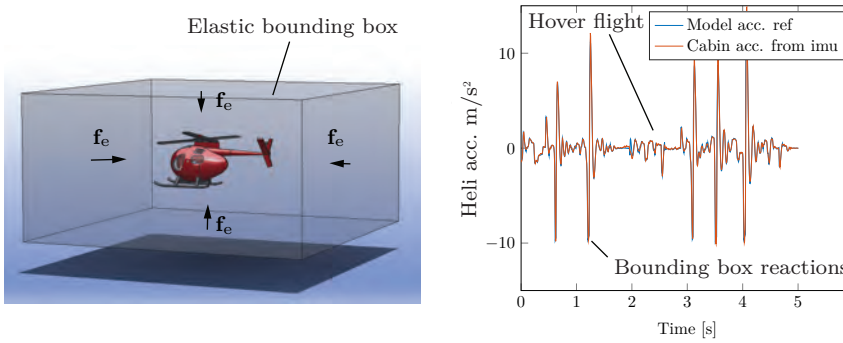

(a) Helicopter simulation with elastic safety bounding box, mapped 1:1 into the real simulator space

(b) Acceleration tracking behavior of the CableRobot Simulator for the helicopter simulation including bounding box reactions

Figure 5.19: Helicopter physics simulation including physical safety bounding box

5.6 Control Architecture and Hardware

The control architecture of the CRS is based on two separate control systems. One industrial rated real-time controller based on the Beckhoff Twincat solution with a cycle time of 250 µs which is used for the motion control algorithms. The second control system is based on controllers from Waagner Biro stage systems which provide SIL 3 safety features but operate only at a cycle time of 15 ms. An outline of the overall control architecture is shown in Fig. 5.20.

A Cartesian motion signal from a trajectory generator, motion cueing algorithm, or human-in-the-loop physical motion simulation is used to compute the desired platform pose $\mathbf{x}$ and velocity $\dot{\mathbf{x}}$ in the motion generator. The motion control signal $\mathbf{q}_{\theta\,\mathrm{tc}}$ for the motors is generated inside the Twincat controller by transforming the Cartesian pose $(\mathbf{x}, \dot{\mathbf{x}})$ into joint space $(\mathbf{q}_\theta, \dot{\mathbf{q}}_\theta)$ using the kinematics model and forwarding it directly to the motor drives allowing motion control with a cycle time of 1 ms. The same signal together with the Cartesian pose is also routed to the Axio stage system controller and compared for consistency with a redundant motion control signal by computing $\Delta\mathbf{q}_\theta = \mathbf{q}_\theta^* - \mathbf{q}_{\theta\,\mathrm{tc}}$ at a cycle time of 15 ms. In case of inconsistencies between both motion signals, the CRS is forced into a safe emergency stop required by the applicable safety standards. The threshold for the signal misalignment for the CRS drive signal is set to $\Delta\mathbf{q}_{\theta\,\mathrm{lim}} = 100$ mm.

While it is possible to compute complex motion control models on the Twincat controller this holds not true for the Axio stage system controller which was not designed to perform complex computations regarding computation power as well as available system memory.

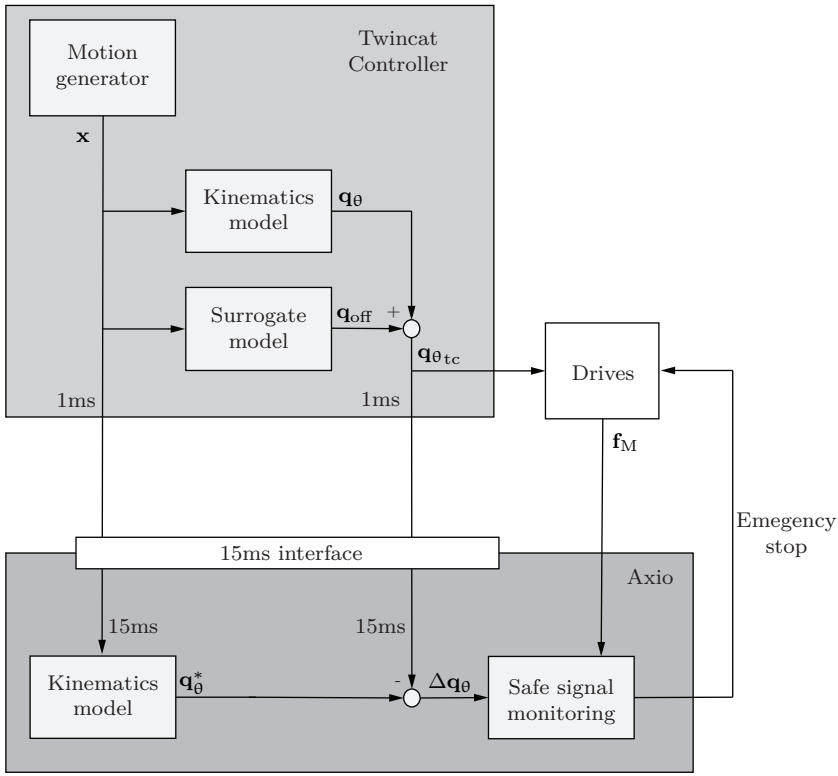

Figure 5.20: Control structure

This aspect combined with the safety requirements for human transport makes it necessary to limit the model complexity for the kinematics to the standard kinematics model from Eq. (2.3). The optimal parameter configuration and best achievable control performance for the standard kinematics model is established in Sec. 6.1. In Sec. 3.5, 3.6 it was shown that the workspace for a kinematics controller without force control is significantly smaller than the possible wrench feasible workspace which is reachable with force control.

Since it is not possible to implement an actual closed-loop force controller as done by (Kraus 2016) due to safety restrictions, a different approach was developed implementing a feed forward force controller which allows force adjustments using model predictions which are rendered into a surrogate model operating on top of the kinematics model as shown in

Fig. 5.20. The surrogate model in general allows to compute arbitrary joint space values for any given pose with

$$\mathbf{q}_{\text{off}} = \boldsymbol{\varphi}_{\text{sg}}(\mathbf{x}). \tag{5.23}$$

The error with respect to the desired pose and force state for the standard kinematics is defined by

$$\begin{bmatrix} \Delta\mathbf{x} \\ \Delta\mathbf{f} \end{bmatrix} = \begin{bmatrix} \mathbf{x}_{\text{M}} & - & \mathbf{x} \\ \mathbf{f}_{\text{M}} & - & \mathbf{f} \end{bmatrix}, \tag{5.24}$$

$$(\mathbf{x}_{\text{M}}, \mathbf{f}_{\text{M}}) = \hat{\boldsymbol{\upsilon}} \circ \boldsymbol{\varphi}(\mathbf{x}). \tag{5.25}$$

Under the assumption that the deviation of the kinematics standard model as stated in Eq. (5.24) is small, one can find an ideal surrogate model

$$(\mathbf{x}_{\text{M}}, \mathbf{f}_{\text{M}}) = \hat{\boldsymbol{\upsilon}} \circ (\boldsymbol{\varphi}(\mathbf{x}) + \boldsymbol{\varphi}_{\text{sg}}(\mathbf{x})) \tag{5.26}$$

such that $(\Delta\mathbf{x}, \Delta\mathbf{f}) \to (0, 0)$ while respecting the limits

$$\boldsymbol{\varphi}_{\text{sg}}(\mathbf{x}) < \Delta\mathbf{q}_{\theta\,\text{lim}}. \tag{5.27}$$

This allows to control the platform pose and cable force state without violating the bounds of the safety controller. As an additional requirement for the surrogate model to work properly, it is assumed that the influence of external process forces is small and that a feed forward controller can be applied without using real-time sensor data during operation. This holds true for motion simulation where no significant interaction between the environment and the simulator cabin is taking place during operation. The variable process wrench exerted by the passengers and additional equipment during the loading phase can be measured before operation but turned out to be negligible. The unknown process wrench exerted by the passengers during operation can also be neglected.

The surrogate model approach is real-time capable using a fixed computation time while allowing the use of arbitrary complex models which are computed and sampled into the surrogate model beforehand.

6 Experimental Evaluation

This chapter evaluates the process described by the meta-model and tested by simulative analysis Chap. 3 to compare the models of different complexity from Chap. 2 with respect to their nominal and optimal configuration which is established by measurements from the CRS testbench system Chap. 5 and optimization according to Chap. 4. Comparing the physical measurements with the parameters obtained by input-output optimization, it is shown which accuracies can be expected applying different models and parametrizations to a real CDPR. Using the stringent process of incrementally increasing model complexity and the associated parametrization, each stage shows the optimal performance which can be achieved with the respective model class. The problem of overcomplex models is shown by the special case of application where the CRS operation is restricted to a constant orientation workspace. In this case it is shown that the associated model parametrization for the platform geometry is not uniquely identifiable and that the same model predictions can be achieved with a simpler model using a point like platform model. This also demonstrates a case where the physical system parametrization and the optimal version cannot be easily related to each other. So for example it is not possible to combine the data from both approaches. ALso, the effect of force propagation and force control which are described in Chap. 3,4 are shown by experimental data. The following section starts with the standard kinematics using the nominal configuration as reference for the later models and optimization.

6.1 Evaluation Methodology and Reference Model

To show the effectiveness of the proposed meta-modelling approach, this section establishes the reference data, reference model, and reference parametrization which are used for the subsequent evaluations. The evaluations regard the different model parametrizations, comparing the physical parametrization and optimal parametrization of each model as well as the optimal parametrization of the different models against each other. The complexity of the models is evaluated regarding their identifiability i.e. if the model complexity is appropriately and can be uniquely identified according the methods in Chap. 4. The question of optimality for the respective models is answered by successive data recordings and optimization runs which allow to estimate the parameter variation for different data sets and thus show the uniqueness of the model parametrization with respect to optimal performance. The question of optimality is closely related to the question of parameter sensitivity, i.e. the question how robust the CDPR can be operate with respect to changes

in the system geometry. An overview of the methodology for the evaluation is shown in Fig. 6.1. The overall process is structured such that it is representative for most CDRP setups and results from this evaluation should be transferable to other CDPRs.

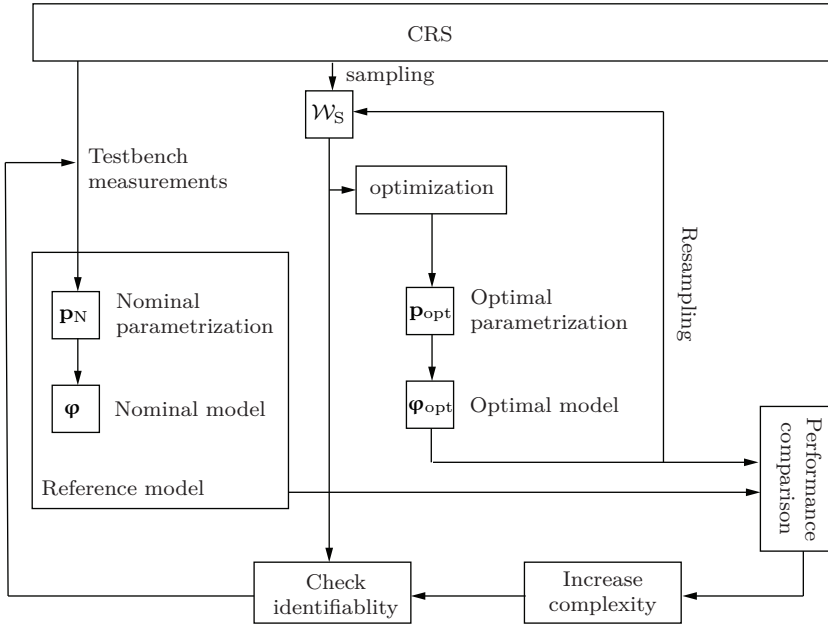

Figure 6.1: Evaluation methodology.

For the reference model, the standard kinematics model from Chap. 2 is chosen. This makes sense as it is the natural starting point for the development of most CDPR applications. Using the standard kinematics model together with methods for direct measurement of the kinematics parameters also defines a situation which can be found for most CDPRs after assembly setup. The standard kinematics model makes the least assumptions about the system and only consists of the geometry parameters $(\mathbf{a}, \mathbf{b})$ which can be measured by coordinate measuring devices such as a laser tracker. Direct use of the nominal parametrization from the design process is also possible if the assembly process can be done with sufficient accuracy. To fully define the reference setup, an initial valid tension state has to be defined making the CDPR operatable. Such setup of the kinematics model, suffers from the unknown tension propagation, limiting the initial reachable workspace. Also, the positioning accuracy is limited due to the effects described in Chap. 3.

Starting with the experimental analysis for the kinematics reference model $\boldsymbol{\varphi}$ from

Eq. (2.3) , the physical geometric parameters are obtained using a Leica laser tracking system. This measurements have to be adjusted to account for the pulley geometry which are not modelled in the standard model leading to the nominal reference model configuration $\mathbf{p}_\mathrm{N} = \begin{bmatrix} \mathbf{a}_\mathrm{N} & \mathbf{b}_\mathrm{N} \end{bmatrix}$ defined by

$$\mathbf{a}_\mathrm{N} = \begin{bmatrix} -5.247 & 7.865 & 6.437 \\ -5.246 & 7.853 & -1.210 \\ 5.263 & 7.581 & 6.484 \\ 5.267 & 7.568 & -0.651 \\ 5.140 & -6.415 & 6.513 \\ 5.148 & -6.430 & -0.633 \\ -5.638 & -6.503 & 6.501 \\ -5.636 & -6.517 & -1.144 \end{bmatrix}, \quad \mathbf{b}_\mathrm{N} = \begin{bmatrix} 0.233 & 0.404 & 0.771 \\ 0.327 & 0.120 & -1.072 \\ -0.327 & 0.050 & 0.883 \\ -0.233 & 0.453 & -0.958 \\ -0.327 & -0.050 & 0.883 \\ -0.233 & -0.453 & -0.958 \\ 0.233 & -0.404 & 0.771 \\ 0.327 & -0.120 & -1.072 \end{bmatrix}. \tag{6.1}$$

The required initial cable tension was manually set to

$$\mathbf{f}_\mathrm{ini} = \begin{bmatrix} 4049 & 1437 & 5190 & 977 & 2857 & 2990 & 4230 & 2213 \end{bmatrix} \text{ N} \tag{6.2}$$

using a common practice for setting the initial tension state $\mathbf{f}_\mathrm{ini}$ by keeping the platform at a certain location while adjusting the cable offsets until a valid tension state is reached. Although this setup is not optimal it is possible to control the CRS within the constrains of positive cable forces to run an initial trajectory $\bar{\mathbf{x}}_\mathrm{ref}$ generating the sample set $\mathcal{W}_\mathrm{S} = \left\{ \bar{\mathbf{x}}_\mathrm{M}, \bar{\mathbf{q}}_\theta, \bar{\mathbf{f}}_\mathrm{M} \right\}$ with $n_\mathrm{s} = 91$ samples. The pose sample set for the parameter identification $\bar{\mathbf{x}}_\mathrm{M}$ is shown in Fig. 6.2. The bounding box of the sampling region is given by $\mathbf{x}_\mathrm{min} = \begin{bmatrix} -1.5 & -1.5 & 1.25 \end{bmatrix}$ and $\mathbf{x}_\mathrm{max} = \begin{bmatrix} 1.5 & 1.5 & 2.0 \end{bmatrix}$. While this sample distribution is sufficient to obtain a well conditioned Jacobian matrix according to criterion Eq. (4.23) with a condition of

$$\kappa(\mathbf{J}_{\mathrm{q}p}) = 31.9, \tag{6.3}$$

the chosen initial sample set had to be limited to a small volume to avoid cable force violations from the cable tension propagation as described in Sec. 3.6. The associated cable forces in a range of $\mathbf{f} = \begin{bmatrix} 272 & 7173 \end{bmatrix}$ N for the eight cables for the given trajectory are shown in Fig. 6.3. While the initial force distribution $\mathbf{f}_\mathrm{ini}$ was chosen in a feasible range of the force limits $\mathbf{f}_\mathrm{min} = 1000$ N and $\mathbf{f}_\mathrm{max} = 9000$ N, one can observe some cable forces approaching critical low tension states during operation. This is caused by the chosen initial cable force states and the model misalignment. The error ϵ_x, $\epsilon_{\bar{\mathrm{x}}}$ define by the error metric from Eq. (3.3, 3.4) of the nominal control model with respect to the measured poses $\boldsymbol{\varphi}(\bar{\mathbf{x}}_\mathrm{ref}, \mathbf{p}_\mathrm{N}) \rightarrow \bar{\mathbf{x}}_\mathrm{M}$ is shown in Fig. 6.4a, 6.4b for the platform positions and rotations respectively.

The mean position error is

$$\epsilon_{\bar{\mathrm{r}}} = 39.80 \text{ mm} \tag{6.4}$$

and the mean rotation error is

$$\epsilon_{\bar{\phi}} = 1.19 \text{ deg}. \tag{6.5}$$

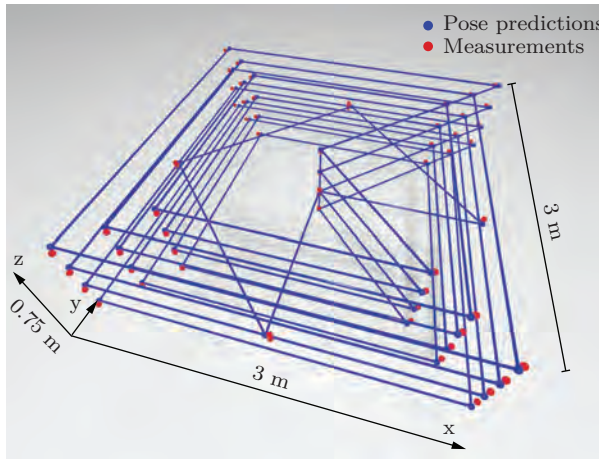

Figure 6.2: Vicon position tracking

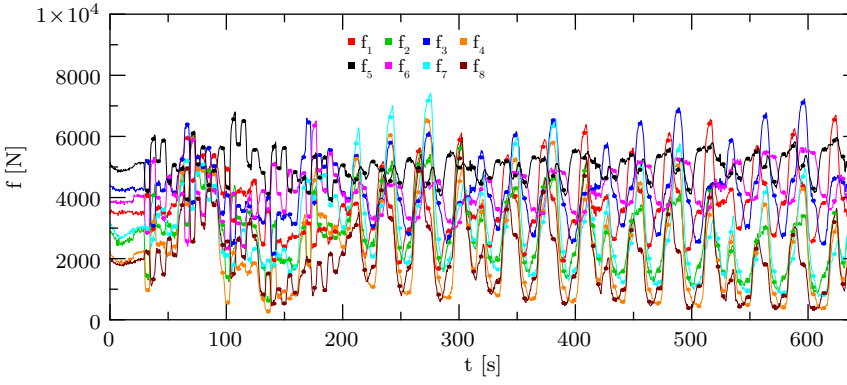

Figure 6.3: Cable forces for sampling set and nominal parametrization

The associated cable length error

$$\epsilon_{\mathrm{q}} = \boldsymbol{\varphi}(\mathbf{x}, \mathbf{p}_{\mathrm{N}}) - \boldsymbol{\varphi}(\mathbf{x}_{\mathrm{M}}, \mathbf{p}_{\mathrm{N}}) \tag{6.6}$$

is shown in Fig. 6.5 with a mean value of $\epsilon_{\bar{\mathrm{q}}} = 23.52$ mm.

Comparing the errors of the initial setup to similar measurements from the IPAnema CDPR at Fraunhofer IPA which was conducted by (Kraus 2016), show position and rotation errors as depicted in Fig. 6.6 with a similar range as measured on the CRS. The mean errors for the IPAnema for the position error where reported to be $\epsilon_{\bar{\mathrm{r}}} = 41.4$ mm for the unladen platform weight and $\epsilon_{\bar{\Phi}} = 1.9°$ for the rotation error compared to $\epsilon_{\bar{\mathrm{r}}} = 39.80$ mm

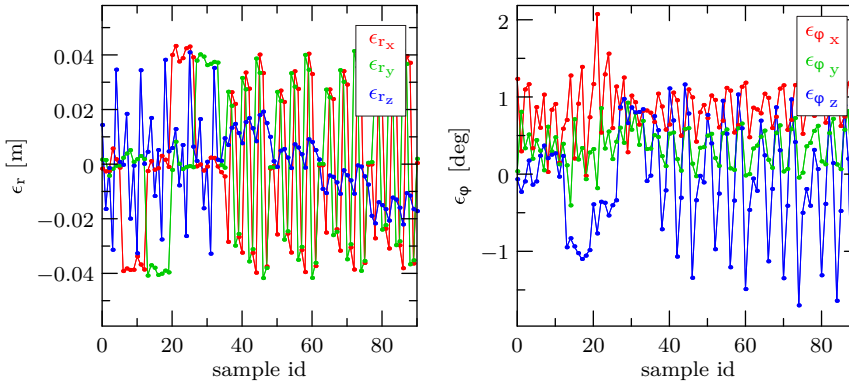

(a) Position error $\epsilon_r = \mathbf{r}_m - \mathbf{r}$

(b) Rotation error $\epsilon_\Phi = \mathbf{\Phi}_m - \mathbf{\Phi}$

Figure 6.4: Pose and rotation error for the nominal model

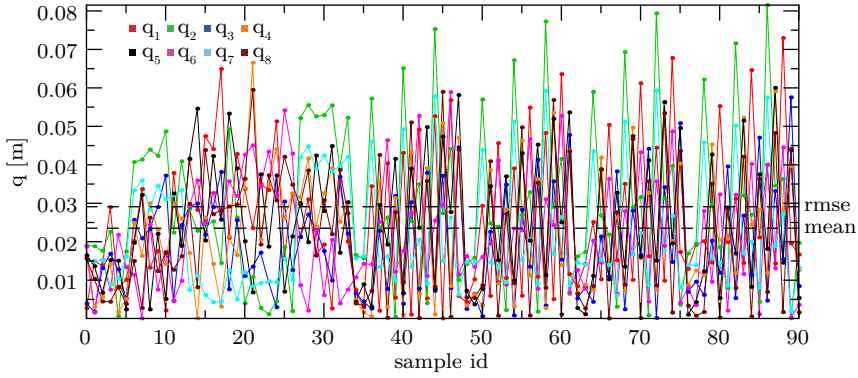

Figure 6.5: Cable length error for nominal parametrization

positioning error and $\epsilon_{\bar{\Phi}} = 1.19$ deg rotational error from the CRS. From this it can be followed that the initial kinematics model provides an appropriate reference to reflect the accuracy which can be achieved by the standard measurement process using direct coordinate measurements conducted by laser trackers or similar equipment. While this result show a certian performance level achievable with the kinematics model, it does not represent the optimal performance which can be reached with this model. Thus before adding additional complexity, optimization of the kinematics model is performed to estimate its true performance value. Optimization and validation of the optimal kinematics model is part of the next section.

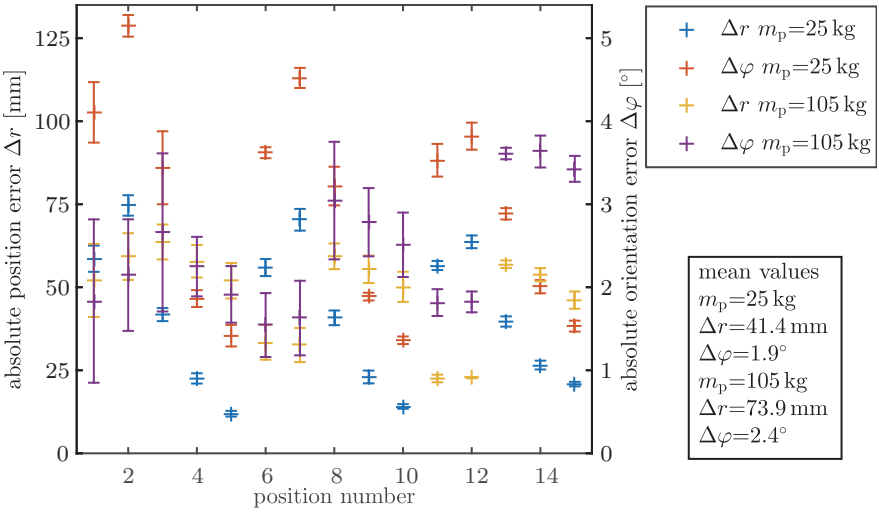

Figure 6.6: Absolute position and orientation accuracy reached with an inverse kinematics model on the IPAnema CDPR (Kraus 2016).

6.2 Kinematics Model Optimization

Optimizing the kinematics control model from the previous section has three purposes. First the question is answered if the model complexity and parametrization is appropriate by showing the identifiability of the parameters and the uniqueness of the optimum. Secondary, the optimal model is used to compute the error for a validation trajectory, providing an estimate for the performance which is achievable with the kinematics model. The results are later used to make a comparison with more complex models. Third, the model is used to show that an optimization in the kinematics domain does not impact the force domain of a CDPR and thus one obtains better positioning accuracy but cannot expect an increase of the reachable workspace or better force distributions in the system. This addresses a common misconception, that poses which cannot be reached by the CDPR or problems with sagging cables may result from errors in the geometry model. In the following, the parameter optimization and validation of the kinematics model is performed in four steps to guarantee that the optimal model has been found:

- Find the optimal model parametrization based on the sample set above.
- Show the error prediction for the optimized model.
- Validating the error predictions by updating the control model and measuring the pose errors for the updated model.

- Using the second recorded sample set to run a second parameter optimization to measure the impact of the parameter adjustments. For an ideal linearized, time invariant, and noiseless system, one would obtain the same optimal parameter set as for the first optimization run.

Running parameter optimization using algorithms such as the Trust Region Reflective algorithm, the Trust Region Dogleg, or the Levenberg Marquardt algorithm (Branch et al. 1999; Moré 1978; Nocedal and Wright 2006) leads in alignment with Eq. (4.8) to the least squares solution with the associated optimal parameter set

$$\mathbf{a}_{\text{opt}} = \begin{bmatrix} -5.436 & 7.663 & 6.518 \\ -5.489 & 7.699 & -1.182 \\ 5.083 & 7.692 & 6.506 \\ 5.104 & 7.707 & -0.619 \\ 5.252 & -6.259 & 6.626 \\ 5.266 & -6.306 & -0.618 \\ -5.417 & -6.619 & 6.635 \\ -5.465 & -6.655 & -1.185 \end{bmatrix}, \quad \Delta\mathbf{a} = \mathbf{a}_{\text{opt}} - \mathbf{a} = \begin{bmatrix} -0.189 & -0.202 & 0.081 \\ -0.243 & -0.154 & 0.028 \\ -0.180 & 0.111 & 0.022 \\ -0.163 & 0.139 & 0.032 \\ 0.112 & 0.156 & 0.113 \\ 0.118 & 0.124 & 0.015 \\ 0.221 & -0.116 & 0.134 \\ 0.171 & -0.138 & -0.041 \end{bmatrix} \tag{6.7}$$

The progression of $\Delta\mathbf{a}$ during optimization is shown in Fig. 6.7a depicting the deviation from the nominal configuration $\mathbf{a}_{\text{N}}$. The changes in the geometric parametrization with $\Delta\mathbf{a}_{\text{min}} = 15.30$ mm and $\Delta\mathbf{a}_{\text{max}} = 242.64$ mm are significant and align with the theoretical results from Sec. 6.1.

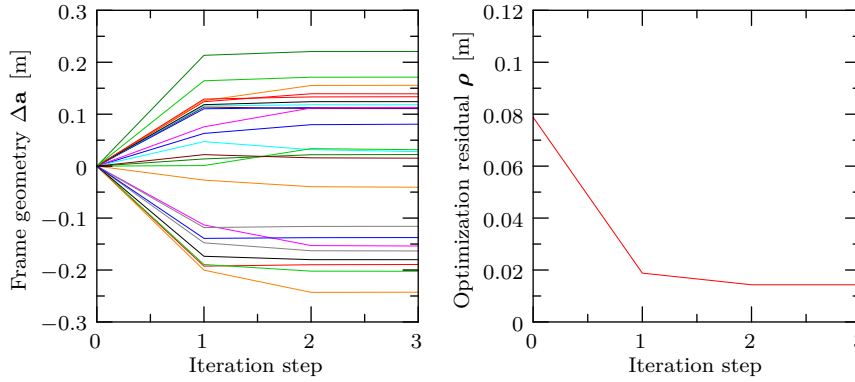

(a) Robot frame geometry $\Delta\mathbf{a}$

(b) Residual error $\boldsymbol{\rho}$

Figure 6.7: Optimization progress

The associated resdiual and condition number of the loss function and associated condition number are shown in Fig. 6.7b. The optimization algorithm converges in three steps

and finds a global optimum as was tested with a uniform random distribution of the initial parameter set using

$$\mathbf{a}_{\text{ini}} = \mathbf{a}_{\text{N}} + \mathbf{a}_{\text{rand}} \text{ with } \mathbf{a}_{\text{rand}} \sim U(-0.5, 0.5) \text{ m}. \tag{6.8}$$

The estimated cable length prediction error yields $\epsilon_{\bar{\text{q}}_{\text{opt}}} = 4.08$ mm. The associated pose prediction error of the optimized model is computed with the forward kinematics model $\mathbf{x}_{\text{P}_j} = \boldsymbol{\upsilon}_{\text{kin}}(\mathbf{q}_{\theta j}, \mathbf{a}_{\text{opt}})$ leading to a mean error of $\epsilon_{\bar{\text{r}}_{\text{opt}}} = 9.66$ mm and $\epsilon_{\bar{\Phi}_{\text{opt}}} = 0.29$ deg . Applying the parameter set to the actual TwinCAT controller for validation leads to Vicon recordings with pose and rotation errors as shown in Fig. 6.8a, 6.8b for all samples with a mean error of $\epsilon_{\bar{\text{r}}\text{V}} = 6.70$ mm and $\epsilon_{\bar{\Phi}_{\text{V}}} = 0.31$ deg. The gray lines in the background of the figures indicate the error of the nominal model $\boldsymbol{\varphi}(\mathbf{p}_{\text{N}})$ from Fig. 6.4 for comparison.

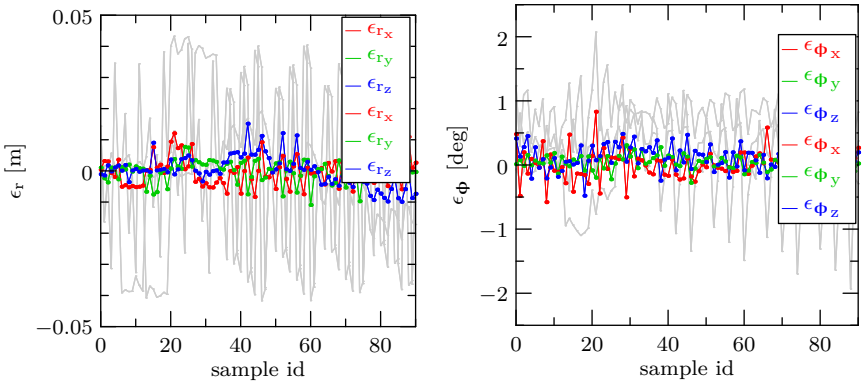

(a) Position error $\epsilon_{\text{r}} = \mathbf{r}_{\text{m}} - \mathbf{r}$

(b) Rotation error $\epsilon_{\Phi} = \boldsymbol{\Phi}_{\text{m}} - \boldsymbol{\Phi}$

Figure 6.8: Measured pose errors with optimized kinematics model.

The associated error in the respective cable length predictions is given in Fig. 6.9 with a mean error over all cables and poses of $\epsilon_{\bar{\text{q}}_{\text{V}}} = 4.15$ mm. The gray lines indicate the nominal error of the model from Fig. 6.5 for comparison. This results show that the error for an optimized kinematics standard model can be significantly decreased with respect to the nominal parametrization whose position error is 594.1% and whose rotational error is 377.2% higher than the optimized version. It should be noted that performance of the nominal model cannot be further improved by more accurate measurements of the physical geometric parameters which is equivalent to an accurate assembly according to the nominal parameters from the technical drawing.

As described in Sec. 6.4, the impact of the geometric optimization on the cable force distribution is small and does not change the workspace volume or stiffness properties in a significant way. Comparing the measurements of the propagating force distributions for

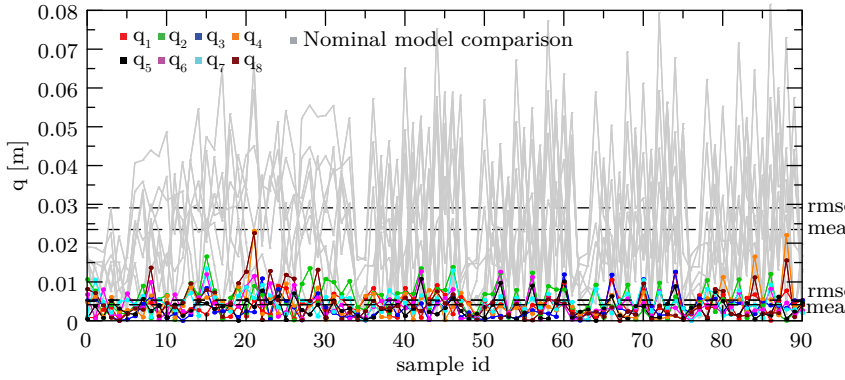

Figure 6.9: Cable length error for the optimized kinematics model in comparison to the nominal model indicated by the gray line in the background (compare Fig. 6.5).

the nominal and optimized model

$$\Delta \mathbf{f} = \mathbf{f}_{\text{opt}} - \mathbf{f}_{\text{N}} \tag{6.9}$$

one obtains the results as shown in Fig. 6.10 for two selected cable forces f_1, f_2 and the difference in the cable forces $\Delta\mathbf{f}$ for all cables. The low impact of the geometric optimization on the overall inner tension state can be understood by consideration of the joint space optimization scheme form Fig. 4.4 where the residual $\boldsymbol{\rho}(\mathbf{p}) = \bar{\mathbf{x}}_{\text{P}}(\mathbf{p}) - \bar{\mathbf{x}}_{\text{M}}$ is minimized. Running the optimization fits the model to the measured system state. In this particular case, the predicted cable lengths to the measured cable lengths. For a perfect model fit with $\boldsymbol{\rho} \to 0$, the cable lengths of the CDPR system in the entirety are unchanged. Only the mapping between the poses $\mathbf{x}$ and the cable lengths $\mathbf{q}$ is changed. For a good initial parametrization, the remapping of cable lengths to platform poses happens in the close vicinity of each pose where the cable forces are quite similar. The observed deviations in Fig. 6.10 are presumably caused by the model imperfections $\mathrm{r}\boldsymbol{\rho} > 0$ and not by the model adjustments where the remapping of the poses lies in the range of few 3 mm. Changes in force distributions for poses that close together are negligible can cannot be measured with the CRS force sensor setup. The mean of the force differences over all cable is $\bar{\Delta\mathbf{f}} = 431$ N.

In the last validation step, a second optimization run with the new recorded data is performed. The difference between the models obtained from the first and second optimization

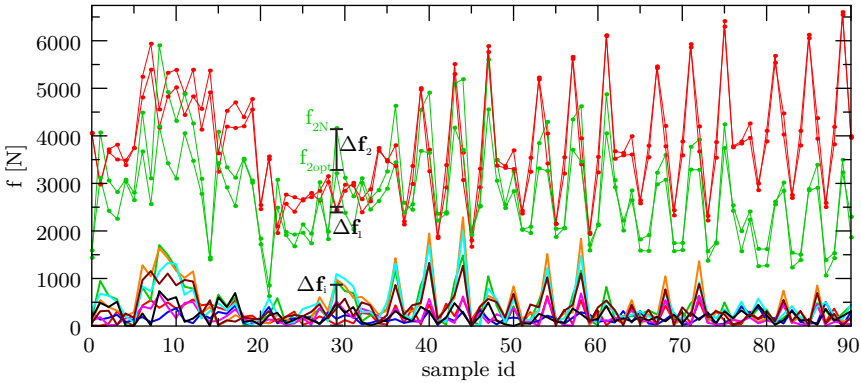

Figure 6.10: Difference $\Delta\mathbf{f}$ of the cable forces before and after optimization of the kinematics model.

yields

$$\Delta\mathbf{a}_2 = \mathbf{a}_{\mathrm{opt}_2} - \mathbf{a}_{\mathrm{opt}} \begin{bmatrix} -0.014 & -0.023 & 0.021 \\ -0.034 & -0.023 & 0.004 \\ -0.009 & -0.001 & 0.013 \\ -0.010 & -0.000 & -0.042 \\ 0.014 & 0.028 & 0.025 \\ 0.021 & 0.018 & 0.007 \\ 0.019 & -0.003 & 0.021 \\ 0.004 & -0.025 & 0.087 \end{bmatrix}. \tag{6.10}$$

The mean position, rotation, and cable length errors of the second optimized model are $\epsilon_{\bar{\mathrm{r}}_{\mathrm{opt2}}} = 10.80$ mm, $\epsilon_{\bar{\Phi}_{\mathrm{opt2}}} = 0.29$ deg, and $\epsilon_{\bar{\mathrm{q}}_{\mathrm{opt2}}} = 3.10$ mm respectively, compared with the errors $\epsilon_{\bar{\mathrm{r}}_{\mathrm{opt}}} = 9.66$ mm, $\epsilon_{\bar{\Phi}_{\mathrm{opt}}} = 0.29$ deg, and $\epsilon_{\bar{\mathrm{q}}_{\mathrm{opt}}} = 4.08$ mm from the first optimized model.

While the residual for the cable length predictions is further minimized this is not the case for the Cartesian pose prediction. This may be caused by the fact that the objective function is stated in joint space and does not consider different weights for the forward kinematics transformation. Considering the overall model performance for the second optimization run, it can be stated that the accuracy remains at a level around 4 mm, although the parametrization of the robot geometry was changed significantly. This is due to the low sensitivity of the cable length error with respect to individual geometry parameters, which also explains the common observation that CDPRs can also be operated with roughly estimated parameter sets, as long as high positioning accuracy is not required. Possible parameter variations and their impact on the residuals are shown in Fig. 6.11 . The orange line at the top shows the residual of the nominal kinematics model $\boldsymbol{\varphi}_{\mathrm{N}}$ After optimization the residual is reduced and reaches the level indicated by the blue line and the optimal

kinematics model $\boldsymbol{\varphi}_{\text{opt}}$. The solid lines show the 24 values of the frame geometry $\mathbf{a}$ and their respective impact on the model residual. Lines with low gradients indicate parameters which can be changed without having much impact on the residual. The gradient for all parameters is below one. While this provides an overview of the general behavior close to the optimal configuration it does not consider other system states such as the cable forces which may add additional constraints limiting the range of possible parameter sets for a given model accuracy class. A more accurate analysis of the parameter variations for a given model error class have to consider the system stiffness as shown in Sec. 3.7. On the other side, some parameters subject to larger variations without violating the error thresholds. This can be seen in Fig. 6.11, 6.12. The intersection of the respective error boundary $\boldsymbol{\varphi}_{\text{opt}}$ and a parameter variation line are the lower limit by which each parameter could by varied without violating the error constraint. The black dots in Fig. 6.12 show the results from a second paramter optimization with a different sample set. One can see the large deviations from the previous optimum leading to $\boldsymbol{\varphi}_{\text{opt}_2}$. Concluding this section, it can be stated that optimization of the kinematics model with a final error of $\epsilon_{\bar{\text{r}}_{\text{opt2}}} = 10.80$ mm, compared to the initial error of $\epsilon_{\bar{\text{r}}} = 39.80$ mm is a very important step with respect to the goal of optimal application performance. The optimization should be conducted before any other measures, especially before the implementation of additional model features. Using an optimized standard kinematics model comes with low computational costs while providing better accuracy than other non-optimized more complex models. To demonstrate the importance of using models with an appropriate level of complexity is shown in the following section by an artificial use-case scenario implemented on the CRS.

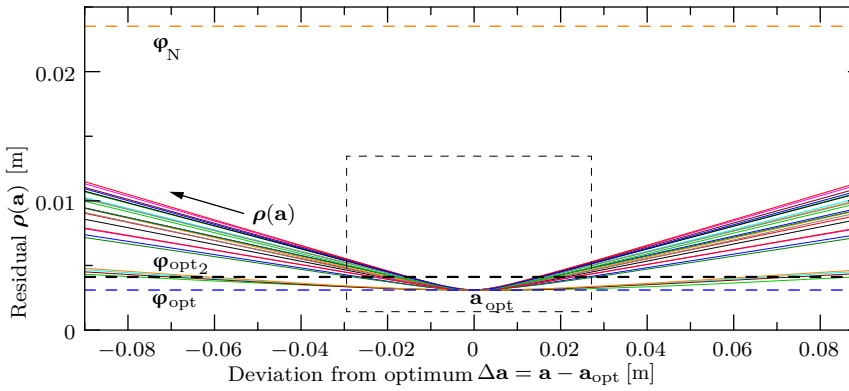

Figure 6.11: Parameter variation with respect to nominal and optimized model residuals

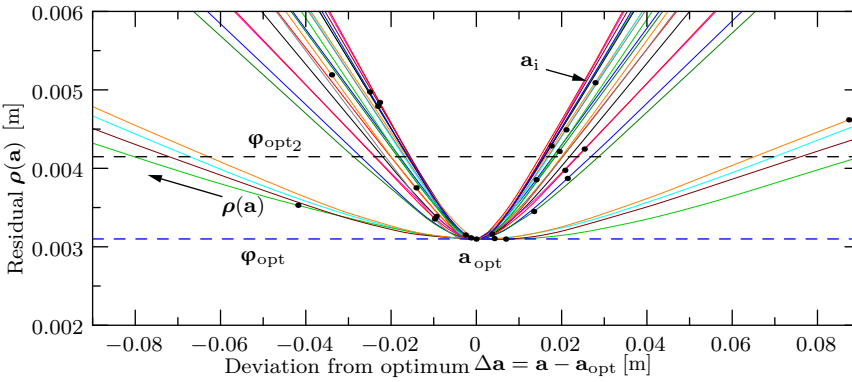

Figure 6.12: Parameter variation with parameter distribution

6.3 Model Complexity

In the following the assumption is made, that the CDPR is only operated in the constant orientation workspace with an arbitrary but fixed orientation. Here, all angles are set to zero $\boldsymbol{\phi} = \mathbf{0}$. Using the same kinematics model as in the previous section and the nominal model parametrization obtained from laser-tracking measurements Eq. (6.1) the mean positioning accuracy of the CRS is $\epsilon_{\bar{\mathrm{r}}} = 37.6$ mm for operation in the constant orientation workspace. This is similar to the value reported before in Eq. (6.4). The kinematics model consists of 48 parameters for the platform. Trying to optimize the model with the same sample set as in the previous section excluding all poses with a rotational part $\boldsymbol{\phi} \neq \mathbf{0}$ leads to a bad conditioned Jacobian matrix $\kappa(\mathbf{J}_{qp}) = 10.3e10$. This can be seen in perspective of an insufficient sample set or in perspective of a insufficient model with too many parameters. While in this case it would be possible to add the rotation samples to make the identification problem solvable, it may not be possible for other over-complex CDPR models to find an appropriate sample set. Keeping the sample set and running the optimization problem with a lasso regularization as described in Sec. 6.4 leads to a condition number of

$$\kappa(\mathbf{J}_{\mathrm{q}p}) = 892.50 \tag{6.11}$$

and the geometry parametrization

$$\mathbf{a}_{\text{opt}} = \begin{bmatrix} -5.672 & 7.262 & 5.791 \\ -5.841 & 7.571 & -0.111 \\ 5.409 & 7.655 & 5.643 \\ 5.340 & 7.255 & 0.299 \\ 5.614 & -6.238 & 5.733 \\ 5.505 & -5.862 & 0.353 \\ -5.660 & -6.249 & 5.868 \\ -5.784 & -6.559 & -0.081 \end{bmatrix}, \quad \mathbf{b}_{\text{opt}} = \begin{bmatrix} 0.002 & 0.004 & 0.008 \\ 0.003 & 0.001 & -0.011 \\ -0.003 & 0.001 & 0.009 \\ -0.002 & 0.005 & -0.010 \\ -0.003 & -0.001 & 0.009 \\ -0.002 & -0.005 & -0.010 \\ 0.002 & -0.004 & 0.008 \\ 0.003 & -0.001 & -0.011 \end{bmatrix}. \tag{6.12}$$

The mean pose prediction error of the model is

$$\epsilon_{\bar{\mathrm{r}}} = 3.15 \text{ mm} . \tag{6.13}$$

The associated pose and cable length errors are depicted in Fig. 6.13. The spatial configuration of this parametrization is depicted in Fig. 6.14 showing the difference between the physical reality (magenta lines) and model parametrization (blue lines). One can see that the model outperforms the physical parametrization although the spatial geometry of platform was effectively removed by zeroing all platform attachment points.

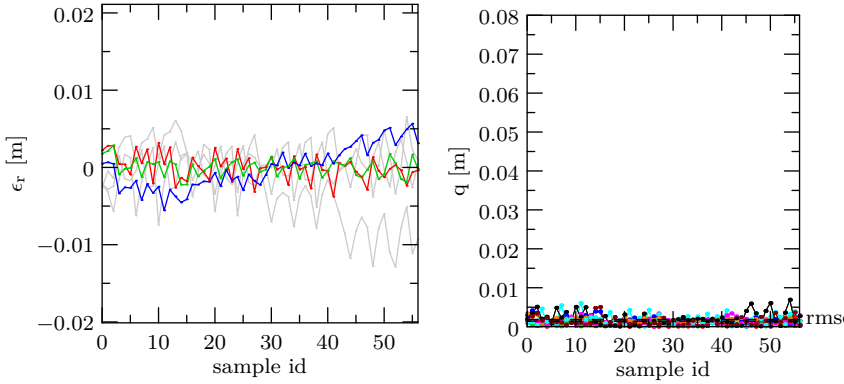

(a) Pose error prediction

(b) Cable length error

Figure 6.13: Predicted pose and cable length error for the for constant orientation workspace.

While the kinematics models form this and the previous sections allow to improve accuracy for a given tension distribution, it cannot be used to improve the tension states. Improving the tension states is desirable to obtain a larger reachable workspaces or to compensate load changes during operation which is part of the next section.

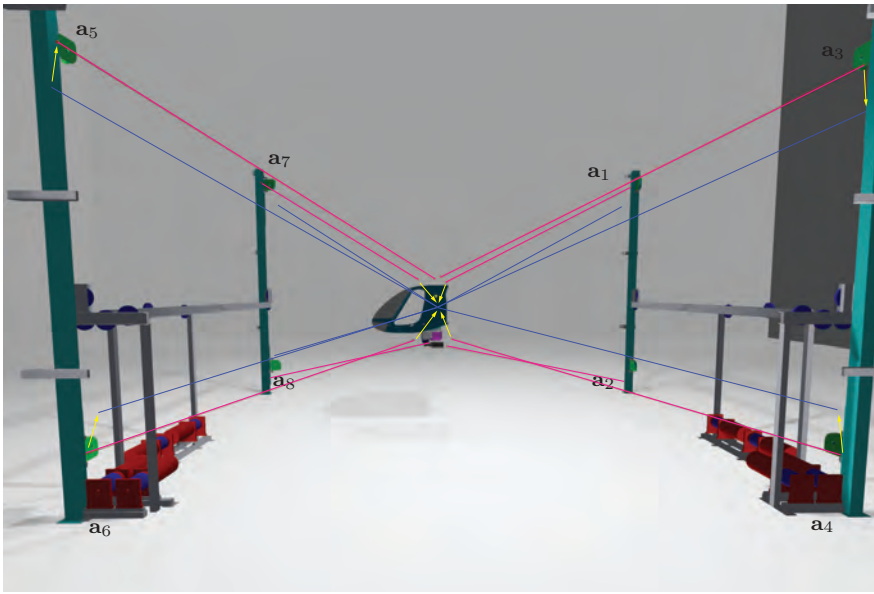

Figure 6.14: Comparison of the physical reality (magenta line) and optimal kinematics model for constant orientation workspace (blue line).

6.4 Elastostatic Model Identification

In the previous section, the capabilities and limits for the kinematics standard model were shown. While it is possible to significantly improve the pose prediction accuracy, the lack of force control leads to a reduced reachable workspace $\mathcal{W}_{\mathrm{R}}$. This is especially problematic when the initial tension state is not chosen carefully in the first stage of the paramter identification process where the CDPR has to be operated with a nominal parameter set. Here the question is answered in how far the modelling of the system compliance affects the pose prediction accuracy and if there is a tradeoff between the pose and force prediction accuracy. Also, the maximum reachable prediction accuracy for the elastostatic model shell be estimated and be compared to the nominal elastostatic model as well as the accuracy of the kinematics model. The identification process again has to be executed in multiple stages starting with an initial kinematics model which allows to explore the close vicinity around the initial position acquiring a data set for the elasto-geometric model identification. The capability of the elastostatic model to control the cable forces now allows to reach a larger proportion of the wrench feasible workspace for further data acquisition which then is used to finalize the elastostatic model.

The initial sample set is chosen from the region with the same bounding box $\mathbf{x}_{\mathrm{min}} =$

$\begin{bmatrix} -1.5 & -1.5 & 1.25 \end{bmatrix}$ and $\mathbf{x}_{\max} = \begin{bmatrix} 1.5 & 1.5 & 2.0 \end{bmatrix}$ as used for the kinematics model optimization resembling the same distribution as shown in Fig. 6.2. To estimate the potential prediction accuracy in the elastic domain of the model, additional tension tests where performed at different poses inside the bounding box. Fig. 6.15 shows a complete overview of the data relevant to the initial parameter identification procedure including the cartesian coordinates of the sample set, the cable length offsets, the resulting cable forces at each sampling point. All of the eight cables are shortened by 30 mm and returned to their original length for each pose separately.

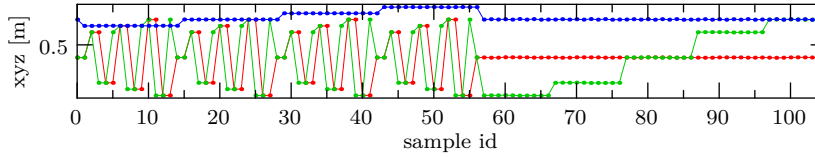

(a) Sample positions for data acquisition.

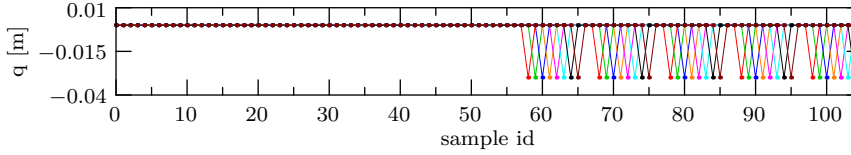

(b) Cable length offsets

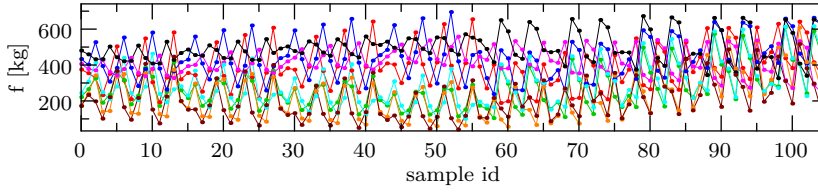

(c) Cable forces

Figure 6.15: Initial sample set for elasto-geometric identification

While the kinematic model requires a reasonable accurate initial parametrization to control the CDPR for the initial sample set, the elasto-static model is not needed for the sampling process. This has the advantage that in general no effort has to be put in the separate estimation of physical parameters such as the platform mass and cable stiffness coefficients which is done here only for comparison of the physical parameterized nominal elastostatic model and the optimized elastostatic model. The identification of the elastostatic model using a kinematics control model can be seen as an identification of the

ground truth model in the meta model as depicted in Fig. 6.16.

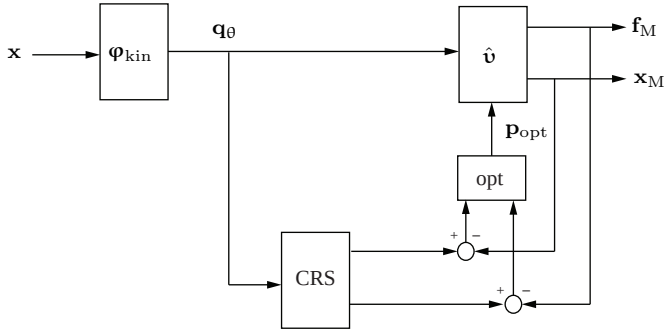

Figure 6.16: Identification of the elastostatic ground-truth model

Using the elasto-geometric model from with the associated 62-dimensional parameter vector

$$\mathbf{p} = \left[\begin{array}{cccc} \mathbf{a} & \mathbf{b} & \mathbf{k}_\mathrm{F} & \mathbf{w}_\mathrm{e} \end{array} \right], \tag{6.14}$$

the initial conditions for the nominal geometric model are chosen the same as for the previous model using laser tracking data

$$\mathbf{a} = \mathbf{a}_\mathrm{N} \text{ and } \mathbf{b} = \mathbf{b}_\mathrm{N} \tag{6.15}$$

from Eq. (6.1). The initial conditions for the force related parameters are derived theoretically and from measurements of the respective components. The nominal values for the cable stiffness is derived from the geometrical and material properties and from a separate test bench experiment as described in the previous section. Using a mean elasticity module of

$$E = 110 \ \frac{\mathrm{kN}}{\mathrm{mm}^2} \tag{6.16}$$

for straightened wire ropes according to (Pott 2018a) the specific cable stiffness is determined by

$$k_{\mathrm{F}i} = \pi \, (0.5 d_\mathrm{r})^2 \, E = 16933 \ \frac{\mathrm{kN}}{\mathrm{m}} \tag{6.17}$$

This value seems to be to high with respect to the measured stiffness coefficients which maybe caused by the additional compliances in the power-train. This are the space frame, the different redirection pulleys, the additional cable length inside the space frame which is not modelled, cable ovalization on the drum, and compliance of the platform attachment points. Considering that the equivalent spring constant of a serial spring system the equivalent compliance is computed by

$$c_\mathrm{powertrain} = c_\mathrm{cable} + c_\mathrm{pul} + c_\mathrm{frame} + c_\mathrm{winch} + \ldots \text{ with } c = k^{-1} \tag{6.18}$$

where the equivalent compliance is dominated by the element with the highest compliance. In case of the ideal linear stiffness model for the cable may not be the leading factor for the overall system compliance. Futher information on the detailed modelling of steel cables can be found in (Feyrer 2015). Test-bench like tests as were performed in Sec. 5.1, Fig. 5.7 regard the elasticity of an entire power train and showing a strong dependency of the measured stiffness coefficients on the tension state. Since the CRS is mainly operated in a force range between 1000 N up to 9000 N, the median value of 5000 N and the associated measured stiffness coefficient

$$k_{\mathrm{F}i} = 2000 \ \frac{\mathrm{kN}}{\mathrm{m}} \text{ with } i = 1 \dots m, \tag{6.19}$$

is chosen for the nominal model. Tests with different initial value sets showed robust convergence to the global optimum. The platform weight for the helicopter cabin can be determined from CAD data and approximated as central mass with

$$\mathbf{w}_{\mathrm{e}} = \begin{bmatrix} 0 & 0 & -5500\ \mathrm{N} & 0 & -480\ \mathrm{Nm} & 0 \end{bmatrix}^{\mathrm{T}} \tag{6.20}$$

or experimentally using the statics model and force sensor measurements. The wrench determination from the force measurements is shown in the next paragraph together with the initial cable offset estimation.

This parametrization fully defines the elastostatic model. To validate the model against the data from Fig. 6.15 an initial cable offset $\mathbf{q}_{\mathrm{off}}$ has to be chosen to control the initial tension state. The cable offset or initial tension state can be seen as an additional parameter for the elastostatic model which is not used in force control mode. If the elastostatic model is used in passive mode the initial tension distribution is propagated to the other poses and must be correctly predicted by an accurate elastostatic model. In force control mode, the cable offsets are changed dynamically with regards to the set points of the force distribution algorithm. While the cable offsets had to be chosen as part of the setup process in the previous part, they had no direct meaning for the kinematics model. For the elastostatic model they can be derived from the initial cable force distribution using the modeled system elasticity. The initial cable force distribution for the helicopter cabin at pose

$$\mathbf{x} = \begin{bmatrix} 0 & 0 & 1.5 & 0 & 0 & 0 \end{bmatrix} \tag{6.21}$$

which is associated with a cabin orientation in the global oriented frame as shown in Fig. 6.17 is given by

$$\mathbf{f}_{\mathrm{ini}} = \begin{bmatrix} 3678 & 2169 & 4250 & 1708 & 3985 & 2394 & 4715 & 1684 \end{bmatrix} \ \mathrm{N}. \tag{6.22}$$

Using this force distribution for load indentification leads to

$$\mathbf{w}_{\mathrm{e}} = \begin{bmatrix} 22.2 & -163.4 & -6005.5 & 179.9 & -755.8 & 43.6 \end{bmatrix} (\ \mathrm{N},\ \mathrm{Nm}) \,. \tag{6.23}$$

The load estimation has a good agreement with the computed approximation from CAD data. The higher load and torque maybe caused by the unmodeled cable mass and additional components which are not included in the CAD model.

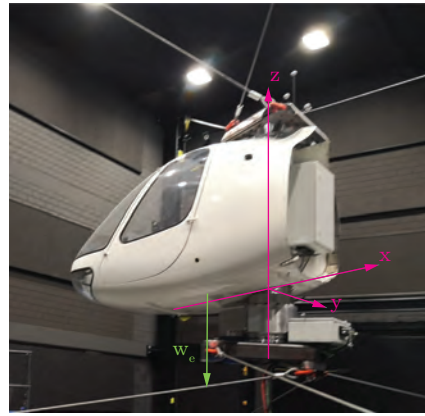

Figure 6.17: Helicopter cabin load estimation with respect to the local reference frame shown in the picture.

Using the estimated cable stiffness coefficients of $\mathbf{k}_\mathrm{F} = 2000\ \frac{\mathrm{kN}}{\mathrm{m}}$ leads to the initial cable offsets

$$\mathbf{q}_\mathrm{off} = \begin{bmatrix} -0.019 & -0.011 & -0.022 & -0.008 & -0.019 & -0.010 & -0.023 & -0.008 \end{bmatrix}\ \mathrm{m}. \tag{6.24}$$

One should note that the estimation of $\mathbf{q}_\mathrm{off}$ is an essential step to obtain good agreement of the model and measurements and has to be performed after every setup. Alternatively the inverse process can applied for the robot setup. This would include the computation of the initial force distribution and its associated cable length offsets which then have to be applied to the CDPR. In practice this is difficult to achieve since the cable offsets are given with respect to the nominal cable length in a tensionless state which is obfuscated by cable sagging and other effects influencing the cable lengths in low tension states such as cable withdrawal at the redirection pulleys and drums. The performance of the obtained elastostatic model with the locally identified subsystem paramterization is shown in Fig. 6.18 for the pose prediction accuracy and in Fig. 6.19 for the force prediction accuracy.

The error of the force prediction mainly is caused by the inaccurate stiffness model, since the estimation of the external cabin wrench is already quite accurate. For a CDPR in suspended configuration, the force propagation could be solely computed from the geometric properties. For an overconstrained CDPR as the CRS, the cable forces are not only caused by the external wrench, but also by the internal tension state whose propagation is influenced by the system stiffness as described in Chap. 3. While the force distribution caused by the external wrench is not very sensitive to errors in the geometry model, the sensitivity of the internal tension state with respect to geometry is amplified by the system stiffness. This can be seen in Fig. 6.19 where the forces of the upper cables f_1, f_3 are mainly

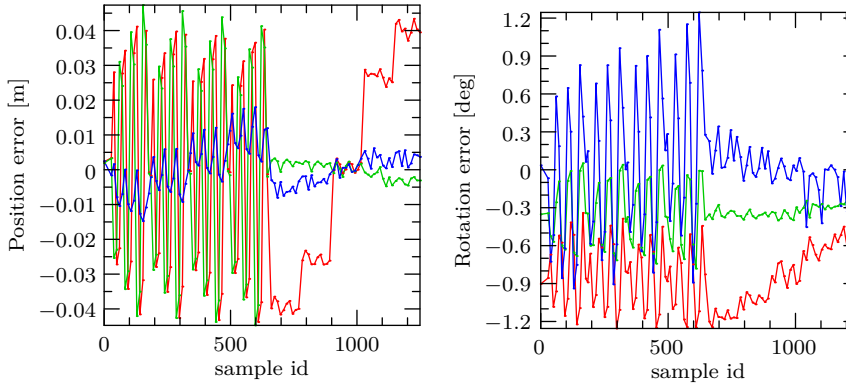

(a) Pose error prediction for the nominal elasto-static model.

(b) Rotation error prediction for the nominal elastostatic model.

Figure 6.18: Pose prediction accuracy

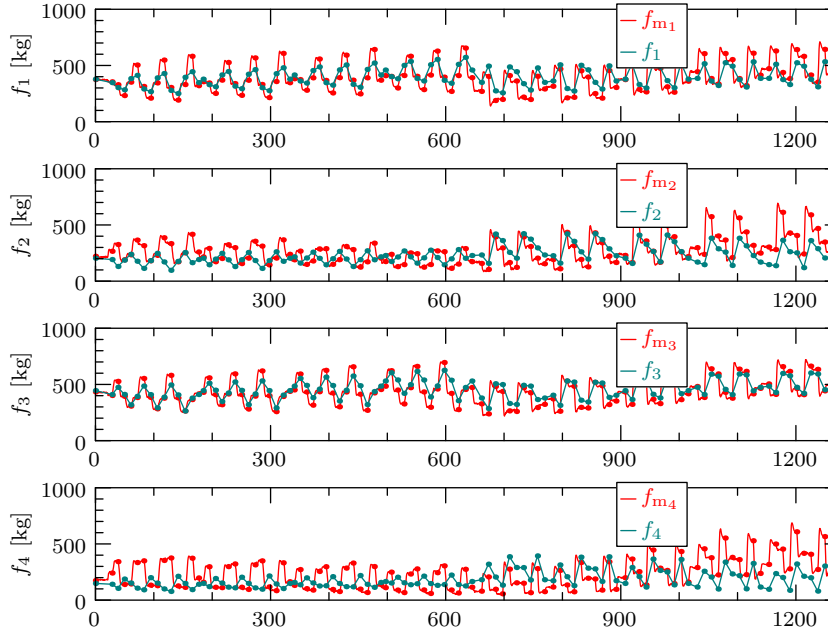

Figure 6.19: Cable force predictions vs. measurements for force propagation cable 1-4

caused by the cabin wrench and the forces of the lower cables f_2, f_4 are mainly caused by the internal tension state which leads to larger errors in the force predictions. The mean position and rotation tracking error for the elastostatic model are

$$\epsilon_{\bar{\mathrm{r}}} = 34.5 \text{ mm and } \epsilon_{\bar{\Phi}} = 1.03^\circ \tag{6.25}$$

respectively. The mean force tracking error of the model is

$$\epsilon_{\bar{\mathrm{f}}} = 2426.84 \text{ N}. \tag{6.26}$$

6.5 Elastostatic Model Optimization

While the elastostatic model in the previous section was parameterized using data from test bench measurements for different subsystems, here the approach of a model optimization is performed to estimate the maximum performance which can be achieved by the elastostatic model class and which is the necessary minimal parametrization. The optimization is performed using the data set from Fig. 6.15 with the measured pose and force data to estimate the platform and frame geometry as well as cable stiffness coefficients and the cabin wrench. The cable offsets are not part of the model parametrization but can be predicted by the model. The sampled rotation space in the recording is small compared to the translational sample space. The parametrization of the platform geometry therefore has limited impact on the model prediction and has to be stabilized using ridge regression from Sec. 6.4 for the parameter optimization adding a penalty function for the optimization of the platform geometry parameters. Using the described sample set leads to condition of the Jacobian varies between $\kappa = \begin{bmatrix} 2838.6 & 2855.7 \end{bmatrix}$ during the optimization run. The optimal parametrization for the elastostatic model which minimizes the pose and force prediction error is

$$\mathbf{a}_{\mathrm{opt}} = \begin{bmatrix} -5.431 & 7.505 & 6.496 \\ -5.773 & 7.840 & -1.195 \\ 5.186 & 7.736 & 6.514 \\ 5.259 & 7.673 & -0.634 \\ 5.329 & -6.298 & 6.556 \\ 5.486 & -6.543 & -0.523 \\ -5.508 & -6.784 & 6.651 \\ -5.597 & -6.881 & -0.998 \end{bmatrix}, \quad \Delta\mathbf{a} = \mathbf{a}_{\mathrm{opt}} - \mathbf{a} \begin{bmatrix} 0.005 & -0.158 & -0.022 \\ -0.284 & 0.141 & -0.013 \\ 0.103 & 0.044 & 0.008 \\ 0.155 & -0.034 & -0.015 \\ 0.077 & -0.039 & -0.070 \\ 0.220 & -0.237 & 0.095 \\ -0.091 & -0.165 & 0.016 \\ -0.132 & -0.226 & 0.187 \end{bmatrix} \tag{6.27}$$

$$\mathbf{b}_{\text{opt}} = \begin{bmatrix} 0.238 & 0.246 & 0.707 \\ 0.076 & 0.267 & -1.100 \\ -0.220 & 0.090 & 0.865 \\ -0.094 & 0.430 & -0.907 \\ -0.270 & -0.086 & 0.818 \\ -0.021 & -0.673 & -0.926 \\ 0.142 & -0.541 & 0.790 \\ 0.179 & -0.292 & -0.999 \end{bmatrix}, \quad \Delta\mathbf{b} = \mathbf{b}_{\text{opt}} - \mathbf{b} \begin{bmatrix} 0.005 & -0.158 & -0.064 \\ -0.251 & 0.147 & -0.028 \\ 0.107 & 0.040 & -0.018 \\ 0.139 & -0.023 & 0.051 \\ 0.057 & -0.036 & -0.065 \\ 0.212 & -0.220 & 0.032 \\ -0.091 & -0.137 & 0.019 \\ -0.148 & -0.172 & 0.073 \end{bmatrix} \tag{6.28}$$

for the geometric parameters and

$$\mathbf{k}_{\text{F}} = \begin{bmatrix} 2010 & 1908 & 3356 & 1745 & 3100 & 2638 & 2544 & 1952 \end{bmatrix}^{\text{T}} \frac{\text{kN}}{\text{m}} \tag{6.29}$$

$$\mathbf{w}_{\text{e}} = \begin{bmatrix} 23.6 & 187.3 & 5929.9 & -292.6 & 515.3 & -360.0 \end{bmatrix}^{\text{T}} \text{ N} \tag{6.30}$$

for the cable stiffness and external wrench respectively. The load indentification shows good agreement with the actual cabin setup estimating a total weight of -604.5 kg and a torque of 360.0 Nm around the y-axis for the initial orientation of the helicopter cabin. The progression of all 62 parameters to the global optimum is shown in Fig. 6.20 requiring eight steps to converge.

Validation of the elastostatic model and the force control is done using a extended cube who is sampled along the outer edges. The force control scheme from the meta-model is applied to the CRS controller using a surrogate model which renders the respective cable length variations of the force control into a static polynomial model. The polynomial model is computational efficient, and provides deterministic runtime behavior. It can be run in parallel to the kinematics model and does not create additional safety issues which could be introduced by running the full elastotstatic model on the real-time system. In order to control the cable forces between 1000 N upto 9000 N, a cable length variation of 41 mm is needed. This is also the differences between the controlled cable length outputs from the elastostatic model and the kinematics model which has to be tolerated by the Waagner Biro safety system. Using force control allows to operate the platform in a larger volume which was not part of the ground-truth model identification process. The force tracking accuracy of the elastostatic model with respect to the new sampling area is shown in Fig. 6.21.

Using an elastostatic control model allows to reach optimal pose prediction accuracy as well as optimal tension states during operation. Summarizing the results from this chapter, it can be stated that the use of a parameter optimization scheme as defined in Chap. 4 is mandatory for the accurate operation of CDPRS and a significant improvement in the accuracy can be expected compared to the direct measurement approach. This results where expected from the analytic considerations in Chap. 3 and could be approved by this findings. In the case of the CRS the accuracy was improved from initially 39.8 mm to 9.66 mm for the final kinematics model. The optimal performance of the elastostatic model was

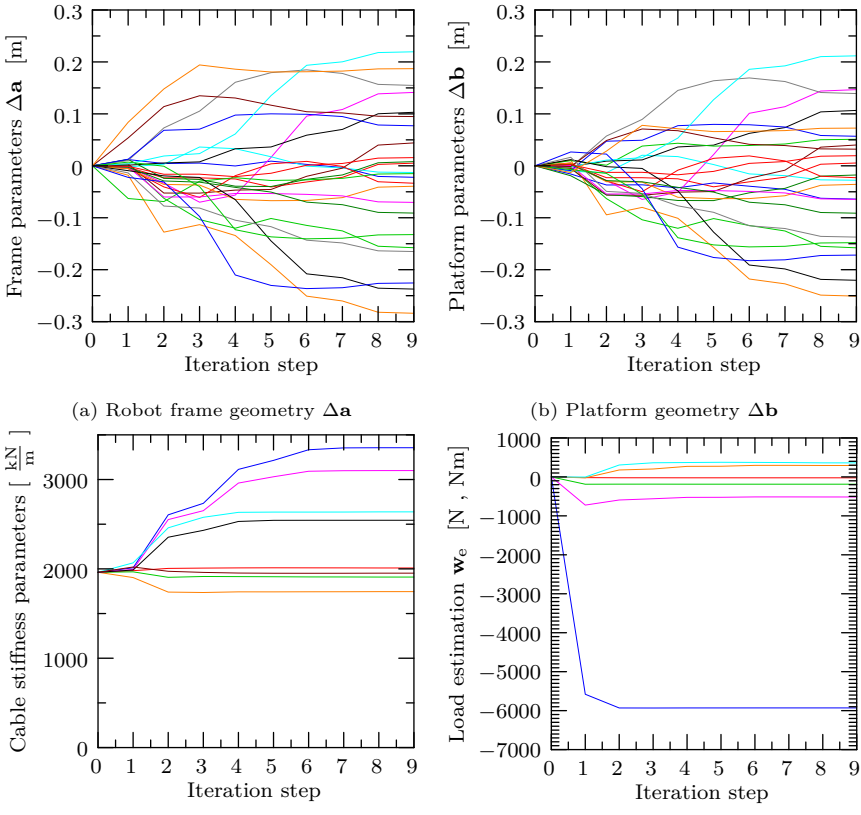

(a) Robot frame geometry $\Delta\mathbf{a}$

(b) Platform geometry $\Delta\mathbf{b}$

(c) Cable stiffness coefficients kF

(d) External wrench $\mathbf{w}_e$

Figure 6.20: Optimization progress for all pamaters of the elastostatic model.

estimated to be 2.73 mm and 582 N. Similar to the kinematics model, this exceeded the accuracy of the direct measurement approach with an initial error of 34.5 mm and 2426 N. Regarding model complexity and optimality it was shown that the investigated models provide an appropriate complexity, which means they were identifiable and lead to similar parameter values for different optimization runs making the parametrization distinct and relatable to the physical reality. This can be seen in contrast to black box models where the combination of generic functions is used to approximate reality. Generic black box models usually have many similar parameter sets which perform equally well. Concerning the importance of model complexity an example was derived limiting platform motion to the constant orientation workspace. The use of direct measurements for parameter estimation showed the same performance for the restricted workspace as for the entire workspace.

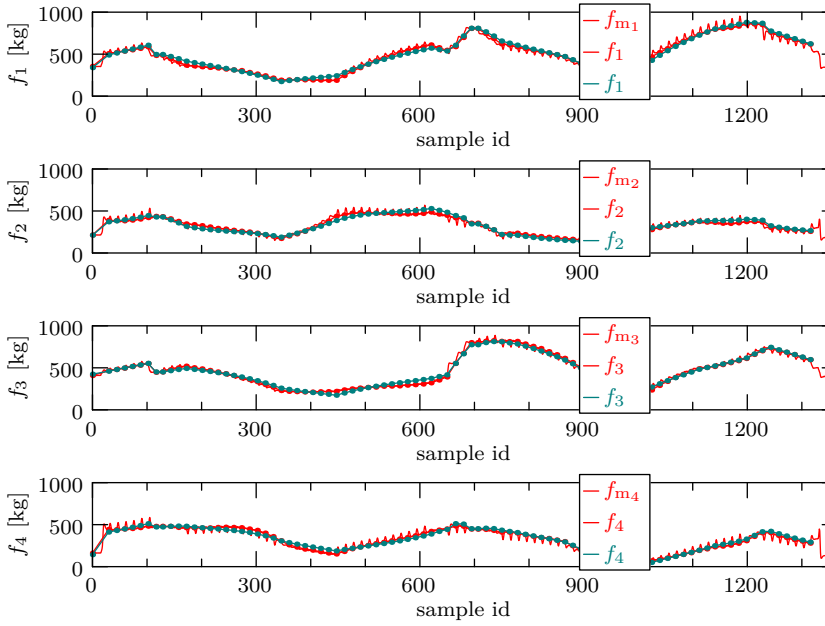

Figure 6.21: Force control with optimized elastostatic model

For model optimization, the model parametrization had to be reduced from 48 parameter to 24 parameters, removing the spatial representation of the simulator cabin to make the model identifiable. The error of the initial model was measured to be 37.6 mm while the reduced and optimized model showed a positioning error of 3.15 mm. From this it can be concluded that the direct measurement approach is more robust for the identification of complex physical CDPR models but comes at the cost of lower accuracy and higher computational cost for the model predictions.

7 Conclusion and Outlook

7.1 Conclusion

In this thesis a meta-model was proposed to define, optimize, and evaluate control models for CDPRS regarding pose tracking accuracy and the reachable workspace in the context of a ground truth model. The use of a ground truth model for the analysis allowed to study the impact of parameter misalignment and varying model complexity on the position accuracy and cable force distribution. Using the force distribution as criterion for the workspace definition, the associated reachable wrench feasible workspace was defined. This allowed to model the effect of parameter optimization on the data acquisition process as well as the final model prediction accuracy.

The model candidates for the investigation were chosen with the focus on safety critical applications such as the motion simulation on the Cable-Robot Simulator where safety integrity level 3 is required for all components. Starting with a kinematics model and gradually increasing complexity to a an elastostatics model, the modelling process was accompanied by the analysis of the expected impact on the model performance level.

Results from the performed simulations and experimental evaluation showed that a simultaneous approach to modelling and optimization is necessary to obtain optimal model performance. Models where individual parameters are not used for input-output optimization but obtained by direct measurement showed to perform worse. Their performance measures cannot be used as reliable source for model comparison since their respective optimal performance level is unknown. Final evaluation on the Cable-Robot Simulator showed the reliability of the approach by comparing the data for models of different complexity to a nominal reference model. Applying the methodology to the control model of the Cable-Robot Simulator allowed to reduce the initial mean position error from 39.8 mm down to 2.73 mm. The associated mean rotation error was reduced from 1.19 deg down to 0.11 deg. Considering the overall size of the Cable-Robot Simulator with $10 \times 14 \times 8$ m it was shown that the proposed approach contributes to the accurate operation of large-scale CDPRs. Considering the Cable-Robot Simulator as highly representative by means of size, architecture, and choice of components, it can be expected that most of the findings in this thesis transfer well to other CDPRs of this class.

7.2 Outlook

Experimental evaluation of the proposed methodology showed the reachable performance level for different models operated on the Cable-Robot Simulator. Although the results can be compared to accuracy reports in literature from other CDPRs, their meaning is quite limited due to the inconsistencies in modelling and performance measurements. Thus based on this work, a more unified comparison of models and measurements from other CDPRs can be obtained which would lead to a more objective estimate of the respective performance measures. Further investigations can be performed in two directions. Running the analysis using the same model assumptions would allow direct comparison of the performance level of the underlying hardware architecture including choice of cable materials, gears, or drive train assemblies. Secondary, further models from literature can be integrated in the proposed framework providing a reliable benchmark which can be used for the future development of CDPR applications and model selection.

Besides optimized modelling and data comparison, insights from the analysis can be used to optimize the design and setup-process of CDPRs. Considering the sensitivity of some parameters with respect to the reachable positioning accuracy, a cost analysis could be performed which estimates the required measurement and assembly accuracy based on predefined error tolerances. Findings from this work suggest that there is space for improvement regarding the cost-performance-optimized design and setup of CDPRs which is a key feature of industrial applicability. Common practice for the installation of CDPRs involves cost intensive measurement equipment for the direct and accurate measurement of system parameters such as laser tracking for the frame geometry. This thesis used two systems, a laser tracker with 0.1 mm accuracy for direct parameter estimation and a Vicon system with around 2 mm tracking accuracy for input output estimation. Considering the better model performance using input-output optimization together with low-accuracy measures leaves room for further improvements regarding the optimal trade-off between accuracy and cost efficiency including model complexity and measurement devices.

Bibliography

Andersen et al. 2014 — Andersen, Torben; Le Coroller, Hervé; Owner-Petersen, Mette, and Dejonghe, Julien, 2014. Linearized Model of an Actively Controlled Cable for a Carlina Diluted Telescope. *Improving the performances of current optical interferometers & future designs*, pp. 153–173.

Antony 2014 — Antony, Jiju, 2014. Design of Experiments for Engineers and Scientists. Amsterdam: Elsevier. ISBN: 9780080994178. DOI: 10.1016/C2012-0-03558-2.

Atkinson 2015 — Atkinson, Anthony C., 2015. Optimal Design. Chichester, UK: John Wiley & Sons, pp. 1–17. ISBN: 9781118445112. DOI: 10 . 1002 / 9781118445112.stat04090.pub2.

Barnett and Gosselin 2015 — Barnett, Eric and Gosselin, Clément, 2015. Large-scale 3D printing with a cable-suspended robot. *Additive Manufacturing*, vol. 7, pp. 27–44. DOI: 10.1016/j.addma.2015.05.001.

Bellmann et al. 2011 — Bellmann, Tobias; Heindl, Johann; Hellerer, Matthias; Kuchar, Richard; Sharma, Karan, and Hirzinger, Gerd, 2011. The DLR robot motion simulator Part I: Design and setup. *Proceedings - IEEE International Conference on Robotics and Automation*, pp. 4694–4701. ISBN: 9781612843865. DOI: 10.1109/ICRA.2011.5979913.

Berger et al. 2010 — Berger, Daniel R.; Schulte-Pelkum, Jörg, and Bülthoff, Heinrich H., 2010. Simulating believable forward accelerations on a stewart motion platform. *ACM Transactions on Applied Percep-*

tion, vol. 7, 1, pp. 1–27. DOI: 10.1145/1658349.1658354.

Blanchet and Merlet 2014 — Blanchet, Laurent and Merlet, Jean-Pierre, 2014. Interference detection for cable-driven parallel robots (CDPRs). *2014 IEEE/ASME International Conference on Advanced Intelligent Mechatronics*. New York: IEEE, pp. 1413–1418. ISBN: 978-1-4799-5736-1. DOI: 10.1109/AIM.2014.6878280.

Branch et al. 1999 — Branch, Mary Ann; Coleman, Thomas F., and Li, Yuying, 1999. A Subspace, Interior, and Conjugate Gradient Method for Large-Scale Bound-Constrained Minimization Problems. *SIAM Journal on Scientific Computing*, vol. 21, 1, pp. 1–23. DOI: 10.1137/S1064827595289108.

Bruckmann et al. 2008 — Bruckmann, Tobias; Mikelsons, Lars; Brandt, Thorsten; Hiller, Manfred, and Schramm, Dieter, 2008. Wire Robots Part I: Kinematics, Analysis & Design. *Parallel Manipulators, New Developments*, April. DOI: 10.5772/5365.

Camanho and Hallett 2011 — Camanho, Pedro P. and Hallett, Stephen, 2011. Composite Joints and Connections. 1st ed. Cambridge, UK: Woodhead Publishing. ISBN: 9780857094926.

Cone 1985 — Cone, Lawrence L., 1985. Skycam: An Aerial Robotic Camera System. *BYTE*, pp. 122–132.

Dietz et al. 2012 — Dietz, Thomas; Andreas, Pott; Alexander, Verl, and De-Gol, Gino, 2012. Patent DE102011114371A1.

Duan et al. 2014 — Duan, Xuechao; Qiu, Yuanying; Duan, Qingjuan, and Du, Jingli, 2014. Calibration and Motion Control of a Cable-Driven Parallel Manipulator Based Triple-Level Spatial Positioner. *Advances*

in Mechanical Engineering, vol. 6, p. 368018. DOI: 10.1155/2014/368018.

Fang 2005 — Fang, Shiqing, 2005. Design, Modeling and Motion Control of Tendon-Based Parallel Manipulators. PhD thesis. University of Duisburg-Essen, 2005.

Feyrer 2015 — Feyrer, Klaus, 2015. Wire Ropes. Berlin, Heidelberg: Springer. ISBN: 978-3-642-54995-3. DOI: 10.1007/978-3-642-54996-0.

Freeman et al. 1995 — Freeman, J.; Watson, G.; Papelis, Y.; Lin, T.; Tayyab, A.; Romano, R., and Kuhl, J., 1995. The iowa driving simulator: An implementation and application overview. *1995 SAE International Congress and Exposition*. DOI: 10.4271/950174.

Gagliardini et al. 2014 — Gagliardini, Lorenzo; Caro, Stephane; Gouttefarde, Marc; Wenger, Philippe, and Girin, Alexis, 2014. Optimal design of cable-driven parallel robots for large industrial structures. *2014 IEEE International Conference on Robotics and Automation (ICRA)*. New York: IEEE, pp. 5744–5749. ISBN: 978-1-4799-3685-4. DOI: 10.1109/ICRA.2014.6907703.

Gagliardini et al. 2018 — Gagliardini, Lorenzo; Gouttefarde, Marc, and Caro, Stéphane, 2018. Design of Reconfigurable Cable-Driven Parallel Robots. Ed. by Erika Ottaviano; Assunta Pelliccio, and Vincenzo Gattulli. Vol. 92. Intelligent Systems, Control and Automation: Science and Engineering. Cham: Springer International Publishing, pp. 85–113. ISBN: 978-3-319-68645-5. DOI: 10.1007/978-3-319-68646-2_4.

Gosselin 2013 — Gosselin, Clément, 2013. Global Planning of Dynamically Feasible Trajectories for Three-DOF Spatial Cable-Suspended Parallel Robots. *Cable-*

Driven Parallel Robots. Ed. by Tobias Bruckmann and Andreas Pott, pp. 3–22. ISBN: 978-3-642-31987-7. DOI: 10.1007/978-3-642-31988-4_1.

Gouttefarde and Gosselin 2004 — Gouttefarde, Marc and Gosselin, Clément, 2004. On the Properties and the Determination of the Wrench-Closure Workspace of Planar Parallel Cable-Driven Mechanisms. *Volume 2: 28th Biennial Mechanisms and Robotics Conference, Parts A and B*. Vol. 2 A. New York: ASME, pp. 337–346. ISBN: 0-7918-4695-4. DOI: 10.1115/DETC2004-57127.

Gouttefarde et al. 2007 — Gouttefarde, Marc; Merlet, Jean-Pierre, and Daney, David, 2007. Wrench-Feasible Workspace of Parallel Cable-Driven Mechanisms. *Proceedings 2007 IEEE International Conference on Robotics and Automation*. New York: IEEE, pp. 1492–1497. DOI: 10.1109/ROBOT.2007.363195.

Gouttefarde et al. 2012 — Gouttefarde, Marc; Collard, Jean-Francois; Riehl, Nicolas, and Baradat, Cedric, 2012. Simplified static analysis of large-dimension parallel cable-driven robots. *2012 IEEE International Conference on Robotics and Automation*. New York: IEEE, pp. 2299–2305. ISBN: 978-1-4673-1405-3. DOI: 10.1109/ICRA.2012.6225159.

Gouttefarde et al. 2014 — Gouttefarde, Marc; Nguyen, Dinh Quan, and Baradat, Cédric, 2014. Kinetostatic Analysis of Cable-Driven Parallel Robots with Consideration of Sagging and Pulleys. *Advances in Robot Kinematics*. Cham: Springer International Publishing, pp. 213–221. ISBN: 978-3-319-06697-4. DOI: 10.1007/978-3-319-06698-1_23.

Gross et al. 2014 — Gross, Dietmar; Hauger, Werner; Schröder, Jörg, and Wall, Wolfgang A., 2014. Technische Mechanik 2. Springer-Lehrbuch. Berlin, Heidel-

berg: Springer. ISBN: 978-3-642-40965-3. DOI: 10.1007/978-3-642-40966-0.

Hanqi Zhuang and Lixin Liu 1996 — Hanqi Zhuang and Lixin Liu, 1996. Self-calibration of a class of parallel manipulators. *Proceedings of IEEE International Conference on Robotics and Automation.* Vol. 2. April. New York: IEEE, pp. 994–999. ISBN: 0-7803-2988-0. DOI: 10.1109/ROBOT.1996.506838.

Hassan and Khajepour 2009 — Hassan, Mahir and Khajepour, Amir, 2009. Analysis of a Large-Workspace Cable-Actuated Manipulator for Warehousing Applications. *Volume 7: 33rd Mechanisms and Robotics Conference, Parts A and B.* Vol. 7. PART A. New York: ASME, pp. 45–53. ISBN: 978-0-7918-4904-0. DOI: 10.1115/DETC2009-87424.

Hastie et al. 2009 — Hastie, Trevor; Tibshirani, Robert, and Friedman, Jerome, 2009. The Elements of Statistical Learning. Vol. 26. Springer Series in Statistics, 4. New York: Springer, pp. 505–516. ISBN: 978-0-387-84857-0. DOI: 10.1007/978-0-387-84858-7.

Hiller et al. 2005 — Hiller, Manfred; Fang, Shiqing; Mielczarek, Sonja; Verhoeven, Richard, and Franitza, Daniel, 2005. Design, analysis and realization of tendon-based parallel manipulators. *Mechanism and Machine Theory*, vol. 40, pp. 429–445. DOI: 10.1016/j.mechmachtheory.2004.08.002.

Hollerbach and Wampler 1996 — Hollerbach, John M. and Wampler, Charles W., 1996. The calibration index and taxonomy for robot kinematic calibration methods. *International Journal of Robotics Research*, vol. 15, pp. 573–591. DOI: 10.1177/027836499601500604.

Husty 1996 — Husty, Manfred L, 1996. An Algorithm for Solving the Direct Kinematic Of Stewart-Gough-Type Platforms. *Mechanism and Machine Theory*, vol. 31, 4, pp. 365–380.

Izard et al. 2017

Izard, Jean-Baptiste; Dubor, Alexandre; Hervé, Pierre-Elie; Cabay, Edouard; Culla, David; Rodriguez, Mariola, and Barrado, Mikel, 2017. Large-scale 3D printing with cable-driven parallel robots. *Construction Robotics*, vol. 1, 1-4, pp. 69–76. DOI: 10.1007/s41693-017-0008-0.

Jin et al. 2018

Jin, XueJun; Jung, Jinwoo; Ko, Seong; Choi, Eunpyo; Park, Jong-Oh, and Kim, Chang-Sei, 2018. Geometric Parameter Calibration for a Cable-Driven Parallel Robot Based on a Single One-Dimensional Laser Distance Sensor Measurement and Experimental Modeling. *Sensors*, vol. 18, 7, p. 2392. DOI: 10.3390/s18072392.

Karnovsky and Lebed 2010

Karnovsky, Igor A. and Lebed, Olga, 2010. Advanced Methods of Structural Analysis. Boston: Springer. ISBN: 978-1-4419-1046-2. DOI: 10.1007/978-1-4419-1047-9.

Khalil and Besnard 1999

Khalil, Wisama and Besnard, Sébastien, 1999. Self calibration of Stewart-Gough parallel robots without extra sensors. *IEEE Transactions on Robotics and Automation*, vol. 15, 6, pp. 1116–1121. DOI: 10.1109/70.817674.

Khalil and Dombre 2004

Khalil, Wisama and Dombre, Etienne, 2004. Modeling, identification & control of robots. London, UK: Kogan Page Science. ISBN: 9781903996669.

Kljuno and Williams 2008

Kljuno, Elvedin and Williams, Robert L., 2008. Vehicle Simulation System: Controls and Virtual-reality-based Dynamics Simulation. *Journal of Intelligent and Robotic Systems*, vol. 52, 1, pp. 79–99. DOI: 10.1007/s10846-008-9204-y.

Knops 2008

Knops, Martin, 2008. Analysis of Failure in Fiber Polymer Laminates. Berlin, Heidelberg: Springer. ISBN: 978-3-540-75764-1. DOI: 10.1007/978-3-540-75765-8.

Kozak et al. 2006 — Kozak, Kris; Qian Zhou, and Jinsong Wang, 2006. Static analysis of cable-driven manipulators with non-negligible cable mass. *IEEE Transactions on Robotics*, vol. 22, 3, pp. 425–433. DOI: 10.1109/TRO.2006.870659.

Kraus et al. 2013a — Kraus, Werner; Spiller, Alexander, and Pott, Andreas, 2013. Energieeffizienz von parallelen Seilrobotern. *SPS IPC DRIVES 2013*. Berlin: VDE Verlag. ISBN: 978-3-8007-3560-0.

Kraus et al. 2013b — Kraus, Werner; Miermeister, Philipp, and Pott, Andreas, 2013. Investigation of the Influence of Elastic Cables on the Force Distribution of a Parallel Cable-Driven Robot. *Mechanisms and Machine Science*. Vol. 12, pp. 103–115. ISBN: 978-3-642-31987-7. DOI: 10.1007/978-3-642-31988-4_7.

Kraus et al. 2015 — Kraus, Werner; Miermeister, Philipp; Schmidt, Valentin, and Pott, Andreas, 2015. Hybrid Position-Force Control of a Cable-Driven Parallel Robot with Experimental Evaluation. *Mechanical Sciences*, vol. 6, 2, pp. 119–125. DOI: 10.5194/ms-6-119-2015.

Kraus 2016 — Kraus, Werner, 2016. Force control of cable-driven parallel robots. *Stuttgarter Beiträge zur Produktionsforschung*. Stuttgart: Fraunhofer Verlag. ISBN: 978-3-8396-0979-8. DOI: 10.18419/opus-6899.

Lamaury and Gouttefarde 2013 — Lamaury, Johann and Gouttefarde, Marc, 2013. Control of a large redundantly actuated cable-suspended parallel robot. *Proceedings - IEEE International Conference on Robotics and Automation*. New York: IEEE, pp. 4659–4664. ISBN: 9781467356411. DOI: 10.1109/ICRA.2013.6631240.

Lamine et al. 2017 — Lamine, Houssein; Laribi, Med Amine; Bennour, Sami; Romdhane, Lotfi, and Zeghloul, Said, 2017. Design study of a cable-based gait training machine. *Journal of Bionic Engineering*, vol. 14, 2, pp. 232–244. DOI: 10.1016/S1672-6529(16)60394-3.

Marquardt 1963 — Marquardt, Donald W., 1963. An Algorithm for Least-Squares Estimation of Nonlinear Parameters. *Journal of the Society for Industrial and Applied Mathematics*, vol. 11, 2, pp. 431–441. DOI: 10.1137/0111030.

Merlet 2004 — Merlet, Jean-Pierre, 2004. Analysis of the Influence of Wires Interference on the Workspace of Wire Robots. *On Advances in Robot Kinematics*. Dordrecht: Springer Netherlands, pp. 211–218. DOI: 10.1007/978-1-4020-2249-4_23.

Merlet and Daney 2010 — Merlet, Jean-Pierre and Daney, David, 2010. A portable, modular parallel wire crane for rescue operations. *2010 IEEE International Conference on Robotics and Automation*. New York: IEEE, pp. 2834–2839. ISBN: 978-1-4244-5038-1. DOI: 10.1109/ROBOT.2010.5509299.

Merlet 2010 — Merlet, Jean-Pierre, 2010. MARIONET, A Family of Modular Wire-Driven Parallel Robots. *Advances in Robot Kinematics: Motion in Man and Machine*. Dordrecht: Springer Netherlands, pp. 53–61. DOI: 10.1007/978-90-481-9262-5_6.

Merlet 2019 — Merlet, Jean-Pierre, 2019. Improving cable length measurements for large CDPR using the Vernier principle. *Mechanisms and Machine Science*. Vol. 74. December, pp. 47–58. ISBN: 9783030207519. DOI: 10.1007/978-3-030-20751-9_5.

Miermeister and Pott 2010 — Miermeister, Philipp and Pott, Andreas, 2010. Modelling and Real-Time Dynamic Simulation of

the Cable-Driven Parallel Robot IPAnema. *New Trends in Mechanism Science: Analysis and Design*, pp. 353–360. ISBN: 978-90-481-9688-3. DOI: 10.1007/978-90-481-9689-0. arXiv: arXiv:1011.1669v3.

Miermeister and Pott 2012 — Miermeister, Philipp and Pott, Andreas, 2012. Auto Calibration Method for Cable-Driven Parallel Robots Using Force Sensors. *Latest Advances in Robot Kinematics*. Ed. by Jadran Lenari and Manfred L Husty. Dordrecht: Springer Netherlands, pp. 269–276. ISBN: 978-94-007-4620-6. DOI: 10.1007/978-94-007-4620-6_34.

Miermeister et al. 2012 — Miermeister, Philipp; Pott, Andreas, and Verl, Alexander, 2012. Auto-calibration method for overconstrained cable-driven parallel robots. *German Conference on Robotics (ROBOTIK-12)*. Berlin: VDE-Verlag, pp. 301–306. ISBN: 978-3-8007-3418-4.

Miermeister et al. 2014 — Miermeister, Philipp; Kraus, Werner; Winkler, Bernd, and Pott, Andreas, 2014. Cable-Driven Robots for the Rapid Deployment of Fully Automated Material Handling Solutions. *41st International Symposium on Robotics; Proceedings of ISR/Robotik 2014;* pp. 143–148. ISBN: 978-3-8007-3601-0.

Miermeister et al. 2015 — Miermeister, Philipp; Kraus, Werner; Lan, Tian, and Pott, Andreas, 2015. An Elastic Cable Model for Cable-Driven Parallel Robots Including Hysteresis Effects. *Mechanisms and Machine Science*. Vol. 32, pp. 17–28. ISBN: 9783319094885. DOI: 10.1007/978-3-319-09489-2_2.

Miermeister and Pott 2015 — Miermeister, Philipp and Pott, Andreas, 2015. Design of cable-driven parallel robots with multiple platforms and endless rotating axes. *Mechanisms and Machine Science*. Vol. 26, pp. 21–29.

ISBN: 9783319107226. DOI: 10.1007/978-3-319-10723-3_3.

Miermeister et al. 2016 — Miermeister, Philipp; Lachele, Maria; Boss, Rainer; Masone, Carlo; Schenk, Christian; Tesch, Joachim; Kerger, Michael; Teufel, Harald; Pott, Andreas, and Bülthoff, Heinrich H., 2016. The CableRobot simulator large scale motion platform based on cable robot technology. *2016 IEEE/RSJ International Conference on Intelligent Robots and Systems (IROS)*. New York: IEEE, pp. 3024–3029. ISBN: 978-1-5090-3762-9. DOI: 10.1109/IROS.2016.7759468.

Miyasaka et al. 2016 — Miyasaka, Muneaki; Haghighipanah, Mohammad; Li, Yangming, and Hannaford, Blake, 2016. Hysteresis model of longitudinally loaded cable for cable driven robots and identification of the parameters. *2016 IEEE International Conference on Robotics and Automation (ICRA)*. New York: IEEE, pp. 4051–4057. ISBN: 978-1-4673-8026-3. DOI: 10.1109/ICRA.2016.7487596.

Montgomery et al. 2012 — Montgomery, Douglas C.; Peck, Elizabeth A., and Vining, Geoffrey G., 2012. Introduction to Linear Regression Analysis. Wiley Series in Probability and Statistics. Chichester, UK: John Wiley & Sons. ISBN: 9780470542811.

Mooring et al. 1993 — Mooring, Benjamin; Roth, Zvi, and Driels, Morris, 1993. Fundamentals of manipulator calibration. *Automatica*. Vol. 29, pp. 1151–1153. ISBN: 0471508640. DOI: 10.1016/0005-1098(93)90119-E.

Moré 1978 — Moré, Jorge J., 1978. The Levenberg-Marquardt algorithm: Implementation and theory. *Watson G.A. (eds) Numerical Analysis*. Vol. 630. Berlin, Heidelberg: Springer, pp. 105–116. ISBN: 978-3-540-08538-6. DOI: 10.1007/BFb0067700.

Nan 2006

Nan, Rendong, 2006. Five hundred meter aperture spherical radio telescope (FAST). *Science in China Series G*, vol. 49, 2, pp. 129–148. DOI: 10.1007/s11433-006-0129-9.

Nesti et al. 2012

Nesti, Alessandro; Barnett-Cowan, Michael; Bülthoff, Heinrich H., and Pretto, Paolo, 2012. Roll rate thresholds in driving simulation. *Seeing and Perceiving*, vol. 25, 0, p. 167. DOI: 10.1163/187847612x647973.

Nguyen et al. 2013

Nguyen, Dinh Quan; Gouttefarde, Marc; Company, Olivier, and Pierrot, Francois, 2013. On the simplifications of cable model in static analysis of large-dimension cable-driven parallel robots. *2013 IEEE/RSJ International Conference on Intelligent Robots and Systems*. New York: IEEE, pp. 928–934. ISBN: 978-1-4673-6358-7. DOI: 10.1109/IROS.2013.6696461.

Nieuwenhuizen and Bülthoff 2013

Nieuwenhuizen, Frank M. and Bülthoff, Heinrich H., 2013. The MPI cybermotion simulator: A novel research platform to investigate human control behavior. *Journal of Computing Science and Engineering*, vol. 7, 2, pp. 122–131. DOI: 10.5626/JCSE.2013.7.2.122.

Nocedal and Wright 2006

Nocedal, Jorge and Wright, Stephen J., 2006. Numerical optimization. Berlin, Heidelberg: Springer, p. 664. ISBN: 9780387303031.

Perreault et al. 2010

Perreault, Simon; Cardou, Philippe; Gosselin, Clément M., and Otis, Martin J.-D., 2010. Geometric Determination of the Interference-Free Constant-Orientation Workspace of Parallel Cable-Driven Mechanisms. *Journal of Mechanisms and Robotics*, vol. 2, 3. DOI: 10.1115/1.4001780.

Piao et al. 2019

Piao, Jinlong; Kim, Eui Sun; Choi, Hongseok; Moon, Chang Bae; Choi, Eunpyo; Park, Jong Oh,

and Kim, Chang Sei, 2019. Indirect force control of a cable-driven parallel robot: Tension estimation using artificial neural network trained by force sensor measurements. *Sensors (Switzerland)*, vol. 19, 11, pp. 1–16. DOI: 10.3390/s19112520.

Pott 2008 — Pott, Andreas, 2008. Forward Kinematics and Workspace Determination of a Wire Robot for Industrial Applications. *Advances in Robot Kinematics (ARK)*. Baz-sur-Mer; France: Springer France, pp. 451–458. ISBN: 978-1-4020-8599-4. DOI: 10.1007/978-1-4020-8600-7_4.

Pott et al. 2009 — Pott, Andreas; Bruckmann, Tobias, and Mikelsons, Lars, 2009. Closed-form Force Distribution for Parallel Wire Robots. *Computational Kinematics*. Berlin, Heidelberg: Springer, pp. 25–34. ISBN: 978-3-642-01946-3. DOI: 10.1007/978-3-642-01947-0_4.

Pott 2010 — Pott, Andreas, 2010. An algorithm for real-time forward kinematics of cable-driven parallel robots. *Advances in Robot Kinematics (ARK)*. Dordrecht: Springer, pp. 529–538. ISBN: 978-90-481-9261-8. DOI: 10.1007/978-90-481-9262-5_57.

Pott 2012 — Pott, Andreas, 2012. Influence of Pulley Kinematics on Cable-Driven Parallel Robots. *Latest Advances in Robot Kinematics*. Ed. by Jadran Lenarcic and Manfred Husty. January 2012. Dordrecht: Springer Netherlands, pp. 197–204. ISBN: 978-94-007-4619-0. DOI: 10.1007/978-94-007-4620-6_25.

Pott 2013 — Pott, Andreas, 2013. Cable-Driven Parallel Robots. Ed. by Tobias Bruckmann and Andreas Pott. Vol. 12. Mechanisms and Machine Science, January. Berlin, Heidelberg: Springer. ISBN: 978-

3-642-31987-7. DOI: 10.1007/978-3-642-31988-4.

Pott 2018a — Pott, Andreas, 2018. Cable-Driven Parallel Robots. Vol. 120. Springer Tracts in Advanced Robotics, 3. Cham: Springer International Publishing, pp. 110–110. ISBN: 978-3-319-76137-4. DOI: 10.1007/978-3-319-76138-1.

Pott 2018b — Pott, Andreas, 2018. Efficient computation of the workspace boundary, its properties and derivatives for cable-driven parallel robots. *Mechanisms and Machine Science*, vol. 50, June, pp. 190–197. DOI: 10.1007/978-3-319-60867-9_22.

Reichenbach et al. 2019 — Reichenbach, Thomas; Tempel, Philipp; Verl, Alexander, and Pott, Andreas, 2019. Static Analysis of a Two-Platform Planar Cable-Driven Parallel Robot with Unlimited Rotation. *Mechanisms and Machine Science*. Vol. 74. June, pp. 121–133. ISBN: 9783030207519. DOI: 10.1007/978-3-030-20751-9_11.

Reichert et al. 2015 — Reichert, Christopher; Glogowski, Paul, and Bruckmann, Tobias, 2015. Dynamische Rekonfiguration eines seilbasierten Manipulators zur Verbesserung der mechanischen Steifigkeit. Aachen: Inst. für Getriebetechnik und Maschinendynamik, pp. 91–96. ISBN: 978-3-00-048814-6. DOI: 10.17877/DE290R-7388.

Riehl et al. 2009 — Riehl, Nicolas; Gouttefarde, Marc; Krut, Sébastien; Baradat, Cédric, and Pierrot, François, 2009. Effects of non-negligible cable mass on the static behavior of large workspace cable-driven parallel mechanisms. *2009 IEEE International Conference on Robotics and Automation*. New York: IEEE, pp. 2193–2198. ISBN: 978-1-4244-2788-8. DOI: 10.1109/ROBOT.2009.5152576.

Ruder 2016

Ruder, Sebastian, 2016. An overview of gradient descent optimization algorithms, pp. 1–14. arXiv: 1609.04747.

Salcudean et al. 1994

Salcudean, Septimiu E.; Drexel, P.A.; Ben-Dov, D.; Taylor, A.J., and Lawrence, P.D., 1994. A six degree-of-freedom, hydraulic, one person motion simulator. *Proceedings of the 1994 IEEE International Conference on Robotics and Automation*. Washington DC: IEEE Comput. Soc. Press, pp. 2437–2443. ISBN: 0-8186-5330-2. DOI: 10.1109/ROBOT.1994.351146.

Sandretto et al. 2013

Sandretto, Julien Alexandre; Daney, David, and Gouttefarde, Marc, 2013. Calibration of a Fully-Constrained Parallel Cable-Driven Robot. *Romansy 19 Robot Design, Dynamics and Control*. 2007. Vienna: Springer, pp. 77–84. ISBN: 978-3-7091-1378-3. DOI: 10.1007/978-3-7091-1379-0_10.

Schenk et al. 2017

Schenk, Christian; Masone, Carlo; Miermeister, Philipp, and Bülthoff, Heinrich H., 2017. Modeling and analysis of cable vibrations for a cable-driven parallel robot. *2016 IEEE International Conference on Information and Automation, IEEE ICIA 2016*, pp. 454–461. ISBN: 9781509041022. DOI: 10.1109/ICInfA.2016.7831867.

Schmidt and Pott 2013

Schmidt and Pott, Andreas, 2013. Implementing Extended Kinematics of a Cable-Driven Parallel Robot in Real-Time. Vol. 12. September 2013, pp. 287–298. ISBN: 978-3-642-31987-7. DOI: 10.1007/978-3-642-31988-4_18.

Schmidt et al. 2014

Schmidt; Müller, Bertram, and Pott, Andreas, 2014. Solving the Forward Kinematics of Cable-Driven Parallel Robots with Neural Networks and Interval Arithmetic. *Computational Kinematics*.

Vol. 15, pp. 103–110. ISBN: 978-94-007-7213-7. DOI: 10.1007/978-94-007-7214-4_12.

Schmidt and Pott 2016 — Schmidt and Pott, Andreas, 2016. Investigating the effect of cable force on winch winding accuracy for cable-driven parallel robots. *Proceedings of the Institution of Mechanical Engineers, Part K: Journal of Multi-body Dynamics*. Vol. 230. 3, pp. 237–241. DOI: 10.1177/1464419315586517.

Schmidt 2013 — Schmidt, Jordan Michael, 2013. People mover, Patent US20140274431.

Shalev-Shwartz and Wexler 2016 — Shalev-Shwartz, Shai and Wexler, Yonatan, 2016. Minimizing the Maximal Loss: How and Why? *jmlr.org*. arXiv: 1602.01690.

Surdilovic and Bernhardt 2004 — Surdilovic, Dragoljub and Bernhardt, Rolf, 2004. STRING-MAN: a new wire robot for gait rehabilitation. *IEEE International Conference on Robotics and Automation, Proceedings. ICRA 2004*. New York: IEEE, 2031–2036 Vol.2. ISBN: 0-7803-8232-3. DOI: 10.1109/ROBOT.2004.1308122.

Tang et al. 2011 — Tang, XiaoQiang; Zhu, WenBai; Sun, CaiHong, and Yao, Rui, 2011. Similarity model of feed support system for FAST. *Experimental Astronomy*, vol. 29, 3, pp. 177–187. DOI: 10.1007/s10686-010-9211-4.

Tempel et al. 2015a — Tempel, Philipp; Schnelle, Fabian; Pott, Andreas, and Eberhard, Peter, 2015. Design and Programming for Cable-Driven Parallel Robots in the German Pavilion at the EXPO 2015. *Machines*, vol. 3, 3, pp. 223–241. DOI: 10.3390/machines3030223.

Tempel et al. 2015b — Tempel, Philipp; Miermeister, Philipp; Lechler, Armin, and Pott, Andreas, 2015. Modelling of Kinematics and Dynamics of the IPAnema 3 Cable Robot for Simulative Analysis. *Applied Me-*

chanics and Materials, vol. 794, pp. 419–426. DOI: 10.4028/www.scientific.net/AMM.794.419.

Teufel et al. 2007 — Teufel, Harald; Nusseck, Hans-Günther; Beykirch, Karl A; Butler, John S; Kerger, Michael, and Bülthoff, Heinrich H, 2007. MPI Motion Simulator: Development and analysis of a novel motion simulator. *AIAA Modeling and Simulation Technologies Conference and Exhibit*, pp. 1–11. ISBN: 978-1-62410-160-1. DOI: 10.2514/6.2007-6476.

Trautwein et al. 2018 — Trautwein, Felix; Tempel, Philipp, and Pott, Andreas, 2018. A Symbolic-Numeric Method to Capture the Impact of Varied Geometrical Parameters on the Translational Workspace of a Planar Cable-Driven Parallel Robot. *2018 International Conference on Reconfigurable Mechanisms and Robots (ReMAR)*. New York: IEEE, pp. 1–7. ISBN: 978-1-5386-6380-6. DOI: 10.1109/REMAR.2018.8449891.

Verhoeven et al. 1998a — Verhoeven, Richard; Hiller, Manfred, and Tadokoro, Satoshi, 1998. Workspace Of Tendon-Driven Stewart Platforms : Basics , Classification , Details On The Planar 2-DOF Class. Zürich: Institute of Robotics, ETH-Zürich.

Verhoeven et al. 1998b — Verhoeven, Richard; Hiller, Manfred, and Tadokoro, Satoshi, 1998. Workspace, Stiffness, Singularities and Classification of Tendon-Driven Stewart Platforms. *Advances in Robot Kinematics: Analysis and Control*. Dordrecht: Springer Netherlands, pp. 105–114. DOI: 10.1007/978-94-015-9064-8_11.

Verhoeven and Hiller 2000 — Verhoeven, Richard and Hiller, Manfred, 2000. Estimating the Controllable Workspace of Tendon-Based Stewart Platforms. *Advances in Robot Kinematics*. Dordrecht: Springer Nether-

lands, pp. 277–284. DOI: 10.1007/978-94-011-4120-8_29.

Verhoeven 2004 — Verhoeven, Richard, 2004. Analysis of the Workspace of Tendon-based Stewart Platforms. PhD thesis. University of Duisburg-Essen, 2004.

Verl et al. 2008 — Verl, Alexander; Boye, Tim, and Pott, Andreas, 2008. Measurement pose selection and calibration forecast for manipulators with complex kinematic structures. *CIRP Annals - Manufacturing Technology*, vol. 57, 1, pp. 425–428. DOI: 10.1016/j.cirp.2008.03.044.

Walther and Moore 2005 — Walther, Bruno A. and Moore, Joslin L., 2005. The concepts of bias, precision and accuracy, and their use in testing the performance of species richness estimators, with a literature review of estimator performance. *Ecography*, vol. 28, 6, pp. 815–829. DOI: 10.1111/j.2005.0906-7590.04112.x.

Wampler et al. 1995 — Wampler, Charles W.; Hollerbach, John M., and Arai, Tatsuo, 1995. An implicit loop method for kinematic calibration and its application to closed-chain mechanisms. *IEEE Transactions on Robotics and Automation*, vol. 11, 5, pp. 710–724. DOI: 10.1109/70.466613.

Wu et al. 2011 — Wu, Ming; Hornby, T. George; Landry, Jill M.; Roth, Heidi, and Schmit, Brian D., 2011. A cable-driven locomotor training system for restoration of gait in human SCI. *Gait and Posture*, vol. 33, 2, pp. 256–260. DOI: 10.1016/j.gaitpost.2010.11.016.

Yuan 2015 — Yuan, Han, 2015. Static and dynamic stiffness analysis of cable-driven parallel robots. PhD thesis. INSA Rennes, 2015.

Zhong and Qian 2018

Zhong, Yanqi and Qian, Sen, 2018. A Cable-Driven Parallel Robot for 3D Printing. *2018 IEEE International Conference on Mechatronics, Robotics and Automation (ICMRA)*. New York: IEEE, pp. 199–203. ISBN: 978-1-5386-5270-1. DOI: 10.1109/ICMRA.2018.8490542.